Performance evaluation of the prototype CBM Silicon Tracking System

Results from operation in the mCBM at the SIS18 demonstrator experiment

Dissertation

zur Erlangung des Doktorgrades

der Naturwissenschaften

vorgelegt beim Fachbereich Physik

der Johann Wolfgang Goethe-Universität

in Frankfurt am Main

von

Dario Alberto Ramirez Zaldivar

aus Holguin, Kuba

Frankfurt am Main 2025

D30

vom Fachbereich Physik der

Johann Wolfgang Goethe-Universität als Dissertation angenommen.

Dekan: Prof. Dr. Roger Erb

Gutachter: Prof. Dr. Alberica Toia

Prof. Dr. Christoph Blume

Datum der Disputation:

Abstract

The study of strongly interacting matter under extreme conditions remains a central challenge in modern particle physics, particularly in the poorly understood regions of the QCD phase diagram at high baryon chemical potential. While the Standard Model and QCD in particular provide a solid theoretical foundation, they face limitations in describing dense systems, both computationally and experimentally. Probing these conditions is crucial for understanding phenomena such as the early universe and neutron stars.

Progress in this field relies on the precise reconstruction of particles produced in heavy-ion collisions, with tracking detectors playing a pivotal role. Their spatial and temporal resolution directly impacts vertex reconstruction and the identification of short-lived particles, especially in high-multiplicity environments. Meeting these demands is key to detecting rare signals of phase transitions or critical phenomena.

The CBM experiment at FAIR is being built to address this challenge. It aims to explore the QCD phase diagram at high baryon chemical potential through high-rate, high-precision measurements of rare observables.

The primary objective of this thesis is to rigorously characterize the performance of the Silicon Tracking System for the CBM experiment under the realistic and challenging conditions typical of heavy-ion collisions. This is done using the mini-CBM (mCBM) functional prototype demonstrator. The setup was operated in different beam-test experiments at the SIS18. This allows for evaluating the operational performance of the STS detector installed in the setup.

Particular emphasis is placed on quantifying the detector's spatial and temporal resolution, the hit reconstruction efficiency, and the detector capability for tracking, vertex, and pointing resolution. By providing a comprehensive assessment of detector capabilities in realistic operational environments, the thesis ensures that the STS detector is sufficiently precise and robust to meet the demands of the CBM experiment. The agreement of performance benchmark measurements with simulations enables reliable projections of detector performance for the final CBM setup.

Extended abstract

The behavior of strongly interacting matter under extreme temperature and density conditions is one of the most compelling frontiers in contemporary particle physics. Despite substantial theoretical and experimental progress, vast regions in the phase diagram of QCD matter remain poorly understood, including the possible location of a critical point and the nature of the phase transition between hadronic matter and the quark-gluon plasma (QGP), especially at large baryon chemical potential.

The Standard Model, especially its QCD sector, provides a well-tested framework for describing the strong interaction, yet it presents significant challenges when applied to dense and hot systems. Lattice QCD techniques, for instance, become unreliable at high baryon chemical potential due to the so-called "sign" problem, while current collider capabilities limit experimental access to these regions. Nevertheless, understanding matter under such conditions is essential for elucidating the early universe's evolution and the internal structure of neutron stars.

Achieving meaningful insight into the QCD phase diagram critically depends on the ability to accurately reconstruct the properties of the particles produced in heavy-ion collisions. Tracking detectors play a central role among the key detector subsystems, enabling precise measurement of charged particle trajectories and momenta. The spatial resolution of these systems directly affects the reconstruction of primary and secondary vertices and the identification of short-lived particles via displaced vertices identification. High track densities, complex event topologies, and high interaction rates place stringent demands on both spatial granularity and timing precision. Enhancing these capabilities is essential for isolating signals of phase transitions or critical behavior from the large background of hadronic interactions, making the performance of tracking systems a determining factor in the success of this physics program.

The Compressed Baryonic Matter (CBM) experiment, currently under construction at FAIR, is designed to explore the QCD phase diagram at high baryon chemical potential through high-rate, precision measurements of rare probes in heavy-ion collisions. The Silicon

Tracking System (STS) is the main tracking detector of CBM, designed to reconstruct the trajectories of charged particles with efficiency larger than 95%, a momentum resolution better than 2% for particle momenta larger than 1 GeV/c inside a 1 Tm magnetic field, and to identify complex decay topologies.

The mini-CBM (mCBM) setup incorporates pre-series components from all major subsystems of CBM in a consolidated, fixed-target configuration operated under realistic heavy-ion collision scenarios. Its primary aim is to validate the entire experimental workflow, encompassing detector performance, readout electronics, the free-streaming data acquisition system, online tracking and event reconstruction, and offline analysis, all within a high-rate environment that simulates the target operational conditions of CBM. Over multiple operational campaigns conducted between 2021 and 2024 at SIS18, utilizing a variety of beam species and energies around 1-2 AGeV, mCBM has established a crucial foundation for evaluating and optimizing detector performance across diverse operational parameters.

This thesis presents a detailed performance evaluation of the prototype STS based on data from the mCBM experiment, including spatial and temporal resolution, hit reconstruction efficiency and capabilities for tracking and vertexing, facilitating extrapolations to scenarios anticipated at CBM@SIS100.

Data analysis of Ni+Ni collisions at 1.93 AGeV

To assess and validate the operational readiness of the Silicon Tracking System (STS) under realistic beam conditions, a comprehensive analysis was conducted on reconstructed data collected during multiple mCBM beamtime campaigns. The analysis presented in this thesis is carried on the Ni+Ni dataset at 1.93 AGeV measured in 2024. The upgraded STS configuration employed in this campaign, featuring three fully instrumented tracking stations and enhanced electronic shielding, enables an improved characterization of detector response, tracking performance, and vertexing precision with a collision rate of about 400 kHz.

Reconstruction chain

A central component of this work is developing and applying the CBM reconstruction chain, which processes raw detector data into structured high-level observables suitable for physics analysis. Due to the free-streaming nature of the CBM data acquisition system, the chain must perform continuous-time data processing without predefined triggered events, requiring precise four-dimensional (x, y, z, t) tracking and event-building algorithms. The workflow includes decoding the raw data, reconstructing clusters and hits, associating hits to particle trajectories, and reconstructing tracks across the various detector subsystems.

Special attention in the analysis is given to the STS data, where accurate track reconstruction directly impacts the spatial and temporal resolution essential for physics goals such as Λ baryon identification. The reconstruction framework is implemented within CBMROOT, a C++-based software suite tailored to meet the high-throughput demands of CBM's triggerless architecture.

Monte Carlo simulations

The reconstruction chain is designed to operate identically on both experimental and Monte Carlo (MC) simulated data to ensure robust and validated performance. This dual compatibility allows for extensive benchmarking of reconstruction efficiency, resolution, and vertexing precision under controlled conditions that mirror experimental scenarios. MC simulations are configured to match the geometry, detector response, and beam conditions of the mCBM setup, enabling direct comparisons between true and reconstructed quantities. This capability is particularly valuable during the development and optimization phase, where reconstruction steps can be debugged, validated, and refined before deployment on real data. Together, these tools enable a comprehensive and flexible platform for assessing the detector's ability to resolve high-density heavy-ion collisions with the precision required for the CBM physics program.

Data quality assurance

After reconstruction, detailed quality assurance studies are conducted on various data levels, including raw signals, clusters, and hits. Inactive and noisy channels are identified by analyzing timeslice–integrated raw signal distributions across all sensor modules. The resulting findings are cross-validated with in-lab ENC measurements. The fraction of inactive channels is stable and limited to a few percent, with noisy channels contributing less than 0.5% of the total, reflecting successful noise suppression in the upgraded readout environment.

Time calibration

This thesis develops a robust time calibration procedure. The algorithm determines time correction parameters for offset and time-walk for each detector ASIC and discriminator. The correction is extracted from the time correlation between STS raw signals and the T0 diamond counter. Those time correlation distributions are built and analyzed for progressively finer subsets of channels, starting from whole sensors and ending at individual amplitude discriminators. This method enables charge-dependent time corrections and guarantees that

the STS detector is synchronized with the data from other subsystems.

Time resolution

Using MC simulations to account for differences in particle time of flight, the time resolution is extracted from the width of the timing correlation and estimated better than 5 ns for high-amplitude signals.

Amplitude measurement

The STS signal-to-noise ratio (S/N) is evaluated by comparing the measured signal amplitude from minimum ionizing particles to the module noise, previously characterized during detector calibration. The noise, quantified as the equivalent noise charge (ENC), is approximately 1000 e, consistent with expectations based on detector capacitance. The signal is derived from the most probable charge deposited by MIPs, extracted via a Landau fit to the amplitude distribution, yielding an average value of 22.7 ke. This results in a S/N ratio of approximately 23. To suppress noise contributions, only hits associated with reconstructed tracks were considered.

Spatial resolution

Spatial resolution is quantified by analyzing the residuals between reconstructed hits and projected track positions, calculated from track extrapolation. These residual distributions, evaluated for each sensor and fitted with Gaussian profiles, allowed the extraction of intrinsic hit resolutions after accounting for multiple scattering. Additional methods were used to account for the impact of misalignment and non-Gaussian effects in the residual distributions. The estimated spatial resolution is 23-29 μm for the x coordinate, consistent with the expectations for the detector pitch.

Hit reconstruction efficiency

Hit reconstruction efficiency is derived by determining the fraction of track-associated hits successfully reconstructed within each sensor module. Fully reconstructed tracks are used as a reference to suppress random coincidences and noise-induced hits. The analysis revealed consistently high efficiencies across the detector, with minor variations attributed to edge effects and local inhomogeneities. These findings demonstrate the capability of the STS to provide high-resolution, high-efficiency measurements of charged particle positions, a foundational requirement for precision tracking and vertexing in the CBM physics program.

Beam spot reconstruction

To explore the vertexing capabilities of the STS in its current three-layer prototype configuration, a detailed study was carried out to reconstruct the beam spot position and evaluate tracking-vertex resolution. The beam spot reconstruction relies on extrapolating reconstructed particle tracks at a given reference plane along the beamline. Transverse projections of track intersections are analyzed at different planes, and beam spot profiles are analyzed to extract centroid positions and width parameters. In the main target plane, the method measures the primary vertices distribution. The comparison with the beam spot measured by the T0 detector provides satisfactory agreement. The projections on different planes corresponding to secondary interaction targets provide consistency with the expected position of known support structures.

Alignment

These measurements are used to check the consistency of the experimental setup's mechanical geometry and alignment, revealing significant misalignment beyond expected tolerances. The method also helps identify minor sensor positioning shifts and substantiates the stability of track propagation under the current reconstruction chain.

Primary vertex reconstruction

An event-by-event primary vertex reconstruction algorithm is developed using the average Point of Closest Approach (PCA) between pairs of reconstructed tracks. This approach provides a statistically motivated approximation of the primary interaction vertex, which is particularly valuable in the absence of a fully redundant tracking configuration. By computing the PCA between all unique track pairs in an event and averaging their three-dimensional positions, a candidate vertex is obtained for each event, consistent with the position determined by the beam spot analysis.

Impact parameter

This allows for a quantitative analysis of the Distance of Closest Approach (DCA) between individual tracks and the estimated vertex. The distribution of DCA values in the transverse plane is a practical proxy for vertex resolution. The observed DCA distributions have a FWHM of $\sim 50\,\mu$m. These results are consistent with simulation expectations and indicate that meaningful vertex localization and spatial discrimination are achievable even with the limited number of tracking layers.

The beam spot reconstruction and PCA-based vertex estimation establish a foundational methodology for validating detector alignment and extracting spatial resolution metrics related to vertex reconstruction. This work provides a critical benchmark for evaluating the performance of the STS prototype setup, establishing a baseline for extrapolating detector performance and guiding expectations for the full STS system.

Abstrak

Die Untersuchung stark wechselwirkender Materie unter extremen Bedingungen stellt eine zentrale Herausforderung der modernen Teilchenphysik dar, insbesondere in den wenig verstandenen Bereichen des QCD-Phasendiagramms bei hohem baryochemischen Potential. Obwohl das Standardmodell und insbesondere die Quantenchromodynamik (QCD) eine solide theoretische Grundlage bieten, stoßen sie bei der Beschreibung dichter Systeme sowohl in Simulationen als auch experimentell an ihre Grenzen. Die Erforschung dieser Zustände ist jedoch entscheidend für das Verständnis von Phänomenen wie der Entwicklung des frühen Universums sowie von Neutronensternen.

Der Fortschritt in diesem Forschungsfeld hängt maßgeblich von der präzisen Rekonstruktion von Teilchen ab, die in Schwerionenkollisionen entstehen, wobei Spurdetektoren eine zentrale Rolle spielen. Deren räumliche und zeitliche Auflösung wirkt sich direkt auf die Vertexrekonstruktion und die Identifizierung kurzlebiger Teilchen aus, insbesondere in experimentellen Szenarien mit hoher Teilchenmultiplizität. Die Erfüllung dieser Anforderungen ist entscheidend für den Nachweis seltener Signale von Phasenübergängen oder kritischen Phänomenen.

Das CBM-Experiment am FAIR wird aufgebaut, um sich dieser Herausforderung zu stellen. Ziel ist die Erforschung des QCD-Phasendiagramms bei hohem baryochemischen Potential durch hochpräzise Messungen seltener Observablen mit hoher Statistik.

Das Hauptziel der vorliegenden Dissertation ist die umfassende Charakterisierung der Leistungsfähigkeit des Silicon Tracking Systems (STS) für das CBM-Experiment unter den realistischen herausfordernden Bedingungen, wie sie typischerweise bei Schwerionenkollisionen am FAIR auftreten werden. Dies erfolgt mit dem funktionalen Prototyp-Demonstratorsystem mini-CBM (mCBM). Der Aufbau wurde in verschiedenen Strahlszenarien am SIS18 betrieben, was eine Evaluierung der Leistungsfähigkeit des in diesem Aufbau integrierten STS-Detektors ermöglicht.

Besonderes Augenmerk liegt auf der Quantifizierung der Orts- und Zeitauflösung des Detektors, der Effizienz der Trefferrekonstruktion sowie der Leistungsfähigkeit des Detektors

in Bezug auf Spurverfolgung und Vertexauflösung. Durch eine umfassende Auswertung der Detektorleistung unter realen Betriebsbedingungen stellt die Arbeit sicher, dass der STS-Detektor hinreichend präzise und robust ist, um den Anforderungen des CBM-Experiments gerecht zu werden. Die Übereinstimmung der gemessenen Leistungskennwerte mit Simulationen erlaubt zuverlässige Prognosen für die Leistung des vollständigen Detektors im finalen CBM-Aufbau.

Zusammenfassung

Das Verhalten stark wechselwirkender Materie unter extremen Temperatur- und Dichtebedingungen gehört zu den faszinierendsten Forschungsfeldern der modernen Teilchenphysik. Trotz erheblicher theoretischer und experimenteller Fortschritte bleiben weite Bereiche des Phasendiagramms der QCD-Materie wenig verstanden – insbesondere die mögliche Lage eines kritischen Punktes sowie die Art des Phasenübergangs zwischen hadronischer Materie und dem Quark-Gluon-Plasma (QGP), vor allem bei hohem baryochemischen Potential.

Das Standardmodell, insbesondere der QCD-Sektor, stellt einen gut getesteten Rahmen zur Beschreibung der starken Wechselwirkung dar, stößt jedoch bei der Anwendung auf dichte und heiße Systeme auf erhebliche Herausforderungen. So sind Gitter-QCD-Methoden aufgrund des sogenannten Vorzeichen-Problems bei hohen baryochemichen Potentialen nur eingeschränkt einsetzbar, während die Fähigkeiten derzeitiger Beschleuniger den experimentellen Zugang zu diesen Bereichen begrenzt. Dennoch ist das Verständnis der Materie unter solchen Bedingungen entscheidend, um die Entwicklung des frühen Universums und die innere Struktur von Neutronensternen zu entschlüsseln.

Aussagekräftige Erkenntnisse über das QCD-Phasendiagramm erfordern die präzise Rekonstruktion der Eigenschaften von Teilchen, die in Schwerionenkollisionen erzeugt werden. Spurdetektoren spielen hierbei eine zentrale Rolle, da sie die genaue Messung von Spuren und Impulsen geladener Teilchen ermöglichen. Die räumliche Auflösung dieser Systeme wirkt sich direkt auf die Rekonstruktion primärer und sekundärer Vertizes sowie auf die Identifikation kurzlebiger Teilchen über verschobene Zerfallspunkte aus. Hohe Spurdichten, komplexe Ereignistopologien und hohe Wechselwirkungsraten stellen dabei höchste Anforderungen an die räumliche Granularität und zeitliche Auflösung. Die Verbesserung dieser Fähigkeiten ist unerlässlich, um Signale von Phasenübergängen oder kritischem Verhalten vom großen Untergrund hadronischer Wechselwirkungen zu isolieren – somit ist die Leistungsfähigkeit der Spurdetektion ein entscheidender Faktor für den Erfolg dieses physikalischen Programms.

Das Compressed Baryonic Matter (CBM)-Experiment, das derzeit am FAIR im Aufbau ist, wurde konzipiert, um das QCD-Phasendiagramm bei hohem baryochemischen Poten-

tial durch präzise Messungen seltener Sonden in Schwerionenkollisionen bei hohen Wechselwirkungsraten zu untersuchen. Das Silicon Tracking System (STS) ist der zentrale Spurdetektor von CBM und wurde entwickelt, um die Spuren geladener Teilchen mit einer Effizienz von über 95% und einer Impulsauflösung besser als 2% für Teilchenimpulse über 1 GeV/c im Inneren eines 1 Tm starken Magnetfeldes zu rekonstruieren sowie hierbei komplexe Zerfallstopologien zu identifizieren.

Der mini-CBM (mCBM)-Aufbau integriert Vorserienkomponenten aller wesentlichen CBM-Subsysteme in einer Fixed-Target-Konfiguration und wird unter realistischen Bedingungen von Schwerionenkollisionen am SIS18 betrieben. Ziel ist die Validierung des gesamten experimentellen Ablaufs – vom Leistungsvermögen der Detektoren und der Ausleseelektronik über das freilaufende Datenerfassungssystem und die Online-Spurrekonstruktion bis hin zur Offline-Analyse – in einer Hochratenumgebung, die den angestrebten Einsatzbedingungen von CBM nahekommt. In mehreren Strahlzeiten zwischen 2021 und 2024 am SIS18, bei denen verschiedene Strahlteilchen und Energien im Bereich 1–2 AGeV verwendet wurden, konnte mCBM eine entscheidende Grundlage für die Charakterisierung und Optimierung der Detektorleistung unter verschiedensten Betriebsparametern schaffen.

Die vorliegende Dissertation präsentiert eine detaillierte Evaluierung und Bewertung der Leistungsfähigkeit der STS-Prototypen auf der Grundlage von Daten des mCBM-Experiments. Dies schließt ein die räumliche und zeitliche Auflösung, die Effizienz der Trefferrekonstruktion sowie die Fähigkeiten zur Spurverfolgung und Vertexrekonstruktion. Diese Ergebnisse ermöglichen eine fundierte Extrapolation zu den für CBM am SIS100 erwarteten experimentellen Szenarien.

Datenanalyse von Ni+Ni-Kollisionen bei 1.93 AGeV

Zur Bewertung und Validierung der Fähigkeiten des Silicon Tracking Systems (STS), unter realistischen Strahlbedingungen betrieben zu werden, wurde eine umfassende Analyse des Datenmaterials durchgeführt, das während mehrerer mCBM-Strahlzeitkampagnen aufgezeichnet wurde. Die in dieser Arbeit präsentierte Analyse basiert auf dem Ni+Ni-Datensatz bei 1.93 AGeV, gemessen im Jahr 2024. Die in dieser Kampagne eingesetzte STS-Konfiguration mit drei vollständig instrumentierten Stationen zur Bestimmung von Spurpunkten ermöglicht eine präzise Charakterisierung des Sensorverhaltens, der Tracking-Leistung und der Vertex-Rekonstruktion bei einer Kollisionsrate von bis zu 400 kHz.

Rekonstruktionskette

Ein zentrales Element dieser Arbeit ist die Entwicklung und Anwendung der CBM-Rekonstruktionskette, welche von Rohdaten der Detektoren ausgeht und diese bis hin zu Observablen für die physikalische Analyse verarbeitet. Aufgrund des freilaufenden Charakters des CBM-Datenerfassungssystems muss die Kette eine kontinuierliche Datenverarbeitung in Echtzeit ohne vordefinierte Trigger-Ereignisse ermöglichen. Dies erfordert präzise vierdimensionale (x, y, z, t) Algorithmen zur Spurerkennung und Definition von Kollisionsereignissen. Der Workflow umfasst das Dekodieren der Rohdaten, die Rekonstruktion von Clustern und Treffern von Teilchen in den Sensorebenen, die Zuordnung von Treffern zu Teilchenspuren sowie die Rekonstruktion von Spuren über verschiedene Detektorsubsysteme hinweg. Besonderes Augenmerk liegt dabei auf den STS-Daten, bei denen eine präzise Spurrekonstruktion entscheidend für die räumliche und zeitliche Auflösung ist – insbesondere für physikalische Ziele wie die Identifikation von Λ-Baryonen. Die Rekonstruktionsumgebung ist in CBM-ROOT implementiert, einem auf C++ basierenden Software-Paket, das auf die hohen Datenraten und die triggerlose Architektur von CBM zugeschnitten ist.

Monte-Carlo-Simulationen

Die Rekonstruktionskette ist so ausgelegt, dass sie sowohl auf Basis experimenteller oder aber Monte-Carlo-(MC)-simulierter Daten identisch angewendet werden kann, um eine robuste und validierte Leistungsbewertung zu gewährleisten. Diese Kompatibilitätseigenschaft ermöglicht umfangreiche Benchmark-Analysen zur Rekonstruktionseffizienz, Auflösung und Vertex-Präzision unter kontrollierten Bedingungen, die reale experimentelle Szenarien nachbilden. Die MC-Simulationen sind so konfiguriert, dass sie die Geometrie, Detektorantwort und Strahlbedingungen des mCBM-Aufbaus widerspiegeln, was direkte Vergleiche zwischen bekannten simulierten sowie experimentell rekonstruierten Größen erlaubt. Diese Fähigkeit ist besonders in der Entwicklungs- und Optimierungsphase von großem Wert, da hier einzelne Rekonstruktionsschritte gezielt getestet, validiert und optimiert werden können, bevor sie auf reale Daten angewendet werden. Zusammengenommen bieten diese Werkzeuge eine umfassende und flexible Plattform zur Bewertung der Detektorleistung im Hinblick auf die hochpräzise Auflösung von Schwerionenkollisionen bei hohen Ereignisraten, wie sie für das CBM-Physikprogramm erforderlich ist.

Datenqualitätskontrolle

Nach der Rekonstruktion werden detaillierte Qualitätssicherungsstudien auf verschiedenen Datenebenen durchgeführt: Rohsignale, Cluster und Treffer. defekte und verrauschte

Kanäle werden durch die Analyse der Daten über alle Sensormodule hinweg identifiziert. Der Anteil inaktiver Kanäle ist stabil und auf wenige Prozent begrenzt, während verrauschte Kanäle weniger als 0.5% des Gesamtsignals ausmachen – ein Hinweis auf die erfolgreiche Rauschunterdrückung im weiterentwickelten Auslesesystem.

Zeitkalibrierung

Im Rahmen dieser Arbeit wurde ein robustes Verfahren zur Zeitkalibrierung entwickelt. Der Algorithmus bestimmt für jeden Detektor-ASIC die Zeitkorrekturparameter für Offset sowie für jeden Kanal die amplitudenabhängige Zeitkorrektur (Time-Walk). Die Korrektur wird aus der Zeitkorrelation zwischen den STS-Rohsignalen und als Referenz dem T0-Diamant-Zähler abgeleitet. Diese Zeitkorrelationsverteilungen werden für zunehmend feinere Kanaluntergruppen erstellt und analysiert – beginnend bei gesamten Sensoren bis hin zu einzelnen Diskriminatoren für die Signalamplituden im ADC. Dieses Verfahren ermöglicht ladungsabhängige Zeitkorrekturen und gewährleistet die präzise Synchronisation des STS-Detektors mit den Daten anderer Subsysteme.

Zeitauflösung

Unter Verwendung von MC-Simulationen zur Berücksichtigung von Unterschieden in der Flugzeit der Teilchen wird die Zeitauflösung aus der Breite der Zeitkorrelation abgeleitet. Für Signale hoher Amplitude von minimal ionisierenden Teilchen (Minimum Ionizing Particles, MIPs) ergibt sich eine Zeitauflösung von besser als 5 ns.

Amplitudenmessung

Das Signal-Rausch-Verhältnis (Signal-to-Noise; S/N) des STS wird durch den Vergleich der gemessenen Signalamplitude von minimal ionisierenden Teilchen mit den während der Detektorkalibrierung bestimmten Rauschwerten bestimmt. Das Rauschen, ausgedrückt als äquivalente Rauschladung (Equivalent Noise Charge, ENC), beträgt etwa 1000 e und entspricht den Erwartungen basierend auf der durch Sensor und Analogkabel bestimmten Eingangskapazität der Analogelektronik. Das Signal ergibt sich aus der wahrscheinlichsten deponierten Ladung durch MIPs, welche durch einen Landau-Fit an die Signalverteilung bestimmt wurde, mit einem durchschnittlichen Wert von 22.7 ke. Daraus ergibt sich ein S/N-Verhältnis von etwa 23. Um Rauschbeiträge zu unterdrücken, wurden nur Treffer berücksichtigt, die einer rekonstruierten Spur zugeordnet werden konnten.

Räumliche Auflösung

Die räumliche Auflösung wird durch die Analyse der Residuen zwischen rekonstruierten Treffern und den aus der Spurextrapolation projizierten Trefferpositionen quantifiziert. Diese Residuenverteilungen, die für jeden Sensor ausgewertet und mit Gauß-Profilen angepasst wurden, ermöglichen die Bestimmung der intrinsischen Trefferauflösung unter Berücksichtigung von Mehrfachstreuung. Zusätzliche Verfahren wurden angewendet, um den Einfluss von Fehlern in der geometrischen Ausrichtung der Detektorelemente und von nicht-Gaußschen Effekten in den Residuenverteilungen zu berücksichtigen. Die geschätzte räumliche Auflösung liegt bei 23–29 μm für die x-Koordinate und entspricht den Erwartungen auf Grundlage des Streifenabstands im Sensor.

Effizienz der Trefferrekonstruktion

Die Effizienz der Trefferrekonstruktion ergibt sich aus dem Anteil der Spur-assoziierten Treffer, die innerhalb eines Sensormoduls erfolgreich rekonstruiert wurden. Vollständig rekonstruierte Spuren dienen als Referenz, um zufällige Koinzidenzen und durch Rauschen verursachte Treffer zu unterdrücken. Die Analyse zeigt eine durchgehend hohe Effizienz von ca. 97% im gesamten Detektor, mit geringen Abweichungen, die auf Randeffekte und lokale Inhomogenitäten zurückzuführen sind. Diese Ergebnisse belegen die Fähigkeit des STS, hochauflösende und effiziente Messungen von geladenen Teilchenpositionen bereitzustellen – eine grundlegende Voraussetzung für präzises Tracking und Vertexing im CBM-Physikprogramm.

Rekonstruktion des Strahlflecks

Zur Untersuchung der Vertexing-Fähigkeiten des STS in seiner derzeitigen Drei-Lagen-Prototypkonfiguration wurde eine detaillierte Studie zur Rekonstruktion der Strahlfleckposition und zur Bestimmung der Tracking-Vertex-Auflösung durchgeführt. Die Rekonstruktion des Strahlflecks basiert auf der Extrapolation rekonstruierter Teilchenspuren in eine definierte Referenzebene entlang der Strahlachse. Transversale Projektionen der Spurenschnittpunkte werden in verschiedenen Ebenen analysiert; die Strahlfleckprofile dienen zur Bestimmung von Schwerpunktpositionen und Breitenparametern. In der Hauptebene des Targets liefert das Verfahren die Verteilung der Primärvertexe. Der Vergleich mit dem Strahlfleck, der durch den T0-Detektor gemessen wurde, zeigt eine gute Übereinstimmung. Projektionen auf andere Ebenen, die sekundären Wechselwirkungszielen entsprechen, stimmen mit den erwarteten Positionen bekannter Trägerstrukturen überein.

Ausrichtung

Die Rekonstruktion des Strahlflecks wird zur Überprüfung der mechanischen Geometrie und genauen Ausrichtung des experimentellen Aufbaus verwendet und zeigen signifikante Abweichungen von den erwarteten Toleranzen. Die Methode erlaubt die Identifikation kleiner Verschiebungen der Position einzelner Sensoren und bestätigt zudem die Stabilität der Spurpropagation unter Verwendung der aktuellen Rekonstruktionskette.

Primärvertex-Rekonstruktion

Ein Rekonstruktionsverfahren für den Primärvertex einzelner Ereignisse wurde entwickelt, welches den durchschnittlichen Punkt der geringsten Annäherung (Point of Closest Approach, PCA) zwischen Paaren rekonstruierter Spuren verwendet. Dieser Ansatz liefert eine statistisch motivierte Näherung des primären Wechselwirkungsvertexes, was insbesondere beim Fehlen einer vollständig redundanten Tracking-Konfiguration von Bedeutung ist. Durch Berechnung des PCA zwischen allen Spurenpaaren eines Ereignisses und nachfolgender Mittelung deren dreidimensionalen Positionen wird für jedes Ereignis ein Vertex-Kandidat bestimmt, der mit der Position aus der Strahlfleckanalyse übereinstimmt.

Impaktparameter

Die ereignisweise Messung des primären Vertex ermöglicht eine quantitative Analyse des Abstands der nächsten Annäherung (Distance of Closest Approach, DCA) zwischen einzelnen Spuren und dem geschätzten Vertex. Die Verteilung der DCA-Werte in der transversalen Ebene stellt eine praktikable Näherung für die Vertexauflösung dar. Die beobachteten DCA-Verteilungen zeigen eine FWHM von etwa $\sim 50\,\mu$m. Diese Ergebnisse stimmen mit den Erwartungen aus Simulationen überein und zeigen, dass eine präzise Vertexlokalisierung und räumliche Trennung auch mit der begrenzten Anzahl an Spurstationen möglich ist.

Die Rekonstruktion des Strahlflecks und die PCA-basierte Vertexbestimmung stellen eine grundlegende Methodik zur Validierung der Detektorausrichtung und zur Extraktion räumlicher Auflösungskennwerte im Zusammenhang mit der Vertexrekonstruktion dar.

Diese Arbeit liefert eine entscheidende Referenz zur Bewertung der Leistungsfähigkeit des STS-Prototyps und legt eine wichtige Grundlage für die Extrapolation auf das finale STS-System.

Acknowledgments[1]

First and foremost, I must acknowledge the long-lasting contributions of those "who are no longer with us" for their impact on both my academic life and my development as a human being: my grandfather, Nemecio Dario Zaldívar Cruz, and my friend and academic father, **Prof. Dr. Fernando Guzmán Martínez.**

Those who live among us, the first place is, an example of strength, resilience, and love, my mother, **Leticia Zaldívar Gonzalez**. A shared place is occupied by my father **Eries Ramirez Salomón**, whose integrity and advocacy for justice will remain with me till my last days. Also, my older sister **Zailín Perez Zaldívar**, for playing as a mother to the best of her capacities for so long and so well. Thanks to my family who shape who I am today, and make me, without knowing it, committed to science. There is, of course, a special place for **Lady Maryann Collazo Sanchez**, my wife. To you who accompanied me all this way.

The person who committed so much to this research, and whom I feel honored to call a friend, is my supervisor, **Prof. Dr. Alberica Toia**. There are no words to express my infinite gratitude for her many lessons. Without her support (the wake-up calls, reality checks, and the strategic eyebrow raises), this thesis would be completely incoherent. Though I am proud of her, I also know how proud Fernando Guzman would be. Without knowing each other personally, they share so many good traits that should be a must in all those who guide others, because you guide me not only in research, but in life.

[1] see appendix E for a detailed Acknowledgments section

Contents

Acronyms

ASIC	**A**pplication **S**pecific **I**ntegrated **C**ircuit.
BMON	**B**eam **MON**itoring.
CA	**C**ellular **A**utomaton.
CAD	**C**omputer **A**ided **D**esign.
CBM	**C**ompressed **B**aryonic **M**atter.
CF	**C**arbon **F**iber.
DAQ	**D**ata **Ac**quisition system.
DCA	**D**istance of **C**losest **A**pproach.
DUT	**D**etector **u**nder **t**est.
ENC	**E**quivalent **N**oise **C**harge.
EoS	**E**quation **o**f **S**tate.
FAIR	**F**acility for **A**ntiproton and **I**on **R**esearch.
FEB	**F**ront-**e**nd **b**oards.
FEE	**F**ront-**e**nd **E**lectronics.
FLES	**F**irst-**l**evel **E**vent **S**elector.
FSD	**F**orward **S**pectator **D**etector.
FWHM	**F**ull **W**idth at **H**alf **M**aximum.
GEM	**G**as **e**lectron **m**ultiplier.
GSI	**G**esellschaft für **S**chwer**i**onenforschung GmbH.
HPC	**H**igh **P**erformance **C**omputing.
HRE	**H**it **R**econstrcution **E**fficiency.
KF	**K**alman **f**ilter.
MC	**M**onte **C**arlo.
mCBM	**m**ini-CBM.

MIP	**M**inimum **I**onizing **P**article.
MPV	**M**ost **p**robable **v**alue.
MRPC	**M**ulti-gap **R**esistive **P**late **C**hambers.
mSTS	**m**ini-**STS**.
MVD	**M**icro **V**ertex **D**etector.
OOP	**O**bject-**o**riented **p**rogramming.
PCA	**P**oint of **C**losest **A**pproach.
QCD	**Q**uantum **C**hromo**d**ynamics.
QGP	**Q**uark **G**luon **P**lasma.
RICH	**R**ing **I**maging **Ch**erenkov detector.
RMS	**R**oot **M**eam **S**quare.
RPC	**R**esistive **p**late **c**hamber.
STS	**S**ilicon **T**racking **S**ystem.
STS-XYTER	**STS X**, **Y** coordinates, **T**ime and **E**nergy **R**ead-out.
TOA	**T**ime **o**f **a**rrival.
TOF	**T**ime **o**f **F**light.
TSA	**T**ime-**S**tamped **A**rchives.

Chapter 1

Introduction

"Das schönste Glück des denkenden Menschen ist, das Erforschliche erforscht zu haben und das Unerforschliche ruhig zu verehren"
"The most beautiful happiness of the thinking man is to have explored the explorable and to revere the inscrutable."
Johann Wolfgang von Goethe

The sentiment expressed in the quotation highlights humanity's innate curiosity, which drives our quest for understanding the complexities of reality. This curiosity is, ultimately, what motivates this research on its essence. This chapter will place the necessary context by elaborating on fundamental questions related to the broad topic of understanding nature.

Why do we humans try to disentangle the mysteries of the universe? Although a captivating question, it seems unresolved, at least from the perspective of the physics field. Therefore, for sanity's sake, let's attribute the answer to what makes humans unique: curiosity.

What are we trying to understand? This can be broken down into more fundamental questions, like why things have mass or how and why matter changes its behavior under different conditions. These questions extend from the elementary particle scales to the stars at the edge of the observable universe. In many ways, these questions have been partially answered with increased improvements in the certainty of the found explanations.

Modern physics has developed a quantitative framework to describe phenomena across an extensive range of space-time and energy scales. The success of these investigations builds upon robust theories governing the four fundamental forces: gravity, electromagnetism, and the strong and weak nuclear interactions. While Einstein's general relativity provides a comprehensive description of gravitation, the interactions of quarks and leptons are encapsulated

within the quantum field theory framework, reconciled with special relativity and quantum mechanics through the Standard Model. The Standard Model describes the fundamental particles—quarks and leptons—and their interactions, with quantum chromodynamics (QCD) governing the strong force between quarks.

Scientists have addressed these questions by examining the matter under specific circumstances to create a multidimensional map. This map is what we refer to as phase space; from each designated point, accurate predictions of the matter's behavior can be made. However, this map is far from complete. Figure 1.1 presents a typical two-dimensional projection of the **Q**uantum **C**hromo**d**ynamics (QCD) phase-space diagram. The horizontal axis represents the baryon-chemical potential (μ_B), while the vertical axis represents the temperature (T).

Regimes of extremely high temperatures and small baryon-chemical potential match the conditions of the early universe, specifically during the first few microseconds after the Big Bang. At this stage, the universe was filled with a hot, dense plasma of quarks and gluons—known as the quark-gluon plasma—where particles moved freely without forming protons or neutrons. This phase existed before the universe cooled enough for hadronization, leading to the formation of matter as we know it.

On the other hand, matter at lower temperatures and higher baryon-chemical potential (μ_B) corresponds to the states found in neutron stars. In these environments, the density is several times higher than that of atomic nuclei, while the temperature is relatively low compared to the early universe. Under such conditions, matter is compressed into a degenerate state primarily composed of neutrons, with possible exotic phases such as hyperons, deconfined quark matter, or even color superconductivity at the core. These conditions reflect the cold, dense end of the QCD phase diagram, distinct from the hot early-universe plasma.

To test theories and prove their limitations, matter must be subjected to conditions that match the scope of the given hypothesis. Ordinary states of matter, characterized by low temperatures and low densities, are fairly accessible without the use of cutting-edge technologies. On the other hand, high-temperature and/or high-density matter pose theoretical and technological challenges for their study.

Some experiments aim to study matter under high temperatures and low μ_B, while others push towards higher density values and lower temperatures. However, most of them, if not all, share the goal of understanding the transit of matter through the possible states. Thus, experimentation is a key part of the answer to **how** to understand nature.

The standard approach to achieving the aforementioned high temperatures and/or high densities is accelerating heavy particles and forcing them to collide. The region of phase space the system can reach can be controlled by the amount of energy pushed into the reaction.

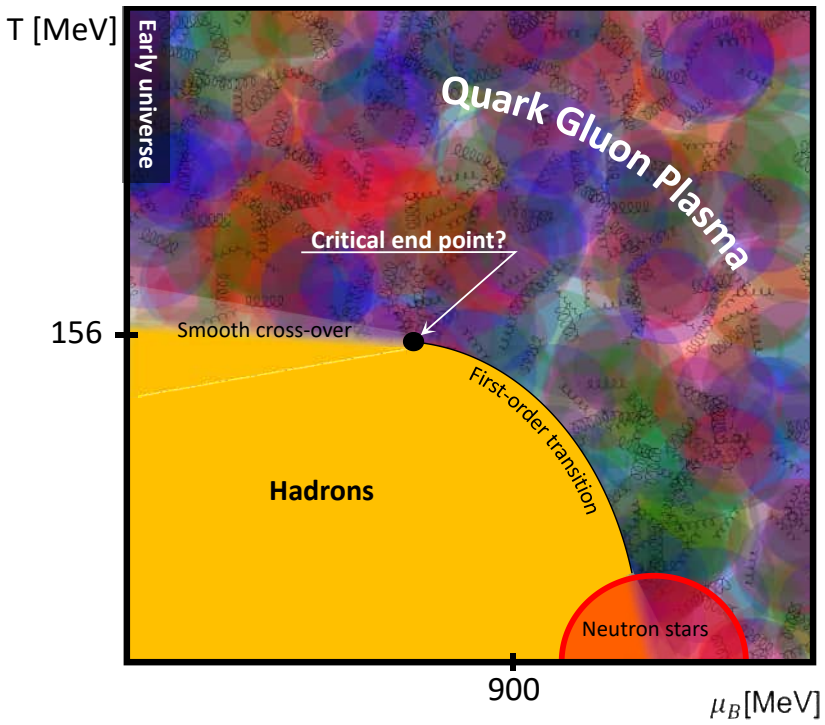

Figure 1.1: QCD Phase Diagram shown as a variation of temperature (T) with baryon chemical potential (μ_B). It displays a hadron phase and a deconfined state as **Q**uark **G**luon **P**lasma (QGP). The phase transition regions, as well as the conjectured critical endpoint, are highlighted. (Adapted from [1, 2])

The technological requirements, in terms of rate capabilities, radiation hardness, and time and position resolution, vary significantly depending on the region of the QCD phase space diagram intended to be explored. This is connected to the chosen methodology, which heavily relies on observables selected to carry unique information about the intermediate states of the reaction evolution.

The central theme of my thesis revolves around the various steps necessary to retrieve information about a physical event (i.e, ion-ion collision) recorded by a detection system. Achieving optimal performance in this process requires detailed research that ensures both the hardware and software perform as expected individually and as an integrated system. This thesis case will involve developing, implementing, and automating several steps of quality assurance of the raw data and higher abstract data levels produced by a particular detection system.

Depending on the region in the phase space the matter reaches before cooling down, unique bound states of quarks are produced. Those particles and the amount produced are of special interest in calibrating theoretical models [3]. Some of those probes are often

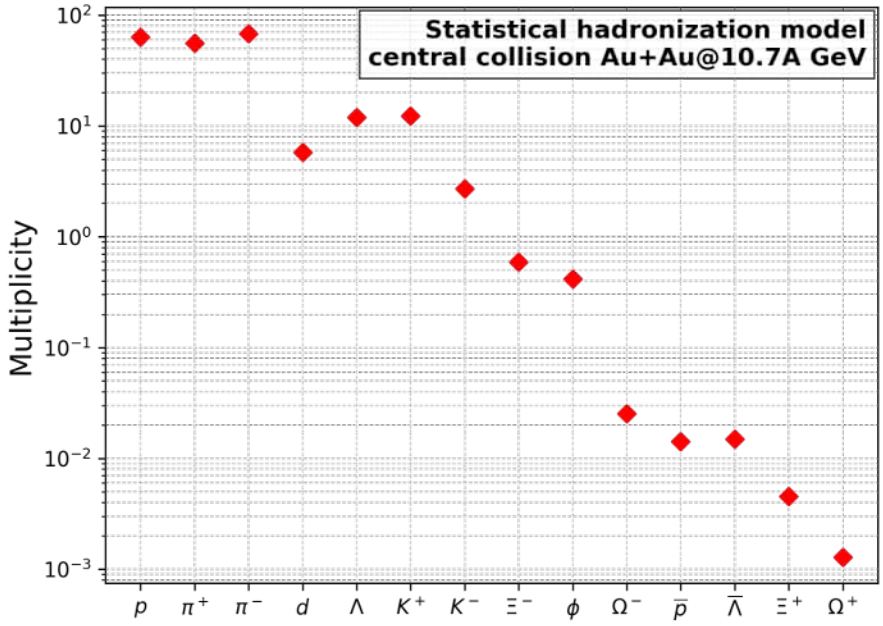

Figure 1.2: Particle multiplicities at central Au + Au collisions at 10.7 AGeV, as calculated from the Statistical Hadronization Model.

very rarely produced. Figure 1.2 shows the expected production yields for some of them extracted from **M**onte **C**arlo (MC) simulations. It can be appreciated that some probes are so rare that experiments would need to run for an unfeasibly long time to accumulate enough statistics to get reliable conclusions.

The solution to such problems lies in increasing the collision rate by orders of magnitude. However, it poses challenges in many directions, requiring the development of new technologies. A pivotal initiative for replicating non-ordinary states of the matter in controlled environments, thereby validating our theoretical understanding of fundamental reality, is the **C**ompressed **B**aryonic **M**atter (CBM) experiment at **F**acility for **A**ntiproton and **I**on **R**esearch (FAIR). The Figure 1.3 shows interaction rates as a function of the collision energy archived by existing and planned research facilities, where CBM experiments occupy a unique role at 10 MHz.

1.1 CBM at FAIR

Upon completion, FAIR[5] is expected to become one of the most extensive and most complex accelerator facilities worldwide, with the capability to manipulate particle beams of di-

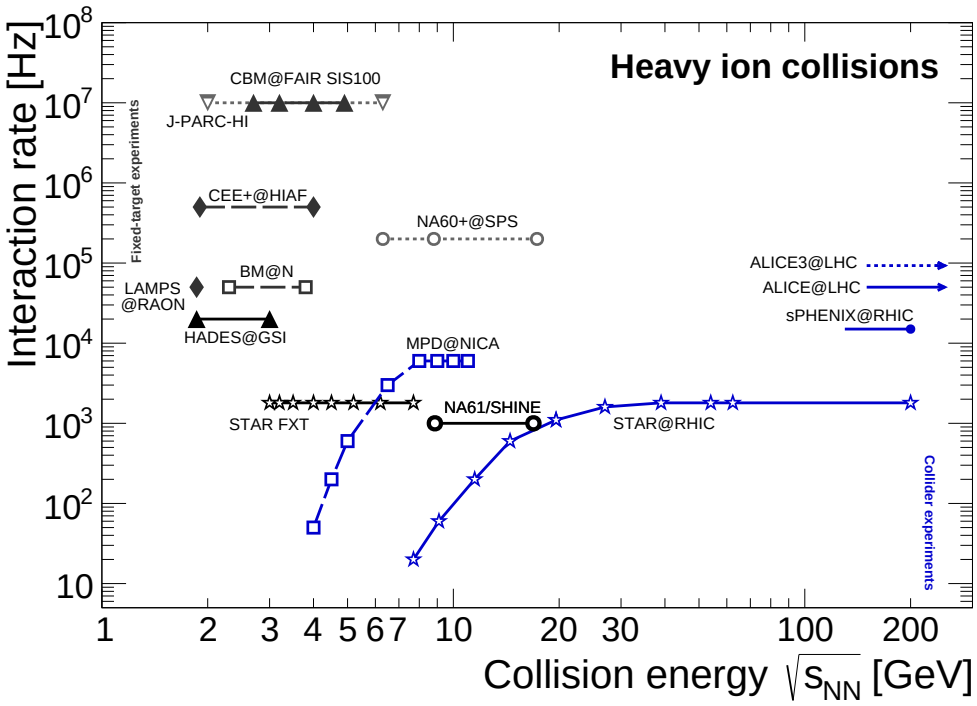

Figure 1.3: Interaction rates achieved by existing and planned facilities as a function of center-of-mass energy. CBM@FAIR SIS100 is displayed in the top range for interaction ranges.([4])

verse chemical elements, ions, and antiprotons. In addition to the CBM collaboration, FAIR will support extensive research initiatives across three other collaborations: **A**tomic, **P**lasma **P**hysics and **A**pplications (APPA) [6], **Nu**clear **St**ructure, **A**strophysics, and **R**eactions (NUSTAR) [7], and anti**P**roton **AN**ihilation at **DA**rmstadt (PANDA) [8].

CBM aims to investigate strongly interacting matter, particularly within regimes of high baryon-net density and moderate temperatures, via high-energy nucleus-nucleus collisions. It is designed as a fixed-target forward spectrometer featuring a sophisticated free-streaming readout system that integrates online event selection and reconstruction capabilities. This initiative stems from a concerted global collaboration among various stakeholders [5].

Figure 1.4 illustrates the current (shown in blue) and future (represented in red) configurations of the GSI-FAIR facility. The existing accelerators operated by GSI will serve as the initial acceleration stage for the SIS100 synchrotron [5].

This synchrotron is capable of achieving energies of up to 29 GeV for protons and 11 AGeV for gold (Au) ions. Implementing a slow extraction process within the synchrotron enables a continuous beam structure at the CBM cave, which is advantageous for increasing the collision rate by ensuring a uniform temporal distribution of beam particles. The beam

intensity is expected to reach up to 10^9 ions per second, leading to an estimated interaction rate of $10^7\ s^{-1}$ at a 1% interaction probability with the target.

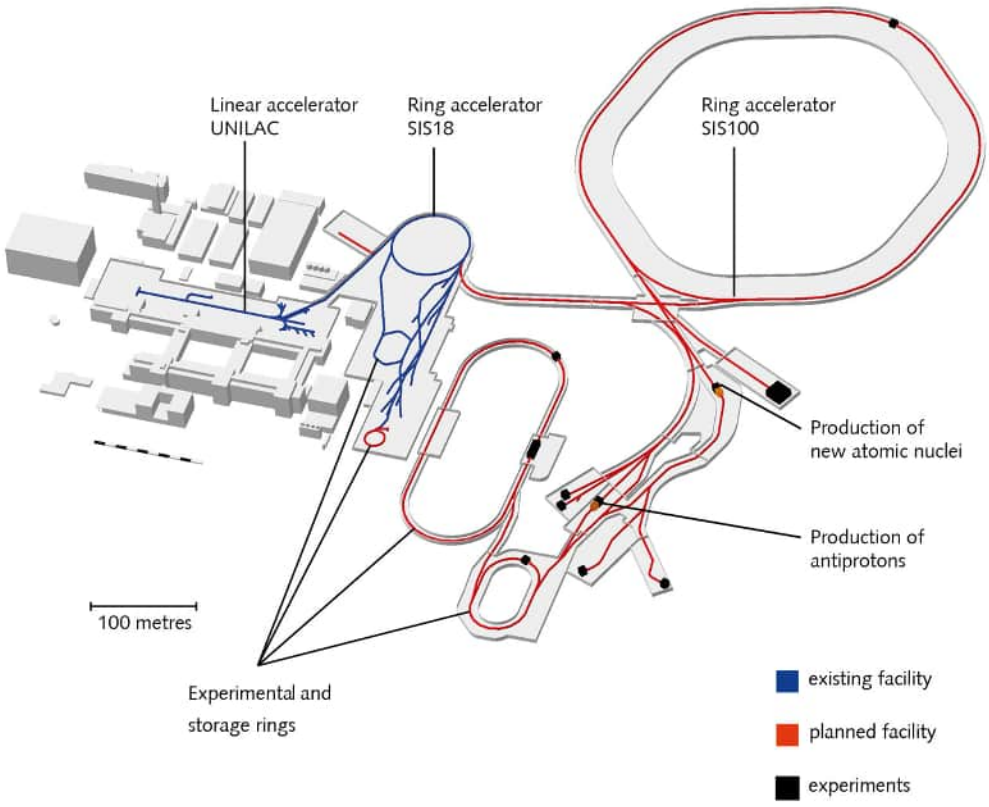

Figure 1.4: Layout of the FAIR facility. Existing infrastructures are highlighted in blue, while the expansions to accommodate the future experiments are highlighted in red.

The physics program of the CBM experiment

The CBM experiment is designed as a pivotal component of a comprehensive physics initiative that complements investigations carried out at experiments such **H**igh **A**cceptance **D**i-**e**lectron **S**pectrometer (HADES) [9], **S**uper **P**roton **S**ynchrotron (SPS), **B**aryonic **M**atter **at** **N**ucleotron (BM@N) [10], **M**ulti-**p**urpose **D**etector (MPD) at **N**uclotron-based **I**on **C**ollider f**A**cility (NICA), and **S**olenoidal **T**racker **a**t **RHIC** (STAR) [11].

Its primary objective is to explore the **E**quation **o**f **S**tate (EoS) of QCD matter at densities comparable to those in neutron star cores. The experiment aims to clarify diverse topics. Among them are the possible shift from hadronic matter to quark-gluon plasma, the location of the critical point on the QCD phase diagram, the existence of quarkyonic matter [12], and indicators of chiral symmetry restoration [13, 14].

The high interaction rate of the CBM experiment presents a unique opportunity for in-depth analysis of rare probes and their properties with remarkable statistical precision, achieving unprecedented sensitivity in particle reconstruction [14]. The final state of heavy ion reactions is complex, making systematic measurements essential to extract meaningful information. It includes analyzing excitation functions, dependencies on system size, and multi-differential phase-space distributions of identified particles. Factors such as flow, event-by-event fluctuations, and various correlations should also be taken into account.

Collective phenomena

The collective dynamics of the final-state hadrons generated in heavy-ion collisions offer critical insights into the underlying interaction mechanisms. The emergence of isotropic radial flow is a key signature for characterizing the system at kinetic freeze-out.

Anisotropic flow emerges from transforming density distribution anisotropies into pressure gradients, thereby providing insights into the EoS of dense nuclear matter [15]. Comprehensive multi-differential flow measurements across a diverse spectrum of hadron species, particularly focusing on strange hadrons and anti-baryons, are essential. It plays a crucial role in thoroughly evaluating the level of thermalization, along with the EoS and in-medium characteristics of strange particles.

The direct flow is sensitive to the details of the phase transition, the softening of the QCD matter EoS, and it is also an essential observable for clarifying the role of partonic degrees of freedom [16]. The elliptic flow strength and its dependence on transverse momentum provide key insights into the dominant degrees of freedom in the early stages of heavy-ion collisions. The flow of strange baryons and anti-baryons, affected by their in-medium interactions, enables investigations into chiral symmetry restoration.

Event-by-event fluctuations

Near the deconfinement phase transition, critical fluctuations in density are anticipated to induce significant non-statistical event-by-event variations in conserved quantities such as baryon number, strangeness, and electric charge. These fluctuations are intrinsically linked to thermodynamic susceptibilities, offering valuable insights into the properties of matter generated in high-energy collision events [17]. Lattice QCD computations indicate that higher-order moments of these distributions—specifically skewness and kurtosis—are sensitive indicators of the underlying phase structure resulting from such collisions. Furthermore, a critical point is expected to manifest as a non-monotonic behavior in these statistical moments [18, 17].

Despite previous collaborative efforts to explore these fluctuations in search of the critical point, no measurements of higher-order event-by-event fluctuations have been conducted at SIS100 energies. The forthcoming CBM experiment aims to address this gap by undertaking precise measurements of high-order fluctuations across a range of beam energies within the high net-baryon density interval of $\sqrt{S_{NN}} = 2.7 - 4.9\,\mathrm{GeV}$, corresponding to $\mu_B \approx 800 - 500\,\mathrm{MeV}$ [14].

Strangeness and hypernuclei production

Substituting an up or down quark with a strange quark in a nucleon within a nucleus results in the creation of a hypernucleus. This transition introduces the quantum number of strangeness, thereby adding dimension to the nuclear chart. The investigation of single and double hypernuclei facilitates the exploration of this third dimension, thereby enhancing our understanding of hyperon-nucleon and hyperon-hyperon interactions, which are crucial for comprehending the structure of neutron stars [19]. Thermal model calculations indicate that the peak of the hypernuclei excitation function occurs in the FAIR energy ranges.

Open and hidden charm

The yield of charmed hadrons serves as a sensitive indicator of the fireball conditions and the initial state of the nuclear collision. Given their substantial mass, charm-anticharm ($c\bar{c}$) pairs are primarily generated through hard scattering processes occurring early in the nucleus-nucleus interaction. The charm and anti-charm quarks will hadronize into states such as D mesons, charmed baryons, or charmonium, depending on their interactions with the surrounding medium, whether hadronic or partonic [20].

The formation of charmonium states is an observable that is sensitive to the conditions within the fireball. In a deconfined medium, charmonium states are expected to dissociate into charm (c) and anti-charm ($\bar{c}$) quarks due to color screening effects. This phenomenon was identified as one of the first predicted signatures of QGP formation [20].

Studying J/ψ production in collisions of symmetric nuclei at energies up to 15 AGeV and below threshold in Au+Au collisions at 10 AGeV presents particular challenges. For this specific observable, the CBM experiment will employ very high interaction rates and a dedicated experimental setup optimized for the identification of J/ψ [14].

Di-leptons spectroscopy

The search for signatures of chiral symmetry restoration, which is expected to occur at very high baryon net densities and/or temperatures, is one of the primary goals of heavy-ion

collision experiments. An observable consequence of this restoration would be the modification of hadron properties within nuclei or in hot and dense matter. The degeneracy of the spectral functions of chiral partners, such as the ρ-meson and the a_1-meson, indicates this chiral symmetry restoration [21]. While the a_1-meson is challenging to measure in the nuclear medium, the in-medium spectral function of the ρ-meson can be accessed by observing its decay into lepton pairs. Furthermore, the excess yield of lepton pairs in the energy range of around 1 GeV/c is sensitive to the temperature of the created matter and its space-time extension. The slope of the dilepton invariant mass spectrum between 1–2.5 GeV/c directly reflects the average temperature of the fireball [22].

The CBM experiment will perform pioneering multi-differential measurements of lepton pairs over the whole range of invariant masses emitted from a hot, dense fireball. The experimental challenges are low signal cross sections, decay probabilities in the order of 10^{-4}, and high combinatorial background [14].

1.1.1 Physics motivated requirements

At this point, it is clear that the physics program can be fulfilled based on the energy ranges and interaction rates expected at CBM. On the other hand, the development of the detectors and the chosen technologies had to be carefully examined, as key requirements must be satisfied.

Rare probes with complex decay topology as multi-strange Baryons (e.g., Λ, Ξ, Ω) will demand the detector to operate in free streaming mode and the full event reconstruction. A detector operating in such modes, at high intensities, will demand fast readout electronics and high data acquisition rates capabilities. Additionally, imposing stringent radiation hardness requirements on the employed materials.

Particle identification is key, and momentum determination can be linked to it [24]. With an expected track multiplicity of $\sim O(1000)$, full event reconstruction requires a fast, high-granularity tracker. Their rarity demands highly accurate measurement systems to discern subtle signatures from background noise. Even minor inaccuracies can lead to misidentification or complete signal loss.

Reconstructing the exact point where the particle decayed with high precision is fundamental to studying rare probes. The precision required for such measurements can be inferred from the typical distances at which some of these particles decay after departing from the event vertex. Table 1.1 shows the decay length for some relevant probes for the

Table 1.1: Decay Lengths of Rare Probes in the CBM Program. Quark composition and particle mass are listed. (extracted from [23])

Particle	**Quark Content**	**Mass (MeV)**	**Decay Length ($c\tau$)**
Ξ^0	uss	1315	8.71 cm
Λ	uds	1116	7.89 cm
Ξ^-	dss	1322	4.91 cm
Σ^-	dds	1197	4.43 cm
K_S^0	$d\bar{s}$	498	2.68 cm
Ω^-	sss	1672	2.46 cm
Σ^+	uus	1189	2.40 cm
D^+	$c\bar{d}$	1869	309.8 μm
D_s^+	$c\bar{s}$	1968	151.2 μm
D^0	$c\bar{u}$	1865	123 μm

CBM experiment. Although the exact mathematical form depends on the method utilized, the track parameter uncertainties will directly impact the precision of the decay vertex.

Various factors influence tracking performance, with detector position resolution being particularly important. Excellent position resolution enhances the accuracy of the particle trajectory reconstruction, thereby improving the fidelity of momentum and vertex determination. Any degradation in position resolution directly translates to a loss in momentum resolution and, consequently, a reduced capability to identify and separate the origins of the particles.

Multiple scattering presents another challenge that directly affects tracking performance. This phenomenon, where particles deviate from their initial path due to interactions with the detector material, compromises the precision of the reconstructed tracks. Figure 1.5 shows schematics for a multiple Coulomb scattering of a particle. Relevant quantities to describe the modification of the trajectory are marked down. The resulting angular dispersion θ_{plane} is distributed with a sigma value given by θ_0, estimated by the Lynch & Dahl formula (equation 1.1).

$$\theta_0 = \frac{13\,\mathrm{MeV}}{\beta\, c\, p}|z|\sqrt{\frac{x}{X_0}}\left[1 + 0.038\ln\left(\frac{x\, z^2}{X_0\,\beta^2}\right)\right] \tag{1.1}$$

The multiple scattering effect is inherently linked to the material budget of the detector through the term x/X_0 in the equation 1.1. Thus, reducing the material budget minimizes scattering events, preserving the optimal position resolution.

An appropriate formalism that links multiple scattering effects and position resolution to momentum resolution is tackled at [26, 27]. In a detector setup (see Figure 1.6) comprising

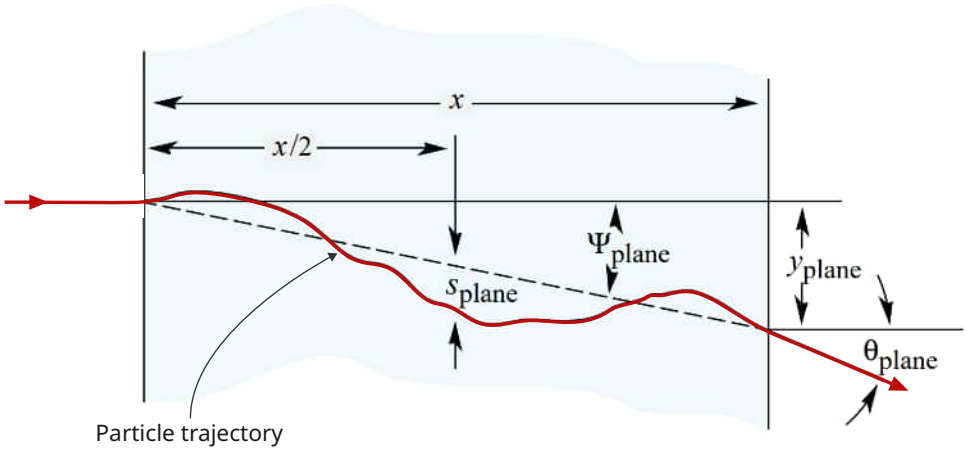

Figure 1.5: Representation of multiple Coulomb scattering with relevant quantities (adapted from [25]).

N equidistant layers covering a distance L, under a magnetic field with $\vec{B}$, momentum resolution in the bending plane (σ_{pT}/pT) is given by equation 1.2:

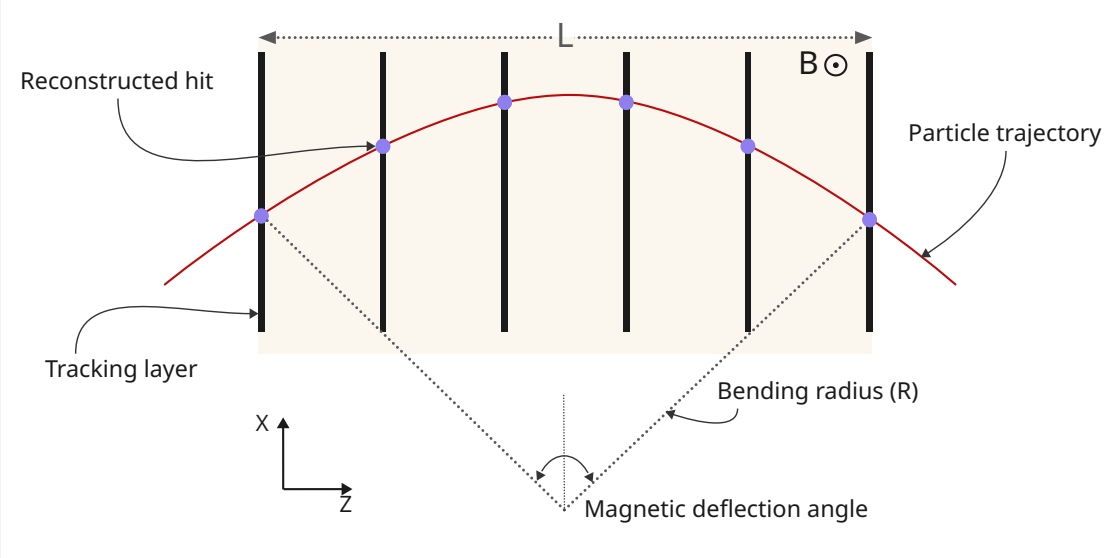

Figure 1.6: Particle trajectory (red) recovered from reconstructed hits (purple) from crossing tracking layers under the influence of a magnetic field perpendicular to the XZ plane.

$$\frac{\sigma_{p_T}}{p_T} = \sqrt{\left(\frac{\sigma_{p_T}}{p_T}\right)^2_{ms} + \left(\frac{\sigma_{p_T}}{p_T}\right)^2_{meas}} \quad , \tag{1.2}$$

where the term $\left(\frac{\sigma_{p_T}}{p_T}\right)_{meas}$ correspond to the uncertainties propagated from the detector

measurement, and $\left(\frac{\sigma_{p_T}}{p_T}\right)_{ms}$ correspond to the effects of multiple scattering. These effects have approximated values given by:

$$\left(\frac{\sigma_{p_T}}{p_T}\right)_{meas} \approx \frac{p_T}{0.3\,|z|} \cdot \frac{\sigma_{meas}}{BL^2} \cdot \sqrt{\frac{720}{N+4}} \quad , \tag{1.3}$$

$$\left(\frac{\sigma_{p_T}}{p_T}\right)_{ms} \approx \frac{0.0136\,GeV/c}{0.3\,\beta c} \cdot \frac{1}{BL} \cdot \sqrt{\frac{N}{\sin\theta}\frac{x}{X_0}} \quad . \tag{1.4}$$

The interplay between precise tracking, vertex resolution, detector position accuracy, and material budget is fundamental to successfully identifying rare probes.

1.2 The CBM experimental setup

The experiment will operate at reaction rates up to 10 MHz to collect sufficient statistics with a continuous (non-bunched) beam. Since most observables have complex trigger topologies, the experiment will implement a novel free-streaming readout mode [14]. Timestamped data from all detectors will be sent to a computing farm, where track reconstruction, event formation, and analysis will be performed online. In such an experimental scenario, the estimated data rate for the whole experiment in Au+Au collisions is approximately 2 TB/s. It represents a prohibitive data rate; therefore, fast reconstruction and event selection algorithms will be performed in real time to reduce the orders of magnitude of the stored data.

Magnetic field: a superconducting dipole magnet

The dipole magnet is one of the key devices used to determine the charged particle momenta in the CBM experiment. Its job is to bend the paths of charged particles emerging from collisions. Its magnet is designed to be superconducting, reducing operation costs. It will provide a vertical magnetic field of 1 T · m from the interaction point to approximately 1 m downstream of the target [28].

Detection systems

The primary function of the **M**icro **V**ertex **D**etector (MVD) is to effectively differentiate between primary and displaced vertices, which is crucial for reconstructing the decays of charmed hadrons such as D-mesons and Λ_c baryons. The stringent requirements for high spatial resolution, low material budget, and robust radiation tolerance are achieved using

Complementary **M**etal-**O**xide **S**emiconductor (CMOS) **M**onolithic **A**ctive **P**ixel **S**ensors (MAPS), equipped with a fine pixel size on the order of several tens of micrometers. This setup enables the reconstruction of low-momentum tracks, which aids in suppressing background noise for di-electrons. [29, 30].

The **S**ilicon **T**racking **S**ystem (STS) is an essential detector in the CBM setup that tracks charged particles and determines their momentum. Given that this detection subsystem is the core of the performance studies carried out in the scope of this thesis, special attention will be paid. For a detailed description of the STS design, see Section 1.3.

The **R**ing **I**maging **Ch**erenkov detector (RICH) is engineered for particle identification through Cherenkov radiation [31]. It effectively distinguishes electrons from pions up to momenta of 8 GeV/c, achieving a pion suppression factor exceeding 300 with electron identification efficiency above 85%. The photo-detector planes leverage **M**ulti-**A**node **P**hoto-**M**ultiplier**s** (MAPMTs), ensuring high granularity and significant geometrical acceptance.

The **Mu**on **Ch**ambers system (MUCH) is designed to precisely identify muon pairs generated in high-energy heavy-ion collisions [32]. It comprises five layers of hadron absorbers with tracking detector planes interspersed between these layers. The tracking planes utilize **G**as **e**lectron **m**ultiplier (GEM) technology [33] and **R**esistive **p**late **c**hamber (RPC) detectors. Together with the STS, the MUCH system is essential in studying di-muon decay channels of vector mesons such as ρ, ω, and J/ψ. Accurate muon identification is crucial for reconstructing these particles [32].

The main task of the **T**ransition **R**adiation **D**etector (TRD) is to identify electrons above momenta of 1 GeV/c and thus to extend the electron identification capabilities of the RICH detector above momenta of $p \sim 5$ GeV/c. This identification must be achieved with a pion suppression factor in the range $10 - 20$ to allow for a measurement of di-electrons in the mass range from below the ρ and ω masses to beyond the J/ψ mass with a good signal-to-background ratio [34].

The primary function of the **T**ime **o**f **F**light (TOF) detector is to differentiate among hadrons, specifically pions, kaons, and protons. Constructed with **M**ulti-gap **R**esistive **P**late **C**hambers (MRPC), which offers outstanding time resolution on the order of approximately 60 picoseconds and high detection efficiency [35]. To meet the stringent rate capability requirements, the MRPCs utilize low-resistivity glass as a key component [36].

The **F**orward **S**pectator **D**etector (FSD) is a scintillator-based apparatus strategically positioned at forward rapidity to capture spectator nucleons and fragments generated in target collisions. This detector plays a critical role in accurately reconstructing the reaction plane and assessing collision centrality, particularly given the high interaction rates anticipated for

the CBM experiment [37].

CBM Operation

The CBM detector system can operate in two modes: the first is optimized for electron identification (electron configuration), and the second is specialized for muon identification (muon configuration). In the first one, all subsystems, except MUCH, will be involved. In the muon configuration, the RICH detector is replaced by MUCH, and the electromagnetic calorimeter is removed. A schematic view of the detector setup concept is shown in Figure 1.7.

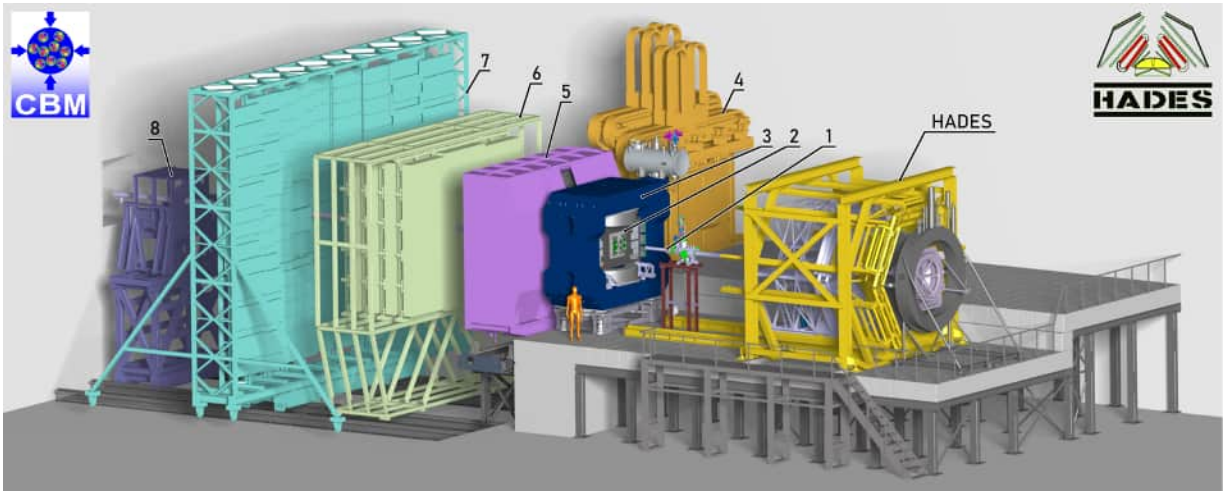

Figure 1.7: The CBM experimental setup at FAIR

Table 1.2 summarizes the CBM subsystems used for registering the different particle types [38]. Below, each detector subsystem is briefly explained. The STS is described separately in the next section.

Table 1.2: *CBM detectors used for registering the different particle types are marked with* ✓ *symbol. Those subsystems that can also contribute to reducing the background are marked with* (✓) *(adapted from [38]).*

Particle	MVD	STS	RICH	MUCH	TRD	TOF	FSD
π, K, p	✓	✓	(✓)		(✓)	✓	✓
Hyperons		✓			(✓)	(✓)	✓
Open charm	✓	✓	(✓)		(✓)	✓	✓
Electrons	✓	✓	✓		✓	✓	✓
Muons		✓		✓		(✓)	✓
Gamma							✓
Gamma via $e^{\pm}$ conversion	✓	✓	✓		✓	✓	✓

1.3 The heart of CBM tracking: the Silicon Tracking System

The CBM experiment relies on the STS as its primary tracking detector, tasked with efficiently reconstructing tracks of charged particles (95% for $p \geqslant 1\,\mathrm{GeV/c}$) and measuring their momenta with high resolution (1.5% for $p \geqslant 1\,\mathrm{GeV/c}$). The STS comprises 876 double-sided double-metal silicon micro-strip sensors organized into eight tracking stations, covering a physics aperture ranging from $2.5^\circ \leqslant \Theta \leqslant 25^\circ$. Positioned between 30–100 cm downstream of the target within a $1\,\mathrm{T}\cdot\mathrm{m}$ magnetic field [39], the system's configuration is illustrated by **C**omputer **A**ided **D**esign (CAD) in Figure 1.8. It presents the most stringent demands regarding bandwidth and density among all CBM detectors. Additionally, it introduces unique challenges not encountered in other silicon strip detectors commonly employed in large-scale high-energy physics experiments. Key design considerations for the system encompass the following requirements:

- the setup is contained in a volume of approximately 1.4 × 2.3 × 1.3 m^3 inside the superconducting CBM dipole magnet;
- the detector must be capable of measuring up to $O(1000)$ particles per central $Au+Au$ collision at interaction rates up to 10 MHz without hardware trigger;
- since the momentum resolution is dominated by multiple scattering, the material budget of the STS has to be kept as small as possible;
- the system requires radiation-hard silicon sensors, capable of withstanding up to $10^{13}\,\mathrm{MeV}\,n_{eq}$ during the operation at SIS100;
- sensors will be readout using fast and self-triggered **F**ront-**e**nd **E**lectronics (FEE), which must keep a reliable performance in a radiation environment of up to 100 krad/yr [39];
- efficient cooling system, capable to remove up to 50 kW of dissipated heat from inside the detector box.

The design specifications require the front-end electronics and readout components to be positioned at the periphery of the detector, outside the physics acceptance region. Each detector module is mounted on low-mass carbon-fiber supports [40, 41]. Sensor signals are transmitted to the front-end electronics via ultralight readout cables, with lengths reaching up to 50 cm.

It is anticipated that the innermost sensors within the STS detector will need to endure a non-ionizing energy loss damage threshold of up to $10^{13}\,\mathrm{MeV\,n_{eq}/cm^2}$ and an ionizing dose of approximately 1.1 Mrad during the operation of SIS100. The sensors have demonstrated radiation hardness validated up to twice the expected lifetime fluence [40, 42].

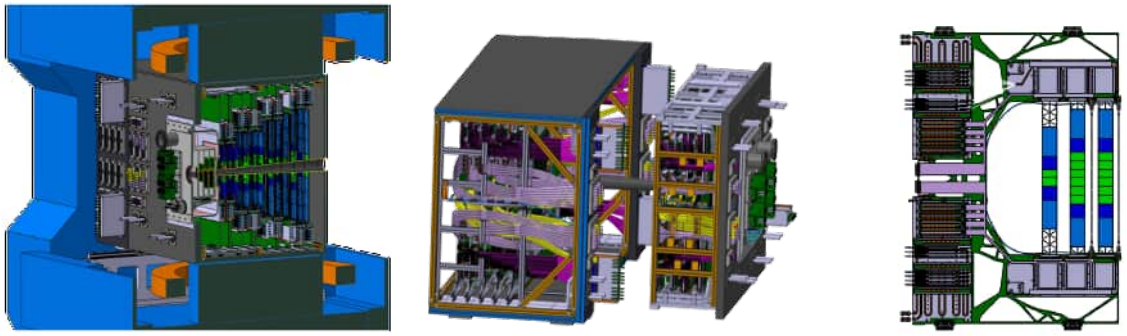

(a) (b) (c)

Figure 1.8: STS CAD. a) Inside-magnet view; b) Modular concept of the STS box; c) Half-unit design.

The STS detector will be integrated into a thermally isolated enclosure (Figure 1.8b) within the aperture of the dipole magnet. This enclosure functions as a structural support for the STS and MVD detectors, as well as for the target and the beam pipe [43]. The system continuously dissipates a thermal power of approximately 50 kW throughout its operational phase. An increase in operating temperature results in a rise in the detector's leakage current, which in turn affects the noise level, proportional to the square root of the leakage current ($\sqrt{I_{leak}}$). Consequently, excessive heat can lead to thermal runaway in the entire detector [44]. The proof of concept for the STS cooling design has been successfully carried out by [45].

The building block of STS

The STS module, the functional building block of the STS, consists of a double-sided, double-metal silicon microstrip sensor (Figure 1.9a) connected to two **F**ront-**e**nd **b**oards (FEB)s (Figure 1.9c) via ultra-thin microcables. Each side of the sensor features 1024 strips linked to a FEB that includes eight custom-designed **A**pplication **S**pecific **I**ntegrated **C**ircuit (ASIC). Groups of 128 strips are connected to two sets of micro-cable stacks, which carry the analog signals to the FEE [39]. The sensors will be affixed to 106 carbon-fiber support structures that populate the eight tracking stations (see Figure 1.8c).

The sensor technology implemented in the STS has been specifically selected to enhance detector performance, with a focus on improving track reconstruction efficiency and minimizing mass requirements. Double-sided microstrip sensors offer the benefit of projective space-point determination using the same volume of silicon, in contrast to single-sided strip sensors, which require double the sensitive material for equivalent functionality [39].

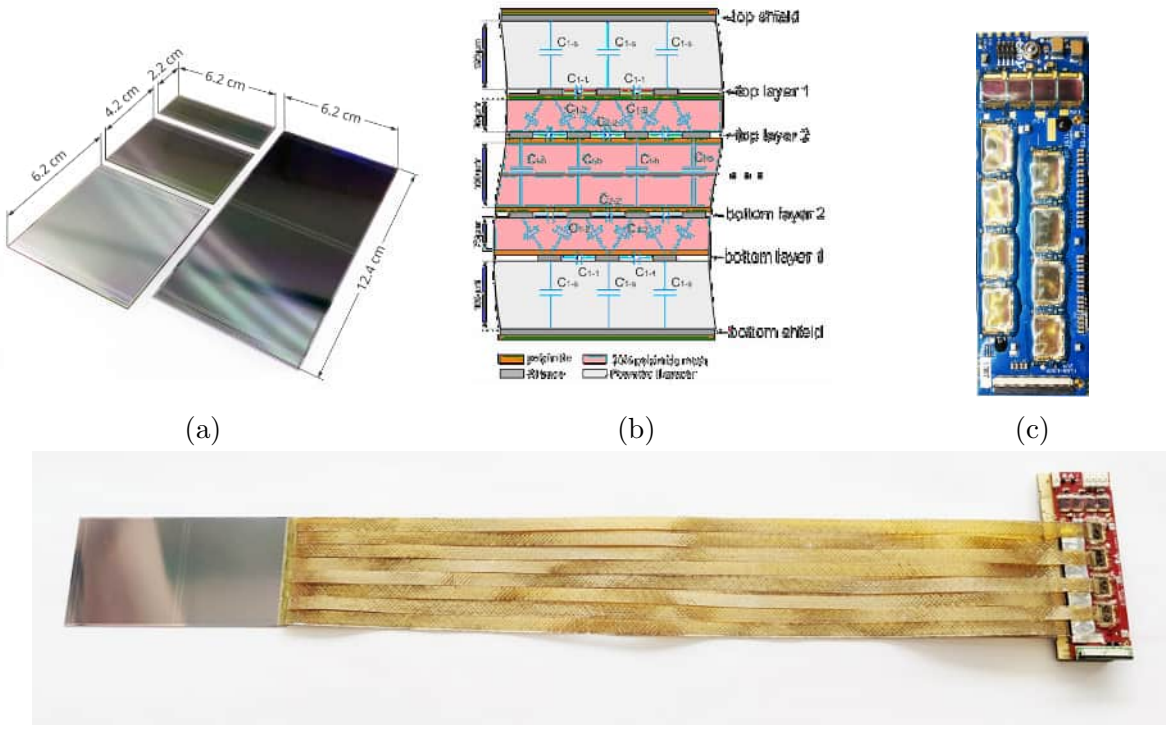

(a) (b) (c)

(d)

Figure 1.9: STS module and sub-parts: a) Sensor of different size formats; b) Micro-cable stack cross-section diagram illustrating the effective capacitance between different cable-layers; c). State of the art FEB; d). Fully assembled module.

The STS sensors are produced on 320 μm thickness wafers by Hamamatsu Photonics K.K. The strips are positioned with a pitch of 58 μm. The sensors will feature integrated AC coupling to avoid the need for leakage current compensation circuitry in the FEE. The orientation of the strips on the *n-side* of the sensor is designed to be perpendicular to the top and bottom sensor edges, whereas on the *p-side*, the strips will be inclined at an angle of 7.5°. This configuration has been carefully optimized to minimize the occurrence of ghost hits while simultaneously maintaining sufficient resolution along the n-side strip direction. The 7.5° stereo angle results in shorter strips at the sensor's edges interconnected through a second metalization layer on the sensor, as outlined in [46].

To fulfill the critical requirement of a low-material budget, low-mass micro-cables will be employed to convey signals from sensors to the front-end electronics situated in the periphery of the detector. These micro-cables are enveloped in a shielding layer to mitigate electromagnetic interference and minimize noise levels. Two layers of micro-cable incorporating aluminum strips with a pitch of 116 μm are used for effective signal transmission. A meshed spacer spatially separates the layers to diminish parasitic inter-layer capacitance. The supporting material for the aluminum strips consists of 20 μm polyimide (see Figure 1.9b).

The silicon sensor signals will be handled by a custom-designed **STS X**, **Y** coordinates, **T**ime and **E**nergy **R**ead-out (STS-XYTER) ASIC. This ASIC will perform the discrimination and digitization of signals from individual sensor strips, followed by the serialization of the digitized data. Due to the distinct channel occupancy anticipated across various detector regions, individual ASICs can be customized to support 1, 2, or 5 readout links, each operating at a speed of 320 Mb/s.

Considering the expected high interaction rates and the absence of straightforward criteria for triggering and selecting collisions involving signatures such as Ω hyperons or D mesons, a full reconstruction of the collision is essential. The experimental setup incorporates self-triggered FEE, rapid free-streaming data transmission, and real-time event selection and online reconstruction. This architecture is specifically engineered to enhance data throughput and analytical efficiency in a demanding experimental landscape.

1.4 Research goals and thesis structure

Based on the previous sections, the CBM experiment is not only feasible from a technological standpoint but also promising for the field of particle physics. However, ensuring that detectors operate reliably and meet the design requirements is fundamental to their success. This process begins at the prototyping phase, where rigorous validation and optimization are performed to guarantee long-term stability and performance. In particular, a special focus on operational aspects involves maintaining the quality of each step in the reconstruction chain.

This doctoral research seeks to systematically evaluate and refine the operational efficacy of the STS within the CBM experiment once commissioned. With the main focus on the STS subsystem, by analyzing the recorded data by the mCBM@SIS18 setup during several beamtime campaigns. The mCBM@SIS18 [47] **m**ini-CBM (mCBM) is a functional prototype for the CBM system. As this research is data-driven and the mCBM@SIS18 setup has recorded the employed data, a brief chapter describes the most relevant aspects.

The key point of this research will be to assess the following:

- Development and performance of the preliminary time calibration.
- Performance of the STS hit reconstruction.
- STS capabilities for beam profile and vertex reconstruction.

The thesis is organized as follows:

Chapter 1 – Introduction: A general introduction to the CBM experiment and its physics program. Relevant details of the Silicon Tracking System challenges and design.

Chapter 2 – The mCBM@SIS18: Description of mCBM@SIS18 setup, focusing on mSTS setup operation and relevant data-taking details.

Chapter 3 – Reconstruction chain: A detailed description of the complete reconstruction chain on its most up-to-date status. It includes details from the data streaming up to the track reconstruction.

Chapter 4 – Data Analysis: This chapter outlines the data analysis at various stages of the reconstruction chain. It also develops the results of the time calibration procedure and noise channel detection.

Chapter 5 – Hit Reconstruction Performance: This chapter is dedicated to the performance of the STS hit reconstruction, specifically spatial coordinate correlations, position resolution, and hit reconstruction efficiency analysis.

Chapter 6 – Beam Spot and Vertex Reconstruction: Using the reconstructed STS hit together with the other subsystems in the mCBM@SIS18 setup, beam spot and vertex capabilities have been explored by a preliminary approach.

Appendices – Several appendices have been included to support the detailed aspects of the analysis. Furthermore, a compressed version of the entire research, as it has been published at arXiv under the identifier https://arxiv.org/abs/2505.20517, has been attached, containing this research contribution and detailed information related to the operational performance of the STS detector.

Chapter 2

The mini-CBM experiment at SIS18

The mini-CBM (mCBM) setup has been crucial for advancing the CBM experiment and represents a collaborative effort involving all members of the CBM collaboration. In this experiment, prototype or pre-series components of all major CBM systems are installed in a common test setup (see Figure 2.1), operational as a fixed-target setup with heavy-ion collisions at the GSI SIS18. The goals of mCBM focus on testing and optimizing the operation as a full system of complex hard- and software components – from the detectors and the front-end readout electronics, as well as the free-streaming data acquisition system, the online data processing, including tracking and event reconstruction, the offline data analysis, and the detector control system under realistic experimental conditions [37].

As a benchmark physics observable for the CBM data-taking concept, the production probability of the Λ baryon, measured with its weak decay into a pion and a proton, was chosen. Produced close to or below the free NN production threshold at SIS18-energies, its cross-section is sufficiently small to pose challenges to the reconstruction and selection task similar to those expected by CBM at SIS100.

Various tasks related to CBM hard- and software work packages, as well as specific mCBM tasks, are being undertaken prior to the experiment, including: design of the experimental setup; simulations on benchmark observables; design and reconstruction of the mCBM cave; design and construction of the beam-line, including the target chamber; design and procurement of the vacuum chamber for the switching magnet; design and construction of the individual sub-systems; installation of the common setup; set up and commissioning of the DAQ hardware, including connection to the Green-IT Cube.

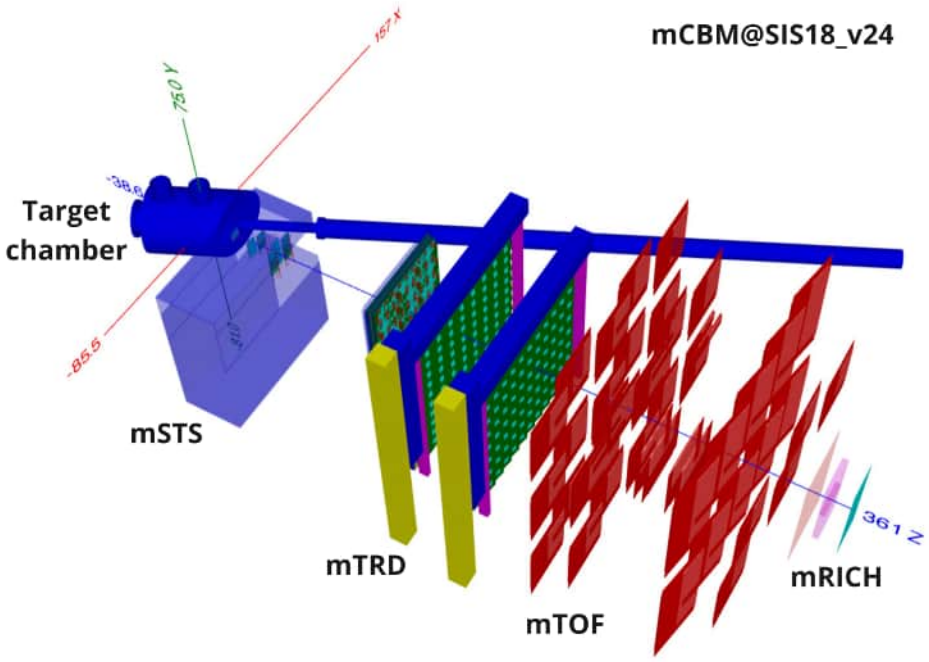

Figure 2.1: mCBM@SIS18 ROOT geometry for 2024 setup.

The mCBM setup has been operational since 2018, featuring various prototype detectors, including the STS. Since 2021, the nominal **m**ini-**STS** (mSTS) subsystem has been installed and upgraded in 2024. Different nuclear reactions have been studied specifically:

- O+Ni and Ni+Ni reactions at top SIS18 energies or below, used for the study of detector performance and physics observables;
- U+Au and Au+Au reactions at top SIS18 energies, specifically targeting detector performance with beam intensity scan.

In the context of this thesis, most data from O+Ni and Ni+Ni from 2021, 2022, and 2024 have been analyzed to study the performance of the STS system. A significant selection, mainly collected in 2024, will be presented.

2.1 The beam from SIS18

The accelerator complex at **G**esellschaft für **S**chwer**i**onenforschung GmbH (GSI), Darmstadt, has the worldwide unique capability to generate intense beams of almost all heavy ion species, from protons to Uranium ions. The GSI-Synchrotron SIS18 is a heavy-ion synchrotron with a circumference of 216.72 m and a magnetic rigidity of $18\,\mathrm{T}\cdot\mathrm{m}$, capable of accelerating particles coming from the **UNI**versal **L**inear **Ac**celerator (UNILAC) with an

energy of about 10 MeV per nucleon up to 2 GeV/u. As it is set to serve as a booster for the primary synchrotron of the FAIR facility SIS100, an upgrade program has been executed to optimize the booster's operational performance [48].

Currently, this facility can deliver a uranium beam with an intensity $N = 4 \cdot 10^9$ ions having a particle energy of a few hundred MeV. The particles are delivered in a single bunch, a few hundred nanoseconds long. For the mCBM experiment, beam particles are extracted into a spill from the SIS18 ring employing kicker magnets. The term *spill* refers to the controlled extraction of a particle beam from the accelerator over a defined duration. This terminology is commonly applied during extraction from a storage ring or synchrotron (in this case, SIS18) as the beam is directed toward an experimental target or detector.

The accelerator modulates particle emission over extended periods, from milliseconds to several seconds, allowing for a continuous and controlled particle rate that is essential for applications requiring a steady flux. The SIS18 synchrotron at GSI employs resonant extraction for slow beam extraction, utilizing two electrostatic septa: one for injection and one for extraction, which differ in function despite similar structures [49]. The extraction septum targets a deflection angle of 205 mrad at a maximum rigidity of 5.3 GV and an electric field of 90 kV/cm. However, recent studies indicate the observed deflection angle may be about half of the theoretical prediction [50].

A critical feature of slowly extracted beams is spill quality, particularly in terms of time structures. At SIS18, micro-to-millisecond variations in spill time structures, known as spill micro-structure, were identified. These variations were caused by power supply ripples affecting quadrupole magnets, leading to unintended machine tune variations [51]. These structures must be minimized to meet experimental detector requirements, as they can cause interaction rate fluctuations of up to 10 times.

Additionally, beam emittance, which represents the area in position-momentum phase space, is of importance. Due to horizontal multi-turn injection, horizontal emittance is significantly larger than vertical emittance. The transverse emittance exchange effect allows for reduced beam size at the extraction plane under suitable conditions, resulting in a horizontal beam size of 3.1 mm and a vertical size of 5.2 mm [51].

Table 2.1: mCBM station angular coverage and approximate positioning downstream.

Station	Horizontal angular range	Vertical angular range	Z
mSTS0	13.0° - 37.0°	±12.0°	∼ 16 cm
mSTS1	13.0° - 37.0°	±12.0°	∼ 28 cm
mSTS2	13.0° - 37.0°	±12.0°	∼ 42 cm
mMUCH	13.1° - 36.9°	±11.9°	∼ 80 cm
mTRD	11.4° - 38.6°	±13.6°	∼ 190 cm
mTOF	11.1° - 46.6°	±15.3°	∼ 225 cm

2.2 The mCBM setup

The detector subsystems of the mCBM test setup are positioned downstream of a solid target under a polar angle of 25° with respect to the primary beam at the beam entrance of the experimental area Cave-C (HTD). The beam dump is located 7 m downstream of the target at the south end of the experimental area.

Given that mCBM uses a right-handed coordinate system, with the origin located in the target position, the x-axis (red) is horizontally aligned, the y-axis (green) is pointing vertically upwards, the z-axis (blue) is also horizontally oriented but rotated around the y-axis by 25° away from the direction of the primary beam (see figure 2.1). The test setup does not comprise a magnetic field. Therefore, reaction products will follow straight trajectories.

According to the needs, the initial configuration of the mCBM test setup is rather versatile. It has been variably adapted to the test program foreseen in the different beamtime runs performed since 2018. Table 2.1 shows the nominal values for the acceptance of different subsystems and their nominal position along the z-axis [52].

2.2.1 The data acquisition and the mFLES

As demanded by the high rates expected in the CBM experiment, the data acquisition (DAQ) and data transport system used in the mCBM setup include ultra-fast and radiation-tolerant ASICs as front-end chips, followed by CERN GBTx-based radiation-tolerant data aggregation units. The detector front-end digitizes signals above a threshold and assigns a time stamp to the hit. By a Timing and Fast Control (TFC) system, the detector front-ends are time-synchronized to the nanosecond level. This data is then forwarded via an electrical connection to the GBTx readout board, where the electrical signals are converted and merged into an optical GBT link operating at a link speed of 4.48 Gbit/s. These GBT links interface the detector subsystems with the PCIe-based CRI boards, which are integrated into the FLES input node installed in the DAQ container near the HTD cave. A dedicated topology

allows micro-slices from all active mCBM subsystems in a single FLES compute node to be received in the Green IT Cube. The FLES compute node combines all those micro-slices into a single time-slice, which is then passed to the reconstruction and analysis stage.

2.2.2 The mCBM target

The target for the mCBM setup is enclosed in the beam pipe by a target chamber manufactured at GSI. It provides mechanical support and a vacuum environment for the T0 detector and the target station. The target station adheres to a five-fold target ladder, which can accommodate targets of various materials and thicknesses, enabling the exchange of samples without manual intervention (see Figure 2.2). Typical targets used during beamtime are [53]: silver (Au) thick (2.5 mm) and thin (0.25 mm); nickel (Ni) thick (4.0 mm) and thin (0.40 mm) target.

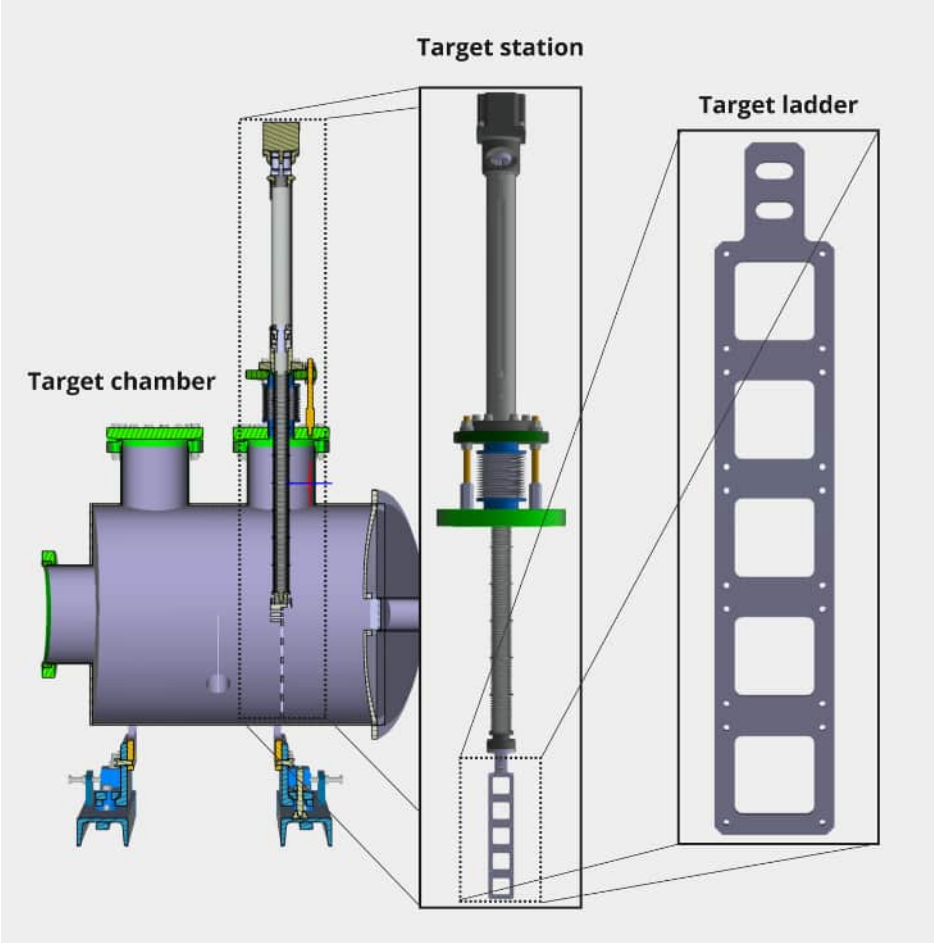

Figure 2.2: Cross-section view of the mCBM@SIS18 target chamber. A perspective zoom-in of the target station and the target holder is illustrated and enclosed in a dashed line box.

2.2.3 The mCBM beam monitoring system

For the CBM experiment, the **B**eam **MON**itoring (BMON) system consists of a high-speed time-zero (T0) and halo detector. Such a system must meet the requirements of the time-of-flight (TOF) measurement system for proton and heavy-ion beams. Time resolution must be better than 50 ps (σ) and maintain stable long-term operation at high interaction rates of 10^7 particles/s. The required detection efficiency should approach 100 %. A prototype **p**oly-**c**rystalline **C**hemical **V**apor **D**eposition (pcCVD) T0 detector was built and tested during several benchmark test runs [54]. In the context of this work, the T0 detector is used as a reference for the time calibration of the STS detector.

2.2.4 The mCBM detection subsystems

The mini-MUCH (**mMUCH**) subsystem consists of two stations positioned immediately after the STS detector, employing GEM technology, and two stations located at the end of the mCBM setup, which use a RPC. The choice of technology is dictated by the expected data rates, which are higher for the first two and lower for the latter ones. For the beamtime campaigns used for the present work (2021, 2022, and 2024), the mMUCH setup is taken out and is not part of the common data acquisition.

In the data analyzed in the present work, the mini-TRD (**mTRD**) setup is placed directly downstream of the STS. In the mCBM set, two TRD chambers are installed with pads oriented respectively along the X(Y) direction, which provide a space point with a good (a few mm) resolution only in the X(Y) dimension. Additionally, two modules of the TRD-2D version, intended for the innermost region of the detector in the CBM experiment, were operated in the setup, upstream of the TRD modules. A novel readout design replaces the rectangular read-out inductive plane with readout elements of a right triangular shape, bringing the resolution across pads into the hundreds of microns range. The time resolution of those detectors is in the order of 100 ns. In the context of this work, the mTRD detector is used to provide space points for track reconstruction, which serves as a reference for studying the STS performance.

The mini-TOF (**mTOF**) subsystem consists of six modules grouped into two stacks; each module comprises five MRPC with different rate capabilities for the different regions of the detector. The mTOF subsystem features an excellent time resolution (60–80 ps). In the mCBM experiment, where the absence of a magnetic field prevents momentum measurement, the TOF detector calculates the velocity for track candidates matched to a TOF point, thanks to its good spatial resolution (order of a few millimeters). With a selection on the non-zero impact parameter of the track, a mass hypothesis is used to determine pion

and proton secondary candidates, which, combined, can lead to the reconstruction of the benchmark signal of a Λ baryon. In the context of this work, the mTOF detector is also used to provide space points for the track reconstruction. Moreover, the excellent time resolution enables us to use it for time calibration, similar to the BMON detector.

A prototype of the RICH (**mRICH**) is used in mCBM in proximity-focusing operation mode with an aerogel radiator. It is placed behind the mTOF detector in a selected acceptance window. Although it offers excellent time resolution (around 5 ns for rings) and good spatial point resolution, the limited acceptance of the MultiAnode Photomultipliers prevents its use in correlation with the STS in the present work.

2.3 The mSTS

Closest to the target chamber, the STS setup, as installed in 2021 and operational til now, consists of 11 modules arranged in two tracking stations of an active area of 12 cm × 12 cm and 18 cm × 18 cm. It was upgraded in 2024 by installing a single module equipped with a 6.2 cm×6.2 cm sensor, resulting in an additional tracking station upstream of the pre-existing ones [55].

Figure 2.3 shows the setup in detail. The mSTS box consists of 11 modules: two modules sized 6.2 cm × 12.4 cm and nine modules of 6.2 cm × 6.2 cm silicon sensors. These are organized into four physical units mounted on aluminum support structures, referred to as C-frames[1] [43, 37]. The assembly of these modules incorporates FEBs with a single up-link per ASIC.

The mSTS upgraded, installed for the 2024 beamtime, comprises a module featuring a $62 \times 62\,\mathrm{mm}^2$ sensor, meeting cutting-edge standards under CBM quality specifications. The module is equipped with ASICs that provide five uplinks, thereby significantly boosting the data acquisition capacity and facilitating the validation of the STS's high-rate performance [55]. The mechanical implementation is illustrated in Figure 2.3.

The tracking system therefore comprises three stations with transversal dimensions of 6.2 cm × 6.2 cm, 12 cm × 12 cm, and 18 cm × 18 cm. The z value indicated in Table 2.1 represents the average position of the sensors for each station, which are adjusted so that the three stations have consistent geometrical acceptance for the reaction products. The electronic components within these modules display considerable heterogeneity, reflecting the natural progression in their development. Some modules are prototypes and a combination of pre-series stage components, while others are made of final or close-to-final equipment.

[1] custom-designed C-frames for mCBM@SIS18

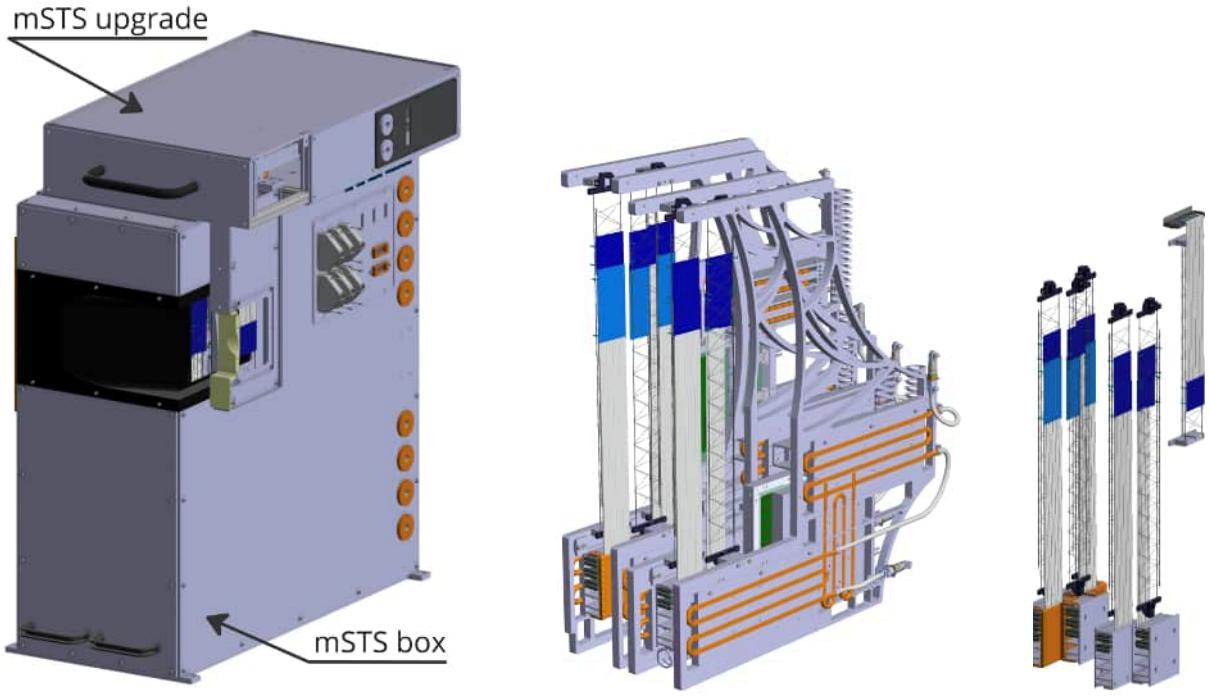

(a) (b) (c)

Figure 2.3: (a) The mSTS setup, as of 2024, consists of the mSTS upgrade on top of the mSTS box. (b) Mechanical units inside the mSTS box. (c) mSTS ladders.

Figure 2.3 shows the CAD of the mSTS setup. The four mechanical C-frames were custom-designed for the sole purpose of the mCBM experiment (see Figure 2.3b). The second mSTS station comprises two ladders supported by two independent C-frames. Each ladder contains two modules assembled using $62\,\text{cm} \times 62\,\text{cm}$ sensors. The third mSTS station comprises three ladders supported by two independent C-frames. The first of those supports the middle ladder built with two different modules: the top one uses a $62\,\text{cm} \times 62\,\text{cm}$ sensor while the bottom one uses the $62\,\text{cm} \times 124\,\text{cm}$ format. From the lateral ladders in the last C-frame, the one closer to the beam pipe has the same structure as the middle ladder, while the other one comprises three modules with $62\,\text{cm} \times 62\,\text{cm}$ sensors. The ladder assembly procedure precision is in the order of $100\,\mu\text{m}$, which has undergone progressive optimization [43, 37, 41].

In contrast to the pre-existing setup, the module installed for the 2024 upgrade is not mounted on a C-frame. The sensor is mounted on a short ladder. It is connected to the two FEB8-5 installed in a separate service box, mounted on top of the existing mSTS box, together with the common read-out boards (CROB) and the power board, which provides supply voltages for the FEBs.

2.3.1 Modules naming convention

Modules within the setup have a unique associate identification number known as *address*. This address encodes the exact position where the module is placed. Within the mCBM scope, some of the encoded information is redundant due to the small number of sensors. Shortening the reference to specific modules will be done by three (letter, number) pairs: unit index (U), ladder index within the unit (L), and module within the ladder (M). In the STS, the unit U represents a tracking station. The notation is valid when referring either to modules or sensors. Counting always starts at zero; in the context of mCBM, M0 is the top module, L0 is the ladder furthest from the beam, and U0 is the most upstream station closest to the target. For example, the first sensor in the second ladder at the second tracking station can be referred to as U2 L1 M0 . Nevertheless, such notation can be extended in the scope of full CBM, where specifying half-ladder (HL), top or bottom w.r.t the horizontal axis is relevant. This is possible, given that the address encoding was foreseen for the full CBM STS setup.

2.3.2 Commissioning and operation

All the assembled electronic components have undergone an exhaustive QA control where minor imperfections that will not strongly impact the final STS module performance are allowed. After assembly and prior to the integration in the setup and installation in the cave, fully assembled modules are tested in the STS Laboratory to set the necessary operation parameters and verify the working potentials, the noise levels, the signal readout, and the number of functional channels [56, 57, 43, 37, 55].

The noise performance is also re-measured after integration on the ladder in the STS box and final installation in the mCBM cave. Refer to Section 4.2 and Figure 4.1 for a detailed explanation.

An essential step towards successfully operating the STS modules demands the calibration of the analog front-end circuits. In the SMX ASIC, each channel's ADC possesses 31 discriminators. The procedure of fine-tuning the $N_{ADC}^{Chn} \times N_{Chn}^{ASIC} \times N_{ASIC}^{Mod}$ calibration param-

eters for a single module (with 31 discriminators per channel N_{ADC}^{Chn}, 128 channels per ASIC N_{Chn}^{ASIC}, 16 ASICs per module N_{ASIC}^{Mod}) has been automated and optimized. It ensures high linearity (Figure 2.4a), small dispersion for thresholds (Figure 2.4b) and gain (Figure 2.4c). Calibration results in an effective value of ADC gain (β) and threshold for each channel. It provides the input necessary to convert the digitized signal amplitude in arbitrary ADC units back to physically meaningful units as e. For such, it is sufficient to determine the threshold (Thr) and the dynamic range (Dyn) during operation by equations 2.1 and 2.2. The parameters α and β are determined during the calibration procedure [58].

$$\mathrm{Thr} = \mathrm{Thr}_{\mathrm{cal}} - \alpha(\mathrm{Vref}_{\mathrm{T}}^{\mathrm{cal}} - \mathrm{Vref}_{\mathrm{T}}^{\mathrm{opr}}) \tag{2.1}$$

$$\mathrm{Dyn} = \beta \mathrm{N}_{\mathrm{ADC}} \tag{2.2}$$

The mSTS setup was operated with a highly heterogeneous configuration for its various modules. It results in significant differences in thresholds and dynamic ranges across different modules. Thresholds ranged within 3–6 ke for most modules but also reach 12 ke for particularly noisy prototypes, while dynamic ranges are typically around 65 ke but span in 60–80 ke due to some outliers in the gain. Moreover, this configuration is susceptible to minor changes from one beamtime campaign to the next.

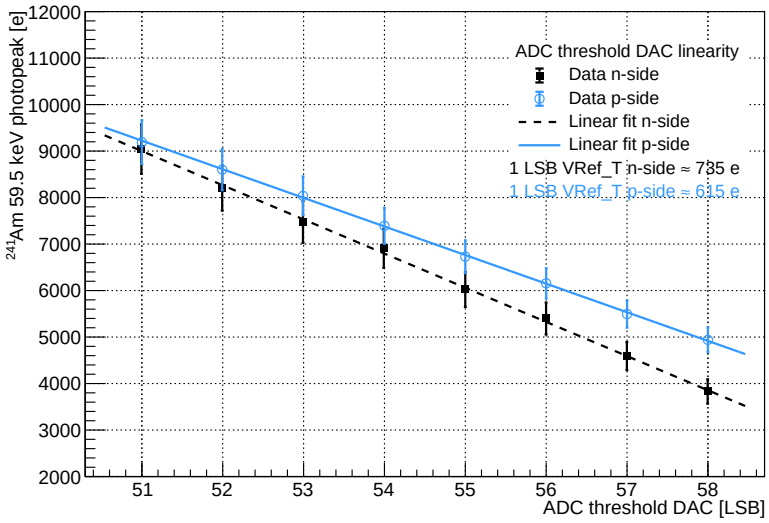

(a)

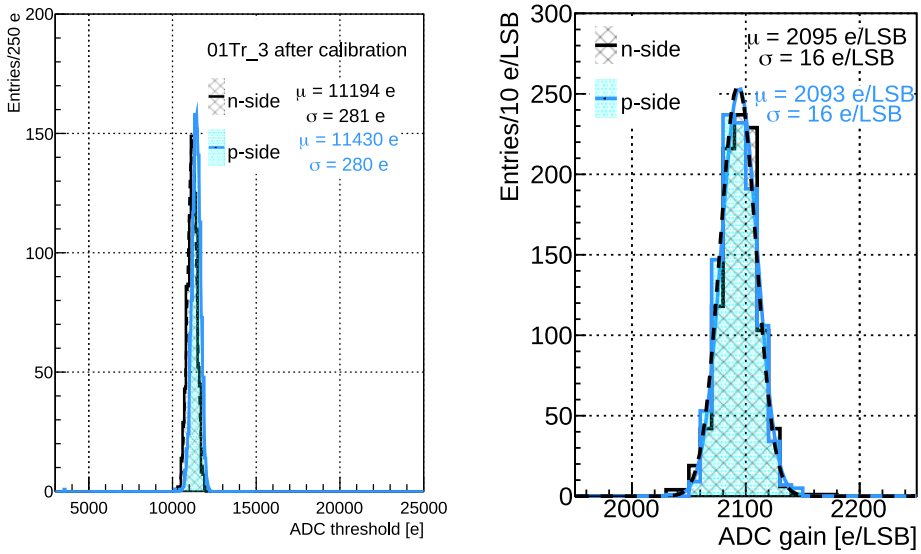

(b) (c)

Figure 2.4: mSTS setup module U1 L0 M0 calibration checks plots. (a) Linearity check of the threshold DAC using the 59.5 keV γ line of a reference ^{241}Am source. (b) The ADC threshold distribution. (c) The ADC gain distribution. (Taken from [58])

Chapter 3

The reconstruction chain

We refer to the **reconstruction chain** as the sequence of steps that starts from the raw signal from the triggerless free-streaming detector readout and finally produces a structured set of high-level data for physics analysis (**tracks**). This is shown in a simplified data flow diagram in Figure 3.1. It includes decoding the raw data from each sub-detector, collecting signals that belong to the same particle traversing the sub-detector, and recovering its trajectory, which is known as tracking. Due to the free-streaming nature of the experiment, the reconstruction chain also needs to include an event builder, i.e. an event association that requires four-dimensional (x, y, z, t) reconstruction routines. This can be applied at different stages of the reconstruction, leading to possible bifurcation in the reconstruction chain.

The CBM experiment is designed for processing online massive volumes of data. This leads to high-performance standards for computing, in terms of highly efficient and robust software components, as well as special requirements for all data structures, interfaces, and algorithms. It is, however, possible to store the data in a file at every step of the reconstruction and interface it to the offline reconstruction. This is crucial during the development phase.

As shown in Figure 3.1, the reconstruction chain works the same way for real and MC simulated data, provided that the MC data have consistent configuration as the real ones. This means that either event-by-event simulated data is processed as real data, after events are defined, or MC data are prepared to simulate the free-streaming data as expected to be delivered from the DAQ system of the running experiment.

This chapter provides a general overview and relevant details of the reconstruction chain, from storing and decoding the raw detector data to arranging the reconstructed information by event. Examples will focus on the reconstruction chain of the STS data, but can be generalized to other detectors where needed.

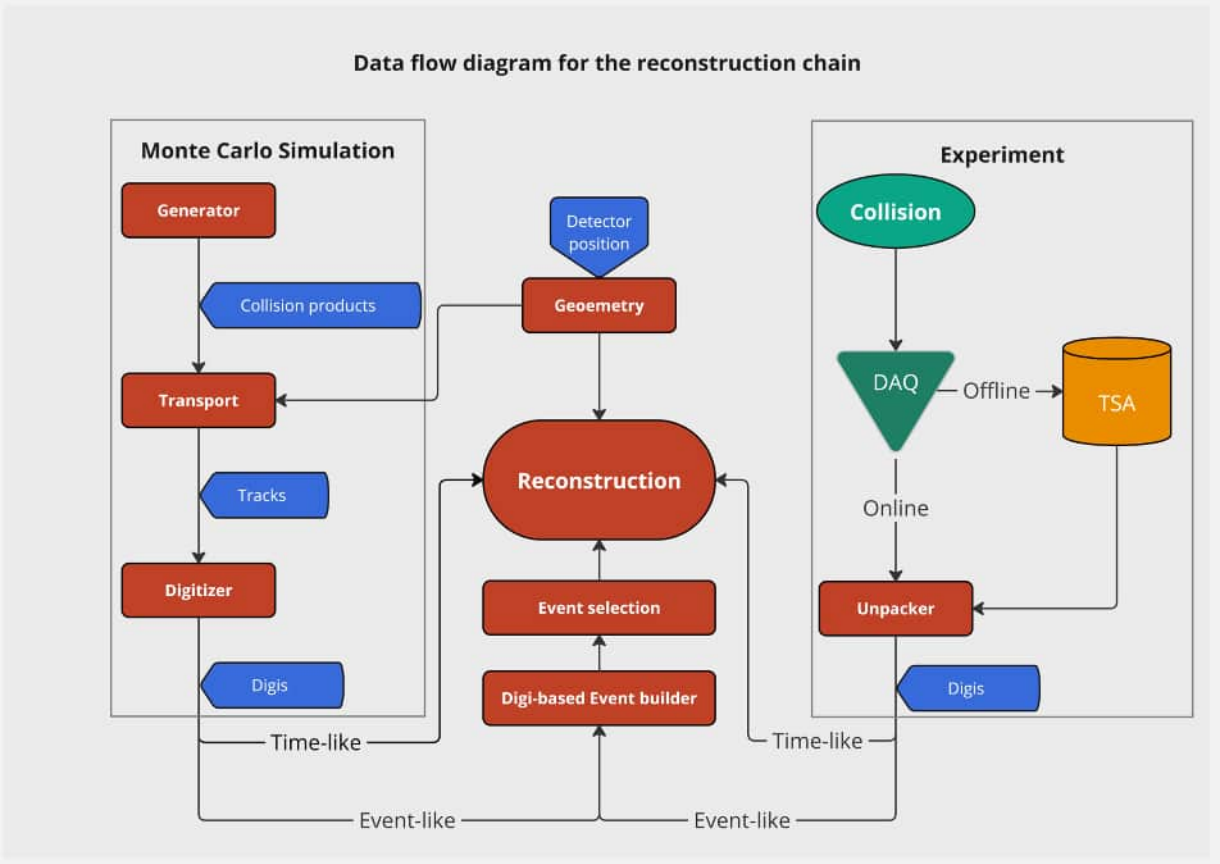

Figure 3.1: Simplified reconstruction chain data flow. Red shapes show software processing steps. Blue shapes show examples of the relevant information flowing.

3.1 The CBMROOT software

The CBM experiment is intended for handling large-scale online data processing, which demands high-performance computing standards. This requires a robust framework capable of processing the data in a reliable and timely fashion. Like most of the current high-energy experiments, if not all, the CBMROOT analysis framework is built upon ROOT, a high-performance object-oriented software developed at CERN and implemented almost entirely in the C++ programming language. Created in 1994 by René Brun and Fons Rademakers, it provides the mathematical and statistical tools to manipulate and analyze large amounts of data [59].

The CBMROOT framework contains codes that are common to the entire CBM collaboration. In particular, it includes:

- an interface for running Monte Carlo simulations (from the event generation to the detector response), event visualization;
- a dedicated task class that calculates the absolute hit time, taking the MC hit time (w.r.t. the event) and a model of the time structure of the beam, and delivers a continuous, time-sorted stream of MC hits to the digitizers;
- a description of the detector geometry as well as the material budget;
- the alignment and calibration of the detectors;
- the real and simulated data reconstruction, including the event builder task, which performs the association of detector signals to a physical event;
- and the management of the data formats.

CBM is designed to run the full event reconstruction online. The goal is therefore to use the same framework, i.e. data structures, interfaces, and algorithms in the online and offline reconstruction.

3.2 Monte Carlo data

As mentioned in Section 3.1, the CBMROOT framework can run Monte Carlo simulations that attempt to reproduce as accurately as possible the stochastic processes observed in the detector by sampling a given set of probability density distributions. Such a simulation consists of two consecutive steps. It begins with generating an event, which involves a collision, including the associated physics processes that ultimately lead to the creation of primary particles. This first step, relying on different models, is known as event generators, each with its own paradigm and production mechanisms. Event generators are tuned to mimic the topology of the collision, including multiplicity, momentum distribution, and other characteristics. Among the most commonly used, for heavy-ion collisions at CBM energies, there are UrQMD [60, 61], SMASH [62], PHQMD [63], or DCM-QGSM-SMM [64].

After the event is generated, the primary particles are propagated through the CBM detector. This requires modeling the apparatus and the various elements composing the sub-detectors, including their geometric shape and positioning. It must also account for noisy or dead channels, detector defects, and magnetic field intensity. These characteristics are, in general, run-dependent. The transport and interaction with the detector material typically rely on dedicated software, such as Geant3 [65] or Geant4 [66, 67, 68].

Considering the detector response, the energy deposited by the passage of charged particles is converted into and stored in raw data format, equivalent to Digis. From this point, the reconstruction of the event can start. It follows the same procedure (see Sections 3.5, 3.5) as the one applied for real data and produces CBMROOT trees with clusters and hits in events. This is how Monte Carlo data is typically used in conventional trigger-based experiments and how we use it in the present work.

In order to cope with the trigger-less free streaming readout of the CBM experiment, Monte Carlo data can be prepared to simulate the free-streaming data as expected to be delivered by the **D**ata **Acq**uisition system (DAQ) system of the running experiment. This requires including a model of the time structure of the beam and a model for the absolute hit time calculation of the MC hit time (w.r.t. the event) in the detector digitizers.

Neglecting possible fluctuations in the beam intensity and, thus, non-constant average collision rate, the CBM collision distribution in time can be described as a Poisson process. A time stamp assigned to each MC hit is calculated as a sum of the event's start time and the time shift due to the time of flight from the collision point to a hit. Finally, the hit time is smeared according to the detector time resolution.

At this point, digis are stored in raw data format, which is equivalent to free-streamed Digis. The reconstruction that will follow includes not only the reconstruction (see Sections 3.5, 3.5) but also the event builder (see Section 3.7) to produce CBMROOT trees with clusters and hits in events.

The key feature of MC data resides in its complete information about an event, often referred to as **MC truth**. Every aspect of the simulation is fully known: the number and types of generated particles, their charge and momentum, whether they are primary or secondary, where they deposit energy in the detector (resulting in hits or track references), and more. This extensive dataset enables a range of specific investigations. In the design phase of a new experiment, it allows for predicting results and, if necessary, refining or optimizing the design. It also offers a means to evaluate detector performance, such as efficiency, and investigate systematic features. Finally, comparing real data measurements with predictions from an MC model (simulated data) enhances our understanding of the underlying physics.

3.3 Time Stamped Archives

The processing nodes of the **H**igh **P**erformance **C**omputing (HPC) cluster provide the needed computing power to execute the online analysis tasks. These nodes are involved in the timeslice building process as part of the entry stage of the central data handling and event selection entity of the CBM experiment. A timeslice contains raw data from the entire CBM detector system for a small and limited duration. Input data streams are divided into time intervals covering the same period for all inputs. Data of a single stream acquired in such an interval are called a **T**ime**s**lice **C**omponent (TSC). All TSCs of a given period are combined into a whole processing interval, a timeslice. With most parts of the system still under development at the time of writing, the optimal timeslice size has not been optimized. It is a trade-off between overhead and required buffer capacity. Larger timeslices are less demanding for the system. On the other hand, the demand for buffer space for the timeslice building process depends directly on the size [69]. For the data that concern this research, the timeslice size was configured as 128.5 ms.

A defined stream of serialized classes, a single **TimesliceDescriptor**, followed by a sequence of **StorableTimeslice** objects[1], can be dumped into a file: **T**ime-**S**tamped **A**rchives (TSA). Although writing TSA files for the full statistics of collected data is not foreseen as a part of the main data flow in the future running of (m)CBM experiments, a small downscaled fraction of this data is relevant for debugging and special use cases.

3.4 The unpacker

Decoding the serialized raw data contained in timeslices is referred to as **unpacking**. Although timeslices contain information from the entire detection system, decoding a timeslice can be done for an arbitrary selection of detectors. The further online processing will include an exhaustive but highly efficient analysis to decide where the data should or should not be stored in real-time, contributing to the final data reduction [70].

The process of building a manageable software object out of the energy deposition of a particle traversing the silicon layer of the STS sensors is relatively simple but replete with crucial intricacies. The electronics processing of a single-strip signal is done independently of the neighboring strips or strips on the opposite side signals [71, 72]. This information is streamed into timeslices as a 32-bit STS signal.

Digi is often used as an abbreviation for digital information, referring to the digital signals

[1] object in the scope of **O**bject-**o**riented **p**rogramming (OOP)

or information generated by the detectors. In the context of CBM, a specific software object exists for every detector system to store such digital data. This data contains information about the energy deposition, time, and space coordinates of the interaction.

The `StsDigi` is a software object that stores for every fired strip the following information:

- Address of the module, encoding a unique position of the sensor within the almost 900 modules for the full STS.
- Channel: strip index that enables the local position determination of the collected charge.
- Time of the interaction (ns relative to the time slice).
- Charge: digitized signal amplitude by the fired strip in arbitrary units (ADC).

Several operations are performed on the Digi while unpacking. The output for specific channels can be ignored based on the configuration readout and parameters files. This often occurs when the channel is not functioning properly. Necessary steps involve Digi's time modification, which is crucial in time calibration (see Section 4.3). This procedure also reflects the synchronization among detection systems.

The equivalent step for the Monte Carlo simulation corresponds to digitization, where the output is consistent in structure with the one from the unpacking algorithm. During digitization, the detector response is simulated, including possible suppression of signals for arbitrary channels. This mimics the realistic recreation of the experimental conditions regarding inactive areas. Moreover, different effects on detector response can be imposed, as is the case with the random firing of strips to emulate noise. The most relevant effect, in this regard, corresponds to the variation of the ADC digitization threshold for efficiency analysis (see Section 5.3). Using the same detector configuration for charge calibration in the simulation as in real detector operation validates the comparison to MC data.

Thesis contribution: Development of time walk effect removal at Digi level for STS system (see Section 4.3).

3.5 The Cluster and Hit reconstruction

The Cluster finder

The charge collected by the strip-segmented surface depends on the charge distribution generated by the particle during its passage through the active detector material. The larger the charge distribution spread is, the more strips will be involved in the collection process. The first step in reconstructing the interaction point coordinate is finding those

active channels associated with one particle crossing the detector. A detailed description of the algorithm for cluster finding from free-streaming input data can be found at [73, 74].

The algorithm's working principle relies on [74]:

- Two measurements are defined to belong to a cluster if they are in adjacent channels and their time difference is smaller than a threshold defined by the time resolution of the detector: $\Delta_{\mathrm{t,thr}} = 3\sqrt{2\sigma_t}$.
- Since the data are time-ordered, a cluster can be considered complete if there is a new measurement in one of its channels or one of its neighboring channels not belonging to the cluster, i.e., not compatible in time.

Digis are treated one by one as delivered by the data acquisition. The state of the respective detector channel and its two neighbors is examined for each new measurement. The following cases can be distinguished:

- The channel and its two neighbors have no registered measurements. Therefore, the new measurement is added, hence updating the status of the given channel.
- The channel has a previously registered measurement. A cluster is created, and the status of the contributing channels is reset. Afterward, a new measurement is added to the status vectors.
- The channel status is empty, but one or both neighbors previously registered a measurement. Two options are presented:
  - The time difference is larger than the threshold $\Delta_{t,thr}$. Hence, a cluster is created, and the corresponding channels are cleared. The new measurement updates the status for the given channel.
  - The time difference is smaller than the threshold $\Delta_{t,thr}$. The new measurement is added to the status.

The algorithm requires time-sorted digis, guaranteed during the time-slice-building process. However, cluster output will not be time-sorted, and an additional step might be needed later in the reconstruction chain.

In addition to the cluster finding, the accurate determination of the particle's position during interaction with the sensor's active area is required. The cluster position is determined by averaging the weighted digis belonging to the cluster, where the weights are based on the measured charge. The algorithm is based on an unbiased approach, motivated by minimizing position residuals in the case of uniform energy loss, and was developed by [75]. The position for a two-strip cluster is then given by equation 3.1 while the position for an N-strip cluster with activated strips from x_i to x_j is given by equation 3.2. Improvements

are added to the formula to mitigate the impact of significant fluctuations on energy loss and other effects, such as noise [75].

$$x_{\mathrm{rec},2s} = \frac{1}{2}(x_1 + x_2) + \frac{p}{3}\frac{q_2 - q_1}{\max(q_1, q_2)} \tag{3.1}$$

$$x_{\mathrm{rec,Ns}} = \frac{1}{2}(x_i + x_j) + \frac{p}{2}\frac{q_j - q_i}{\max(q_i, q_j)} \tag{3.2}$$

Charge distribution and cluster size dependence with the particle incident angle have been discussed at [75]. Incident particles with a trajectory perpendicular to the sensor will create electron-hole pairs collected by only one strip on each. When trajectories start to deviate from this simple case, more strips participate. The amount of traversed silicon material increases for large angles, resulting in higher energy deposition. The resulting cluster total charge rises. These correlations between the cluster charge and cluster size were investigated and discussed by [76, 77].

The Hit finder

With its respective uncertainty, cluster position determination is crucial for proper hit reconstruction performance. The algorithm for hit reconstruction considers the non-uniformity of an incident particle energy loss, the detector noise, the signal discretization, and the error introduced by the cluster position-finding algorithm [78, 75]. These considerations come from the cluster position reconstruction algorithm briefly described in Section 3.5. A hit is formed by combining the two cluster centers on opposite sides of the sensor that geometrically intersect each other. Geometrically, these lines can cross outside the active sensor volume. Thus, the hit position is defined as the crossing point of the clusters on the p- and n-sides of the sensor, provided it falls within the active area. Figure 3.2 illustrates the geometrical interception 1-strip cluster: left panels in a perspective view, and the right panel shows an orthographic view. Interception of fired strip provoked for the passage of the same particle will be reconstructed (real hits). The additional interception of strips fired by different particles will also produce reconstructed hits: **ghost** hits.

Reconstructed hits are the first step in reconstructing the particle trajectories, also known as tracks. Track reconstruction algorithms require knowledge of the hit positions and the precision of such measurements. The CBM STS detector employs an analytic approach to estimate the reconstructed hit position uncertainty. The intrinsic detector resolution is influenced by the error of the **C**luster **P**osition **F**inding **A**lgorithm (CPFA) σ_{CPFA} and the error caused by non-ideal charge measurement σ_{charge} 3.3. [78, 75]

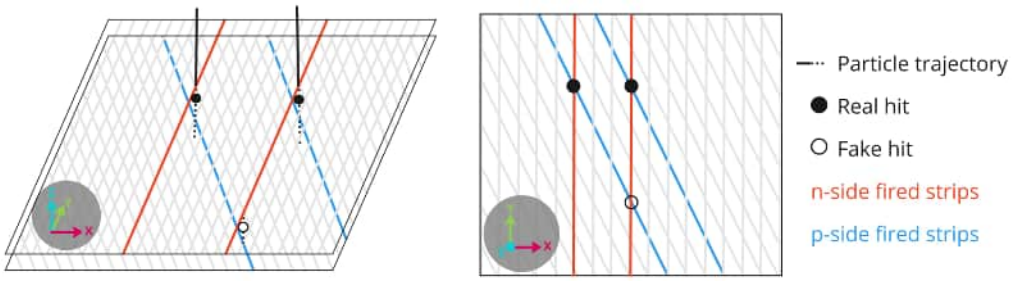

Figure 3.2: Hit reconstruction for 1-strip cluster. The fired strip position is represented by blue lines (p-side) and red lines (n-side). A combination of solid and dashed black lines represents particle trajectories. Reconstructed hits are shown as solid (real hits) and empty (fake hits) black dots. (Stereo-angle is exaggerated for representation purposes)

$$\sigma^2 = \sigma^2_{\text{CPFA}} + \sigma^2_{\text{charge}} \tag{3.3}$$

A way to verify the hit reconstruction resolution through Monte Carlo is by the pulls. Pull is a residual normalized to the estimated error: pull = residual/error. For a set of hits with an identical error estimate for each hit (for example, the set of all one-strip clusters or the set of 2-strip clusters with the same charge ratio), the pull distribution is nothing but the residual distribution 3.4 divided by a number. The pull shape, therefore, reproduces the residual shape. If the error is estimated correctly, the pull distribution width (second central moment) is unity. Figure 3.3 shows the residuals and pull distribution for the x coordinate.[2]

$$\rho = x^{\text{reco}} - x^{\text{MC}} \tag{3.4}$$

Thesis contribution: Experimental evaluation of the hit position resolution (see Section 5.2) and hit reconstruction efficiency (see Section 5.3).

3.6 The tracking

The tracking is done with the **C**ellular **A**utomaton (CA) 4D track reconstruction algorithm [79]. It comprises two essential assignments: track finding and track fitting. Track finding is, in general, a pattern recognition problem. Finding and combining those reconstructed hits produced by the same particle into groups enables the reconstruction of the particle's trajectory. Track finding, in most cases, employs raw detector hit measurements. No significant data reduction can be done at this stage without incurring information loss.

[2] Adapted from [79]

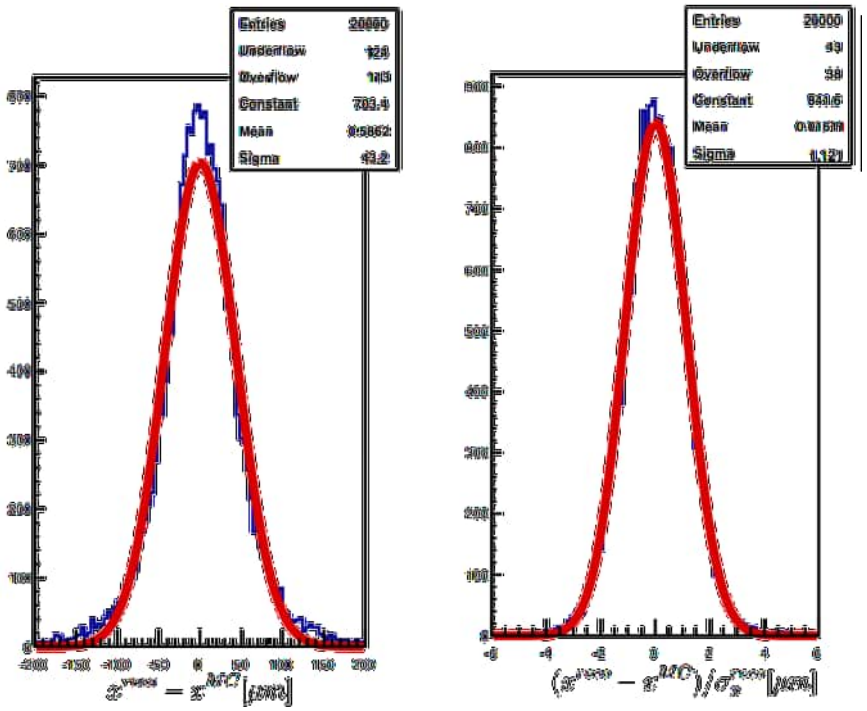

(a) (b)

Figure 3.3: Residual and pull distribution for reconstructed x hit coordinated.

Hence, this stage is often considered the most challenging and time-consuming part of the reconstruction. The track-fitting task involves finding the parameters that describe the trajectory based on a mathematical model (i.e., a straight line for charge particles in a non-magnetic field: mCBM@SIS18 case).

Track finding and track fitting tasks for CBM are not independent but very much linked. Track finding involves estimating parameters to enhance the search for subsequent measurements, using the reconstructed track with refined fitted parameters. This is driven by the **K**alman **f**ilter (KF) method, which has become a standard algorithm in high-energy physics for track fitting. The Kalman filter method allows for a computationally more straightforward and numerically optimized implementation. These advantages stem from the fact that the method operates with matrices whose dimensions equal the number of fitted parameters, unlike other cases, such as the least squares fit, which operates with a matrix whose dimension equals the number of measurements in the track. A fundamental feature of the KF method is that, instead of requiring a global track model valid for the entire track length, it utilizes a local track model valid only between consecutive measurements. This is especially relevant for particle trajectories that are partially contained within a magnetic field.

In the case of the CBM experiment track fit, the state vector of track parameters 3.5 was chosen in a convenient form for a forward detector geometry. The z-coordinate is directed downstream the beam along the detector, x and y are the track coordinates at a certain z-position, $t_x \equiv tan(\theta_x)$, and $t_y \equiv tan(\theta_y)$ are the track slopes in the XZ and YZ planes, respectively, and q/p is the charge to momentum ratio. Dependency between the x and y coordinates at STS sensor planes is considered. [79]:

$$\vec{r} = \{x, y, t_x, t_y, q/p\} \tag{3.5}$$

Studies with double-sided silicon sensors of 300 μm thickness have shown that **M**inimum **I**onizing **P**article (MIP)s create about 24 k electron-hole pairs [80]. This translates to at least a 24 k scattering process, which must be considered for the slope parameters. The algorithm uses the Highland-Lynch-Dahl formula (see equation 1.1) to estimate the total scattering angle from the width of the angular distribution.

Similarly to the reconstructed hits, the track fitting quality assurance task is reviewed by the pull distribution of the track parameters. Figure 3.4 shows the residual and the pull distribution for t_x[3]. All pull distribution widths are close to 1.0, indicating the correctness of the fitting procedure.

The KF track fitting algorithm also estimates the track parameters at the STS layers with their respective uncertainties. As aforementioned, the link between the track fitting and the track finding steps lies in using the KF algorithm to fit partially reconstructed tracks to search for the subsequent hit measurement.

A significant obstacle to be solved by a track finder algorithm is the enormous track density produced by the combinatorial nature. The CA track finder algorithm provides a solution to such an obstacle, regarded as a local version of the Hopfield neural network [81]. The performance of this approach has been studied in various scenarios [82, 83].

Intermediate steps involve creating track candidates. By the last stage, only the longest tracks with the best χ^2 sharing no hits in common with better candidates are to survive. The input hits used by the reconstructed tracks are removed from consideration in the next stage, thereby decreasing the possible random combinations of hits and improving the algorithm's performance at high track multiplicities. Detector inefficiencies can negatively impact the CBM CA tracking.

[3] Adapted from [79]

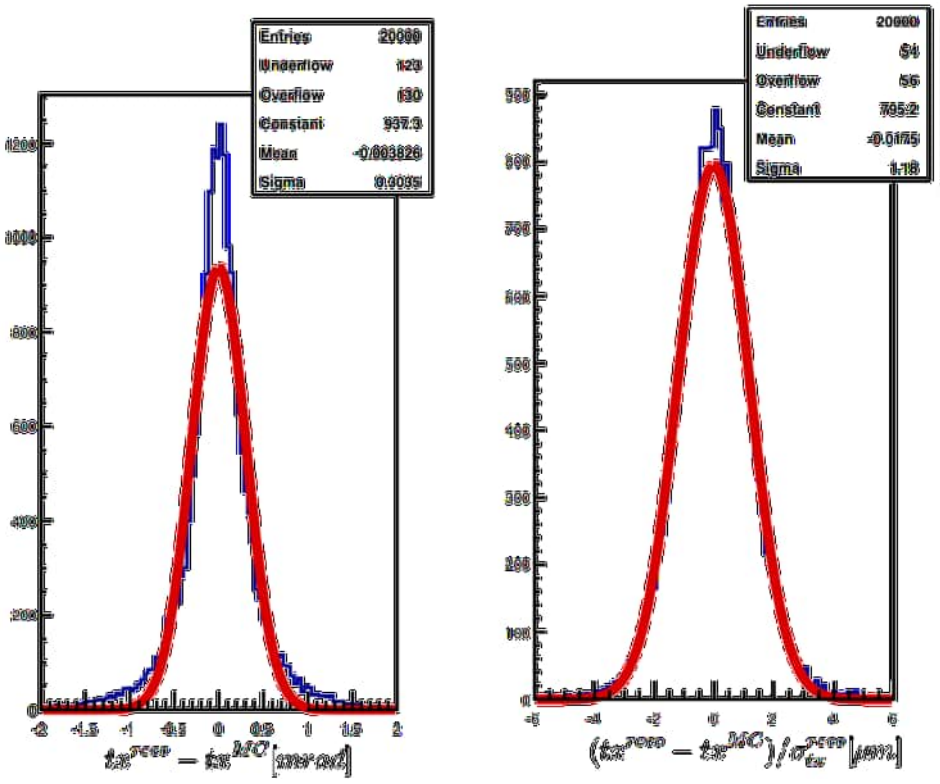

(a) (b)

Figure 3.4: Residual and pull distribution for track components.

A detailed description of the CA tracking in the context of the CBM experiment can be found at [79]. Although the source code of the CBM tracking algorithm is in an advanced stage, it is still undergoing active testing and optimization in CBMROOT [57, 43, 37].

Topology-based track selection criteria notation

In the upcoming chapters, the track selection criteria will be frequently referenced. The selected approach for track selection is based on the track topology. Additional constraints to track characteristics, such as χ^2, will be specified if necessary. A specific notation will be used to simplify referencing different criteria. The label will represent the system track component. Subscript and superscript will represent the lower and upper bounds for the track component size, respectively, while the center script represents a fixed exact value. Global tracks are the concatenation of tracks of individual detector sub-systems. The track topology selection criteria labels contain the specifications for each subsystem. For example, $\mathrm{STS}_1\mathrm{TRD}^2\mathrm{TOF}^3$ represents those global tracks with components such that it has attached at least one `StsHit`, exactly two `TrdHit`, and at most three `TofHit`. The symbol "-" will indicate that no condition is imposed on the given system.

3.7 The Event builder

Due to the novel free-streaming readout concept of CBM, the association of detector signals to a physical event is no longer given a priori by a hardware trigger. This association is, however, a prerequisite of any physics reconstruction algorithms. It must thus be performed in software before the reconstruction chain, or the reconstruction algorithms should process not event-associated data, and the event association should be performed using reconstructed tracks. In principle, there are two limiting cases. Suppose the average time between events is much longer than the period of hits within an event. In that case, event associations can rely solely on hit time, which is typical for moderate interaction rates. In this case, a simple sorting algorithm before reconstruction suffices. However, if the event rate is high, such that the time between events is similar to the time difference of hits, disentangling hits from different events becomes complex. Here, both time and spatial information of the hits are needed, making event reconstruction four-dimensional. Events will be separated after track reconstruction based on the reconstruction of their primary vertex, where many tracks will intersect, again both in coordinate space and in time.

Though the cluster and hit reconstruction, as well as the CA tracking algorithm are designed to work taking into account the fourth dimension (time) [79], and can therefore process free-streamed data, a Digi-based event builder has been implemented [57, 43, 37] and used in the current analysis since the interaction rates were relatively low.

A single time slice typically contains data from several thousand physical events. The strategy of the Digi-based event builder is to group detector signals that potentially belong to the same event from the data stream. Once a trigger signal is detected, the algorithm performs a loop over all trigger times, collecting all Digis from each detector within pre-configured time windows around the trigger time to form event candidates. Candidate events can be filtered by applying a set of predefined cuts. Commonly used selections are based on the minimum and maximum number of Digis registered for each detector. This algorithm supports three operation modes:

- Digis cannot be shared among events. This is suitable for very low event rates, as the time distribution of Digis within an event is significantly smaller than the event separation in time.
- Event can overlap, sharing Digis as long as the trigger time windows do not overlap.
- Triggers whose time windows overlap are merged into the previous event. This is suitable for high event rates. However, it produces events pile-up.

Figure 3.5 represents the event builder for two events. The double-end arrows represent the time windows for the given system. The top panel displays the first operation mode, featuring two well-separated events with no overlapping time windows and no sharing of Digis. The bottom panels illustrate the operation mode that allows sharing Digis, with no overlap in the trigger time windows.

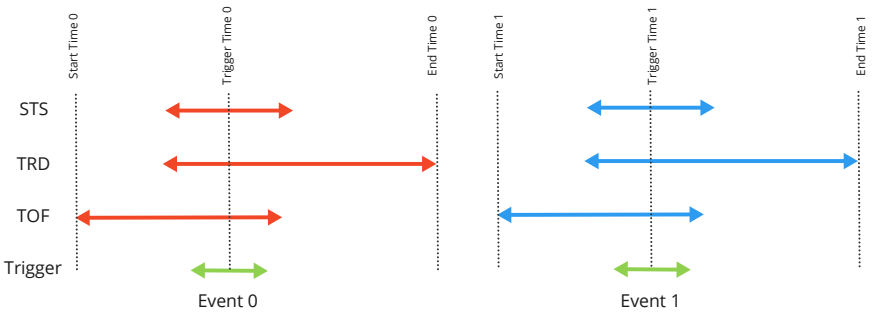

(a) No overlap.

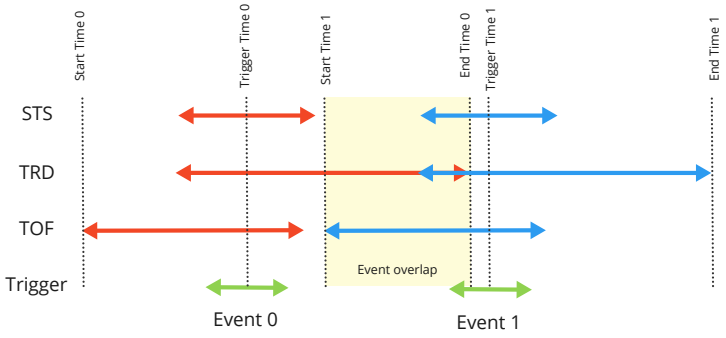

(b) Event overlap.

Figure 3.5: Schematic of event builder for different operation modes.

Generally, any detector in the CBM setup can be used as a trigger detector. However, a good choice requires the detector to provide a narrow distribution of Digi times within an event and a low noise level. As no event selection criteria beyond the data rate are applied, it represents a minimum-bias trigger, roughly equivalent to a level-0 trigger in a conventional experiment with hardware triggers. The trigger algorithm is based on the Digi time distribution. The working principle of the algorithm lies in that, for a given Digi, a time window is expanded until the number of Digis within this trigger window exceeds a predefined threshold or the maximum window size is reached. The trigger time is defined as the mean of the first and the last Digi time. Different trigger configurations have been tested using MC simulation. [43]

Based on the Digi time distribution, the developed minimum-bias trigger algorithm constitutes a simple and computationally inexpensive approach. It requires that the number of Digis in a typical event exceeds the statistical noise fluctuations and that the temporal event shape is narrow compared to the average event separation. Although the Digi times are used for deriving event triggers, the same algorithm can be applied to any time-stamped data series for higher-level objects, such as hits or tracks. [43]

Event builder configuration for data analysis

The event builder offers several configuration flexibilities. A typical configuration specifies the minimum and maximum number of Digis, as well as the corresponding time windows for each detector. Additionally, requirements for the number of layers for a given subsystem are configurable. This flexible configuration enables complex setups to meet specific analysis requirements. For the data analysis presented in the upcoming chapters, the event builder was configured with the parameters detailed in Table 3.1.

Table 3.1: Event builder configuration for detection subsystems. Detector marks with (*) are used as a trigger.

	Bmon*	**STS**	**TRD 1D**	**TRD 2D**	**TOF**
Minimum amount of Digis	1	1	-	-	8
Maximum amount of Digis	-	-	-	-	-
Minimum amount of layers	-	1	-	-	4
Time windows lower bound [ns]	-50	-60	-300	-200	-60
Time windows upper bound [ns]	+50	+60	+300	+200	+60

Chapter 4

Data Analysis

The reconstruction chain is a stream of consecutive tasks. The individual steps produce data that can be analyzed to extract valuable information. This chapter describes the methods and results of the implemented analysis and performance studies for different reconstructed data levels.

As detailed in Chapter 3, the reconstruction chain is a sequence of consecutive tasks that begins from the raw signal from the individual detectors' readout collected in the **F**irst-**l**evel **E**vent **S**elector (FLES) and ends with tracks, i.e., candidate particle trajectories.

The individual steps, i.e., data unpacker, hit reconstruction, tracking, and event builder, produce a data output set that contains increasingly refined data levels. For the STS, this means STS Digis, STS Digis inside Events, STS Clusters, and STS Hits. Each of these datasets is thoroughly analyzed for Quality Assurance of the reconstruction task that generated them, as well as to prepare a good data sample for studying the performance of the STS detector for tracking and vertexing, described in Chapter 3.

This chapter describes the methods and results of the analysis and performance studies implemented for different reconstructed data levels in the STS detector.

4.1 Data set

During my PhD, I analyzed data from all 2021, 2022, and 2024 beamtime campaigns. The analysis methods were improved, optimized, and generalized to account for the different settings of the STS detector and the other detectors in the setup. The results presented here, however, focus on the 2024 data.

For the 2024 data set, the STS configuration was upgraded and consists of three tracking stations, as described in 2.3, resulting in a superior setup compared to the previous beamtime campaign for studying tracking, vertexing, and efficiency. In contrast to the modules previously installed in the two downstream stations, the new upgrade has all the final components and was built in 2023. Moreover, thanks to a mechanical rearrangement of the cooling pump of the chillers, the entire STS box is less exposed to pick-up noise from the surrounding environment.

The data presented here have been collected in May 2024 in Ni+Ni collisions with a beam kinetic energy of 1.93 AGeV/u. As measured by the BMon detector, the beam profile has a σ of 1.5 mm. The beam intensity was about 4×10^7 ions per spill, and a spill length of 10 s, resulting in a collision rate of about 400 kHz. The Ni-target employed in the experiment measures 15 mm × 35 mm, with a thickness of 0.4 mm, corresponding to 10% interaction probability, and is mounted in a thin Al cutout of 31 mm diameter.

The analyzed statistics are 250 time-slices per run, corresponding to more than 1 TB of data in total. For Monte Carlo, we have analyzed 1 M events generated with UrQMD. After the event is generated, the propagation of the primary particles through the mCBM detector is done using a transport code based on GEANT4. Considering the detector response, the energy deposited by the passage of charged particles is converted into Digis and then stored in raw data format. This step was performed for different detector readout configurations to study the effect of broken channels. From this point, the reconstruction of the event starts with the cluster finder, the hit finder, and tracking. The full-time structure of the free streaming readout of CBM has not been simulated, so no event builder is applied in Monte Carlo.

4.2 STS Digis

The quality assurance control on the STS Digis starts with a detailed analysis of the signal of individual channels, which is mandatory to avoid compromising the detector's performance. Two pertinent aspects characterize the performance of channels. These are *broken* and *noisy*. Both classifications demand a precise definition, though they are related.

Broken channels must be classified to accurately mask them in Monte Carlo simulations that aim to replicate the actual detector conditions. Noisy channels may need to be masked in the analysis of real data, and then, consequently, in Monte Carlo, to avoid a large number of fake combinations with strips that are always fired.

4.2.1 Broken channel identification

A *broken* channel refers to a specific channel that is non-functional or unresponsive. A channel failing to produce a signal may occur for various reasons, such as production defects, damage during operation, or radiation exposure, which can degrade the module's performance. Broken channels directly impact the overall efficiency and spatial resolution, affecting the reliability of the experimental results.

Within STS modules, not all broken channels always manifest as unresponsive. **E**quivalent **N**oise **C**harge (ENC) measurements, typically performed in the final module characterization but also repeatable on the fully installed module during a calibration run prior to data taking, have proven to be a reliable tool for identifying broken channels. Moreover, from the ENC parametrization as a function of the strip capacitance [58], it is possible to identify on which level the channel is broken. Figure 4.1 (top panel) (adapted from [58]) shows ENC histogram for one of the mSTS modules. Broken channels have been categorized by [58] as follow:

- No analog response (NAR): ENC = 0. The channel is permanently damaged; no charge collection and amplification is done.
- Broken TAB bond at the ASIC (ASIC): faulty connection between ASIC and micro-cable.
- Broken TAB bond at the sensor (SENS): faulty connection between the micro-cable and the sensor or across the signal line in the micro-cable. This is a dynamic limit that depends on the average noise of the module and also takes into account possible fluctuations between ASICs.

Figure 4.1 (bottom panel) shows the charge (in ADC units) vs. channel distribution for U1 L1 M0 . Unresponsive channels appear as empty vertical lines, indicating that there are no entries for the channels. Only when the channel has no analog response is it safe to assume that no Digi will be created. Electromagnetic pickup can still induce signals, resulting in a Digi creation. Those cases will have a distinct signature. The charge distribution for broken channels, although still exhibiting some analog responses, will differ significantly from that of the functional neighboring channels. These channels often present an interrupted pattern

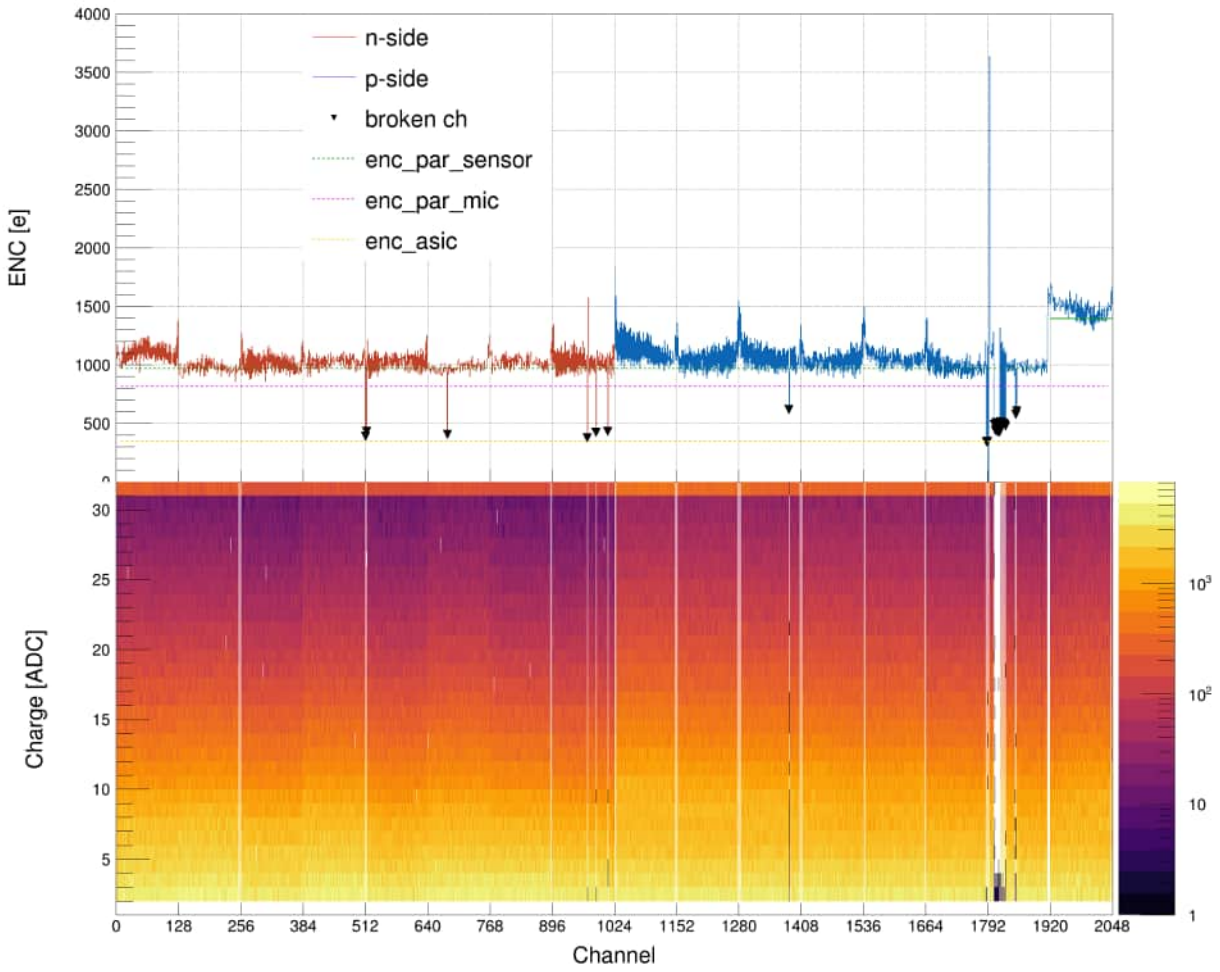

Figure 4.1: Module U1 L1 M0 : ENC laboratory module test measurement (Top panel); charge (in arbitrary unit ADC) vs. channel distribution (Bottom panel)

on the charge distribution 4.1 (top panel). Moreover, a distinctive ENC level is appreciable, i.e, for the last group of broken channels for the p-side. This pattern can be confused with uncalibrated channels, resulting in a distorted charge distribution. However, the amount of Digis produced is usually quite inferior. Suspect broken channels are cross-checked with the ENC measurement to avoid ambiguities. These channels are especially harmful during the time calibration procedure 4.3. Additionally, broken channels can be found after the module testing procedure due to the fragile nature of STS modules.

The finding of the broken channel provides no solution to the problem itself, but a clear description of the experimental condition is crucial for MC comparison analysis. Non-functional ASICs will appear as 128 consecutively inactive channels. For one particular module, a non-functional FEB accounts for a significant portion of the broken channels found, reducing the module's ability to reconstruct hits. The entire setup's broken channel analysis throws 789

broken channels out of 22528 (11 modules $\times$ 2048 channels/module), representing $\sim 3.5\%$, excluding non-functional ASICs, which account for 9% of the total inactive channels.

4.2.2 Noisy channel identification

A *noisy channel* is defined by the presence of undesirable or extraneous signals, frequently manifesting as electronic noise. The emergence of noisy channels can be attributed to various factors, including electronic crosstalk, electromagnetic interference, and assembly imperfections in the module, among others [84]. These unwanted signals can potentially distort the signal amplitude or timing and/or saturate the DAQ, diminishing the sensor's precision in capturing and deciphering signals deriving from particle interactions [85]. Additionally, a high noise level translates to high ghost rates, which can harm the overall detector's performance.

To identify noisy channels, a common baseline for all channels is necessary as a reference. Such a common baseline is easily extracted by the integrated occupancy for a module when the beam is off, corresponding to a background measurement. This channel distribution can then be compared to on-spill measurements after normalization. Figure 4.2b shows the normalized channel distributions corresponding to on(red)/off(black)-spill measurements. The number of time slices on/off-spill does the normalization. The TSA files contain time-sorted but not necessarily consecutive time slices. Therefore, to determine if the time slices correspond to on/off-spill, the T0 detector rate is used. The criteria used to decide where the corresponding time slice is on/off spill are:

- On-spill: Number of Bmon Digis ≥ 0.6 Max(Bmon)
- Off-spill: Number Bmon Digis ≤ 30

The upper bound for the off-spill accounts for noise in the BMon setup, while the lower bound for the on-spill helps to exclude spill ramp-up/down.

Noisy channels arise as channels for which the normalized distribution amplitudes of the on-spill and off-spill are comparable. Therefore, the measured distribution is dominated by the background. The signal-to-background (S/B) ratio was used to characterize a noisy channel. The intention is to set a threshold for those channels that should be removed from the analysis cause the noise is considerably more significant than the signal. The chosen threshold was $S/B < 0.5$. The total number of noisy channels found for the mSTS setup is 344, representing $\sim 1.7\%$ of the total active channels.

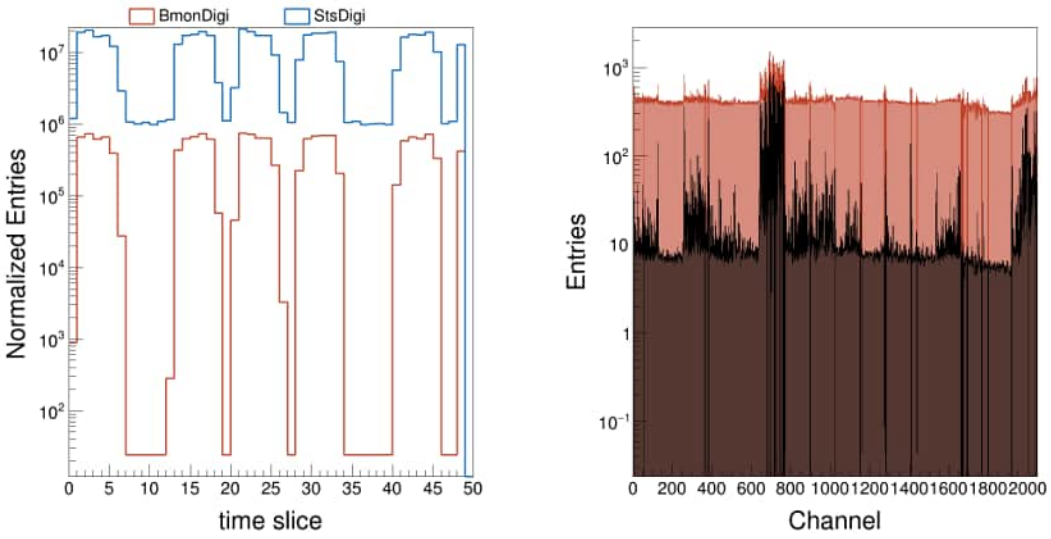

(a) (b)

Figure 4.2: Digi rate distributions. (a) Normalized Digis per time slice for T0 and STS. (b) Normalized On/Off-spill channel distribution.

There are many ways to proceed with a noisy channel, excluding letting the reconstruction algorithm deal with it. The most straightforward approach is to disable the channel directly in the hardware configuration. This is typically done by the operator when a specific channel causes the readout to become saturated. Those channels will appear as inactive after the data is collected.

Similarly, channels can be disabled at the unpacking step by ignoring any output from those. This last is known as *channel masking*. Channel masking can have dire consequences, as an artificial creation of inactive areas can lead to cluster splitting. Odd-even channel differences in terms of occupancy have been observed [77]. In some cases, the differences are enough to classify an odd group or even group of channels as noisy. If masked, this results in a detector response consisting of multiple single-strip clusters, rather than the expected few larger clusters.

A straightforward approach to avoid such inconvenience is to explore the charge distribution of the pre-classified noisy channels. The typically observed noise channel differentiates from a non-noisy channel by a significant number of low-charge region entries. Therefore, imposing an ADC cut enhances the channel's performance by discarding noisy signals in the low-charge region. This is not entirely risk-free, as information from real particle interactions is also discarded. However, the fact that no inactive region is created is strong enough to implement such a practice, especially for many consecutive channels classified as noisy. Figure 4.3 shows both the on/off spill comparison and the charge vs channel distribution. It

can be seen that after implementing an ADC>1 for ASICs 6th and 16th, the On/Off spill ratio is improved.

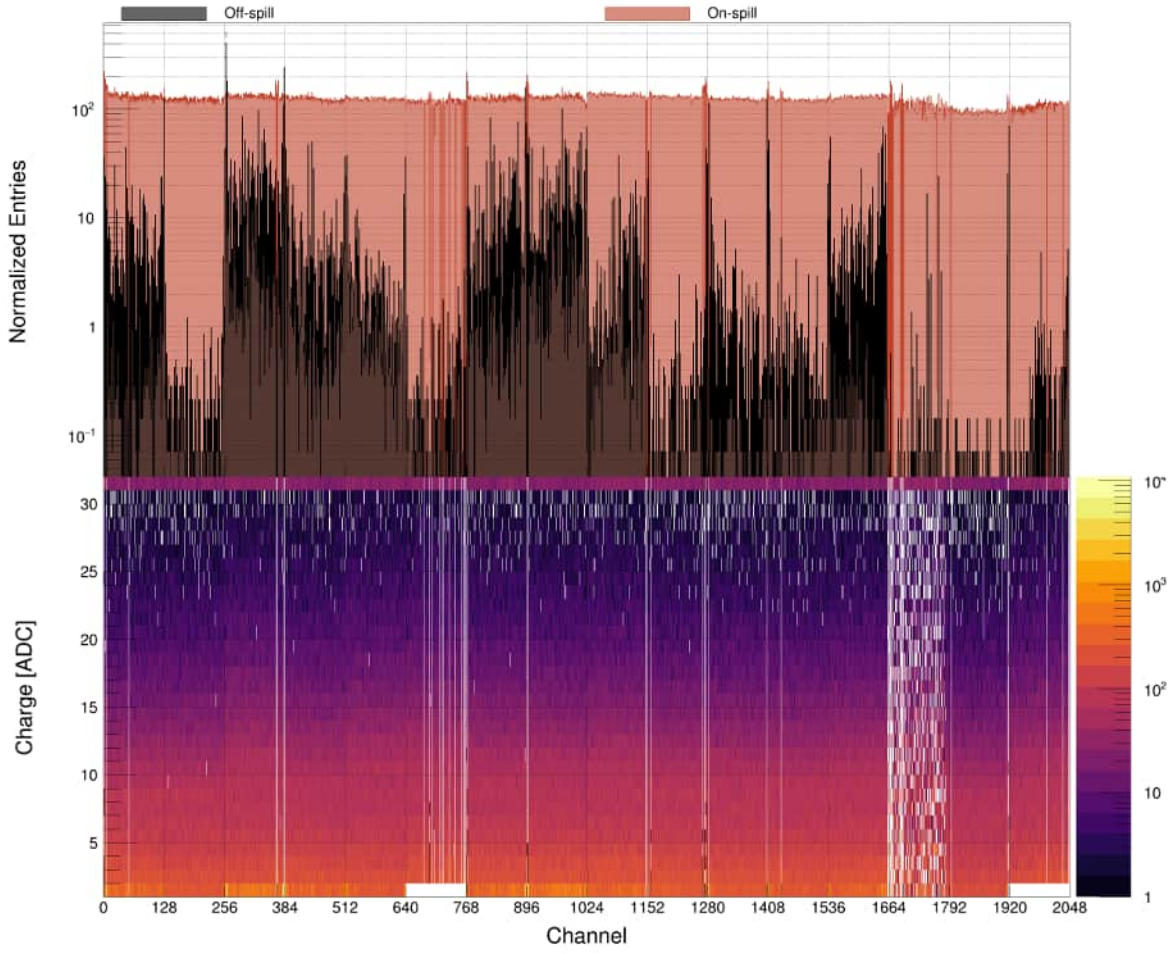

Figure 4.3: Normalized On/Off-spill channel distribution after arbitrary ADC cut is applied.

For a trigger-less free-streaming experiment, it is crucial to recognize noisy channels, mask them, or impose a more stringent ADC cut. It should be possible to do so on an operational online detector by adjusting the detector readout settings or the online reconstruction chain parameters. For this purpose, methods for channel manipulation have been implemented in the online analysis.

4.3 Time calibration

For a triggerless free-streaming experiment, achieving optimal time resolution is crucial, as it influences the precision and reliability of experimental outcomes. Time resolution determines the detector's ability to separate and timestamp two-particle interactions that

occur close in space and time. The detection system must be time-calibrated appropriately to enable the extraction of conclusions in terms of time resolution and overall synchronization. A reference system capable of measuring precise time is needed to extract such magnitude. The T0 diamond counter placed upstream of the target enables time resolution studies of STS, as it provides precision on the order of picoseconds (see Section 6.1.1) [86]. It is also the most robust signal in the entire setup, as it is essentially free of noise. This is shown by the off-spill rate shown in 4.2a. Moreover, being placed before the target, the multiplicity of T0 signals per event is significantly smaller than that of any other detector. In the optimal case of low pile-up, it should have just one hit per event, thereby minimizing the combinatorial background from incorrect combinations.

The analysis involves retrieving the time difference between `StsDigi` and `BmonDigi` (Digis for the diamond counter) within a time window large enough to account for non-synchronized detector signals (typically hundreds of ns). The `StsDigi` time measurements mark the **T**ime **o**f **a**rrival (TOA) of the reaction product, while `BmonDigi` time sets the reaction time. In general, the TOA depends on the reaction product velocity and the position of the **D**etector **u**nder **t**est (DUT). Consequently, building this time difference distribution should result in the inverse velocity distribution, scaled depending on the DUT position. The time calibration procedure involves adjusting the time difference to zero. This is done at the Digi level, allowing the event builder (see Section 3.7) to process the raw Digi signals. At this point, one is ignorant of the particle velocity; therefore, the distribution spread due to the velocity collapses. However, the resulting spread is given by the precision with which T0 and STS can timestamp the interaction. Moreover, correlating the slowest (fastest) reaction product with the next (previous) reaction timestamp might occur. It is a random effect that adds to the combinatorial background. The time-of-flight of beam particles toward the target plane introduces an additional time offset. However, this value Δt_{T0-trg} can be extracted from the known beam properties, and it is a common parameter for all mCBM@SIS18 subsystems.

The time difference distribution between `StsDigi` and `BmonDigi` is built for all STS sensors in the setup (see Figure 4.5). As mentioned above, each entry in the distribution has an uncertainty related to it and can be propagated from the STS detector time resolution σ_{STS} and the Bmon detector resolution σ_{T0}. Given that the T0 detector resolution is much smaller than the STS clock, the STS time resolution can be estimated as the width of the time difference distribution. Such distributions mean values, used for time calibration, and widths are extracted by fitting with a Gaussian on top of a $P_2(\Delta t)$ to account for the combinatorial background.

Time Walk correction

A critical effect to consider for time calibration when using a fixed threshold discriminator is the signal timing dependence on signal amplitude. This phenomenon is known as the *time walk* and comes from the dependence of the signal's rising time on its amplitude. Therefore, for two signals, A and B, generated at the same point in time but with different amplitudes, the moment when the signal crosses the threshold will be different: t_A, t_B. This is illustrated in the diagram shown in Figure 4.4. The picture illustrates that the time difference between the registered signals depends on the chosen threshold and the amplitude difference. Since this effect may lead to delays around $20 - 25\,\text{ns}$ [87], it can impair the cluster and hit reconstruction, as well as the event builder.

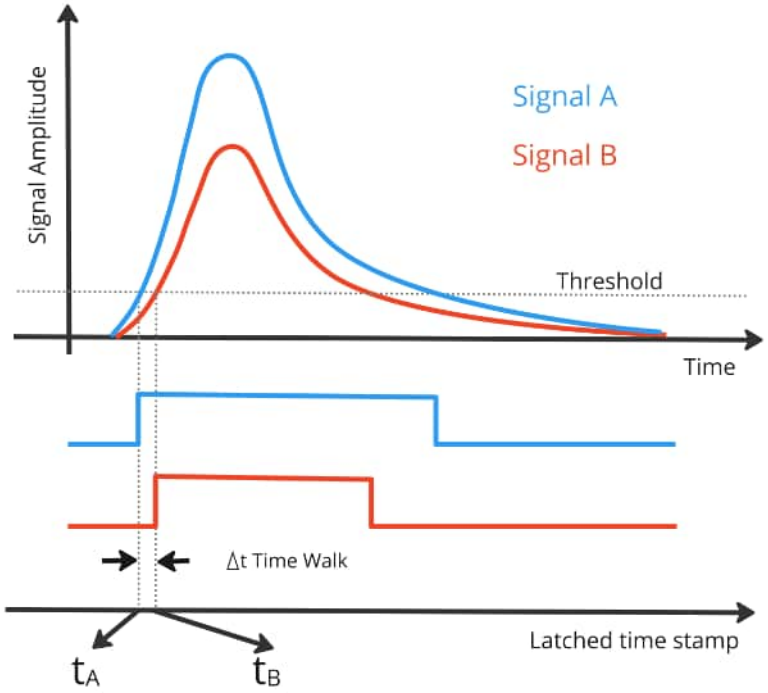

Figure 4.4: Timing for two simultaneous signals of different amplitudes.

Within the STS module, each channel is equipped with 32 discriminators; one of them, the *fast discriminator*, is in charge of the timing of the registered signal. The threshold of the fast discriminator sets the threshold for time-stamping the signals [87]. As a unique set of calibration parameters exists for each ASIC, a unique set of time calibration parameters should exist for each.

An alternative solution to avoid searching for many calibration parameters implies finding a universal parameter set. The parameters set could then be expressed as a function of the signal amplitude in electrons. Technically, employing such a universal set of parameters

implies recalculating individual values for each ASIC, as fluctuations in the transfer function should not be neglected [58]. Therefore, extracting the time calibration for each chip is more straightforward and effective. Additionally, time calibration is performed at the Digi level when no charge calibrations are applied due to the optimizations to the `StsDigi` object[1].

Figure 4.5 shows the two-dimensional distribution of the time difference of STS signals with respect to T0 signals as a function of the STS signal amplitude (in ADC units). This figure contains data for a single ASIC of the module U1 L1 M0 . As mentioned, the charge calibration might differ, and data from different ASICs should not be mixed at this level.

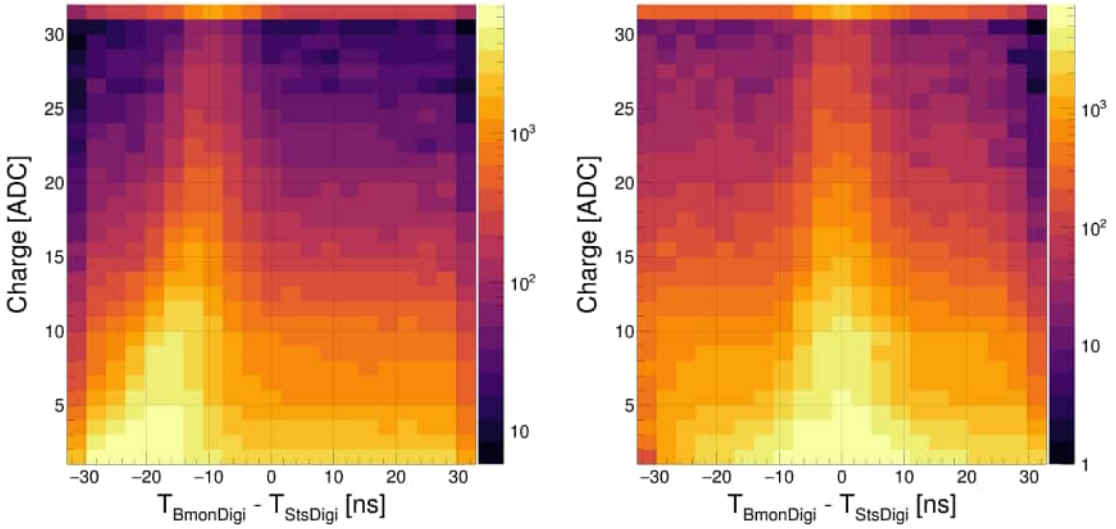

(a) (b)

Figure 4.5: STS signal amplitude vs. time difference with respect to T0 detector Digis. Before (a) and after (b) time walk correction.

For each amplitude bin corresponding to the 31 discriminators of the slow path for signal shaping, the offset is extracted by fitting the projected distribution. A dataset comprising 31 pairs of (charge, Δt) can be fitted by a polynomial, effectively decreasing the time calibration parameters. However, this approach is not robust against bad-quality data. For example, the obtained data set may encounter fitting problems when a few ill-configured or non-functional discriminators are present. Additionally, it has a technical disadvantage, as the polynomial would need to be mapped for each ADC value at initialization time to avoid repetitive evaluation at runtime. Finally, the most effective and robust method has been proven to extract the offset values for each of the 31 discriminators for each ASIC. Using an offset for each discriminator provides a straightforward approach to correct for the time

[1] such optimization refers to programming optimizations

walk effect and simultaneously account for synchronization of the entire setup. The result is shown in Figure 4.5b for the same selected chip.

Figure 4.6a shows the time offset extracted from the fitted projection for each ADC value, where the bar represents the standard deviation of the distribution. The signal amplitude dependency of the time offset can be appreciated before calibration is applied (blue data set), consistent with the laboratory measurement [58]. Once the time correction is found, the time walk effect is removed, represented by a near-zero offset distribution (red data set in Figure 4.6a).

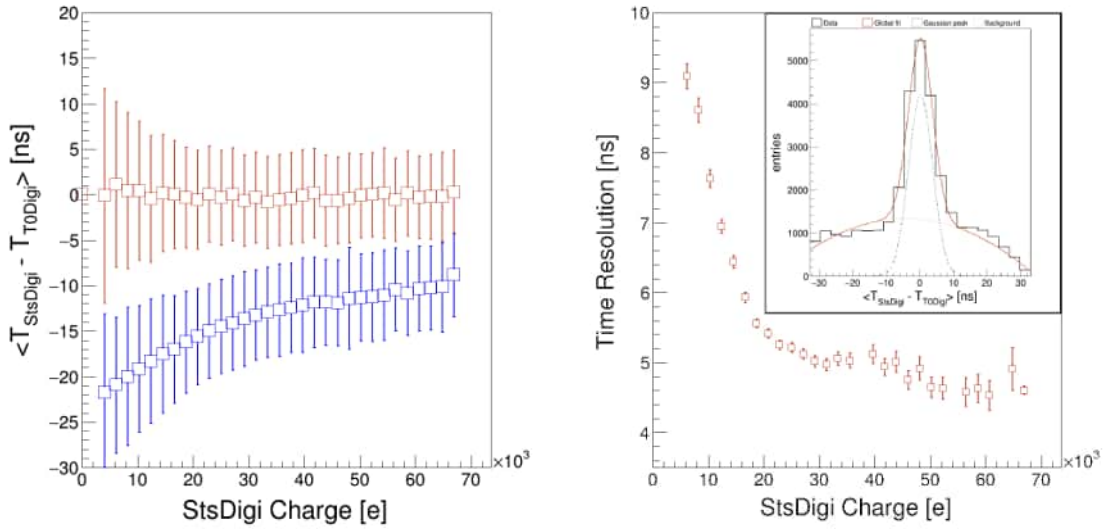

(a) (b)

Figure 4.6: a) Time offset as a function of the STS signal amplitude in ADC units before (blue) and after (red) time calibration is applied; b) Estimated STS time resolution as a function of the STS signal amplitude given in elementary charge units. The inlet plot shows the fit for high ADC values from which the estimated values come.

4.3.1 Time resolution

The correlated time signals between the STS and T0 detectors contain the uncertainty of both time measurements. Additionally, the differences in the TOA due to different reaction product velocities produce fluctuations in the measured value of the $t_{\texttt{BmonDigi}} - t_{\texttt{StsDigi}}$.

The fluctuation due to particle velocity will depend on the distance between the target and the detector. This distance varies from sensor to sensor, but only differences in distance among tracking layers ($\sim$ 12 cm) are significant due to the large values of velocities in question. MC simulation enables the study of the time-of-flight of particles and their impact

on the TOA measured by the mSTS setup. The time-of-flight of interest in this quest is from the primary vertex within the target to the sensors.

TOA distributions are shown in Figure 4.7 for the most abundant reaction products: protons (Figure 4.7b) and pions (Figure 4.7a). The distributions are built for each tracking station by dividing the average distance along the z-axis from sensors to the target plane by the longitudinal component of the particle velocity. Due to the small acceptance of the mSTS setup, the variation of the true time-of-flight when considering the full distance is negligible. Such a scenario would differ for the full STS, where the track length can vary around $\sim 10\,\%$ for particles with straight tracks.

Protons and pions TOA distributions have a skew shape, influencing a non-symmetric effect on the measured magnitude $t_{\texttt{BmonDigi}} - t_{\texttt{StsDigi}}$. The most probable value in all cases is below 2 ns. It is smaller than the STS time-stamping clock 3.125 ns that sets the lower limit to resolve two close signals in time. Hence, those signals are not expected to modify the shape of the time correlation, but rather provide a quantifiable amount that must be considered for proper synchronization.

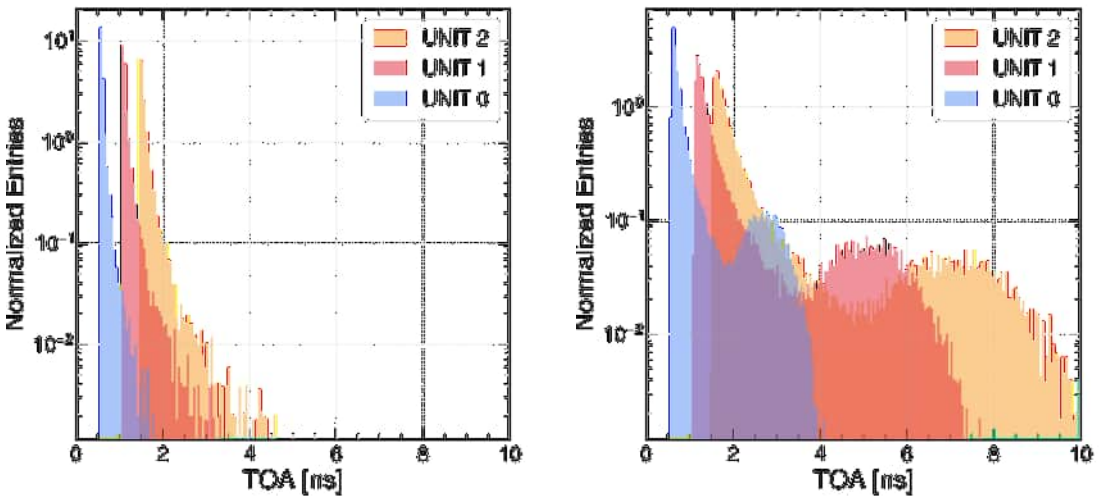

(a) (b)

Figure 4.7: Time of arrival distributions for pions (a) and protons (b) at each tracking station.

The pion distribution does not exhibit a large spread. Hence, the time difference between the fastest and the slowest signals produced by pions, in the worst case spanning ~ 4 ns, contributes in two orders of magnitude smaller than the main TOA structure. On the other hand, the proton TOA distributions feature a second structure, also two orders of magnitude

smaller. However, this produces a larger spread around $\sim 8\,\text{ns}$ for the last tracking station.

The T0 detector time resolution is three orders of magnitude smaller than the time effect produced by the time-of-flight of particles and STS time stamp uncertainty, both in the order of nanoseconds [86]. Therefore, it is expected that the uncertainties in T0 are negligible when estimating the STS time resolution. The expression 4.1 incorporates uncertainty propagation, considering the systematic effects of both detectors. However, this expression does not contain the non-symmetric spread produced by the TOA distribution. Hence, σ_{STS} values extracted by using this expression are larger than the true STS detector time resolution. Such deviations are in the order of $\sim 2\,\text{ns}$ from the TOA most probable value, and around $\sim 8\,\text{ns}$ with a much smaller impact.

$$\sigma = \sqrt{\sigma_{STS}^2 + \sigma_{T0}^2} \tag{4.1}$$

$$\sigma = \sigma_{STS}\sqrt{1 + \frac{\sigma_{T0}^2}{\sigma_{STS}^2}} \tag{4.2}$$

$$\sigma \approx \sigma_{STS} \tag{4.3}$$

In general, time-of-flight is not measured during the time calibration procedure. Hence, the TOA distribution is collapsed, introducing an additional spread that the RMS of such a distribution can estimate. In the case of protons, where this spread is more significant, the RMS for TOA distribution is approximately 0.7 ns, 1.3 ns, and 1.8 ns for stations 0, 1, and 2, respectively. These values represent an STS time resolution estimation correction from the time correlation signal fit.

Figure 4.6b shows an uncorrected estimation of time resolution as a function of the signal amplitude, which is now given in electrons using the charge calibration employed for the sampled ASIC (see Section 2.3.2). The values ranges from $4.8 - 9.2\,\text{ns}$ for the given charge range $\sim 8 - 68\,\text{ke}$.

The distribution shown is for an arbitrarily selected subset of measurements corresponding to a single ASIC of module U1 L1 M0 . Taking into account the correction due to particle time-of-flight, the resulting time resolution would range $3.5 - 7.9\,\text{ns}$, where the lower bound is close to the maximal STS timing capabilities.

4.4 STS clusters

As explained in Section 3.5, the proper performance of the cluster finding algorithm is crucial to the hit reconstruction. Two STS clusters' primary characteristics are their size (number of Digis) and charge. Figure 4.8 shows the 2-dimensional distribution of cluster size vs. cluster charge for recorded data of Ni+Ni at 1.93 AGeV at mCBM@SIS18. Four panels are displayed and arranged in two rows and two columns: top panels for **all found clusters**, bottom panels for **hit clusters** (only clusters later correlated and used during hit reconstruction), left panels for n-side, and right panels for p-side.

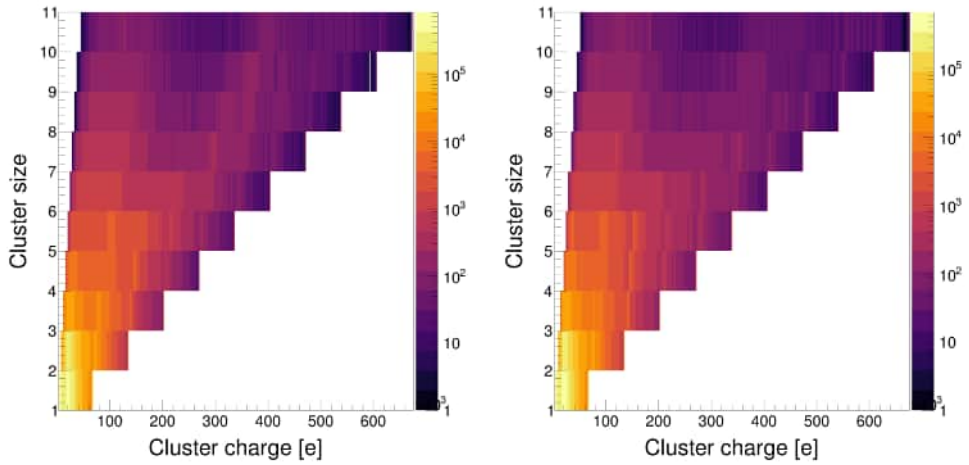

(a) all clusters n-side

(b) all clusters p-side

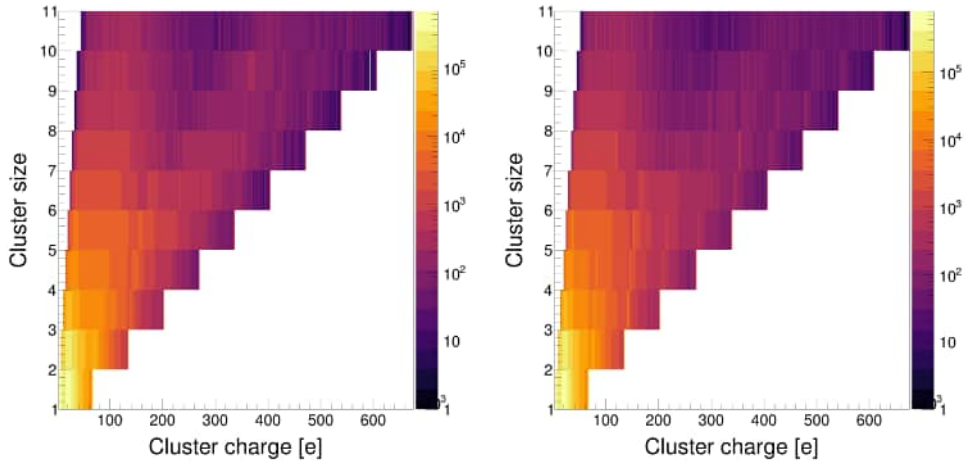

(c) hit clusters n-side

(d) hit clusters p-side

Figure 4.8: Cluster size vs. cluster charge distribution for different found clusters.

All distributions are alike. Individual components (size and charge) can be compared in the corresponding projections: cluster size in Figure 4.9a, cluster charge in Figure 4.9b for the 1-strip cluster. The cluster size distributions **M**ost **p**robable **v**alue (MPV) in the

mSTS setup is a 1-strip cluster with a mean value of 1.2. This is expected as most tracks traverse the silicon sensor with an almost perpendicular trajectory [75]. The overall usage of found clusters per event for the given sensor sample data is $\sim 53\,\%$. As clusters that belong to no hits are discarded, this partially accounts for data reduction. Figure 4.9b shows the

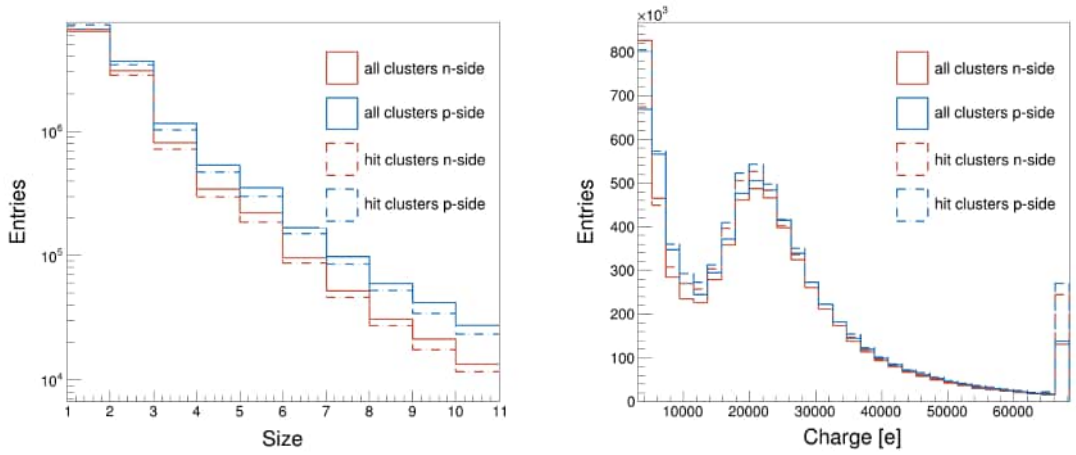

(a) (b)

Figure 4.9: Comparison of cluster size and charge distribution between all found clusters and clusters that belong to hits.

charge distribution for 1-strip clusters. Distributions for **all clusters** and **hit clusters** are overlaid. This comparison reveals no significant difference in the cluster charge between the groups in question. The signal generated in a silicon detector depends on the thickness of the depletion zone and the dE/dx of the particle following a Landau distribution.

The most probable value of dE/dx of a MIP for $300\,\mu$m silicon is about 24000 electron/hole pairs, which is indeed where the main peak is observed. However, some minor discrepancies between the peak MPV and the expectations can be observed, which can serve as a baseline for charge calibration correction, although this has not yet been implemented. At the upper end of the charge digitization range, the overflow bin is filled.

The time difference between neighboring fired strips plays the leading role during cluster finding, as explained in the previous chapter (see Section 3.5). The cluster finder algorithm was run using a very large window to investigate the typical spread of the time difference between neighboring digis. Figure 4.10 shows such distributions and their correlation to cluster size and charge. There are four panels arranged in two rows and two columns: top(bottom) panels show cluster size(charge) vs. neighboring Digis time difference; left(right) panels for n-side(p-side) clusters.

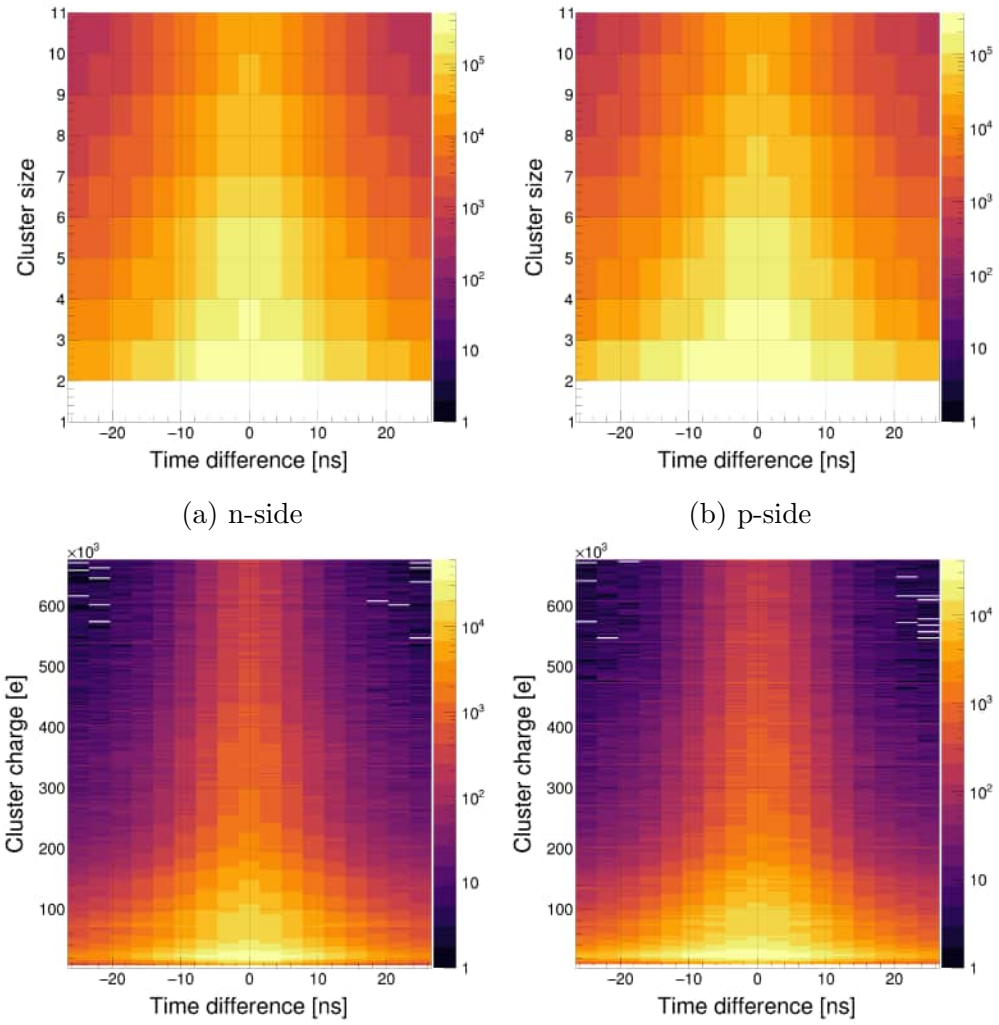

(a) n-side (b) p-side

(c) n-side (d) p-side

Figure 4.10: 2D distribution of cluster size (top panels) and charge (bottom panels) vs. time difference between neighboring *Digis*.

The distribution of time differences narrows as the cluster size and charge increase. The higher the charge and size, the less likely the cluster will be impacted by noise, and the less the influence of the uncorrected time walk effects will be. The spread behavior is coherent with the time resolution as a function of the signal amplitude at the Digi level. Hence, a neighboring Digis time difference cut is set using an absolute value of 20 ns. The result obtained from the upcoming steps in the reconstruction chain will be derived from the new cluster finder algorithm configuration.

4.5 STS hits

Data analysis of reconstructed hits provides insight into features such as position and internal cluster structure. This section examines some cluster characteristics that correlate with the formation of a hit. Moreover, n- and p-side correlations for cluster charge and size shall be inspected. The distributions for all reconstructed hits and hits attached to the track found will be compared under the flags: **all hits** and **track hits**. For such purpose, a track selection criterion has been applied: the track must contain at least two `StsHit` attached -STS_2TRD-TOF-.

Figure 4.11 shows cluster size and cluster charge correlations between the p-side and the n-side. Four panels are arranged as follows: all hits (left), track hits (right), size correlation (top), and charge correlation (bottom). In all panels, a dashed green symmetry line has been drawn.

In both cases, a clear correlation between the size and the charge on the p-side and the n-side can be observed, as expected. However, inactive areas and inhomogeneous threshold configurations can produce asymmetry in the correlation between the two sides. Moreover, the cluster correlation algorithm analyzes only cluster position and time to create hits, regardless of the cluster size, from which ghosts (wrong combinations) can play a role. Similarly, this might affect charge correlation.

Regarding the charge distribution, the significant suppression of low charge clusters is more pronounced when comparing the correlation for **all hits** versus **track hits**. Bins 31 and 62's vertical and horizontal structures correspond to the overflow bin of the clusters. Additional structures at $Qp(n) > 120\,\text{ke}$ are related to binning artifacts produced by sampling the discrete distribution of n-strip clusters charge using the partition of 1-strip clusters.

Hit charge

A strong charge correlation is appreciable, and the charge distribution of **all hits** and **track hits** can be compared for the two sensor sides shown in Figure 4.12b. A suitable way to quantify charge symmetry is by the distribution of Q_{sym} given by equation 4.4:

$$Q_{sym} = \frac{Q_n - Q_p}{Q_n + Q_p} \tag{4.4}$$

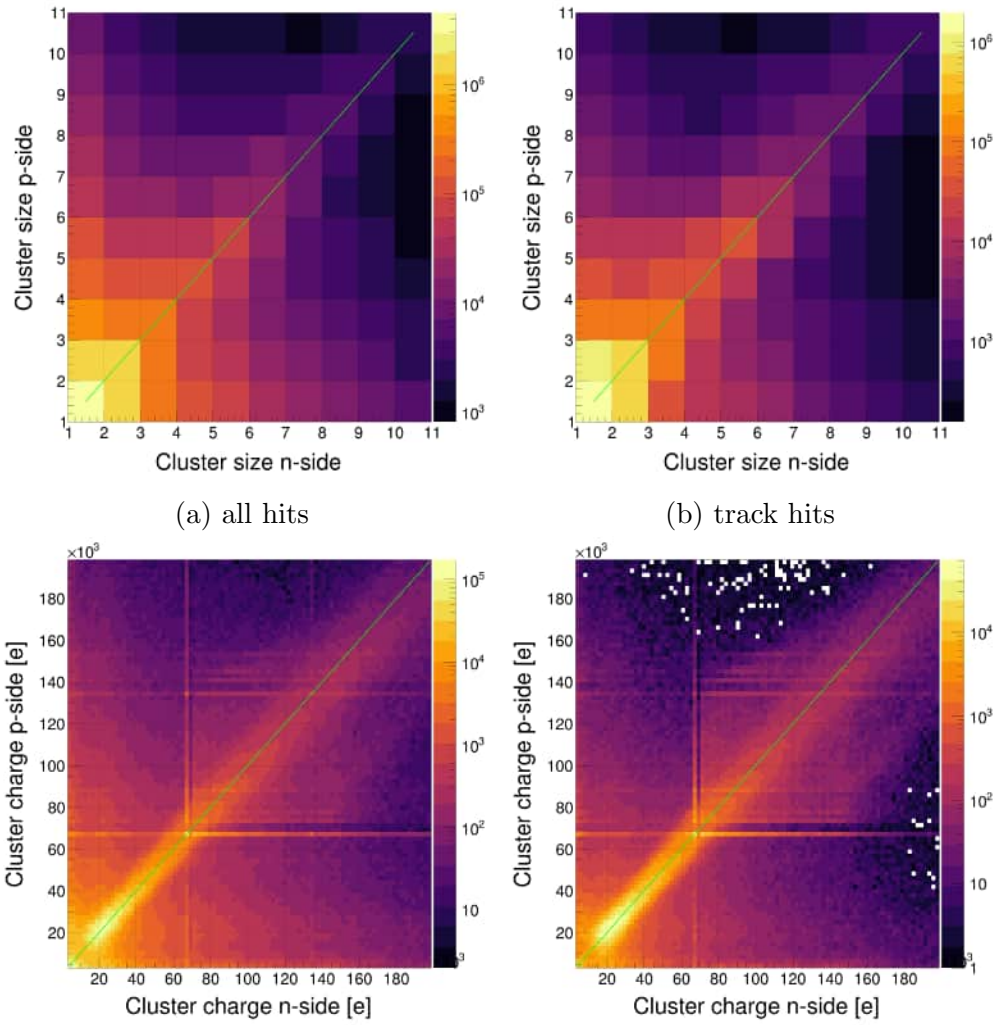

(a) all hits

(b) track hits

(c) all hits

(d) track hits

Figure 4.11: Correlation distribution of hit cluster size (top panels) and charge (bottom panels) between different sensor sides.

The Q_p and Q_n represent the cluster charge for the p- and n-side hit cluster, respectively. Such distribution is shown in Figure 4.12a. Multiple factors influence the symmetry of the signal amplitude between p-side and n-side [44]. Trying to factorize it is beyond the scope of this work. Nevertheless, a slight narrowing of the Q_{sym} for **track hits** with respect to **all hits** can be seen.

For the **all hits** subset, the charge distribution resembles the one obtained from all clusters; however, a strong suppression at low charge values is observed when requiring the hits to belong to a track. The low region charge is contaminated by noise and potentially low-energy particles whose trajectories are not long enough to be fully registered in the mCBM@SIS18 setup (e.g., by TRD and TOF).

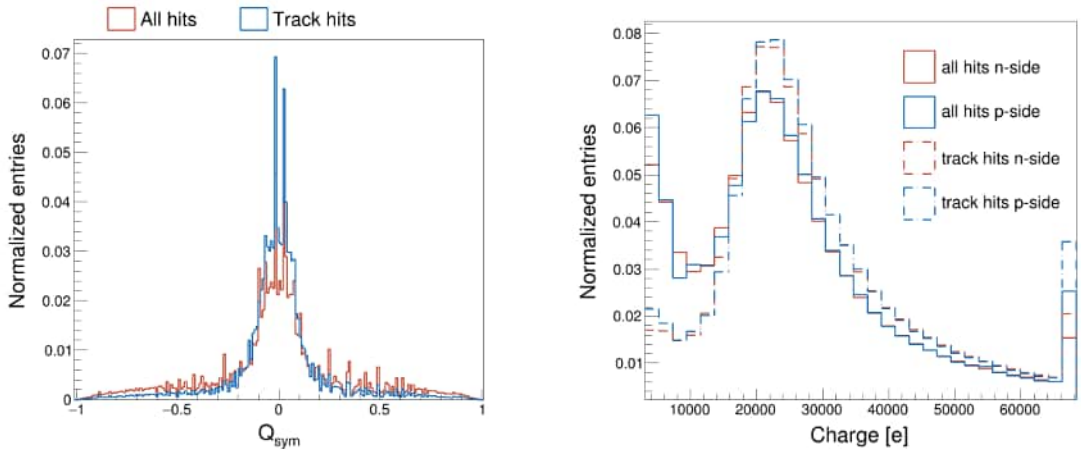

(a) (b)

Figure 4.12: Charge features for `StsHit` (Module U1 L1 M0): a) charge symmetry between n-side and p-side; b) Charge distribution 1-strip hit cluster for all reconstructed hits and track hits.

Hit map

Figure 4.13 shows the XY projection of the reconstructed hit for the mSTS stations. The setup presents inactive regions within the nominal acceptance (see Section 2.2). The impact of broken channels is evident as vertical empty lines for the n-side, which are directly correlated with the X geometrical coordinate, and tilted empty lines matching the strip stereo angle for the p-side. Larger inactive areas are produced by inactive ASIC. The empty area in the middle of the right column at the last station is caused by the p-side non-functioning FEB of the corresponding module, making the hit reconstruction unfeasible (see Section 3.5). Fluctuations in the homogeneity of the hit distribution occur at a specific detector portion where operational thresholds were significantly lower (see Section 2.3), thereby increasing the presence of noise. However, there is a slight trend towards lower entries for negative x-coordinates. Positive x sits closer to the beam pipe in the direction of the beam axis (see Figure 2.1); hence, it can measure higher particle flux.

The observed occupancy can be understood from MC simulations. Figure 4.14 shows kinematics (p_T vs. y and θ vs ϕ) distributions. Two subsets of the primary track are distinguished: all tracks (left panels) and inside mSts acceptance (right panels). The setup acceptance is highlighted, and the (pT,y) curve for the maximum mSTS acceptance along θ has been drawn for protons and pions. The trend discussed in the above paragraph is obvious from the θ distribution.

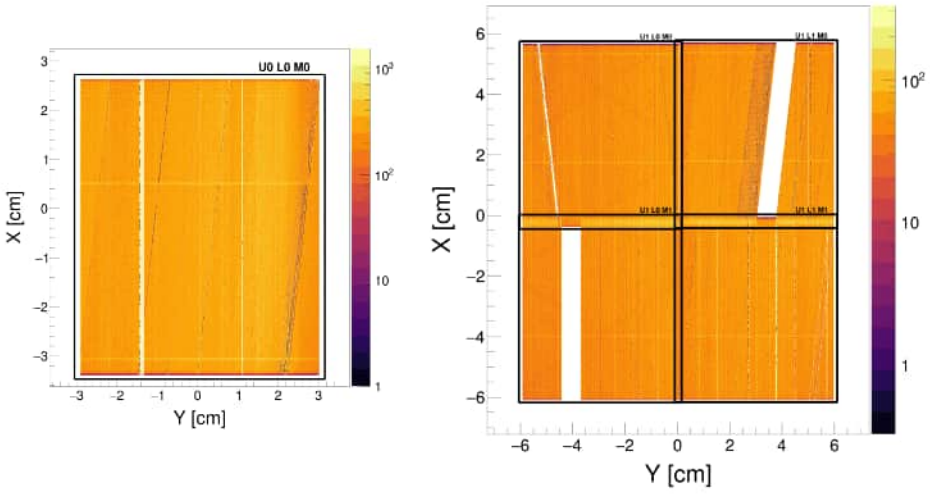

(a) mSTS station 0

(b) mSTS station 1

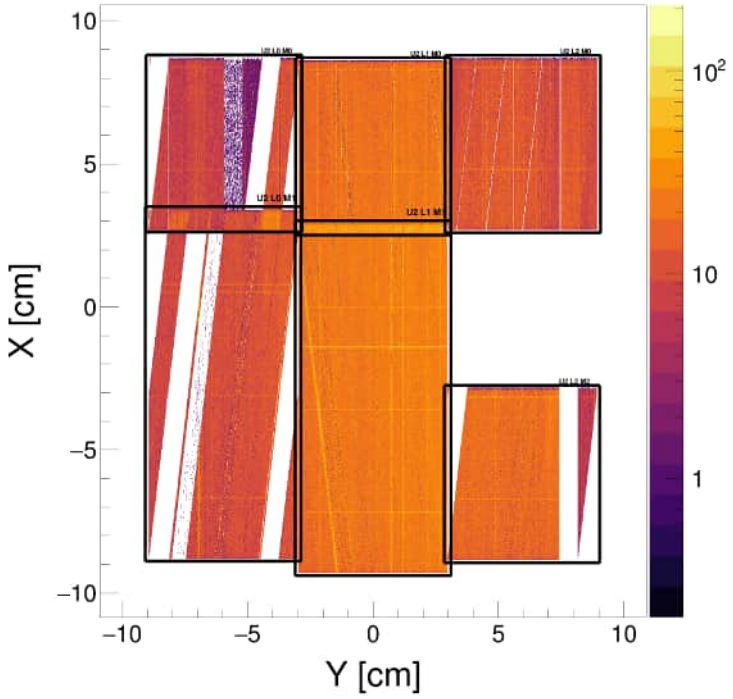

(c) mSTS station 2

Figure 4.13: Reconstructed hit position projection XY plane.

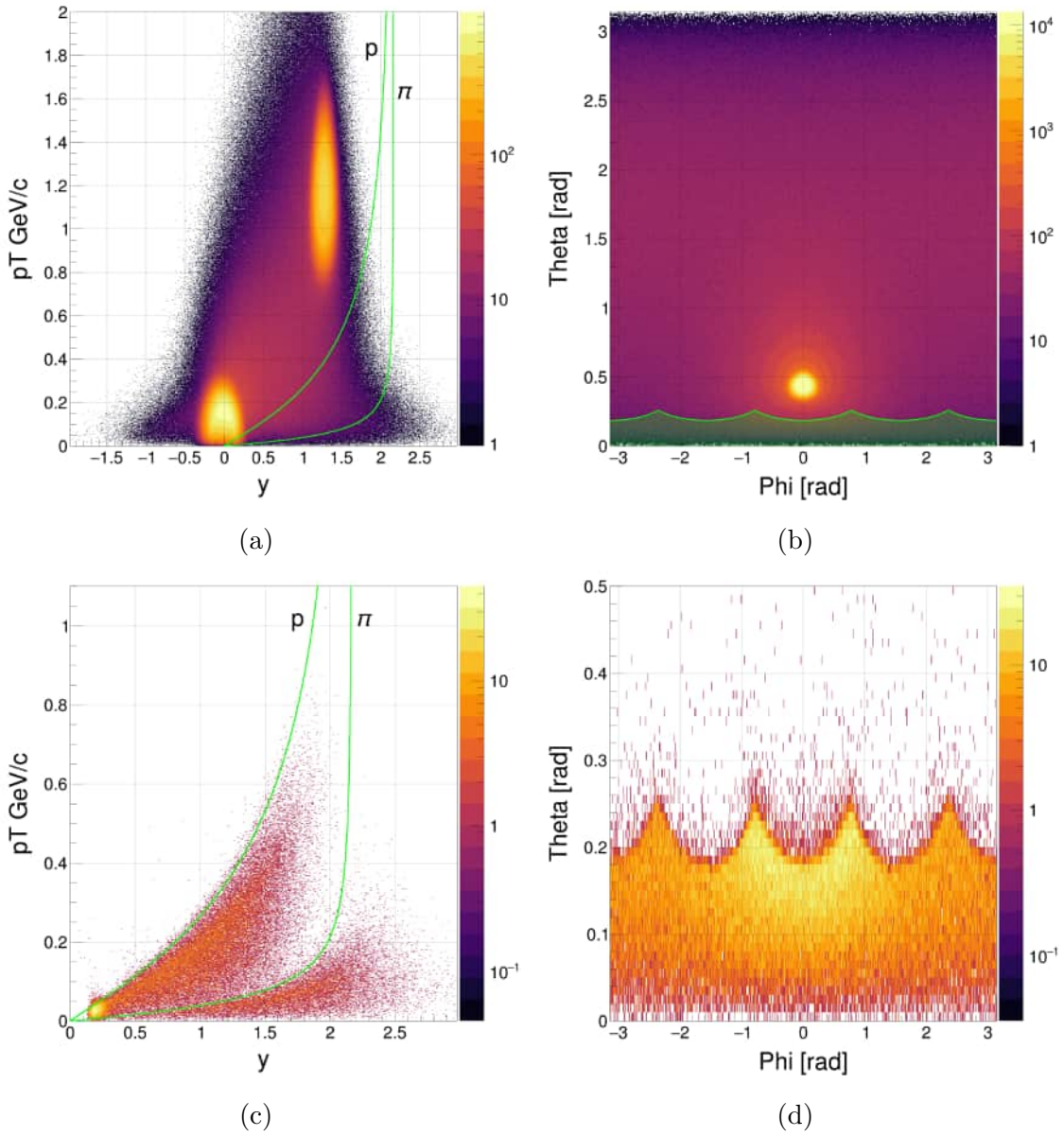

Figure 4.14: Kinematics distribution for primary tracks. Monte Carlo simulation for one million events, minimum-bias Ni+Ni at 1.93 AGeV. a) Transversal momentum vs. rapidity. b) Polar vs. azimuthal angle. mSts acceptance is highlighted in green color. c) and d) for MC tracks inside mSTS acceptance

Already from the hit map, the intentional overlap regions of sensors in the same ladders can be appreciated as horizontal bands with increased entries: i.e., $[-3, +3] \cap [+2, +3]\,\mathrm{cm}^2$. Remnant misalignment not considered during reconstruction can artificially magnify the overlap region. However, this is not the case between sensors on the extreme left in the second station (see Section 2.3), where the more considerable overlap is known from the assembly step.

Triangular structures are visible as "shadows", especially in the first ladder of the first station, like a "negative picture" of the **C**arbon **F**iber (CF) support structures (see Figure 2.3). The shadow results from a screening of particle signals by the CF structures that sit between the path from the target to the sensor. Although these structures are present in the middle ladder of the second station, a trained eye is required to appreciate them.

Chapter summary

- Problematic channels have been identified based on the number of entries for the channel distribution.
- ENC measurements from modules testing in the STS laboratory are used to cross-check the found broken channels.
- Noisy channel identification is based on the S/B ratio extracted from the ON/OFF spill channel distribution.
- A robust time calibration procedure was developed, including time walk effect corrections.
- Time resolution of $\sim 5\,\mathrm{ns}$ was estimated in the charge calibration range $8 - 68\,\mathrm{ke}$.
- The STS cluster distribution at mCBM@SIS18 shows a mean value for cluster size 1.2.
- Charge distribution peak related to MIP can be observed where expected (24,000 electrons).
- A good correlation in charge and size between p- and n-side is found, with minor asymmetries due to inactive channels and corrections of the charge calibration, not yet implemented.
- Charge distributions for hit cluster matches with minor differences.
- Inactive areas produced by different defects are well described by the projection of the reconstructed hit to the transversal plane.

Chapter 5

Hit reconstruction performance

The primary aim driving the development of particle detectors and the careful arrangement of high-precision sensitive materials is to identify traces resulting from the phenomena under investigation. The previous chapter analyzed the general properties of reconstructed hits in terms of their internal structure. This chapter will deal with quantities such as spatial resolution and efficiency. It is important to note that the upcoming analysis is performed event-like (see Figure 3.1), which means that only hits within an event 3.7 are involved at the same time.

5.1 Position correlation

The reconstructed hit correlation between the different detection layers on the mCBM setup offers an overall view of some performance aspects. It includes alignment and combinatorial background issues that the detector might face. The coordinate correlation analysis involves constructing a 2-dimensional distribution of the hit coordinate components across different reconstruction layers. The hits' z coordinate is a constant for each sensor. Hence, correlations are built for pairs $x_j, x_i(XX)$ and $y_j, y_i(YY)$, where indexes $i \neq j; i, j = 0, 1, 2$ stand for different setup layers.

Figure 5.1 shows such distributions for one sensor pair U1 L0 M0 : U2 L1 M0 . Additional combinations can be found in Appendix B.2. The intense diagonal region reflects the strong coordinate correlation between the reconstructed hits. It is dominated by hits from the same particle's passage through both layers. Similarly, the combinatorial background is mostly produced by mixing hits from different particle trajectories. In both correlation plots, secondary structures appear. These are produced by secondary track sources addressed in the upcoming chapter.

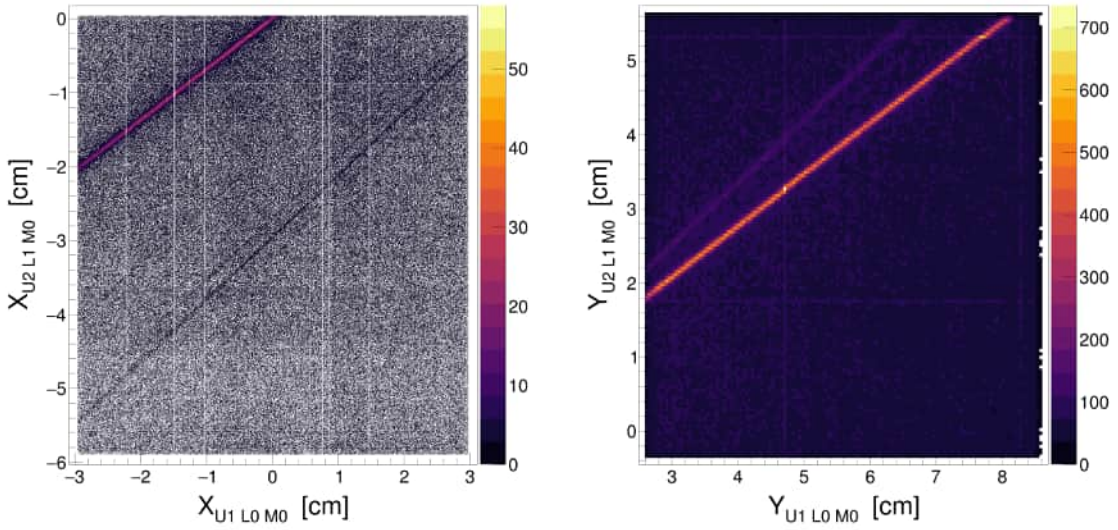

(a) (b)

Figure 5.1: Reconstructed hit coordinate correlation for mSTS sensor pair U1 L0 M0 : U2 L1 M0 .

These correlations are a simplistic, brute-force tracking method step that aims not to find the tracks but to perform preliminary checks. These correlations are subject to multiple sources of bias discussed in Section 5.3.1. However, simple cuts, such as the maximum time between the correlated hits, reduce the combinatorial background.

An auxiliary 1-dimensional distribution of the distance d_{ij} from (x_i, x_j) to the correlation line can be constructed to study such distributions quantitatively. The geometrical configuration of the setup ultimately determines the parameters of the correlation line. Due to the straight-line trajectories of the particles in the absence of a magnetic field, the coordinates of the reconstructed hits are linked by the same track directional vector components, as shown in Figure 5.2. The (h_i, h_j) hits corresponding to the same track will generate an intense correlation diagonal. Multiple scattering, detector resolution, and geometrical beam characteristics contribute to the smearing of such linear relationships. Due to the variety of sensor positions within the same detection layer, a differential analysis is necessary for sensor pairs.

Monte Carlo simulations are used as a benchmark in the correlation comparison. Differences in the correlation line slope for different sensor pairs become more prominent for YY correlations (see Figure 5.3). This effect is purely a geometrical feature due to the vertical placement of the ladders. It is produced because the difference in sensor z position between those on the same ladder is smaller than the difference among those on different ladders. This statement is particularly true for small ladders with a few sensors, as in the case of

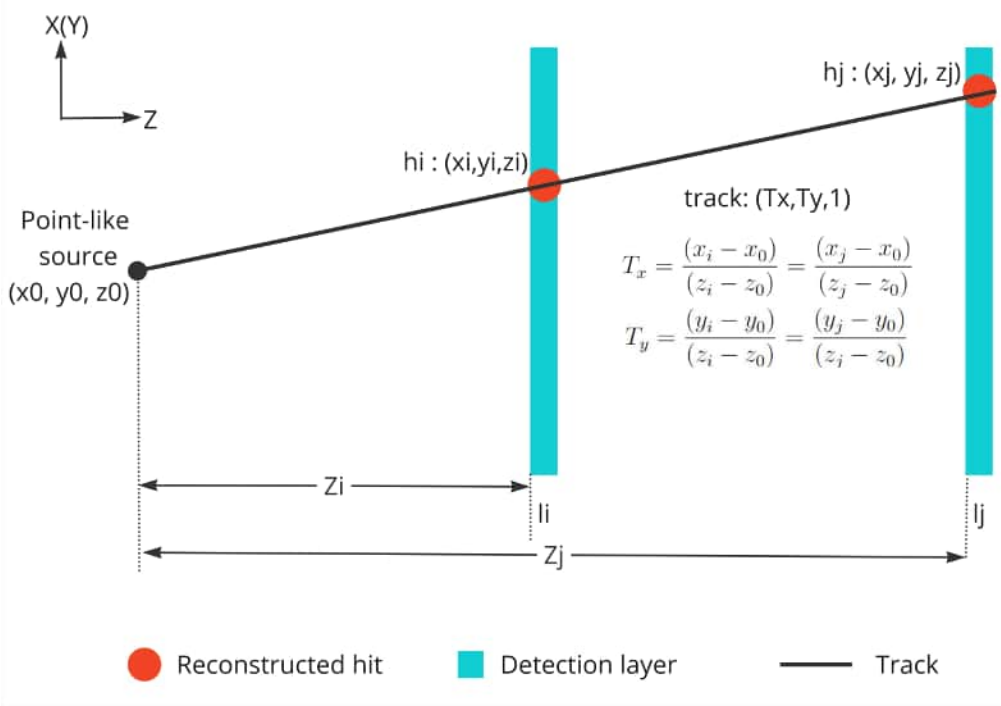

Figure 5.2: Hit correlation line originated from the track component relation to hit coordinates.

mSTS. For a full CBM ladder with multiple stacked sensors, sensor z-position differences become comparable to ladder z-position differences within the same unit.

The XX and YY correlation distributions can be compared to MC expectations using the distribution of the distance to the correlation line shown in Figure 5.4. Tracks are assumed to be generated at the coordinate system origin to build this distribution. Deviations of the correlation peak centers translate to misalignment in that regard. The comparative plots of such distribution show a centered correlation peak corresponding to the correlation diagonal distribution on top of a combinatorial background. The agreement between the Monte Carlo simulation is remarkable till the background reproduction. Such an agreement has important implications. From it, the detector resolution can be inferred to match the estimated values from the MC simulations. It also validates the treatment of the uncertainty for hit position for different cluster sizes (see Section 3.5).

Peak width can be numerically compared by fitting the distribution with a Gaussian peak on top of a quadratic background. Table 5.1 reports the sigma of the fitted Gaussian peak by sensor pairs (mSTS unit 1 : mSTS unit 2). This analysis is susceptible to remnant misalignment, which can simulate broader peaks by altering the slope of the correlation line.

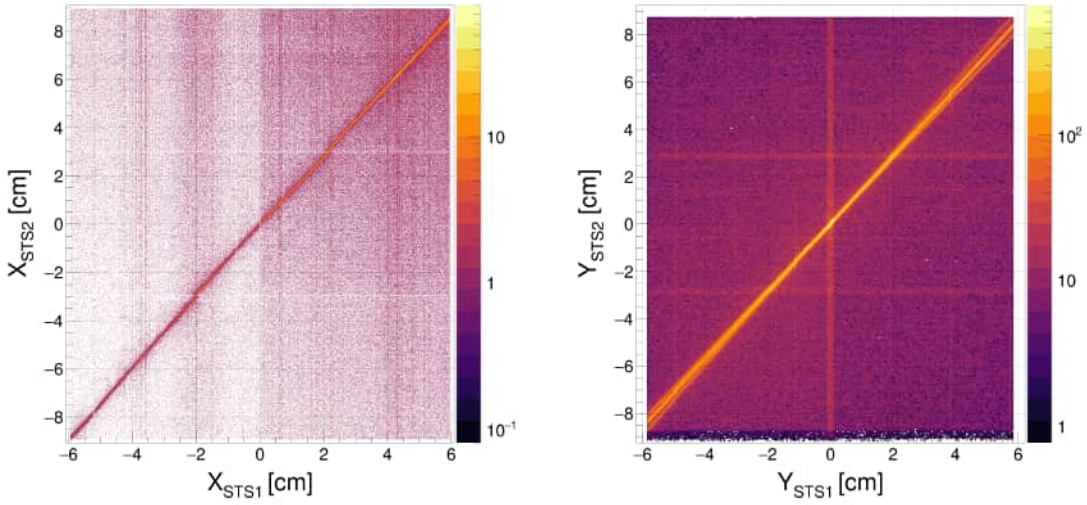

(a) (b)

Figure 5.3: Reconstructed hit coordinate correlation between mSTS layers on Monte Carlo simulations.

Correlation peak width

Disentangling the primary sources of the correlation peak width is mostly a geometric problem. A toy Monte Carlo experiment was run to explore the effect of different sources that broaden the peak.

A multivariate Gaussian distribution $N(\mu_x = 0, \mu_y = 0, \sigma_x^{bs}, \sigma_y^{bs})$ is sampled at the origin to generate the track vertices. It mimics the distribution of event vertices produced by the beam particles when interacting with the target, known as the beam spot. An area of $6 \times 6\,\mathrm{cm}^2$ in the range of $[-3; 3]\,\mathrm{cm} \cup [-3; 3]\,\mathrm{cm}$ corresponding to detection layer $z = z_i$ is uniformly sampled to build a directional track vector. This track is projected onto the layer l_j at $z = z_j$. A multivariate normal distribution smears the coordinates of the point $N(\vec{\mu}, \sigma_{STS})$ to simulate detector resolution effects.

Three cases were sampled for one million tracks. No multiple scattering effects were simulated within this toy MC experiment. The measured distribution has been randomly sampled for STS_2TRD-TOF- to mimic a realistic combinatorial scenario due to track multiplicity.

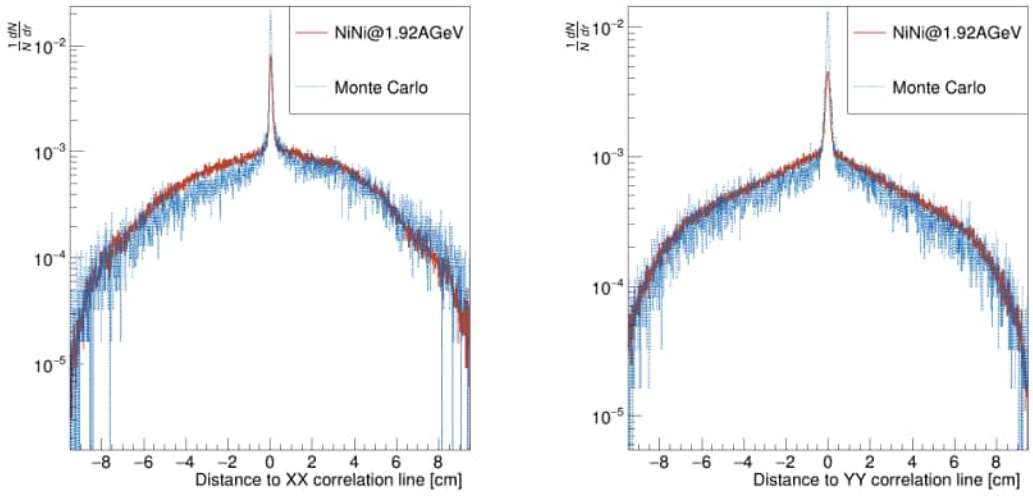

(a) (b)

Figure 5.4: Correlation projection for a) X coordinate, b) Y coordinate.

The distributions for the d_{ij} were built for each of the following cases:

- There is no smearing of hit coordinates, no impact from detector resolution, and no point-like beam spot.
- Smearing of the hits coordinates by the respective detector resolution ($9\,\mu$m) and a point-like beam spot (Figure 5.5a).
- Smearing of the hit coordinates and beam spot width of 0.15 cm.

The μ value used during the smearing of the sampled point is always null. Recreating a non-centered beam spot or misalignment is out of scope. Figure 5.5 shows the correlation peak for the abovementioned cases. The last case comes close to the most realistic scenario. Changes produced by the detector resolution seem negligible compared to the beam spot effects. However, an analytical approach is developed in the Appendix B.1.

Additional widening of the correlation peak can be provoked by secondary particle tracks produced far from the event vertex. Although not included in this dummy experiment, such a case is contained in the MC conducted before and the one used for comparing the correlation peaks in the previous section.

For the first case, as no modification is applied to the track points, the distance to the correlation line will always be zero. However, the apparent peak width will depend on the selected binning used to sample such a distribution. Although analytically the expected distribution is a Dirac delta-like distribution, any observed deviation would arise from binning artifacts and would be present in any scenario.

Table 5.1: Correlation peak widths by sensor pairs: mSTS unit 1 - mSTS unit 2.

Sensor Pair	NiNi@1.92AGeV		Monte Carlo	
	σ_{XX} [cm]	σ_{YY} [cm]	σ_{XX} [cm]	σ_{YY} [cm]
U1 L0 M0 : U2 L0 M0	0.0458(10)	0.0647(17)	0.0424(4)	0.0694(7)
U1 L0 M0 : U2 L0 M1	0.0461(12)	0.0639(16)	0.0414(4)	0.0675(7)
U1 L0 M0 : U2 L1 M0	0.0403(6)	0.0617(12)	0.0384(3)	0.0628(5)
U1 L0 M0 : U2 L1 M1	0.0399(9)	0.0647(17)	0.0371(4)	0.0619(7)
U1 L0 M1 : U2 L0 M1	0.0444(9)	0.0671(15)	0.0420(3)	0.0672(5)
U1 L0 M1 : U2 L1 M1	0.0411(5)	0.0663(11)	0.0383(2)	0.0619(4)
U1 L1 M0 : U2 L1 M0	0.0332(5)	0.0584(11)	0.0328(2)	0.0536(4)
U1 L1 M0 : U2 L1 M1	0.0376(7)	0.0587(16)	0.0330(3)	0.0537(6)
U1 L1 M0 : U2 L2 M0	0.0413(5)	0.0613(9)	0.0441(2)	0.0629(4)
U1 L1 M1 : U2 L1 M1	0.0377(5)	0.0651(12)	0.0348(2)	0.0570(4)
U1 L1 M1 : U2 L2 M2	0.0423(6)	0.0639(8)	0.0398(2)	0.0607(3)

This simplistic experiment allows for some approximations (see Appendix B.1.1). Considering both the smearing of the beam spot and the detector resolution, the expected value for the distribution width is 377 μm. The fitted value shown in Figure 5.5b deviates from the analytical expression by 1.5 %.

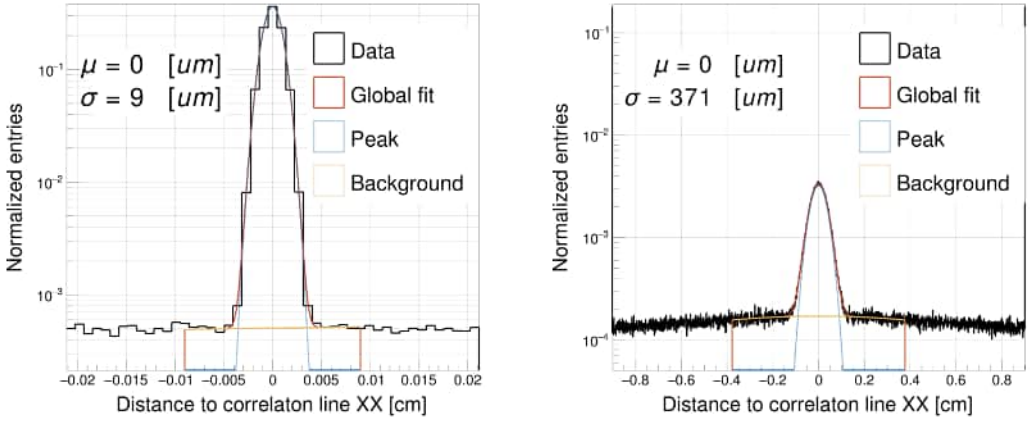

(a) (b)

Figure 5.5: Dummy correlations peaks for each case. a) detector resolution effect, b) realistic case.

5.2 Position resolution

The detector resolution can be extracted from the quadratic sum of variances for a three-layer setup where the track model is a straight line. The unbiased residual sigma (σ_{UR}) is the sum of the uncertainty related to track extrapolation (σ_{trk}), the detector resolution (σ_{STS}), and the multiple scattering (σ_{MS}). The multiple scattering effects will be estimated from the Lych-Dahl equation. The upcoming subsections discussed extracting the σ_{UR} properly. Additionally, the track evaluation uncertainty will be treated for a particular case.

$$\sigma_{UR}^2 = \sigma_{trk}^2 + \sigma_{STS}^2 + \sigma_{MS}^2 \tag{5.1}$$

5.2.1 Track reconstruction and residual analysis

After a global track t_i passes all topological and geometrical cuts, the next step is to evaluate the track at the study layer. Each (m)STS layer $\{l_i\}$ comprises a set of sensors $\{s_{ij}\}$ whose z-coordinate differs as explained in previous chapters. Each layer is then characterized by the position and shapes of each sensor (see Figure 5.2). Therefore, the track evaluation at the study layers is not a single operation but one for each sensor.

$$l_i = \{s_{ij}\} = \{(s_{ij}^x, s_{ij}^y, s_{ij}^z, s_{ij}^{dx}, s_{ij}^{dy}, s_{ij}^{dz})\} \tag{5.2}$$

The track evaluation results in an (x_{ij}, y_{ij}) point at which the sensor s_{ij} is expected to reconstruct a hit corresponding to the traversing particle. The extrapolated point is not free from uncertainties and is systematically calculated during track fitting. Track fitting uncertainties are impacted by all detection subsystems contributing to the track.

A residual analysis provides valuable insight in such regards. Two relevant magnitudes can be extracted from it: the mean value (μ) providing remnant misalignment and the standard deviation (σ). The σ contains information about the convoluted resolution and uncertainties from all subsystems involved in the track. Both magnitudes are critical to evaluate if a hit can be attached to a track. Mathematically, it is expressed by equation 5.3.

$$\|t(s_{ij}^z) - h_{ij} - \mu_{ij}\| < \kappa\sigma_{ij} \tag{5.3}$$

A reconstructed hit h_{ij} is considered *found*, so it can be attributed to the passage of the particle described by the track t if the distance between the extrapolation of the track to the plane of the STS sensor s_{ij}^z corrected by the remnant misalignment μ_{ij} is smaller than $\kappa\sigma$, where κ is an arbitrary number. More than one reconstructed hit can fulfill the

above criterion. The hit with the smallest distance to the extrapolation point is used for the efficiency analysis.

It becomes clear that misalignment is also a direct source of bias in the analysis. The internal alignment of the STS setup and the alignment among all detection subsystems can negatively impact efficiency. Using the mean value from the residual analysis (μ_{ij}) allows for further alignment corrections. However, the distribution width (σ_{ij}) is involved in the *found* criterion. Hence, large values of this sigma increase the likelihood of mistakenly considering a hit as *found*, positively biasing the efficiency result.

Misalignment in the spatial orientation might also be present and pose as a mixed translation. Dependencies between the residual distribution and the sensor coordinates might indicate rotations misalignment. Consequently, preliminary analysis of the unbiased residual distributions must be assessed before using the distribution μ and σ.

Figure 5.6 shows the unbiased residuals between global track $\mathrm{STS^2TRD_1TOF_1}$ and reconstructed STS hits at U1 L1 M0 as function of the hit coordinates x(5.6a, 5.6c) and y(5.6b, 5.6d) . It is called unbiased because the usage of hits from the layer under test is disabled for the tracking algorithm. Therefore, the hit at the DUT does not modify the track parameters.

There is a coordinate dependency of the distribution manifested in different ways. In some cases, the intense region of the distribution does not reach the whole sensor acceptance, and the distribution's intensity fluctuates with the hit coordinate. Additionally, there is a rotation of the distribution. The apparent distribution tilt is the most obvious reason why projection without correcting for such rotation would result in a wrong estimation of both μ and σ.

There are several methods to find the rotation angle of the distribution. The one used consists of a linear regression of the $x(y)_{hit}$ profile distribution shown for all four panels in Figure 5.6. The profile was built using a restricted horizontal axis range (corresponding to $\Delta x = x_{trk} - x_{hit}$) to mitigate background contamination. Once the rotation angle is found, the 2-dimensional is vertically aligned, and the projection for the sensor residual is obtained. A Gaussian distribution fits the 1-dimensional unbiased residual distribution to describe the peak on top of a quadratic background. The resulting fit is depicted in Figure 5.7 with the corresponding mean and sigma values.

The picture shows a failed attempt to fit a distribution with a clear deviation from Gaussian behavior. Therefore, in order to create a subset of tracks with improved quality, additional constraints must be implemented. Using the sigma extracted from the aforementioned residual fit would throw a heavily biased detector resolution.

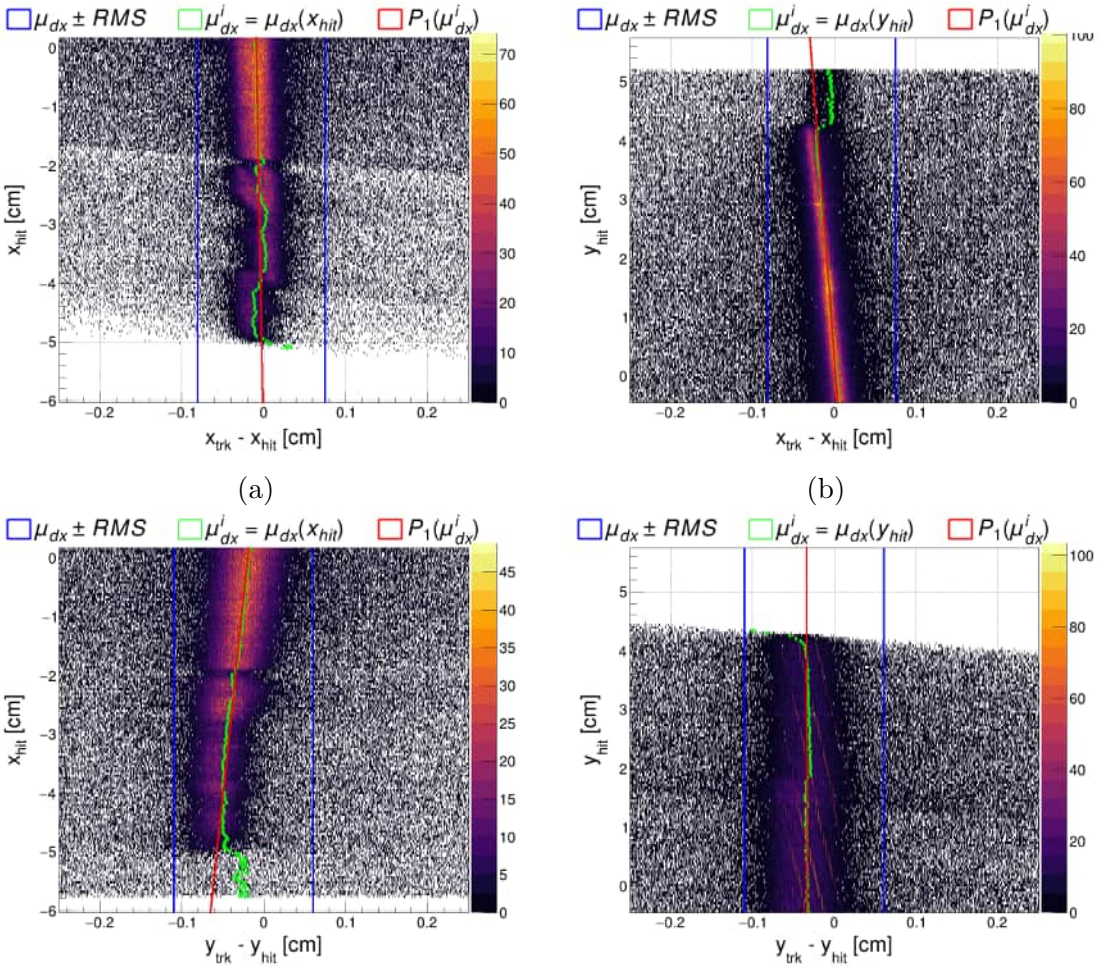

Figure 5.6: Correlation plot between the hit transversal coordinate and the unbiased residual using global tracks. The y-profile is drawn in green colors with (+) markers. Vertical blue lines are drawn to represent the RMS of the distribution along the x-axis. The result of linear regression analysis is drawn as a red line. The sample data module U1 L0 M0 .

5.2.2 Track extrapolation from STS hits

The tracking algorithm provides a robust method for discarding false combinations of hits. However, track parameters are recalculated to avoid propagating uncertainties from other detection subsystems and partially suppress the misalignment effect. The two STS hits attached to the track recalculate Tx, Ty. Using STS hits that have already been identified as belonging to the same track allows us to preserve the combinatorial background suppression that the tracking algorithm provides.

Additionally, selecting a single sensor in the enabled tracking stations provides a way to discard the superposition of residual distributions with different means due to misalignment.

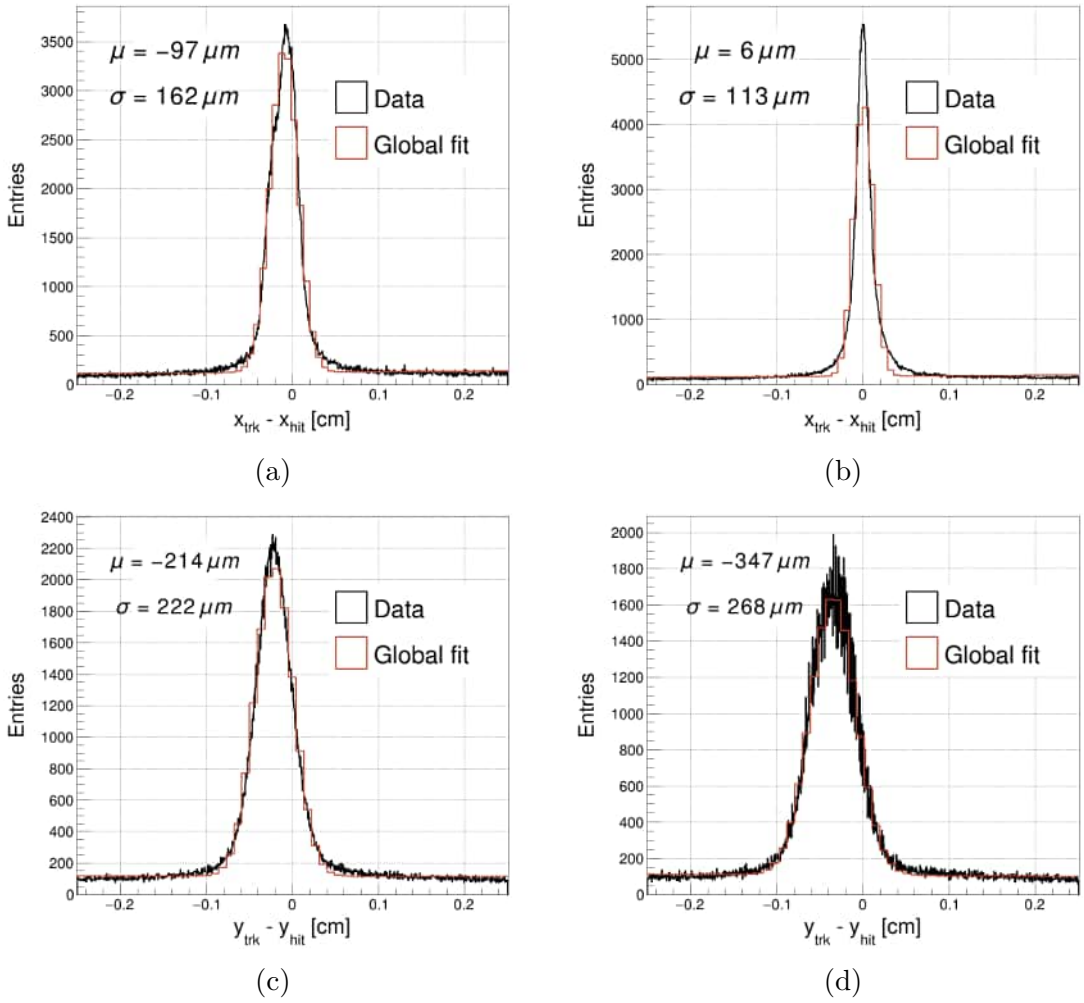

Figure 5.7: Residual distribution from global tracks and STS sensor: module U1 L0 M0 . The red curve represents Gaussian + quadratic fit analysis.

This has, as a consequence, an even more reduced acceptance. Although the first station only comprises a single sensor U0 L0 M0 , the second layer provides different options. The ladders U2 L0 and U2 L2 performance was questionable regarding noise and charge calibration. Therefore, those sensors will not be utilized. From the two sensors in the middle ladder in the last station, the U2 L1 M1 will be used to minimize the loss in acceptance, as the sensor chosen is a 6.2 cm × 12.4 cm.

The track parameters recalculation becomes trivial, as there are only two STS hits per track because the tracking is performed with only two out of the three STS tracking stations. Therefore, the evaluation of the track at the DUT is a simple straight-line extrapolation given by 5.4. Using these two-hit track parameter recalculations, the residual analysis can be redone. The resulting correlations between the unbiased residuals and the hit coordinates are

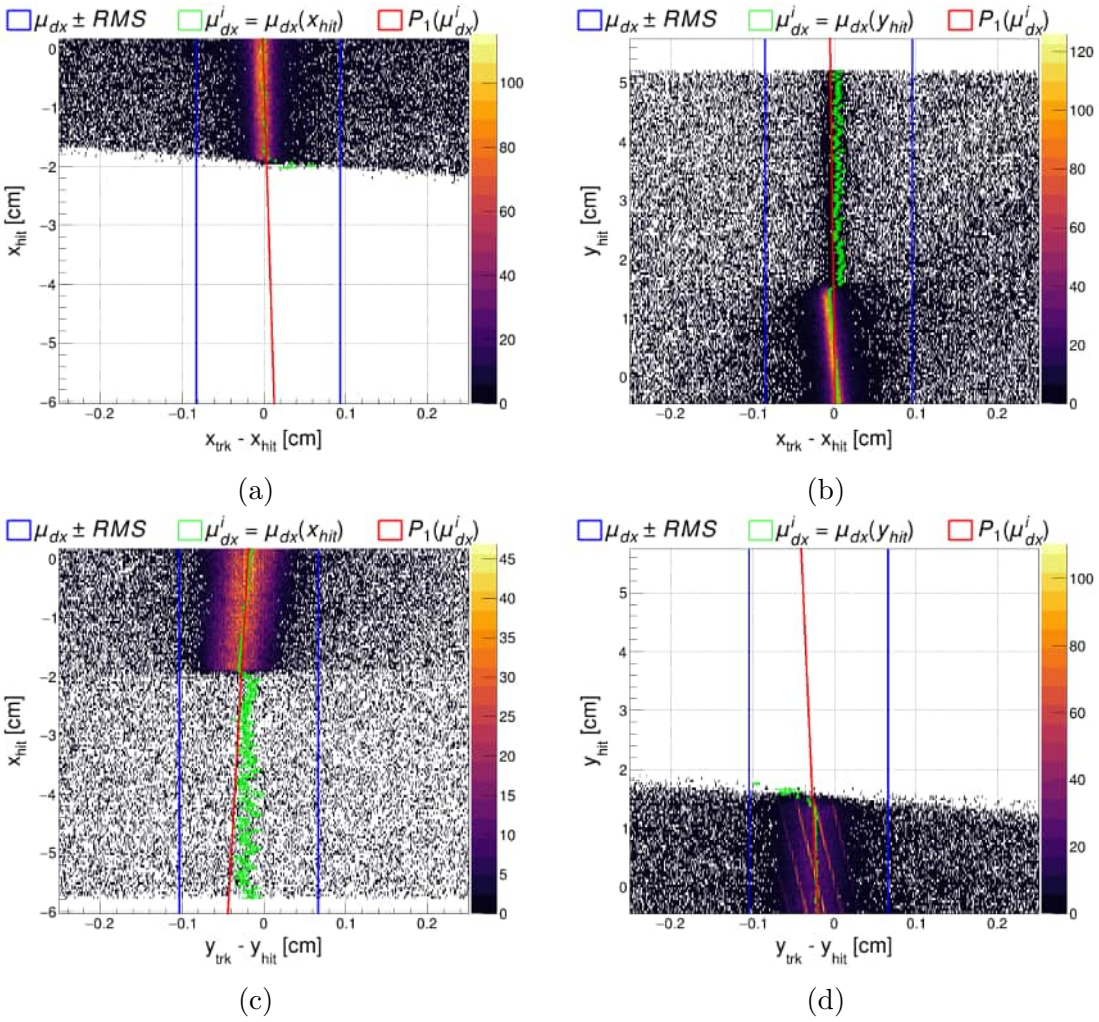

Figure 5.8: Correlation plot between the hit transversal coordinate and the unbiased residual. The y-profile is drawn in green colors with (+) markers. Vertical blue lines are drawn to represent the RMS of the distribution along the x-axis. The result of linear regression analysis is drawn as a red line. The sample data module U1 L0 M0 .

shown in Figure 5.8. The resulting distributions display a limited range compared to those in Figure 5.6 provoked by the sensor selection. However, the correlation is a homogeneous trend represented by a rotation. Performing a similar analysis to find the rotation angle, new unbiased residual distributions are obtained and displayed in Figure 5.9.

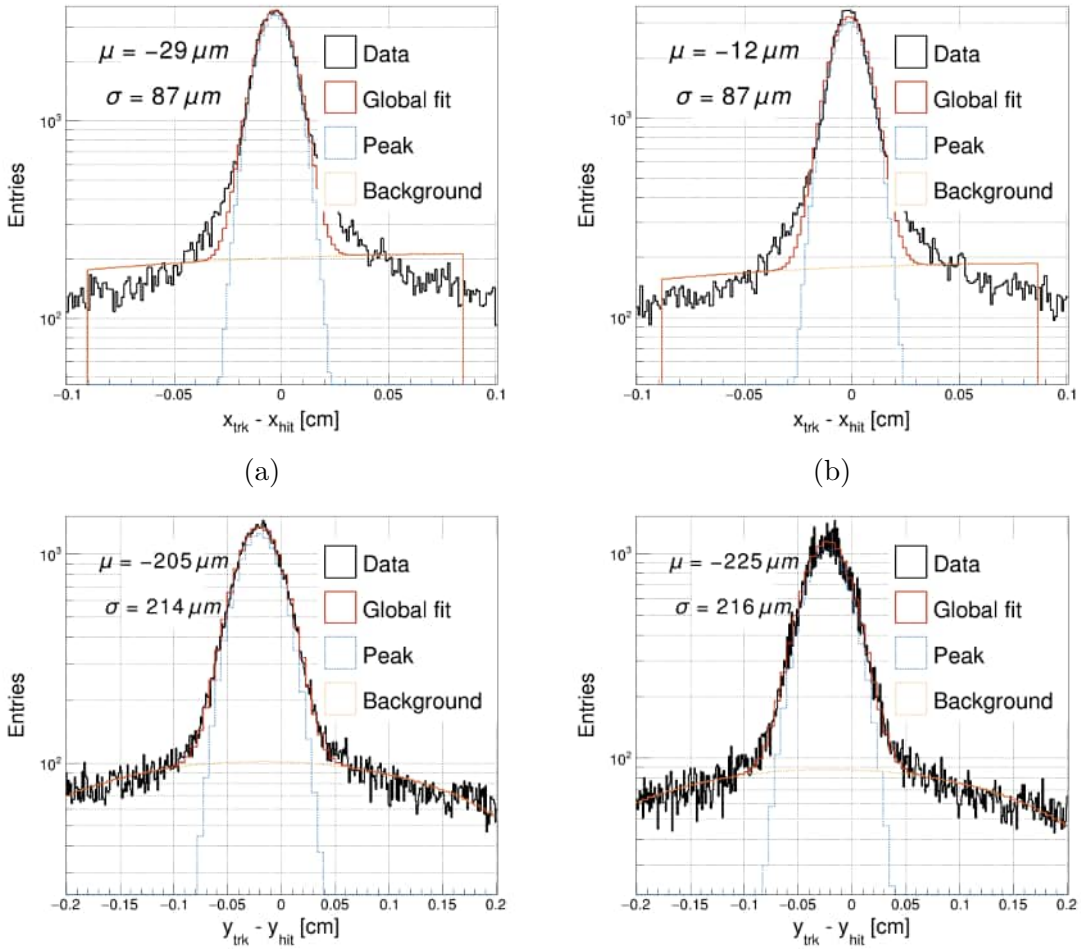

Figure 5.9: Residual distribution using after track refit using only STS system information: module U2 L1 M0 .

Given two `StsHit` (h_i, h_j) from layers i and j, respectively, the expected position at DUT is given by:

$$x_{DUT} = x_i + T_x(z_{DUT} - z_i) \quad , \tag{5.4}$$

$$y_{DUT} = y_i + T_y(z_{DUT} - y_i) \quad , \tag{5.5}$$

where Tx, Ty are the components of the track directional vector $\vec{T}$,

$$\vec{T} = (Tx, Ty, 1) = (\frac{x_i - x_j}{z_i - z_j}, \frac{x_i - x_j}{z_i - z_j}, 1) \quad . \tag{5.6}$$

Being $\sigma_{x(y)_i}$, $\sigma_{x(y)_j}$, the uncertainties for the x(y) coordinate at layer i, j respectively, the

error propagation from 5.4 takes the form:

$$\begin{aligned}\sigma_{trk}^2 = {\sigma_{x_i}}^2 \left(\frac{z_{DUT}-z_i}{z_i-z_j}+1\right)^2 \\ + {\sigma_{x_j}}^2 \left(\frac{z_{DUT}-z_i}{z_i-z_j}\right)^2 \\ + {\sigma_{z_i}}^2 \frac{(x_i-x_j)^2(z_{DUT}-z_i)^2}{(z_i-z_j)^4} \\ + {\sigma_{z_j}}^2 \frac{(x_i-x_j)^2(z_{DUT}-z_i)^2}{(z_i-z_j)^4} \quad .\end{aligned} \tag{5.7}$$

Properly selecting the order of three equidistant layers, the fraction $(z_{DUT}-z_i)/(z_i-z_j) = \frac{1}{2}$, hence the expression simplifies to:

$$\sigma_{trk}^2 = {\sigma_{x_i}}^2 \left(\frac{3}{2}\right)^2 + {\sigma_{x_j}}^2 \left(\frac{1}{2}\right)^2 + {\sigma_{z_i}}^2 \frac{(x_i-x_j)^2}{4(z_i-z_j)^2} + {\sigma_{z_j}}^2 \frac{(x_i-x_j)^2}{4(z_i-z_j)^2} \quad . \tag{5.8}$$

For tracks parallel to the z-axis, uncertainty along this direction is irrelevant as $\forall i,j : (x_i-x_j) \equiv 0$. In the search of estimating the maximal impact of σ_z, the above expression can be evaluated for the mSTS setup such that $Max(x_i-x_j) = 6\,\text{cm}$ while $Min(z_i-z_j) \approx 24\,\text{cm}$. Assuming identical resolution for all layers, hence $\sigma_{x_i} \equiv \sigma_{x_j}$ and $\sigma_{z_i} \equiv \sigma_{z_j}$. Then, considering the maximal effect due to z position determination uncertainty, the above expression takes the form:

$$\sigma_{trk}^2 \approx \frac{5\sigma_{x_i}^2}{2} + \frac{\sigma_{z_i}^2}{32} \quad . \tag{5.9}$$

In the expression above, the uncertainty in determining the coordinate contains the detector systematic effect σ_{STS} and the multiple scattering σ_{MS}. Therefore, by replacing the term σ_{trk} in equation 5.1, ones obtain an approximate expression for the unbiased residual of the mSTS setup:

$$\sigma_{UR}^2 = \frac{7\sigma_{STS}^2}{2} + \frac{7\sigma_{MS}^2}{2} + \frac{\sigma_{z_i}^2}{32} \quad . \tag{5.10}$$

The obtained relationship is equivalent for both transversal coordinates, x and y. The term of interest is σ_{STS}, which can be isolated as a function of the measure sigma of the unbiased residual distribution, the estimated impact of multiple scattering, and the uncertainty of the position determination of the reconstructed hit z direction.

The sensor thickness, placement metrology, and alignment determine the uncertainty in the z-direction. A sensor thickness of 320(15) μm and a ladder assembly metrology precision of 10 μm make this term significant, emphasizing the importance of good metrology. This relationship also highlights the sensitivity to misalignment along this direction for tracks that are not parallel to the z-axis, for which σ_z plays no role.

On the other hand, the term related to multiple scattering can be estimated from equation 1.1. The most abundant charge particles inside the mSTS setup acceptance that match the track selection criteria $STS^2TRD_1TOF_1$ are protons and pions. This can be observed from Figure 5.10a, showing three particle multiplicity distributions from MC simulations: all charge particles, primary charge particles, and primary charge particles inside the mSTS acceptance. For the two most abundant reaction products, the distributions for σ_{MS} have been built as a function of the momentum and shown in Figure 5.10. The second vertical axis (right axis) is utilized for the momentum distribution of primary protons and pions. The uncertainty due to multiple scattering is only a few (3.5 μm) microns for the first peak in the proton momentum distribution. Contributions from higher momentum are more than one order of magnitude smaller, hence negligible for both protons and pions.

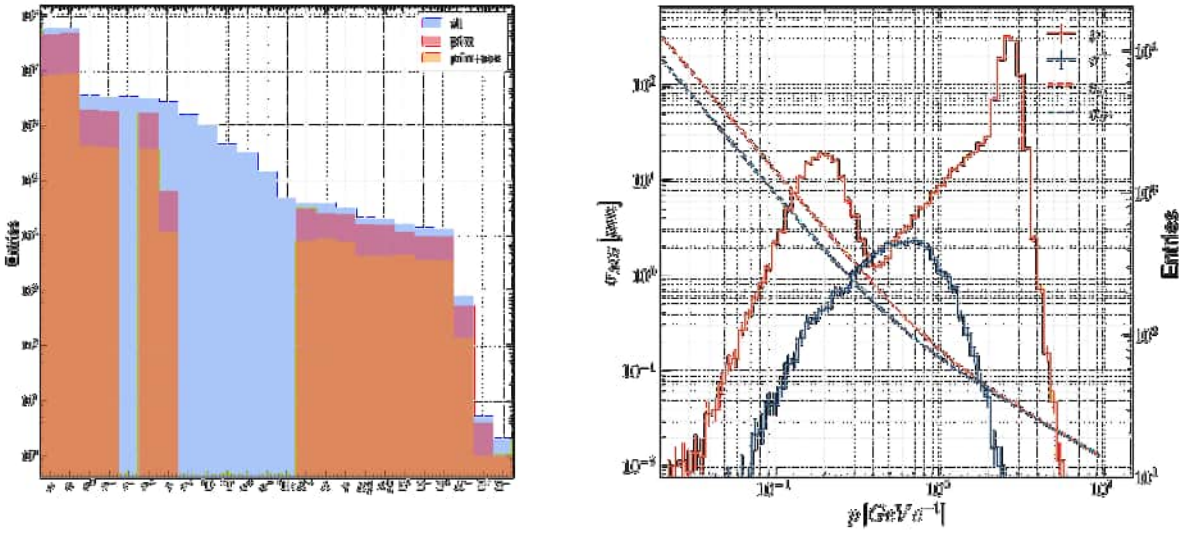

(a) (b)

Figure 5.10: a) Particle multiplicity distributions from MC simulations: all charged particles, primary charged particles, and primary charged particles inside mSTS setup acceptance. b) Uncertainty in the transversal coordinate (σ_{MS}: y_{rms} from Figure 1.5) due to multiple scattering as a function of particle momentum: pions and protons.

The mSTS spatial resolution is estimated by solving the expression 5.10 for σ_{STS} and introducing the average contributions of multiple scattering and uncertainty along the z-axis. The result is shown in Table 5.2, extracted from the residual distributions for different sensors in the layer under test for both transversal coordinates. These values represent the combined spatial resolution of different cluster sizes. However, single-strip clusters are dominant, given the track selection criteria and the geometrical conditions. Values obtained for the y-coordinated should be observed carefully, as the hit position along this direction depends on the x-coordinate.

5.2.3 Accounting for non-gaussian effects

The 1-dimensional residual distribution deviates from a Gaussian profile, even when a quadratic background is accounted for. This discrepancy can stem from various factors, with the primary contributors being sensor misalignment and the presence of ghost hits.

The first factor, misalignment, impacts the residual distribution by altering the coordinates between the extrapolated and reconstructed hits. Nevertheless, certain aspects like sensor warping and rotation are not accounted for during the alignment process. This oversight leads to skewed distribution patterns and variations in the measurement of σ_{UR} across both transverse coordinates, x and y.

Ghost hits can significantly degrade the tracking performance by introducing distortions to the track parameters, potentially leading to the fake tracks generation in extreme cases. Furthermore, these ghost hits can contaminate the residual evaluation at the plane of the DUT. To mitigate this issue, constraints can be applied to the charge symmetry of the reconstructed hits at the DUT. However, it is essential to note that real hits can also be inadvertently excluded due to the effects of charge calibration and inactive areas in the detector, resulting in a biased evaluation.

Two strategies are implemented to address local dependencies and non-Gaussian characteristics. The first approach assumes that the Gaussian distribution of the residuals $x_{trk}-x_{hit}$ predominantly influences the peak observed in the residual distribution. Under this premise, we can quantify σ_{UR} by deriving it from its relationship with the **F**ull **W**idth at **H**alf **M**aximum (FWHM).

The second method involves a two-step process. Initially, a flat background is removed from the two-dimensional distributions shown in 5.6. Subsequently, the average **R**oot **M**eam **S**quare (RMS) ($RMS(x_{trk} - x_{hit})$) is computed across both the x and y coordinates of the sensor. This strategy is designed to mitigate the risk of inflated sigma estimates that can arise from the overlapping of multiple Gaussian peaks with differing means. This is based on

Table 5.2: Position resolution for transversal coordinates. Values calculated using σ_{UR} as: sigma from residual fit, FWHM/2.35, and average RMS. Reported values units are micrometers (μm).

Sensor	σ_x^{fit}	σ_x^{FWHM}	$\sigma_x^{\text{<RMS>}}$	σ_y^{fit}	σ_y^{FWHM}	$\sigma_y^{\text{<RMS>}}$
U1 L0 M0	29	25	23	103	101	72
U1 L0 M1	28	27	26	102	105	69
U1 L1 M0	29	25	24	103	85	75
U1 L1 M1	28	29	27	102	110	72

the premise that, for any given sensor coordinate, the residuals can be considered as samples drawn from an identical distribution characterized by the same variance σ but with distinct mean values μ. It is important to remark that arbitrarily removing content can produce truncation effects that must be taken into account.

The estimation of the spatial resolution extracted from the peak FWHM and the average RMS approach is also displayed in Table 5.2. These two last strategies result in a smaller spatial resolution closer to the theoretical expectations (see Section 3.5). However, FWHM cannot account for the Gaussian superposition with different μ, resulting in slightly larger sigma values. On the other hand, the background subtraction is done arbitrarily, incurring selection bias. The chosen value for background subtraction was estimated from the fit, where the quadratic distribution is expected to describe the combinatorial.

5.3 Hit reconstruction efficiency

In double-sided silicon strip sensors, when a particle interacts with the active material, the expected detector response manifests as two correlated signals generated on opposing sides of the sensor. This phenomenon allows for the proper reconstruction of the event as a hit, as detailed in Section 3.5. However, various factors can influence this process and its outcomes. This section focuses on assessing the efficiency of hit reconstruction. The reconstruction efficiency quantifies the proportion of successfully reconstructed interactions from the total number of interactions. Formally, this is defined as the ratio of the number of reconstructed particle hits ($N_{\text{reconstructed}}$) to the total number of particles that traverse the sensor's active area ($N_{\text{particles}}$), as expressed in equation 5.11.

$$\epsilon_{hit} = \frac{N_{\text{reconstructed}}}{N_{\text{particles}}} \tag{5.11}$$

A particular remark is made for "reconstructible interactions." It comes from the fact that energy deposition can occur in inactive areas of the detector, making the numerator of the expression 5.12 always null. This impacts the integrated efficiency and limits the differential analysis. Therefore, careful analysis must be considered so as not to bias the statistical analysis. Moreover, as intentional inactive regions can be created by channel masking, reporting a null efficiency for those cases can be misleading.

Determining the number of particles traversing the active area is intrinsic to the reconstruction process. However, estimating such a quantity as the expected number of interactions is feasible. The track-finding algorithm's task is to combine a group of hits in the different tracking stations to form a track corresponding to the passage of the same particle. The fitted trajectory can be evaluated at any layer (tracking station) z-position, providing the expected transversal coordinates for which the particle should have crossed. Hence, the number of particles traversing our detection system's specific sensitive area is estimated as the number of track extrapolations N_{trk}.

5.3.1 Estimation bias

Particle interaction with matter is characterized by its statistical nature, and there are cases when this method can be biased. Figure 5.11 shows different cases for illustration purposes. The equidistant rectangles represent detection layers. Overlaid orange thick dots designate reconstructed hits attached to the found track, represented by solid black lines. Dashed black lines represent the prolongation of the track to another layer, whose intersections are marked as hollow orange circles. Finally, thick black dots overlaying the layers convey reconstructed hits not connected to the particle's passage, as a hit can be reconstructed from correlated noise or simply from a different particle. The last one becomes dominant at higher particle multiplicity [79].

The first case, 5.11a, shows a well-defined track, and an expected hit will be reconstructed in the third layer. If the hit exists, it contributes positively to the efficiency. Otherwise, inefficiency is considered if such a point falls under an active area of the detector. Efficiency can be unintentionally boosted by a hit unrelated to the particle the tracks represent: 5.11c.

A usual scenario is when the material absorbs a particle. It leads to a track extrapolation to the next layer, for which the expectation of a reconstructed hit is wrongly assumed. In this case, a reconstructed hit contributes positively to the efficiency values, resulting in a false positive. Yet the nonexistence of such a hit lessens ϵ_{hit}. Therefore, it is in the best interest to avoid the end layers, for which there is no way to check if the track continues further in the detection system or was absorbed before reaching the layer under testing.

A particle decaying between layers can produce several tracks that are reconstructed downstream, a scenario that introduces bias in multiple ways. The extrapolation of the track has no connection to the daughter track[1] on the upstream layer. The closer the decay occurs to the upstream layer, the more likely the expected hit is to be mistakenly identified as the one generated by the mother track[2]. Moreover, the mother and daughter tracks might contribute to the reconstructed hit in the test layer for decay or reactions of particles inside the layer material. Distinguishing these reconstructed hits from those produced by overlapping two or more particle energy depositions requires further physical analysis beyond this approach. Nevertheless, these biases can be nullified by avoiding the front layer.

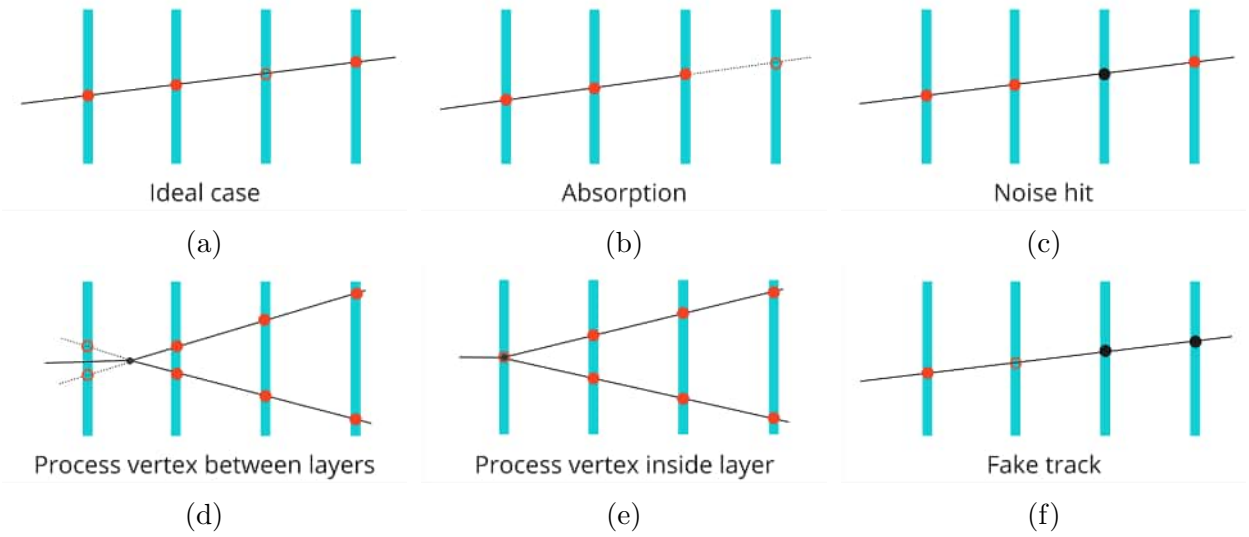

Figure 5.11: Illustration for different scenarios when efficiency analysis is biased.

At the moment, all the scenarios expose possible biases when connecting a reconstructed hit to the track. It is, in the most profound way, connected to tracking performance. Although Monte Carlo studies provide a way to estimate the impact of fake tracks [79]. However, this information is veiled in the experiment, and track selection criteria become critical.

In addition to the selection criteria explained at Section 3.6, a geometrical restriction will be applied to the track, requesting it to originate from the event vertex. The estimation of the event vertex is covered in a dedicated chapter, Chapter 6. Such restriction aims to select primary tracks, minimizing the potential bias for cases depicted in Figure 5.11d, 5.11e.

These track selection criteria allow creating a particular subset of tracks with STS hits only. These STS track-lets represent the most elemental track set influenced only by STS systematics and can be used as a first approach for efficiency assessment. In the mSTS

[1] track corresponding to a particle produced after the interaction

[2] track leading to the interaction that produces a particle with a daughter track associated

case, insufficient layers at the measured interaction rates induce a harmful combinatorial background for such analysis.

5.3.2 Efficiency

Two histograms covering the area of each sensor are filled: one with the number of valid extrapolations and one with reconstructed hits that could be attributed to the track that generates the extrapolation. This mapping represents a grid of rectangular cells, different from the geometrical shape of the area covered by two overlapping strips. The size of the histogram bins has been chosen to match the spatial resolution for a single strip cluster.

Figure 5.12a shows the filled histograms for sensors in the last layer. Careful observation reveals areas with small entries for the track extrapolation due to inefficiencies in the other detector prototypes involved. Moreover, the geometrical cuts imposed on the global tracks reduce the overall acceptance of the entire setup.

$$\epsilon_{ij} = \frac{N_{ij}^{\text{rec}}}{N_{ij}^{\text{trk}}} \tag{5.12}$$

For each cell in the histogram, the efficiency is well-defined as the ratio shown in equation 5.12. The efficiency histogram pixels have been colored differently and grouped into four classes. Additionally, a negative image of the reconstructed hit map has been drawn in gray to highlight inactive areas (gray). Note that this gray area includes cells with no entries, which are likely inactive.

Efficiency for areas covered by inactive strips tends to lower values, but not all cases are null. The ionization charges are distributed inside the silicon, so even when a strip is dead, the charge might be partially collected by the neighboring ones, making the hit reconstruction possible.

The overall picture reflects positive performance for the hit reconstruction, where most cells have values exceeding 97%. Values at the edge of the sensor experience a reduction. This effect is trivial and connected to the method used when evaluating the expression 5.3. The area given by $\kappa\sigma_{ij}$ covers active material in the inner sector of the sensors. However, closer to the edges, the area covers spatial regions outside the active region of the sensor. This translates into a shrinkage of the probability of finding a hit, as it is impossible to reconstruct a hit outside the sensor's active material.

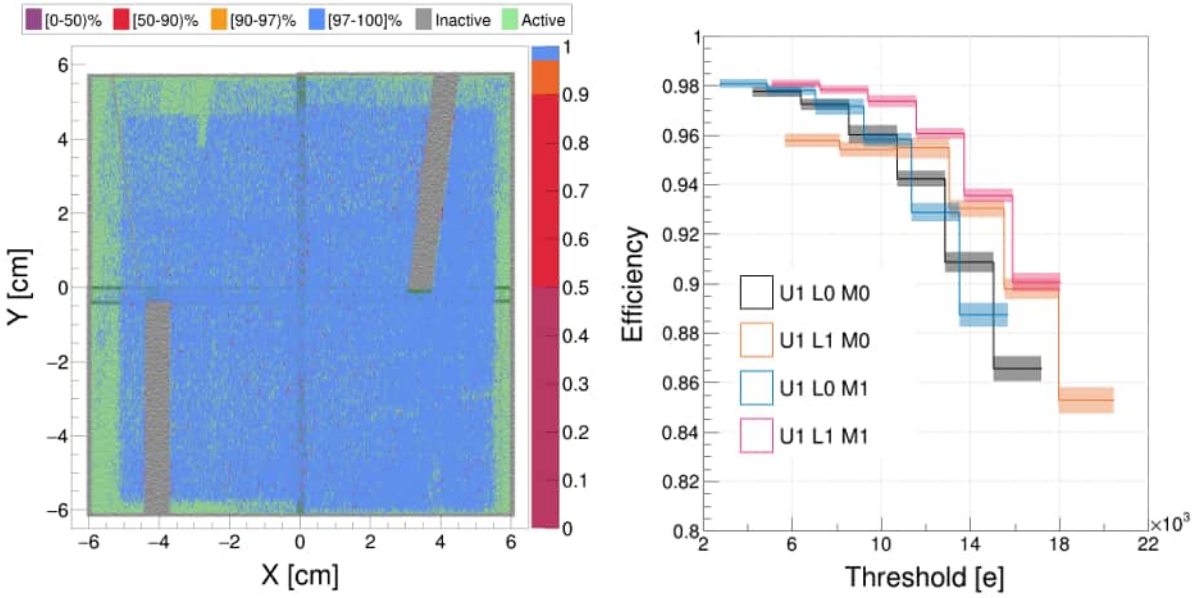

(a) (b)

Figure 5.12: a) Hit reconstruction efficiency as a function of the coordinate overlaid to a negative image of the reconstructed hits. b) Hit reconstruction efficiency as a function of the threshold.

5.3.3 Threshold dependency

Broken channels are an obvious source of inefficiencies. Relying on neighboring strips to reconstruct a particle's passage makes the estimation depend on multiple strip clusters. It has a direct link to non-perpendicular trajectories, revealing the angular dependency. Regardless of the track angle's incidence to the sensor, the charge is known to drift away from the main path and, in many cases, is partially collected by neighboring channels [44]. This effect makes the signal registered at the cluster's edges intrinsically lower. If the signal amplitude in a given strip is below the digitization threshold, the signal in that channel will not be recorded, resulting in information loss. In the worst-case scenario, channels with a threshold low enough to process the signal might be broken, losing all signals and completely missing the hit information, making it non-reconstructible.

In the first instance, the spatial resolution is affected given that the uncertainties for hit position determination become smaller the larger the cluster is [75]. Moreover, additional information is lost when the generated signal amplitude falls below thresholds. For a particle passage that generates two clusters $\{C_p, C_n\}$ in the two sides with the number of fired strips N_p, N_n, the minimal conditions for a hit to be reconstructed are:

- at least one strip from each side is functional;
- the charge collected by those functional strips is above the threshold - a Digi can be generated;
- the geometrical interception falls inside the active area sensor.

Threshold modification inherently changes the unpacked StsDigis data set. Hence, the clustering algorithm's output and the resulting reconstructed hits might differ. Therefore, performing a threshold dependency analysis requires running the entire reconstruction chain for a range of arbitrary threshold values.

The charge calibration for the mSTS setup sensors is non-homogeneous. Differential analysis is therefore required per sensor, as there is no common partition of the charge space domain for the entire setup. The whole reconstruction chain is performed for discrete threshold increments by ADC cut. Threshold dispersion is small enough within a module [58]. This allows for using a single ADC cut value for any given module, as the threshold dispersion is much smaller than that of one ADC unit. Figure 5.12b shows the **H**it **R**econstrcution **E**fficiency (HRE) for some mSTS modules as a function of ADC cuts applied.

The solid lines represent the average efficiency. The value is calculated only for sensor active areas, ignoring inefficiencies due to inactive channels. Additionally, the sample area does not cover the sensor edges. A shadow band represents the estimated error of the mean. The calculated efficiency for each pixel already has some uncertainties associated with the estimation of each term 5.12. Therefore, the shadow band does not represent all uncertainties in the efficiency analysis.

In the mSTS case, most of the primary tracks hit the sensor surface at a close-to-perpendicular angle. This was hinted by the average cluster size in Section 4.4. For a certain amount of deposited charge, the collected charge by each strip in a larger cluster decreases with the increment of the incidence angle. Such an effect could lead to a different distribution than the one shown in Figure 5.12b, where the drop in efficiency can take place at rather lower threshold values. The inability to experimentally test such a scenario within the mCBM@SIS18 setup puts this task out of the scope of this thesis.

Chapter summary

- Spatial correlations analysis was performed using the reconstructed hits from sensor pairs in different tracking stations.
- By the agreement between MC simulation in terms of geometrical correlations, STS spatial resolution should be in line with MC expectations.
- Hit-track residual analysis was performed to extract the spatial resolution.
- Due to the high presence of non-Gaussian effect, spatial resolution is obtained from three predictors: sigma of the fitted distribution, FWHM, and the average RMS for different hit coordinates.
- The spatial resolution for the x coordinate resulted between 23–29 μm, with a low bound close to the single strip cluster theoretical value.
- Analysis of the possible bias in the efficiency studies was described.
- Residual studies using the global track hinted at misalignment present in the setup.
- Residual output is used for efficiency studies, resulting in a positive picture of $> 97\,\%$ hit reconstruction efficiency.
- The efficiency analysis was extended to check the dependency with the thresholds, resulting in a sufficient operational threshold before a significant drop in the studied characteristic.

Chapter 6

Vertex Reconstruction

One of the main tasks of the STS in reconstructing a track with high precision is contributing to the reconstruction of the vertices. Some physics cases strongly depend on the performance of vertex reconstruction. While the full STS setup relies on eight stations for accurate track reconstruction, the mSTS setup is limited to only three layers.

The investigation of vertex reconstruction in detector systems is essential for the analysis of critical physical observables in heavy-ion collisions, particularly when examining rare probes such as open charm decays, hypernuclei production, and event-by-event fluctuations in the vicinity of the QCD critical point. High-precision vertex reconstruction is crucial for effectively separating secondary decay vertices from the primary collision vertex, which facilitates the identification of short-lived particles (i.e. D-mesons and hypernuclei). For such analyses, a vertex resolution of 20–100 μm is required to accurately resolve displaced decay vertices and differentiate overlapping events in high-multiplicity environments.

This thesis does not aim to validate the capabilities of the STS prototype setup in realistic scenarios, considering its current limitations. Instead, the following sections will investigate the potential for exploring related features. Typically, vertex reconstruction in fixed-target experiments hinges on a comprehensive understanding of the beam phase space and the geometric configuration of the target relative to the detector. The next logical step is to focus on beam spot reconstruction.

6.1 Beam spot reconstruction

Section 2.2 elaborated on the mCBM@SIS18 configuration, detailing the role of components such as the T0 detector situated within the beam trajectory. Some negligible beam losses prior to reaching the Ni target can be attributed to the various instrumentation and mechanical assemblies associated with the beam pipe. The experimental setup features different planes hosting material that inevitably interacts with the beam. Beam spot reconstruction can be executed independently for these planes. Table 6.1 summarizes the labels that will be used to refer to those.

Table 6.1: Labeling for different mCBM cave targets.

Description	**Label**
Window of the beam diagnostic chamber	K1
Bmon prototype 2024	B1
Upstream window of the target chamber	K0
Bmon detector(T0)	T0
Target (Ni)	Ni

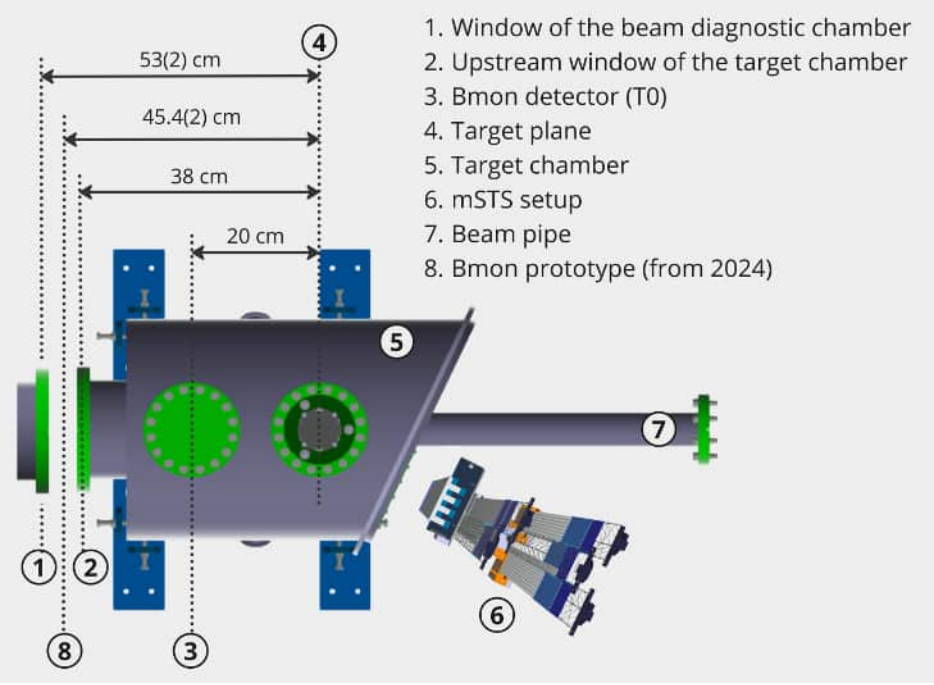

Figure 6.1: Target Chamber scheme of the mCBM setup highlighting the planes of interest for secondary beam interaction points.

The three objects positioned upstream of the primary target (nickel) will be designated as secondary targets. The detection system's aperture becomes narrower for these secondary

targets. Additionally, the material densities (iron for the pipe flanges, carbon for the diamond counter, and nickel for the primary target) contribute the most to the difference in multiplicities for those interaction planes. Consequently, direct comparisons of the beam spot distributions across different target planes are complex and require careful consideration.

The quality of the track plays a crucial role in beam spot reconstruction. Knowing the preliminary status of the alignment, some beam spot features can be obtained so that the alignment effects can be partially neglected. The upcoming sections will address this in detail.

6.1.1 Beam spot by T0

The T0 detector plays a critical role in the mCBM setup, serving primarily as a seed detector for various configurations of the offline event builder, as discussed in section 3.7. It is also essential for Time-of-Flight (TOF) calibration. The diamond counter, consisting of 16 vertical strips, provides insights into the beam profile along the x-axis. This capability allows for estimating the beam's focal position and monitoring its temporal fluctuations.

The distribution of the activated strips can be fitted using a Gaussian function, from which we can extract vital parameters: the focal position from the mean value (μ) and the beam profile's shape from the standard deviation (σ). Nonetheless, the time-dependent variations in these parameters indicate that the reported values represent time averages of these characteristics. The primary contributor to these fluctuations is linked to the beam extraction process. To mitigate this effect, it is advisable to select time slices that correspond to the central region of the spill.

Figure 6.2 shows the channel distribution of the T0 diamond detector, fitted by a Gaussian. During the detector's operation, one strip was inactive, represented by the empty bin in the histogram, and ignored during the fit analysis. The strip distribution shows a beam profile in X with a sigma of 2.41 strips. Geometrical characteristics of T0 are well known [86], having an active area of 10 mm (X) $\times$ 10 mm (Y) $\times$ 70 μm (thickness) (16 strips, each 450 μm wide). This leads to single strip coverage of $\delta x_{T0} = 0.625$ mm along the X direction. Table 6.2 shows the calculated position of the beam focus and the size measured by T0. Only information along the horizontal axis can be extracted, as the strips are vertical.

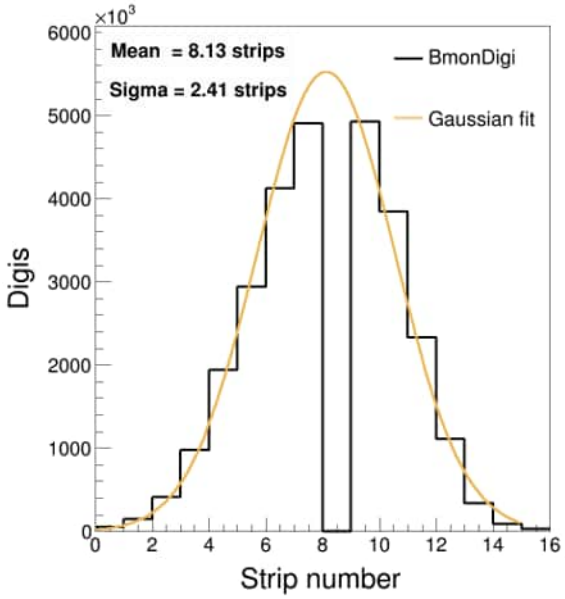

Figure 6.2: BmonDigis(T0) channel distribution, fitted by a Gaussian distribution.

Table 6.2: Fitted values of BmonDigi distribution and the calculated magnitude w.r.t T0 detector first strip.

	strips	**mm**
μ^x_{T0}	8.13	5.079
σ^x_{T0}	2.41	1.508

The fitted values of the distribution are given with respect to the first strip of the T0 detector. Assuming a coordinate system centered with T0 and a z-axis perpendicular to the sensor surface, the time-averaged beam focus would fall at 790 μm. Uncertainties related to the fitting ($\sim 10^{-4}\delta x_{T0}$ mm) are negligible compared to the systematic uncertainties related to the estimation of strip coverage.

6.1.2 Beam spot using STS tracks

Using only the `StsHit` combinatorial to form tracks is a feasible option. However, it is crucial to note that within the CBMROOT software, `StsTrack` object construction goes beyond the simplistic combination of `StsHit`. Yet, by definition, two `StsHit` are still a collection of hits that might belong to a real track. For the sake of simplicity, tracklets out of two `StsHit` will also be referred to as `StsTrack`. There are ways to differentiate between a fake combination and a real one; this is the task of the CBM tracking algorithm and will be used in the next section.

When using only two tracking stations, the two-hits approach should present a strong combinatorial background caused by the high fake rate, with the high noise levels of some modules in the mSTS setup, as already discussed in Section 4.2. The process of `StsTrack` building takes place within the pre-built CbmEvent scope, where stringent event selection is applied. The more straightforward scenario is found by selecting events with only one `StsHit` in each layer. It is a sufficient condition to build a `StsTrack` and simultaneously strongly suppress the combinatorial background typical for high multiplicity events. Later on, this condition might be relaxed and instead apply charge cuts to `StsHit`, as noise hits are usually low in amplitude (see Section 4.2).

The beam spot reconstruction is done by two-hit `StsTrack` extrapolation to the target planes. The rotation of these planes must be considered as the origin of the tracks is estimated as the interception point of the extrapolated track t_{ij} with the target planes given by equations 6.3. Due to the absence of a magnetic field, the `StsTrack` model is a 3D line defined by two `StsHit` on each of the two mSTS detection layers. Such a track finds parametric representation by equations 6.1.

$$\begin{aligned} x &= h_i^x + \alpha t_{ij}^x \\ y &= h_i^y + \alpha t_{ij}^y \\ z &= \alpha \end{aligned} \qquad \begin{aligned} h_i &: (x_i, y_i, z_i) \\ h_j &: (x_i, y_i, z_j) \\ t_{ij} &: (\tfrac{\Delta x}{\Delta z}, \tfrac{\Delta y}{\Delta z}, 1) \end{aligned} \tag{6.1}$$

To define a target plane is enough to specify the normal vector to its surface n and any point that belongs to it; for convenience, it has been selected such that the coordinates represent the geometrical center of the secondary targets 6.3. All target planes, as they are parallel to each other and perpendicular to the beam axis, share the same normal vector, obtained from a rotation along the y-axis by 25° with respect to the coordinate system of the mCBM setup 6.2. The distance relative to the target plane is denoted by d_{T0}, d_{K0}, d_{B1}, d_{K1}.

$$\vec{n} = R_y(\theta = 25^\circ) \begin{pmatrix} 0 \\ 0 \\ 1 \end{pmatrix} = \begin{pmatrix} \cos\theta & 0 & \sin\theta \\ 0 & 1 & 0 \\ -\sin\theta & 0 & \cos\theta \end{pmatrix} \begin{pmatrix} 0 \\ 0 \\ 1 \end{pmatrix} = \begin{pmatrix} \sin\theta \\ 0 \\ \cos\theta \end{pmatrix} \tag{6.2}$$

$$\vec{r} = \vec{O} + \beta\vec{n} \tag{6.3}$$

$$\vec{O}_{Ni} = (0;0;0) \tag{6.4}$$

$$\vec{O}_{T0} = (d_{T0}R_{13}\ ;\ 0\ ;\ d_{T0}R_{33}) \tag{6.5}$$

$$\vec{O}_{K0} = (d_{K0}R_{13}\ ;\ 0\ ;\ d_{K0}R_{33}) \tag{6.6}$$

$$\vec{O}_{B1} = (d_{B1}R_{13}\ ;\ 0\ ;\ d_{B1}R_{33}) \tag{6.7}$$

$$\vec{O}_{K1} = (d_{K1}R_{13}\ ;\ 0\ ;\ d_{K1}R_{33}) \tag{6.8}$$

The track's interception with the plane has a trivial solution. These extrapolations are based on the assumption that the track originates from the primary vertex out of the interaction of the beam particles with the target material. As a consequence, secondary tracks will be an unavoidable source of bias.

The multi-element layer configuration facilitates differential beam spot reconstruction utilizing sensor pairs from distinct stations. As depicted in Figure 6.3, the beam spot reconstruction at the primary target plane is achieved by mSTS U1:U2. Two-dimensional distributions are constructed using sensor pairs, with the sensors in the station closest to the target arranged vertically and the corresponding sensors from the second station arranged horizontally. It is important to note that the absence of data in gray boxes does not indicate a lack of `StsTrack` extrapolations for these pairs; rather, it signifies that the intersection of tracks with the target does not intersect the designated sampling area defined as $\forall x, y : x \in [-2.5, +2.5] \wedge y \in [-2.5, +2.5]$, from which only primary tracks are expected[1].

Although all distributions seem centered, individual sensor pair distributions are fitted with a two-dimensional multivariate Gaussian distribution to determine their center and widths. The upcoming section will focus on determining the distribution position.

Figure 6.4a shows the result of merging all contributions from different sensor pairs. The spread of the merged distribution reflects the status of the preliminary alignment. In Section 6.1.3, a formal definition for spread is given. Residual for the transversal coordinates (x,y) and the distance from distribution centers (r) is presented in Figure 6.4b. Different sensor pairs are arranged horizontally. The residual values are small compared to the beam profile.

[1] the empty column reflects the absence of reconstructed hit for module U2 L2 M1

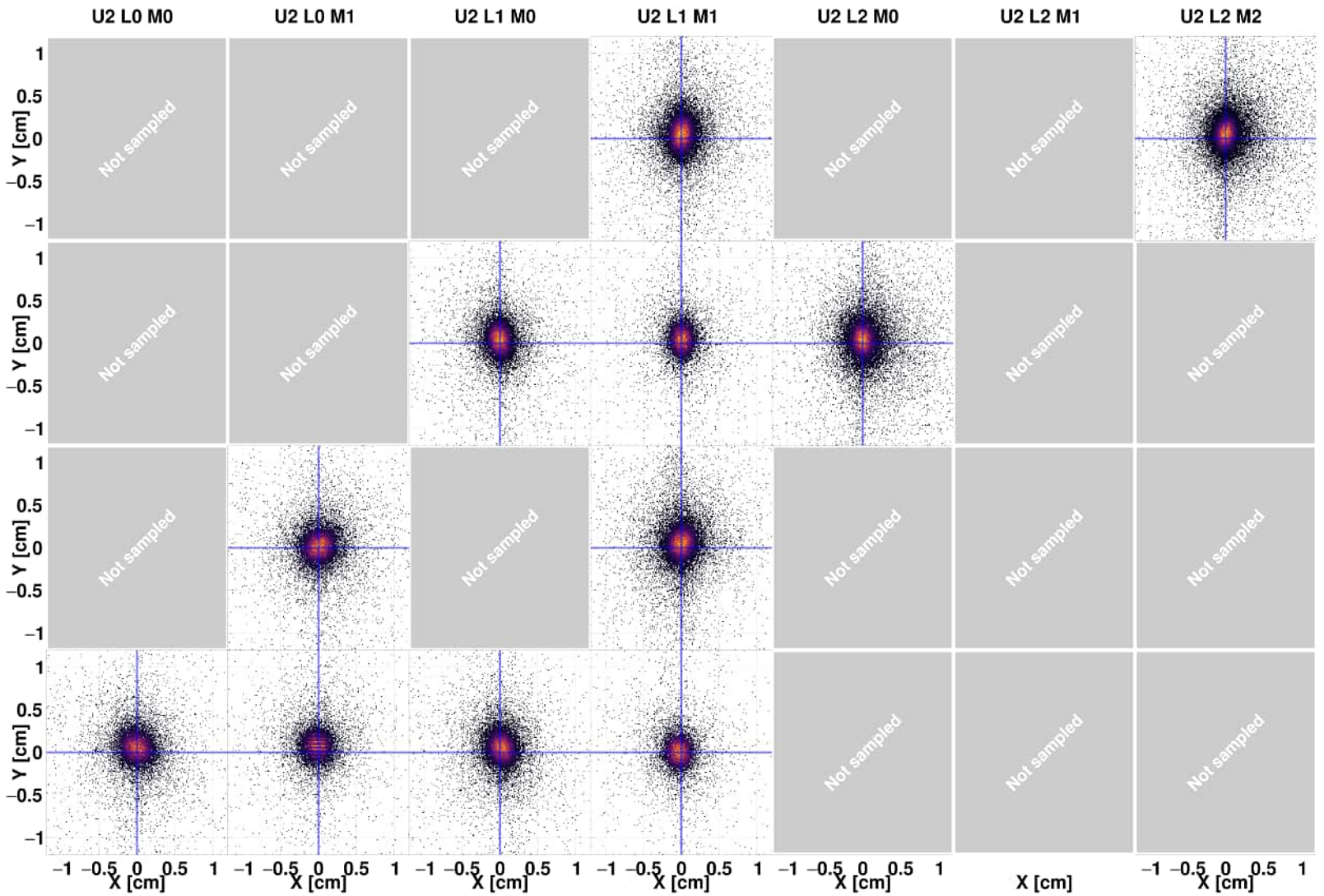

Figure 6.3: Reconstructed beam spot by sensor pairs from mSTS U1:U2.

The order of magnitude of misalignment can be estimated using geometric principles. If the offset observed for any sensor pair were attributed entirely to the misalignment of only one sensor pair, the misalignment would be a few hundred microns. This relationship depended on the z-position of the sensors, similarly to Section 5.1.

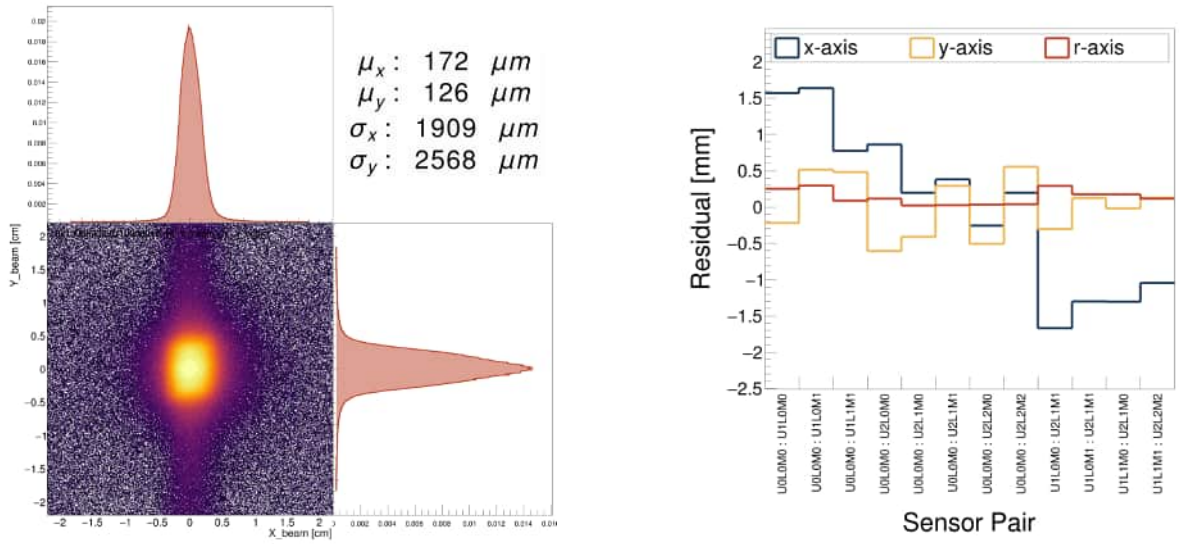

(a) (b)

Figure 6.4: a) Reconstructed beam spot at Ni-target plane by mSTS. b) Residual components of the reconstructed beam spot at the Ni-target plane by individual sensor pair.

6.1.3 mSTS self-alignment

Although the assembly precision of the mSTS setup was on the order of 150 μm, the positioning of the mSTS box relative to the target position had to be measured due to inconsistencies in the preliminary beam spot reconstruction. This led to an attempt at data-driven alignment of individual mSTS components.

As a starting point, MC simulations of the expected beam spot reconstruction shed light on some interesting features of the STS in the mCBM configuration. The exploration begins by analyzing the behavior of the reconstructed beam spots for different displacements Δz of the mSTS box, or equivalently, the displacements applied to the target plane. The following geometrical features were learned:

- Mean values of the 2D distribution behave linearly as a function of Δz, and X, Y distribution intercepts do not coincide with the origin.
- Sigma value approximately behave as $P_2(\Delta z)$, reaching a minimum for $\Delta z \neq 0$, and depending on the sensor pair.

This arbitrary shift along the z-axis is equivalent to misaligning the mSTS setup by moving it upstream or downstream. The first finding was that mean values are non-zero for $\Delta z = 0$. It implies that for perfect alignment, the expected position of the 2D distribution for beam spot reconstruction will differ among individual sensor pair combinations and will not be zero. Similarly, it happens with the sigma distribution as a function of Δz, where the minimum does not correspond to no translation.

Figure 6.5 shows the behavior of the distribution center (a) and the sigma distribution (b) for one sensor pair after scanning through different z-planes. One might expect $P_2(\Delta z)$ to reach a minimum for sigma values when no misalignment is introduced ($\Delta z = 0$), as if two sensors work as a pair of lenses focusing or defocusing the beam spot. Although the sensor pair behaves in this manner, the source to focus on is not isotropic. The fact that the mCBM setup is rotated and the collision is boosted makes this intuitive scenario misleading. Differences among sensor pairs are directly related to the acceptance. However, through simulations, it is possible to determine the expected position of the reconstructed beam spot by individual sensor pairs and account for it in further procedures. Knowing the

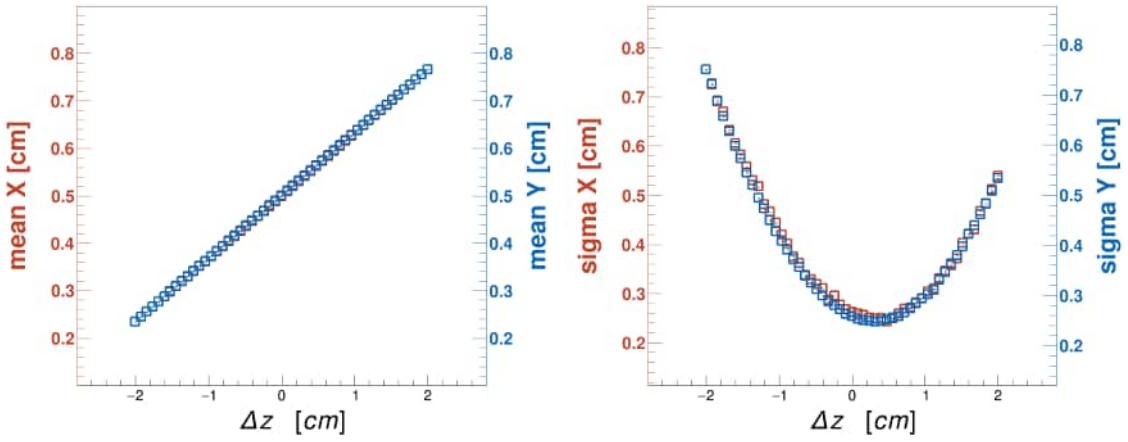

(a) (b)

Figure 6.5: Fitted mean and sigma values of the beam spot reconstruction for different arbitrary shifts along the z-axis of the target plane.

information discussed in the above paragraph, designing a simple algorithm to preliminarily self-align the mSTS setup with the beam spot as a reference is possible. This section will be restricted to misalignment due to translation only.

Any arbitrary shift $\Delta\bar{x}_{im(jn)} = (\Delta x_{im(jn)}, \Delta y_{im(jn)}, \Delta z_{im(jn)})$ to the mSTS sensor $s_{im}(s_{jn})$ will impact only the reconstructed beam spot corresponding to such sensor pair. This distribution is characterized by the distribution center $\boldsymbol{\mu}_{im}^{jn}$ and the shape given by $\boldsymbol{\sigma}_{im}^{jn}$. In general, both quantities will be a function of the translation $\boldsymbol{\mu}_{im}^{jn}(\Delta\bar{x}_{im}, \Delta\bar{x}_{jn})$ and $\boldsymbol{\sigma}_{im}^{jn}(\Delta\bar{x}_{im}, \Delta\bar{x}_{jn})$.

The distribution centers can be corrected by the MC expected position: $\boldsymbol{\mu}^{jn}_{im}(\Delta\bar{x}_{im}, \Delta\bar{x}_{jn}) - \boldsymbol{\mu}^{jn}_{imMC}(\Delta\bar{x}_{im}, \Delta\bar{x}_{jn}) = 0$. Therefore, the condition 6.9 is also true, where N_{mSTS} is the number of sensor pairs on the mSTS setup:

$$(0,0) = \boldsymbol{\mu}_{mSTS} = \frac{1}{N_{mSTS}} \sum_{im,jn} [\boldsymbol{\mu}^{jn}_{im}(\Delta\bar{x}_{im}, \Delta\bar{x}_{jn}) - \boldsymbol{\mu}^{jn}_{imMC}(\Delta\bar{x}_{im}, \Delta\bar{x}_{jn})] \tag{6.9}$$

The condition 6.9 is insufficient for alignment. However, minimizing the spread relative to the calculated $\boldsymbol{\mu}_{mSTS}$ is enough. The beam spot reconstruction spread is a define by 6.10 as a RMS of $\boldsymbol{\mu}^{jn}_{im}(\Delta\bar{x}_{im}, \Delta\bar{x}_{jn})$. The T matrix, is the set of translations, being $T_{im} = \Delta\bar{x}_{im}$:

$$S(T) = \sqrt{\frac{\sum [\boldsymbol{\mu}^{jn}_{im}(\Delta\bar{x}_{im}, \Delta\bar{x}_{jn}) - \boldsymbol{\mu}^{jn}_{imMC}(\Delta\bar{x}_{im}, \Delta\bar{x}_{jn}) - \boldsymbol{\mu}_{mSTS}]^2}{N_{mSTS}}} \tag{6.10}$$

Therefore, the criterion for considering the setup aligned is to find the set of translations such that S(T) reaches a minimum. Multi-parameter optimization is a pillar of most state-of-the-art machine learning algorithms. One widely used and well-studied approach for such situations is the Gradient Descent algorithm [88, 89].

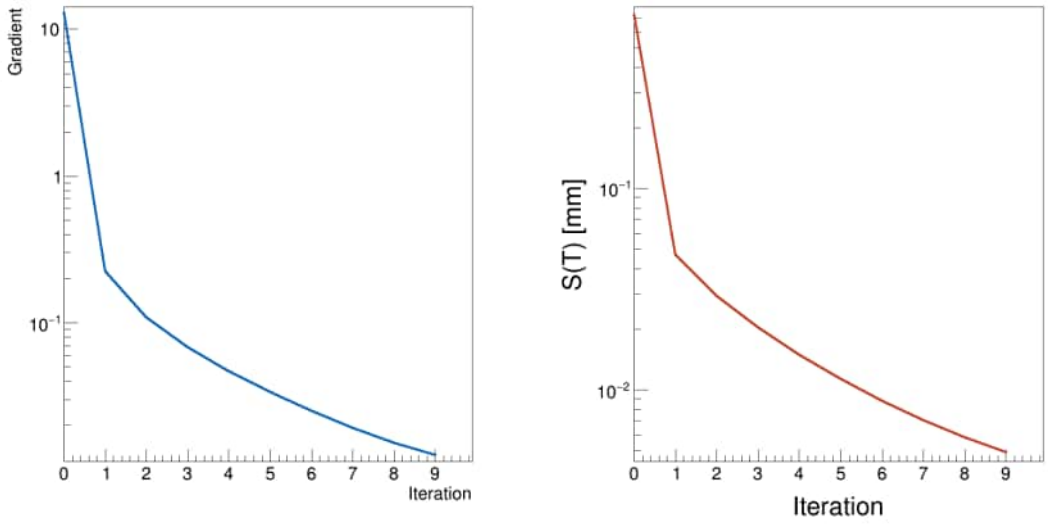

(a) (b)

Figure 6.6: Learning curves of the minimization algorithm. (a) Gradient; (b) target function (spread).

Figure 6.6 shows the performance in terms of convergence of the error given by the gradient (Figure 6.6a) and the S target function (Figure 6.6b). After a few iterations, alignment parameters are found, such as the beam spot spread in the order 50 μm, demonstrating the

method's effectiveness. However, the uniqueness of the parameter set that minimized the spread can be questioned. The lack of solid constraints given by proper cave metrology makes the current approach practical for a preliminary alignment of the entire mSTS setup. The internal alignment of STS elements remains within the assembly precision 150 μm.

Nevertheless, using the same mathematical background, the minimization algorithm is implemented for a different cost function. Different approaches are being explored for CBM alignment. A track-based alignment method aimed at minimizing χ^2, a widely utilized objective function, is currently being developed by [90].

Comparing beam spot profiles

While the differential beam spot reconstruction can be extended to all secondary targets in the cave, only the T0 detector incorporates instrumentation that enables direct comparison. The individual X projection of the beam spot reconstruction at the T0 z-plane can be compared to the values extracted from the beam shape inspection in Section 6.1.1. The same method of track extrapolation is used to build such a distribution. The mSTS setup is not designed to reconstruct the beam spot at such a plane. However, extracting the beam spot position is feasible.

Figure 6.7a shows the mean (dashed horizontal line) and the sigma (shadow yellow band) of the beam profile reconstructed by the T0 detector. Additionally, these quantities estimated by different sensor pairs are overlaid. The central line represents the mean value of the observed peak, while the estimated sigma determines the box height. Although the mSTS sigma bands overlap with the estimation of the T0 detector, a systematic shift towards larger values is appreciable.

The statistical uncertainties of the peak fitting are negligible, so such a discrepancy cannot be attributed to them. For each extrapolation, there is an intrinsic propagation of error related to the hit resolution of the STS sensor. The uncertainty of the hit position determination is in the order of 10-20 μm for the average cluster size. It translates to $\delta x_{T0} \sim \mathcal{O}(50\,\mu\text{m})$, which still cannot account for the few millimeters difference.

This effect can be caused by two types of misalignment that would have an equivalent impact. The first one could be a rotation. The second one is a relative offset of mSTS layers along the x-axis. The alignment procedure for CBM is incipient, and rotations were not considered when reconstructing the corresponding data. However, the difference in the prediction by distinct sensors allowed for identifying and resolving incongruences in the geometrical description.

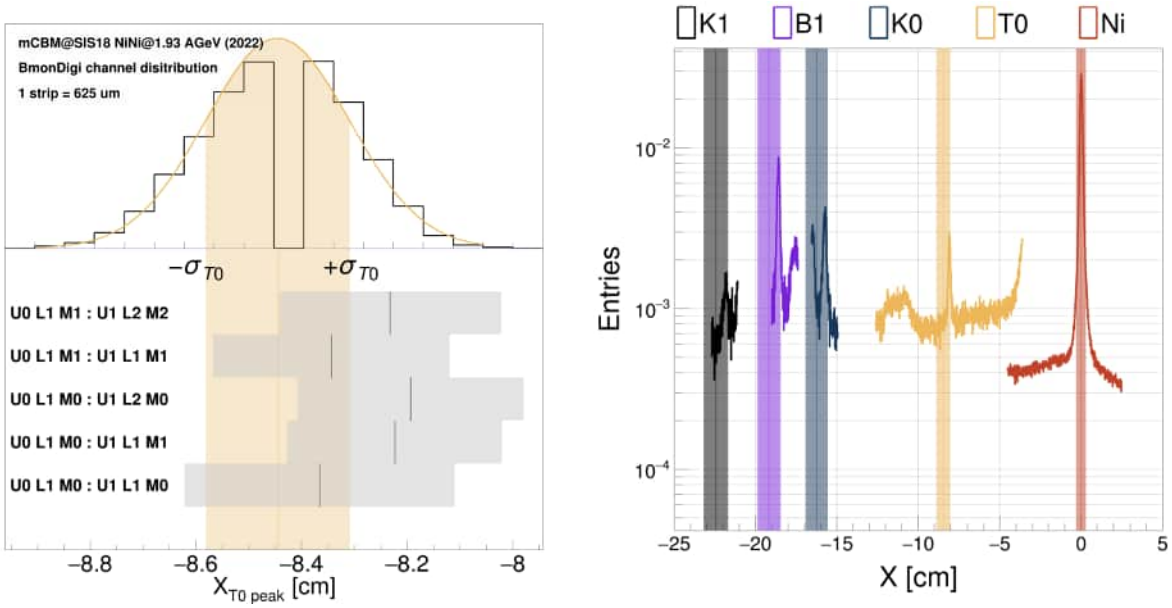

(a) (b)

Figure 6.7: (a) Estimated beam spot x position at T0 z-plane by mSTS sensor pairs compared to BMON estimation. (b) Projection to the mCBM x-axis for different secondary targets at the mCBM cave.

mCBM cave tomography

The beam spot reconstruction methodology is applicable for analyzing and treating all secondary target planes. The sampling range is expanded enough to cover the expected position of the peaks corresponding to the secondary beam interactions following equation 6.3. Different structures can be focused by adjusting the z-position of the extrapolation plane, depending on where the tracks originated. Therefore, structures corresponding to elements listed in Table 6.1 are expected to arise when the track extrapolation is performed for each target plane.

Figure 6.7b shows the X projection of the reconstructed beam spot distributions at each target plane. A vertical dashed line represents the nominal position of each target. The width of each band is proportional to the uncertainty due to track extrapolation and the measurement of the position of each plane. Each projection contains a distorted contribution from the other targets. Consequently, the displayed distributions have been drawn around their expected position.

Similarly to the previous section, not only T0 but all the observed secondary target distribution systematically shit towards larger x values away from its nominal position. The rotation angle necessary to minimize the distances between the observed and the expected

peak locations is approximately $\sim 1^{\circ}$. This ratio would be equivalent to a relative offset between the stations of 2 mm. The second case is improbable due to the assembly precision of the internal element of the mSTS setup.

6.2 3D event vertex reconstruction

After a track is reconstructed, further analysis is needed to classify it as primary or secondary. Contrary to MC simulations, where full information is available for any track, experimenters require methods to infer information such as the track vertex. In the case of primary tracks, the track vertex will match the event vertex, as primary tracks are, by definition, those generated directly from the event. However, event products might produce additional tracks, generating extra vertices. Thus, all secondary track vertices will be called secondary vertices, i.e., proton and pion track vertices from a *Lambda* decay (decay vertex). This definition made it obvious that all primary tracks will share the same track vertex for a single event, defining the event vertex. Although this thesis does not pretend to disentangle primary from secondary, applying geometrical contrarians reduces the bias introduced by secondary when estimating the event vertex. This section exposes track-based 3D event vertex reconstruction using a **P**oint of **C**losest **A**pproach (PCA) approximation for multiple tracks.

The simplest case that allows event vertex reconstruction is two primary tracks. As the primary particles are produced in the same space-time point, both tracks should intercept, and such a point is the vertex of the given process and the corresponding event. The uncertainties related to track parameters and misalignment will propagate to the PCA of any set of tracks. The PCA will represent the best guess of the common origin for two tracks. Two tracks whose distance to the found vertex is much larger than the vertex resolution are not physically bound to this point and can safely be assumed not to belong to the same event vertex. This usually happens when mixing primary and secondary tracks from far-apart vertices. A residual analysis between the track and the vertex candidate will be performed.

For any events with two tracks, the event vertex is well defined by the PCA of those. However, when the number of tracks is larger than two, the estimation of the event vertex is done by averaging the position of all valid PCA. A valid PCA satisfies that the distance between the point and tracks involved is not much larger than the vertex resolution. In the first iteration, there is no prior knowledge about vertex resolution, and all track pairs are considered in the analysis.

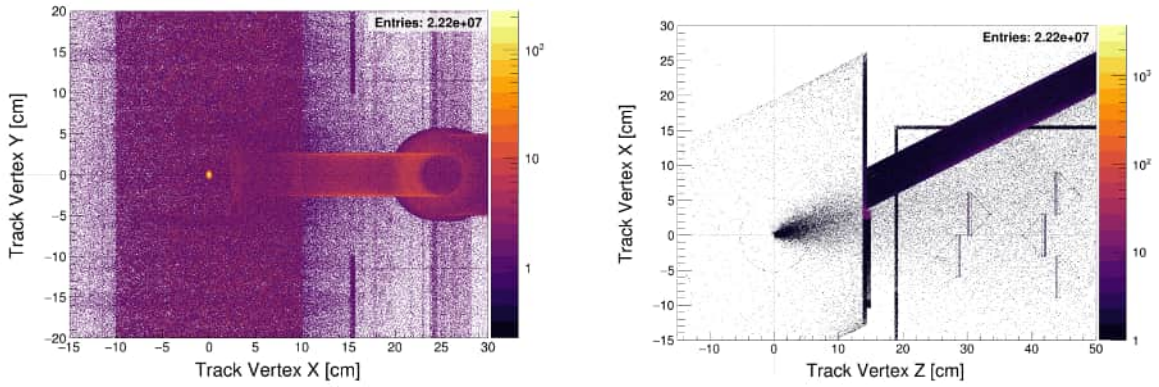

(a) (b)

Figure 6.8: Orthographic projection of the PCA distribution for MC simulations: a) XY, b) XZ.

Figure 6.8 shows the projected distribution of secondary track vertices of the track vertex for MC simulations. Those vertices, as expected, are produced mainly by the interaction of the reaction product with the material budget of the setup. As can be seen, some of the secondaries are produced within the sensor material and support structures. However, a significant fraction is produced within the target chamber and the mSTS enclosure panels.

Figure 6.9 shows the XY (a) and XZ, YZ (b) orthographic projections of the PCA distribution of all track pairs. This includes real vertices as well as the combinatorial. The beam-target interaction point, where most primary tracks are produced, is well-centered in the XY plane. The shape of such agrees with the reconstructed beam spot assessed in the previous section. Such an agreement represents a cross-validation of both approaches.

In the case of the XZ projection, structures corresponding to secondary vertices produced at the mSTS setup elements have been highlighted. The observed structure z coordinates match the nominal position of the mSTS detection layers represented by a gray band. The structure corresponding to the first detection layer is not visible due to the combinatorial population in the region.

The XZ projection in the upstream region ($z < 0$) also features interesting structures. The occurrence of such is led by the vertices produced by the secondary targets in the mCBM@SIS18 setup. Figure 6.10 shows the XZ distribution where structures have been labeled accordingly in the region of interest. Observing these structures is feasible due to the low combinatorial around the nominal position of the secondary targets. However, due to the small acceptance, the position determination is strongly impacted by statistical fluctuations.

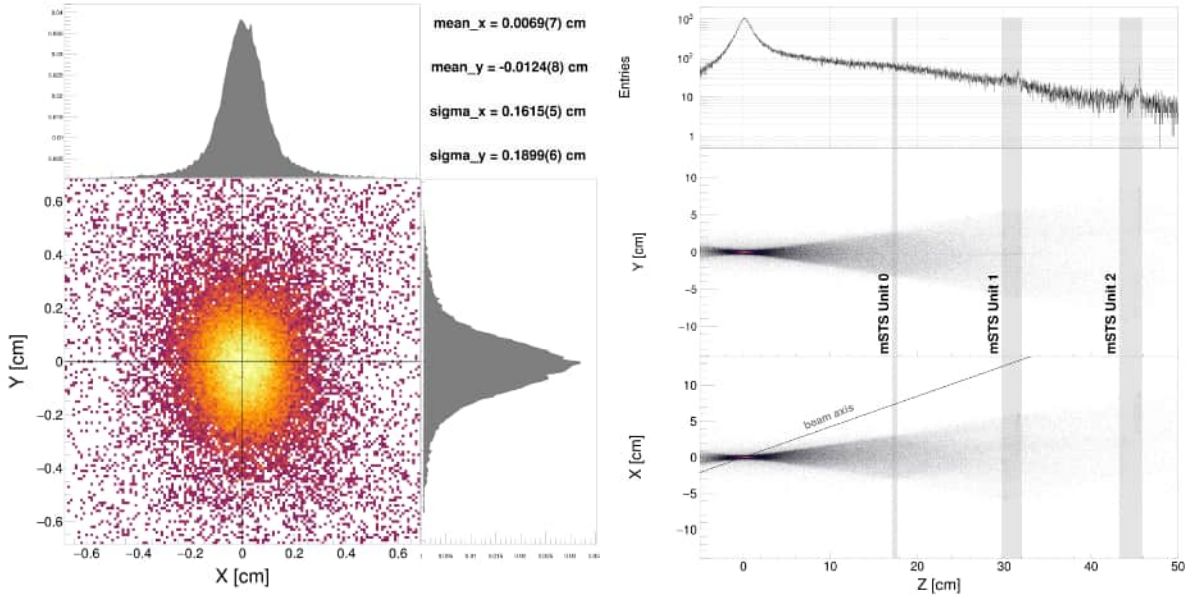

(a) (b)

Figure 6.9: Orthographic projection of the PCA distribution for measured data: a) XY with estimated means and sigmas from a multivariate Gaussian fit; b) From top to bottom: PCA z-coordinate distribution, YZ and XZ projections. The nominal position of the mSTS detection layers is highlighted.

A new transformation is applied to compare the observed position of the different structures with respect to their nominal positions. Every point (z_i, x_i) in Figure 6.10a is mapped to a 1D distribution. The transformation consists of determining the angle between the line (z') that bisects the azimuthal acceptance of the mSTS and the z-axis in the laboratory frame. The transformation is equivalent to translating the origin to (z_i, x_i), and rotating z' around the y-axis by the angle in question.

Only points in the vicinity of the nominal position of secondary targets are included in the mapping to avoid contamination of secondary vertices produced between the target and the setup. This might be understood as playing with a set of lenses and changing the focus point.

Figure 6.10b illustrates the resulting distribution. Additionally, color bands are drawn for the nominal position of the targets (see Table 6.1). The width of the bands reflects the beam spot size transformed to its equivalent angle. This angle becomes smaller, the farther from the origin of the coordinate the point (z_i, x_i) is. Similarly to the effect observed in section 6.1.3, the observed peaks systematically sit towards smaller angles. The rotation around the y-axis that minimizes the residual between the observed and the measured position of the peaks in Figure 6.10b is $\sim 1^\circ$.

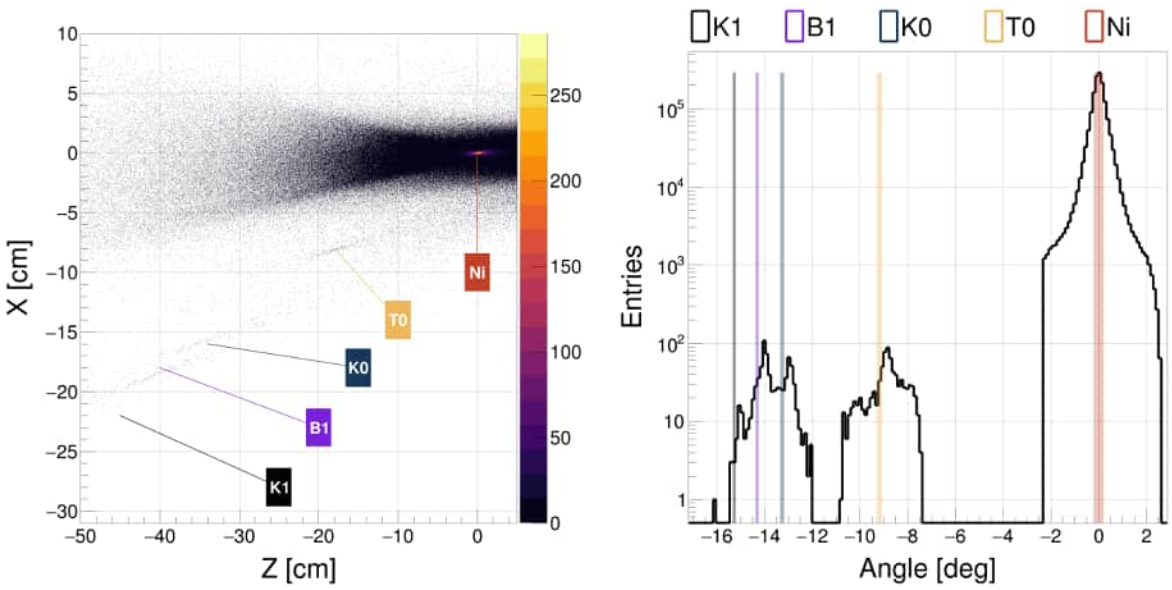

(a) (b)

Figure 6.10: PCA distribution for secondary targets at mCBM@SIS18 cave. a) XZ projection with label nominal positions. b) Mapping of the 2-dimensional PCA distribution to $\sphericalangle(z'z)$.

6.2.1 Impact of Track selection criteria on the determination of the event vertex

CBM aims to reconstruct rare probes that need a tremendous amount of statistics. Applied cuts, such as event selection, must rely on a robust and reliable per-event analysis, ensuring that valuable collected data is not discarded. Track selection criteria are inherent to the event selection process.

Figure 6.11 shows the track multiplicity for different selection criteria. Notice that for the weakest requirement among all, two `StsHit` attached to the global track have already cut away a significant part of the distribution tail for all tracks. For mCBM configuration, the CA tracking requires at least a hit in three consecutive stations. This explains the odd behavior at low values of the total number of global tracks. The requirement of at least two `StsHit` and two `TrdHit` still gives a chance to the first TRD layer not to be hit, and therefore, even with four reconstructed hits, the condition of three consecutive layers is not fulfilled. Notice that the first bin of the distribution corresponds to no global tracks found. All distributions were constructed by processing the same amount of $\sim 1.1 \times 10^7$ events. The most probable value of global reconstructed tracks sits at four tracks, while for any of the groups, the distribution quickly decreases for track multiplicity. Hence, it is a priority to balance how many hits and from which available systems are required to improve vertex

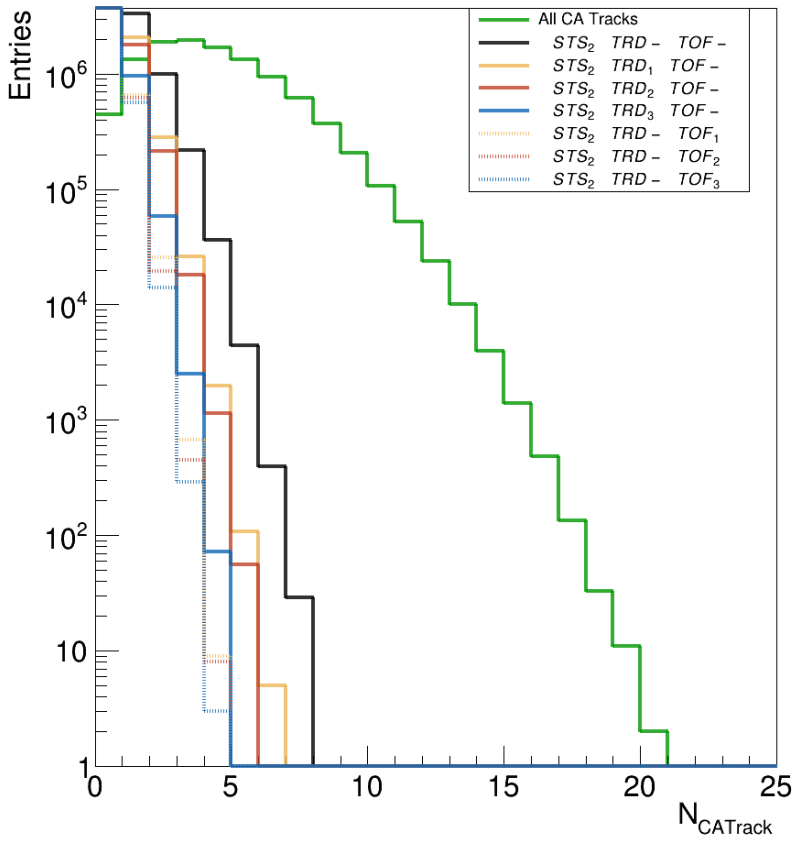

Figure 6.11: Normalized track multiplicity for track criteria classes.

capabilities. For this purpose, residual analysis was performed to explore the expected vertex resolution. The vertex residual is a 3-vector defined by the **D**istance of **C**losest **A**pproach (DCA).

Figure 6.12 shows the normalized DCA distributions of different track selection groups for the transverse coordinates. The normalization factor is selected so that all distributions share the same maximum value, making visual comparison easier. Although all distributions display a similar behavior, it is evident that the distribution width depends on the criteria. The minimum of two or three `TofHit` requirements does not significantly improve the vertex residual for the X and Y coordinates. On the other hand, those are precisely the selection criteria with smaller distribution widths. Notice that STS_2TRD-TOF_2 implies the existence of either an additional hit at TRD or TOF, so the three consecutive layers condition is met. In Appendix C, Cartesian projections of vertex reconstruction using each track selection criterion can be found for further inspection.

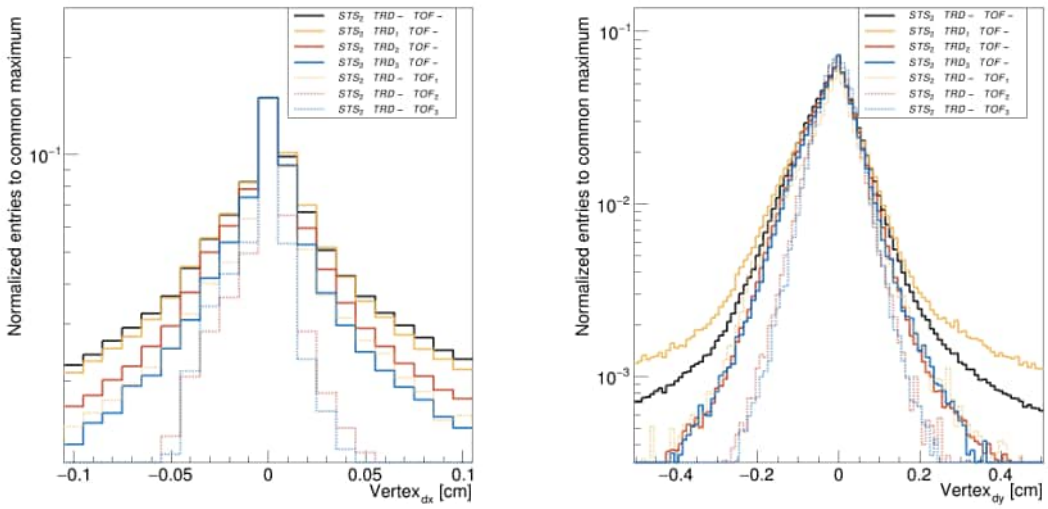

Figure 6.12: DCA distribution for track criteria classes.

A quantitative comparison between distribution widths by FWHM is reported in table 6.3. These values estimate the uncertainties from statistical effects and secondary tracks mixing. These distributions are also impacted by the uncertainties of the track parameters derived from the fitting model.

Table 6.3: FWHM of DCA component distribution.

Track type	$\boldsymbol{X_{FWHM}}$[mm]	$\boldsymbol{Y_{FWHM}}$[mm]	$\boldsymbol{Z_{FWHM}}$[mm]
STS_2TRD-TOF-	0.3	1.0	0.1
STS_2TRD_1TOF-	0.3	0.9	0.1
STS_2TRD_2TOF-	0.3	0.9	0.1
STS_2TRD_3TOF-	0.2	0.8	0.1
STS_2TRD-TOF_1	0.2	0.6	0.1
STS_2TRD-TOF_2	0.1	0.9	0.1
STS_2TRD-TOF_3	0.1	0.8	0.1
STS_3TRD-TOF_3	0.05	0.06	0.1

6.3 Chapter summary

- Beam spot reconstruction is performed by track extrapolation using two `StsHit`.
- Beam spot X projection was characterized using the T0 detector.
- Measurement X beam spot size by mSTS detector matches the estimation of the T0 detector.
- An alignment procedure was developed using beam spot reconstruction as the figure of merit, minimizing the spread of different sensor pair predictions by utilizing the gradient descent method.
- The final translations are consistent with the assembly precision of 100 μm and with the constraints from the mechanical units.
- A simplified event-by-event vertex reconstruction algorithm was designed and implemented. It is based on the average point of closest approach of multiple tracks.
- The event vertex reconstruction reproduces the geometrical features extracted from the beam spot reconstruction.
- The DCA resolution was estimated from the FWHM of the residual distribution, resulting in less than 60 μm for the transversal coordinates.

Chapter 7

Conclusions

The Silicon Tracking System (STS) is the central tracking detector of the CBM experiment, playing a crucial role in charged particle trajectory reconstruction and momentum determination. Designed to handle the high track densities of up to $\sim 10^3$ charged particles per event, the STS faces stringent performance requirements, including a position resolution better than $30\,\mu$m, a time resolution below 10 ns, and a low material budget of $0.3\,\% - 1.4\,\%$ X_0 per station. These demanding specifications are essential to ensure high tracking efficiency ($> 95\%$) and precise momentum resolution ($< 2\%$) necessary for reconstructing complex event topologies, such as weak decays of strange and charmed particles.

This thesis focuses on the evaluation of the operational performance of a prototype STS system under realistic experimental conditions. The system was tested in a heavy-ion collision environment at beam energies of $1 - 2$ AGeV using the mCBM setup at SIS18. Key performance metrics such as precision track and vertex reconstruction were validated through analysis of hit-track residuals, vertex position, and transverse impact parameter resolutions, aligning well with theoretical expectations for sensors with a $50\,\mu$m strip pitch. The timing resolution achieved was 5 ns.

Operating with low thresholds (3-–$4\,\sigma$ of noise), the detector exhibited a low dark rate of ~ 0.5 kHit/s/channel, remaining well below 1% of the expected saturation bandwidth. Under these conditions, a high hit reconstruction efficiency of 98% was achieved in fully functional regions, with a signal-to-noise ratio exceeding 20, affirming the system's suitability for high-rate, high-precision tracking in the CBM experiment.

Subsequent paragraphs summarise the key findings of this work, highlight the achieved performance benchmarks, and outline potential directions for further development and optimization of the STS in preparation for full-scale deployment in CBM.

Time resolution

The first part of the work presented in this thesis focuses on the development and detailed performance evaluation of the preliminary time calibration and hit reconstruction procedures in the STS detector system, addressing the core goal of establishing reliable and precise detector operations. A thorough picture of the detector's operational state was achieved by identifying problematic channels through entry distribution analysis and cross-validating them with ENC measurements from laboratory tests, thus meeting the objective of ensuring detector quality control. The implementation of a robust time calibration procedure, incorporating corrections for the time walk effect, resulted in an estimated time resolution of approximately 5 ns and better over a broad calibration range of 8–68 ke, fulfilling the aim of achieving precise time measurements essential for downstream analyses. Furthermore, the charge and cluster size distributions demonstrated the expected behavior, including observing the MIP charge peak at around 24 ke. Minor asymmetries were detected and attributed to inactive channels and pending charge calibration adjustments, underlining the comprehensive scope of the detector characterization and identifying clear paths for refinement.

Space resolution

The spatial performance of the STS was comprehensively evaluated through spatial correlation analyses between reconstructed hits across the available tracking stations within the mSTS setup, directly addressing the thesis objective of verifying the system's spatial resolution. The strong agreement between experimental data and Monte Carlo simulations regarding geometrical correlations provided solid evidence for the system's spatial fidelity. It fulfilled the goal of benchmarking the detector performance against simulations. Spatial resolution was quantified using hit-track residuals and multiple statistical predictors: the sigma of fitted distributions, FWHM, and average RMS; with the measured x-coordinate resolution falling between 23–29 μm, closely approaching the theoretical single-strip cluster limit. This result validated the design expectations and extended the thesis's reach by demonstrating operational performance under realistic beam conditions.

Hit reconstruction efficiency

Moreover, efficiency studies, which used fully reconstructed tracks as a reference to suppress background from random or fake correlations, revealed a hit reconstruction efficiency of over 97%. Additional analyses demonstrated stable detector performance across a range of operational threshold settings, further confirming the system's robustness and reliability

under realistic experimental conditions. A high hit reconstruction efficiency, exceeding 97%, is essential to ensure the overall tracking efficiency of at least 97% at high momenta and to achieve the target momentum resolution of 2% in the full-scale CBM experiment setup. Importantly, the thesis acknowledges that fundamental scenarios for non-perpendicular track incidence remain to be explored, highlighting both the reach of the current results and areas for targeted future work.

Alignment

A key objective of the thesis was to assess the STS capabilities for beam profile and vertex reconstruction, which was successfully addressed by a beam spot reconstruction method based on track extrapolation using reconstructed hits. The measured beam profile in the X direction matched independent estimations from the T0 detector, providing a crucial cross-check and demonstrating the precision and reliability of the implemented methods. An alignment procedure leveraging beam spot reconstruction across multiple sensor pairs was also developed. While the lack of constraints limited the ability to extract a unique transformation set, the procedure provided critical insights into the system's alignment status, an essential prerequisite for precision tracking.

Vertex reconstruction

The thesis introduced a simplified event vertex reconstruction algorithm to determine the average point of closest approach among multiple tracks. This method not only reproduced the geometrical characteristics observed in the beam spot analysis but also served as an independent validation of the system's spatial performance, thereby addressing the goal of demonstrating the STS's vertex reconstruction capabilities. The DCA resolution, estimated at below 60 μm for transversal coordinates based on the FWHM of the residual distribution, confirmed the high precision of the vertexing procedure and positioned the STS as a reliable tool for future beam and collision experiments.

The thesis comprehensively fulfills its main scientific and technical goals and demonstrates that the STS detector system delivers excellent performance across multiple key dimensions, including timing, spatial resolution, hit reconstruction efficiency, beam profiling, and vertexing. The developed calibration procedures and diverse analyses, implemented and included in the CBMROOT software, validate the current detector capabilities and significantly extend the system's operational envelope, laying a solid foundation for further optimizations and upgrades.

While the methodologies presented in this thesis are specifically designed for the STS de-

tector, they embody principles and techniques that can be applied universally across diverse detection systems. The structured framework encompassing calibration, reconstruction, performance evaluation, and alignment integrates empirical data with simulation cross-checks and statistical validation, forming a comprehensive approach vital for optimizing detector performance.

This systematic protocol is invaluable across various detection technologies, particularly for tracking systems where high-precision spatial and temporal measurements are crucial for effective track reconstruction, vertex finding, and subsequent physics analyses. These methodologies' versatility allows them to be adapted to a range of experimental configurations, facilitating robust detector characterization and enhancing the reliability and accuracy of particle detection initiatives.

Outlook

The measurements presented in this thesis, conducted with the small-scale mCBM setup and in the absence of a magnetic field, primarily address tracks that are nearly perpendicular to the detector planes, resulting in signal collection on one or, at most, two strips -i.e., small cluster sizes. Scenarios involving non-perpendicular tracks, where the signal may be spread over larger clusters, remain to be investigated and could exhibit a more pronounced efficiency loss at higher threshold settings.

A data-driven alignment procedure, using the beam spot as a figure of merit, was performed; although the lack of constraints limited the extraction of a unique set of transformation parameters, the results were consistent with the expected assembly precision of approximately $100\,\mu$m and mechanical constraints, providing critical insights into the system's alignment status—an essential prerequisite for precision tracking and a foundation for developing dedicated hardware and software alignment procedures in future work.

Finally, calibration of the remaining charge asymmetries will enable reliable measurement of the energy loss across the eight STS layers, unlocking new potential for particle identification through dE/dx based methods.

Future work promises to enhance the system's performance further and widen its applicability in upcoming experimental campaigns.

Appendix A

Charge vs. channel distributions

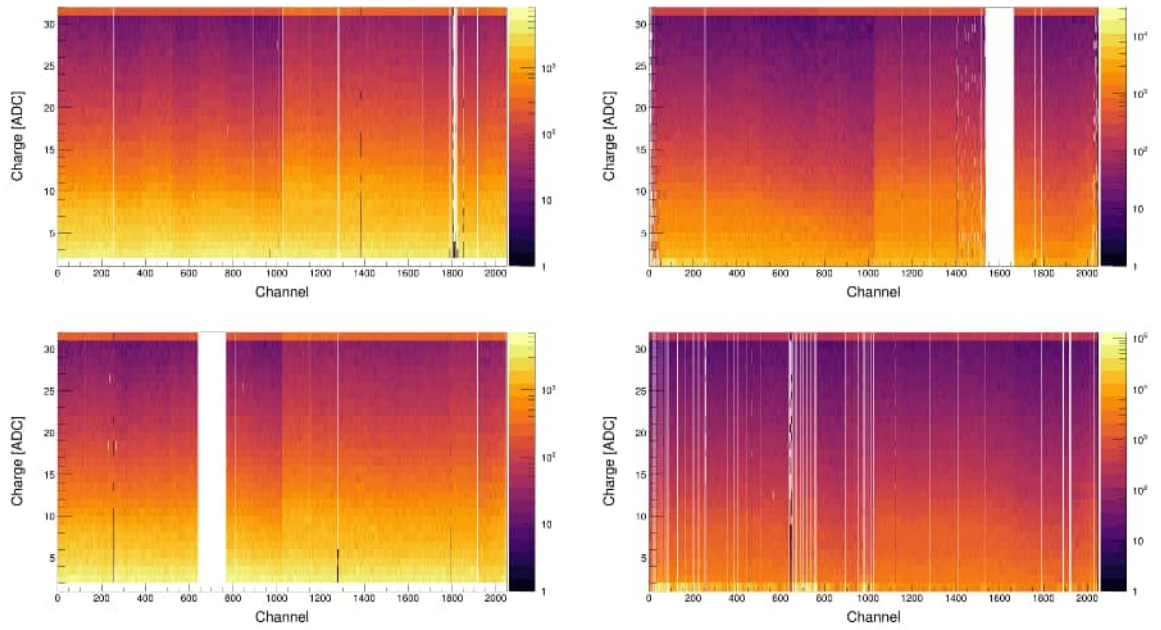

Figure A.1: Charge vs. channel distribution for mSTS second station modules.

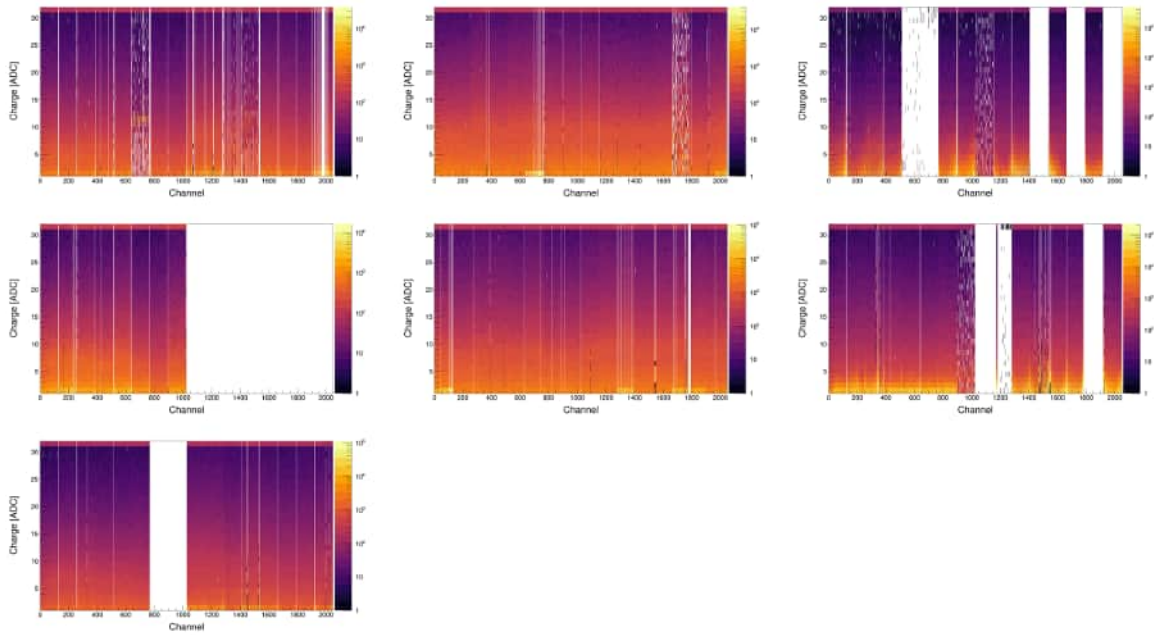

Figure A.2: Charge vs. channel distribution for mSTS third station modules.

Appendix B

Details about STS hits correlation

B.1 Uncertainty of correlation peak

The definition of a track in the absence of a magnetic field is a straight line originating at the beam spot ($\vec{O}$) and extending along the forward direction ($\vec{T}$) within the STS modules acceptance. This allows us to write the parametric equation B.1 determined by the track vertex and the hits in the STS detector planes.

$$\vec{l} = \vec{O} + t\vec{T} \tag{B.1}$$

Due to the fixed rotation angle between STS and the beam (θ), it is convenient to represent the beam spot in a cylindrical reference frame with its symmetry axis along the y axis, where there is no rotation. The z component can normalize the direction vector and can be described only by T_x and T_y.

$$\vec{O} = (x_0, y_0, z_0) = (r_0\cos(\theta), y_o, r_0\sin(\theta)) \tag{B.2}$$

$$\vec{T} = (T_x, T_y, 1) \tag{B.3}$$

Therefore, the direction vector components are constant at any point of the track, which allows us to work from the identity shown below:

$$T_x = \frac{(x_i - r_0\cos(\theta))}{(z_i - r_0\sin(\theta))} = \frac{(x_j - r_0\cos(\theta))}{(z_j - r_0\sin(\theta))} \tag{B.4}$$

Where i and j correspond to a pair of hits in a track.

By rearranging this relation, a linear dependence between x_j and x_j can be extracted:

$$x_j = x_i \frac{z_j - r_0 \sin(\theta)}{z_i - r_0 \sin(\theta)} - \frac{r_0 \cos(\theta)(z_j - z_i)}{z_i - r_0 \sin(\theta)} \tag{B.5}$$

With slope and intercept given by:

$$m = \frac{z_j - r_0 \sin(\theta)}{z_i - r_0 \sin(\theta)} \tag{B.6}$$

$$n = -\frac{r_0 \cos(\theta)(z_j - z_i)}{z_i - r_0 \sin(\theta)} \tag{B.7}$$

This expression will determine the correlation line observed in Section 5.1 figures. The distance from any point in the 2-dimensional plane to a line is given by:

$$d_x = \frac{m x_i - x_j + n}{\sqrt{1 + m^2}} \tag{B.8}$$

Using the linear relation obtained before for hits within a track, the distribution of d_x will generate a correlation peak on top of the combinatorial background. The uncertainty of determining d_x can be obtained by evaluating the quadratic propagation of variances given by:

$$\sigma_{d_x}^2 = \sum_{p_i} (\frac{\partial d}{\partial p_i} \sigma_{p_i})^2 \tag{B.9}$$

After expanding the expression and evaluating the beam spot position as $\vec{O} = (0; 0; 0)$, we obtained:

$$\sigma_{d_x}^2 = \frac{\sigma_{r_0}^2 (z_i - z_j)^2 [a(x_i z_i + x_j z_j) + b(z_i^2 + z_j^2)]^2}{(z_i^2 + z_j^2)^3} + \frac{\sigma_{x_i}^2 z_j^2}{z_i^2 + z_j^2} + \frac{\sigma_{x_j}^2 z_i^2}{z_i^2 + z_j^2} \tag{B.10}$$

$$a \equiv \sin(\theta), b \equiv \cos(\theta) \tag{B.11}$$

For two layers with the same resolution ($\sigma_{x_i} \equiv \sigma_x, \sigma_{x_j} \equiv \ \sigma_x$) the formula changes to:

$$\sigma_{d_x}^2 = \frac{\sigma_{r_0}^2 (z_i - z_j)^2 (a(x_i z_i + x_j z_j) + b(z_i^2 + z_j^2))^2}{(z_i^2 + z_j^2)^3} + \sigma_x^2 \tag{B.12}$$

This reflects the uncertainty of measuring d for a single pair of hits h_i, h_j.

B.1.1 Dummy correlations

The experimental setup corresponding to section 5.1, has a beam axis aligned with the coordinate z-axis. In such a case, the rotation of the target plane is $\phi = 0$. Therefore, the expression for the σ_{d_x} becomes:

$$\sigma_{d_x}^2 = \frac{\sigma_{r_0}^2 (z_i - z_j)^2}{(z_i^2 + z_j^2)} + \sigma_x^2 \tag{B.13}$$

where the x coordinate dependence is lost, and the distribution predictors are now a constant.

The uncertainty of the mean value can be equated to the sigma of the correlation peak. The detector resolution can be estimated by isolating the term from the above expression and evaluating the correlation peak sigma obtained from a fitting procedure to the average value $< \sigma_{d_x} >$.

B.2 STS hit correlations

Coordinate correlations split by sensor pairs.5.1

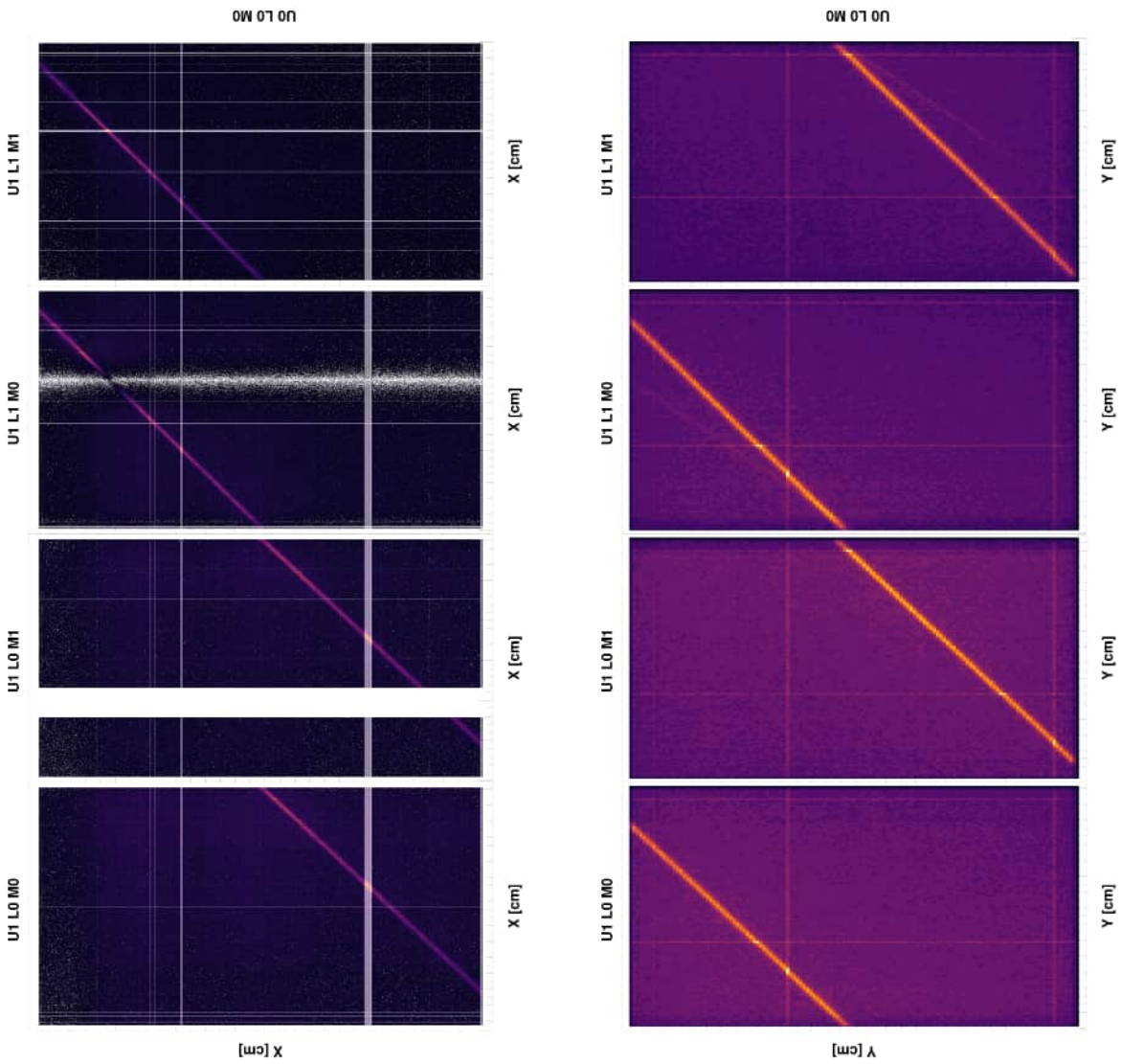

(a) X hit coordinate correlation among mSTS layers: U0:U1

(b) Y hit coordinate correlation among mSTS layers: U0:U1

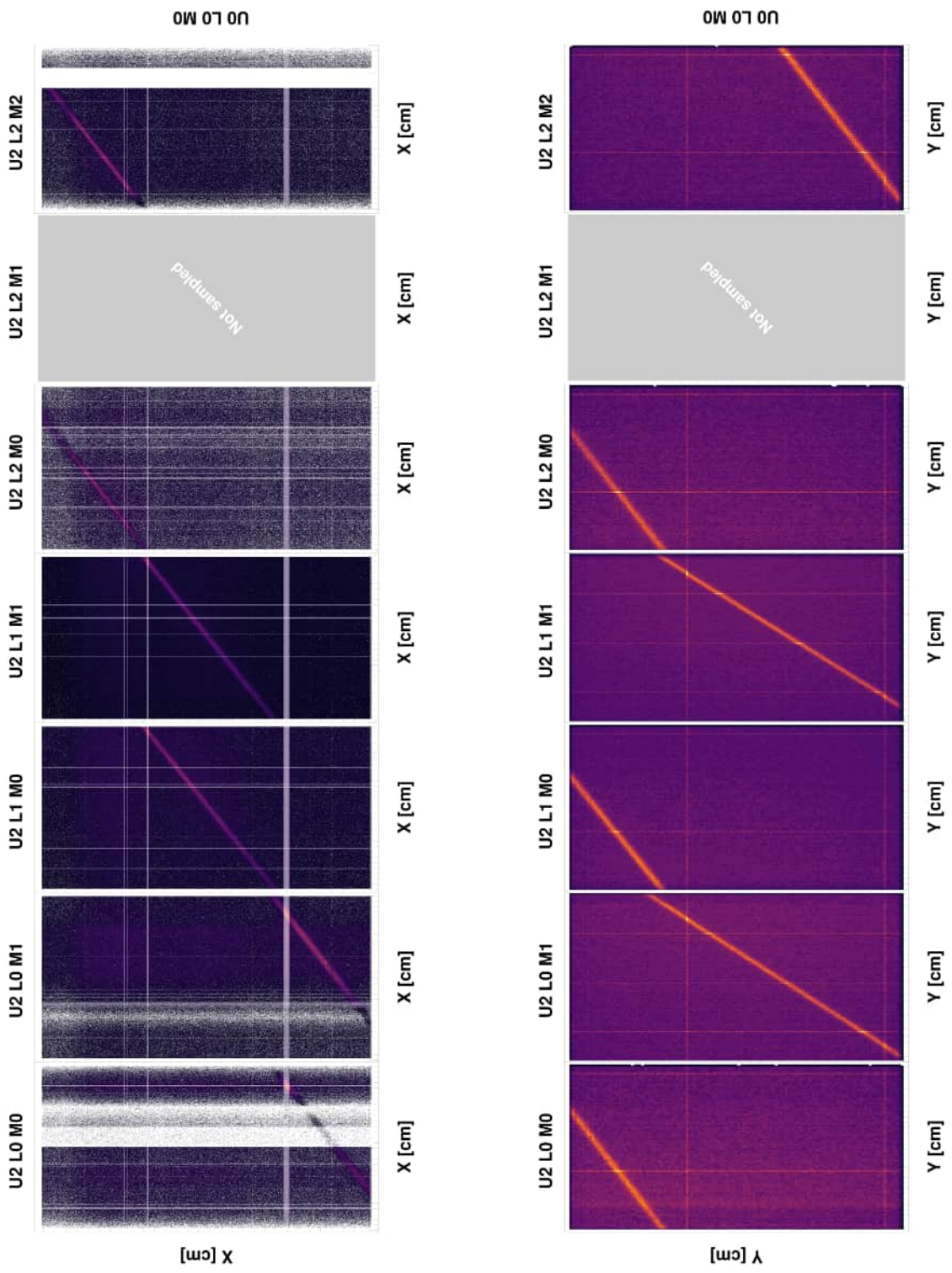

(a) X hit coordinate correlation among mSTS layers: U0:U2

(b) Y hit coordinate correlation among mSTS layers: U0:U2

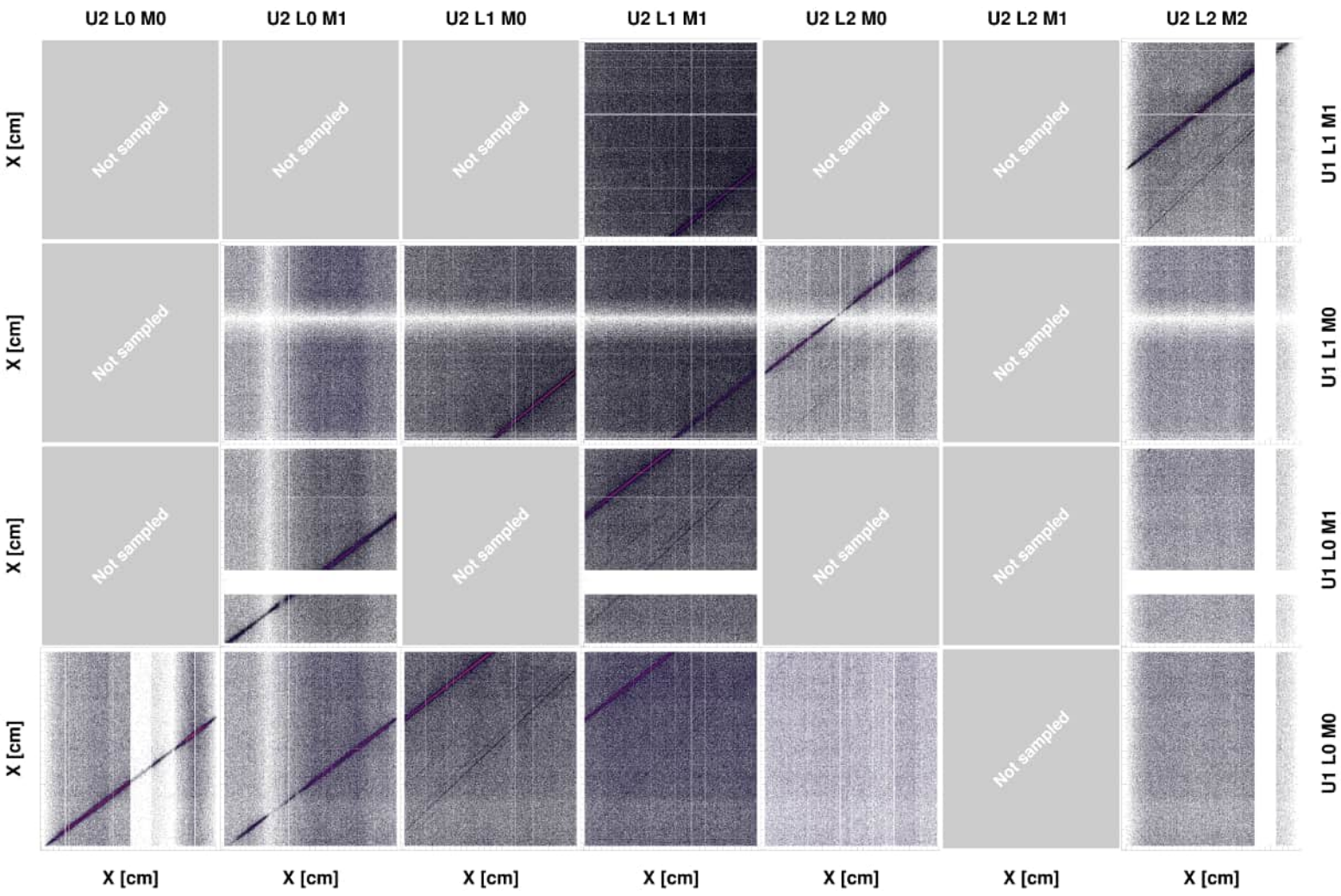

Figure B.3: X hit coordinate correlation among mSTS layers: U1:U2

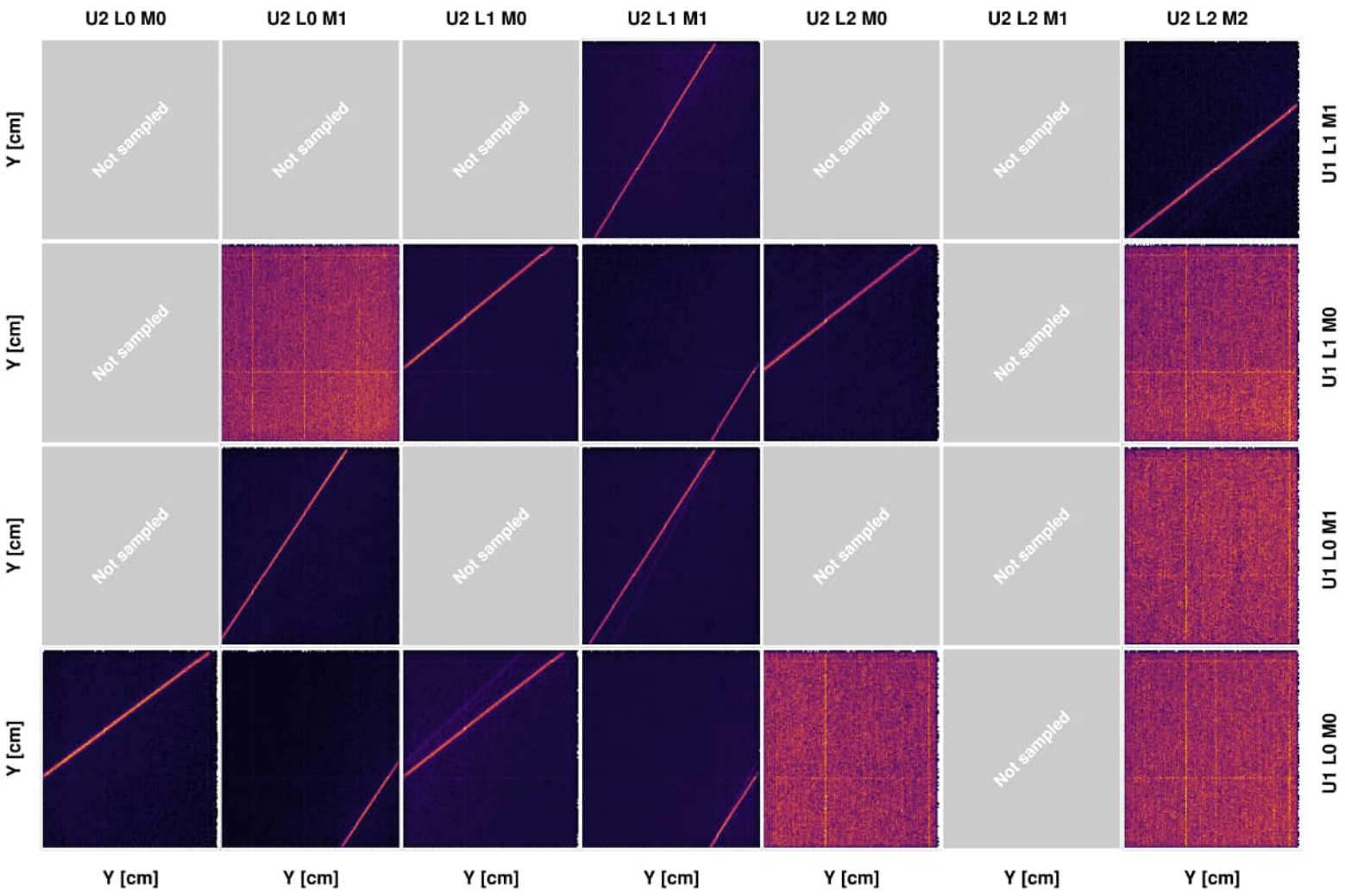

Figure B.4: Y hit coordinate correlation among mSTS layers: U1:U2

Appendix C

3D event vertex projections

This appendix complements the results obtained at 6.

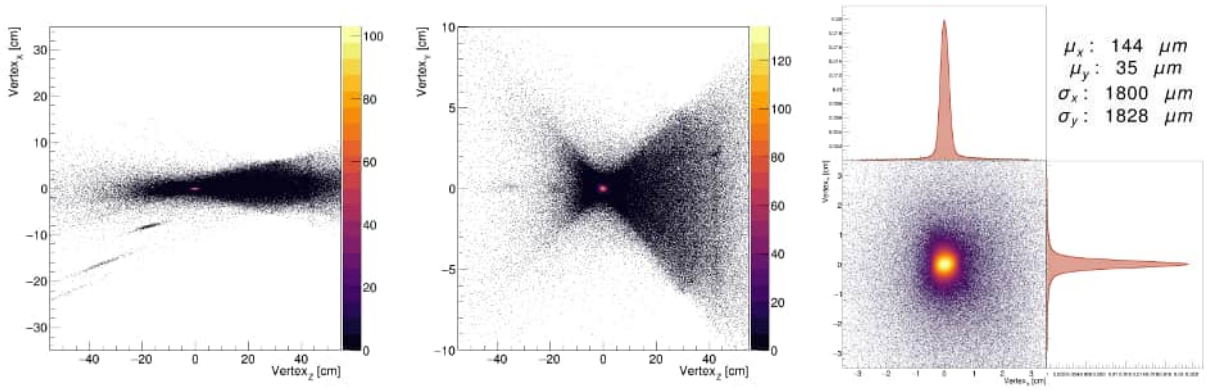

Figure C.1: Reconstructed 3D-vertex projections for tracks STS_2TRD-TOF-.

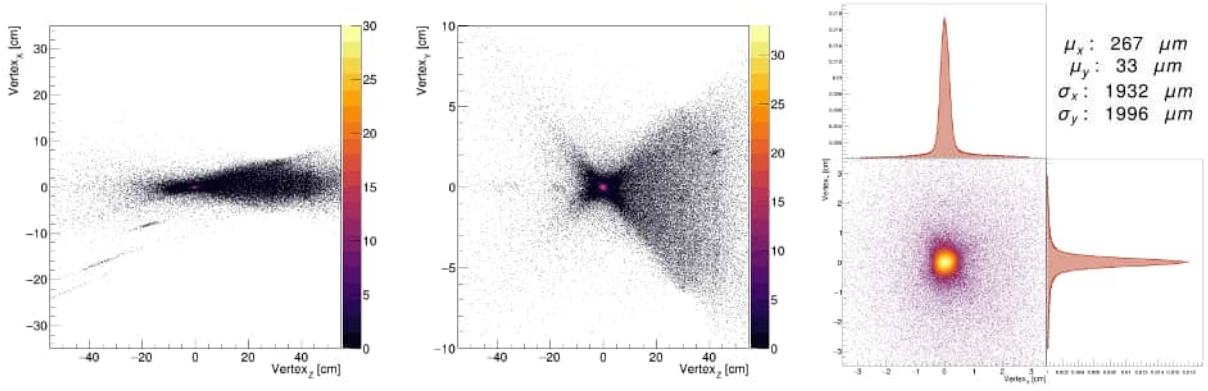

Figure C.2: Reconstructed 3D-vertex projections for tracks STS_2TRD_1TOF-.

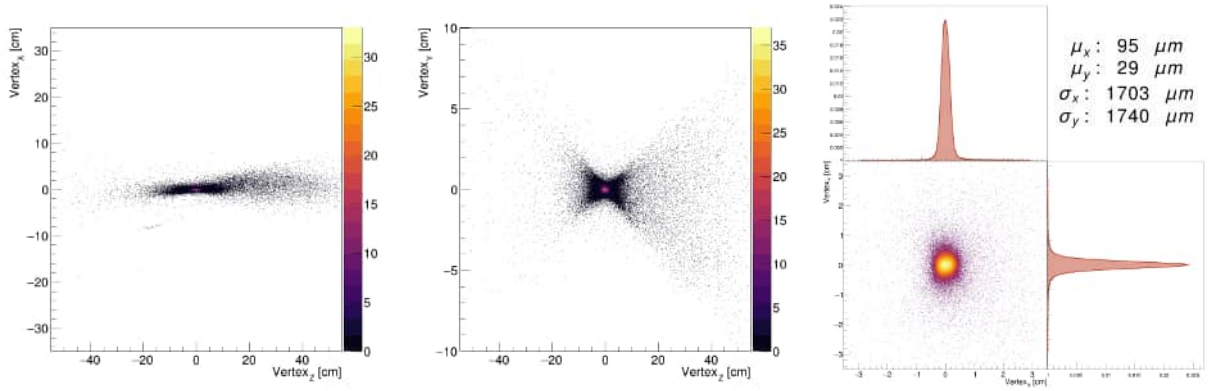

Figure C.3: Reconstructed 3D-vertex projections for tracks STS_2TRD_2TOF-.

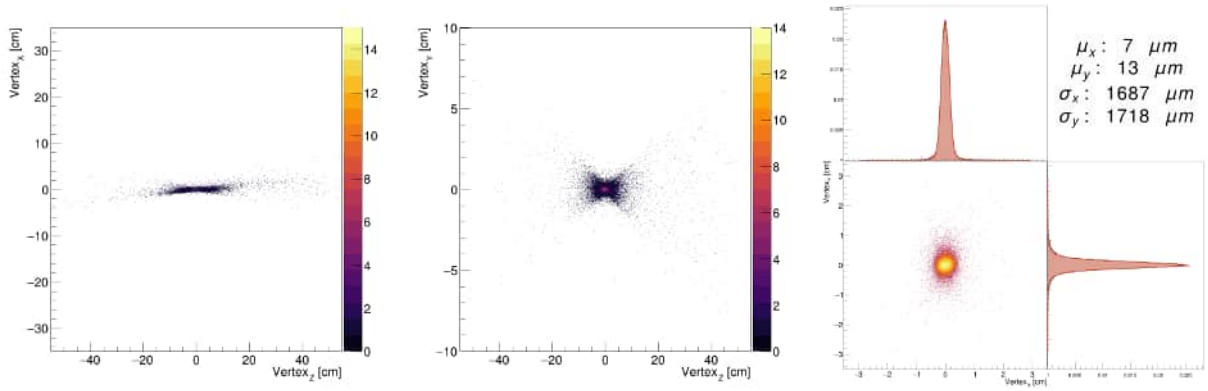

Figure C.4: Reconstructed 3D-vertex projections for tracks STS_2TRD_1TOF-.

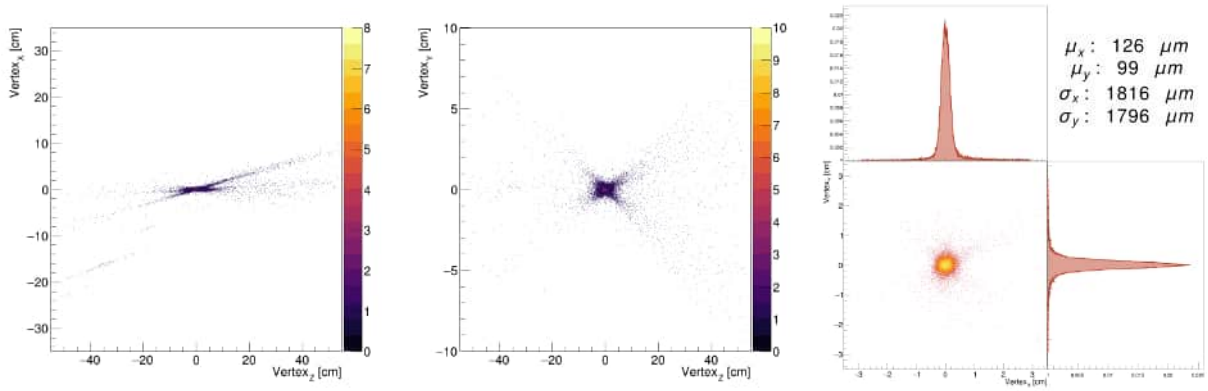

Figure C.5: Reconstructed 3D-vertex projections for tracks $STS_2TRD\_TOF_1$.

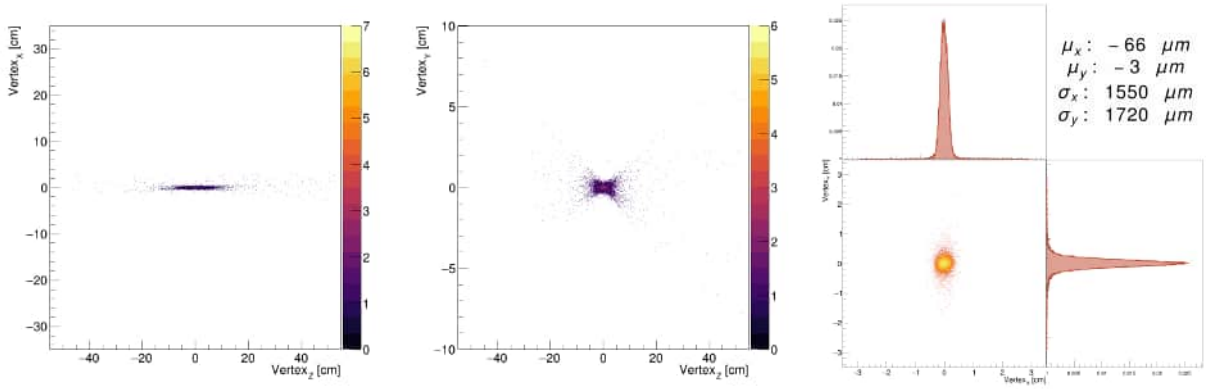

Figure C.6: Reconstructed 3D-vertex projections for tracks $STS_2TRD\_TOF_2$.

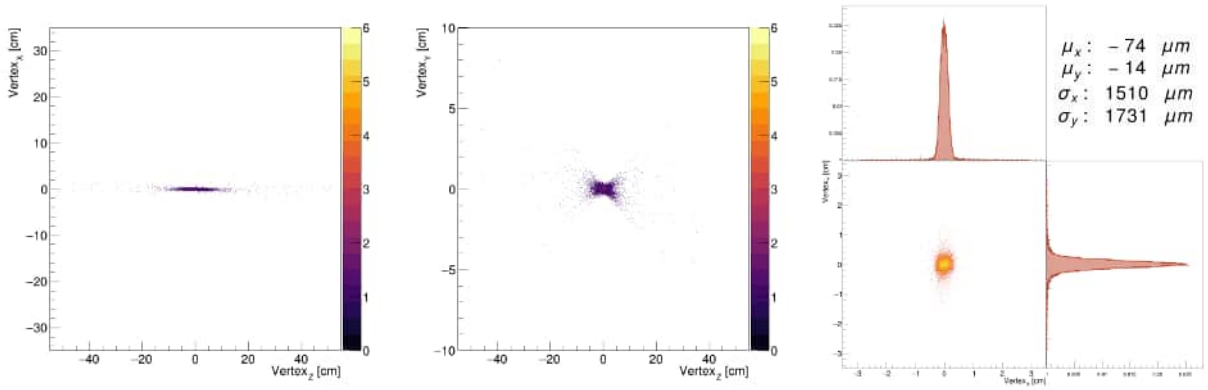

Figure C.7: Reconstructed 3D-vertex projections for tracks $STS_2TRD\_TOF_3$.

Appendix D

Submitted paper

This appendix consists of the submitted version of a manuscript containing the fundamental findings of the present research. It also comprises details regarding the operational performance of the STS detector, including dead time studies. For direct access, the following link can be used: https://arxiv.org/abs/2505.20517.

Performance of the prototype Silicon Tracking System of the CBM experiment tested with heavy-ion beams at SIS18

A. Agarwal[a], Z. Ahammed[a], N. Ahmad[b], L.J. Ahrens[c], M. Al-Turany[d], N. Alam[b], J. Andary[e], A. Andronic[f], H. Appelshäuser[e], B. Arnoldi-Meadows[e], B. Artur[e], M.D. Azmi[b], M. Bajdel[d], M. Balzer[g], A. Bandyopadhyay[a], V.A. Bâsceanu[h], J. Becker[g], M. Becker[c], A. Belousov[i], A. Bercuci[j], R. Berendes[f], D. Bertini[d], O. Bertini[d], M. Beyer[c], O. Bezshyyko[k], P.P. Bhaduri[a], A. Bhasin[l], S.A. Bhat[m], T.A. Bhat[m], W.A. Bhat[m], B. Bhattacharjee[n], A. Bhattacharyya[o], N.K. Bhowmik[a], S. Biswas[p], T. Blank[g], N. Bluhme[i], C. Blume[e], G. Boccarella[q], D. Bonaventura[f], J. Brzychczyk[r], M. Cãlin[h], M. Caselle[g], A. Chakrabarti[o], P. Chaloupka[s], Souvik Chattopadhyay[a], Subhasis Chattopadhyay[d], H. Cherif[e], S. Chernyshenko[t], E. Clerkin[u], L.M. Collazo Sánchez[d], M. Csanád[v], P. Dahm[d], A. Daribayeva[i], H. Darwish[e], R. Das[p], S. Das[p], J. de Cuveland[i], D.-A. Deară[h], H. Deppe[d], I. Deppner[d], A.A. Deshmukh[q], M. Deveaux[d], J. Diehl[c], V. Dobishuk[t], A.K. Dubey[a], A. Dubla[d], M. Dürr[c], R. Dvořák[s], I. Elizarov[d], D. Emschermann[d], J. Eschke[u], L.J. Faber[f], C. Feier-Riesen[c], Sheng-Qin Feng[w], F. Fidorra[f], P. Fischer[x], H. Flemming[d], J. Förtsch[q], P. Foka[d], U. Frankenfeld[d], V. Friese[d], I. Fröhlich[e], J. Frühauf[d], T. Galatyuk[y], G. Gangopadhyay[o], P. Gasik[u], C. Ghosh[a], S.K. Ghosh[p], D. Gil[r], S. Gläßel[e], F. Goldenbaum[z], L. Golinka-Bezshyyko[k], S. Gope[p], S. Gorbunov[d], N. Greve[aa], D. Grzonka[d], A. Gupta[l], D. Gutiérrez Menéndez[d], B. Gutsche[e], Dong Han[ab], Junyi Han[ac], N. Heine[f], N. Herrmann[ac], H. Hesounová[s], J.M. Heuser[d], C. Höhne[c], F. Hoffmann[ad], O. Hofman[s], R. Holzmann[d], Yige Huang[ae], D. Hutter[i], K. Ismail[d], T. Janson[ad], Yixuan Jin[ac], A. Jipa[h], I. Kadenko[k], P. Kähler[f], K.-H. Kampert[q], R.M. Kapell[d], R. Karabowicz[d], V.K.S. Kashyap[af], K. Kasiński[ag], V. Kedych[y], O. Keller[u], I. Keshelashvili[d], M.M. Khan[b], Sukyung Kim[q], M. Kiš[d], I. Kisel[i], R. Kłeczek[ag], Ch. Klein-Bösing[f], R. Kliemt[z], K. Koch[d], P. Koczoń[d], M. Kohn[f], J. Kollarczyk[ah], O. Kovalchuk[t], M. Koziel[e], G. Kozlov[i], D. Kresan[d], W. Krüger[y], M. Kruszewski[ai], O. Kshyvanskyi[t], B. Kubiak[ai], A. Kugler[ah], Ajay Kumar[aj], Ajit Kumar[e], L. Kumar[ak], V. Kyva[t], R. Lakos[i], R. Lalik[r], P. Lasko[r], I. Lazanu[h], J. Lehnert[d], Yue Hang Leung[ac], Shuang Li[w], Wen Li[al], Yuanjing Li[ab], V. Lindenstruth[i], F.J. Linz[d], Feng Liu[ae], S. Löchner[d], P.-A. Loizeau[d], M. Lorenz[e], O. Lubynets[d], Xiaofeng Luo[ae], A. Lymanets[d], S. Mahajan[l], Z. Majka[r], B. Mallick[am], S. Mandal[p], Yaxian Mao[ae], A.M. Marin Garcia[d], J. Markert[d], F.A. Matejcek[e], T. Matulewicz[an], J. Messchendorp[d], A. Meyer-Ahrens[f], J. Michel[e], M.F. Mir[m], D. Miskowiec[d], A. Mithran[i], B. Mohanty[af], D. Moreira de Godoy Willems[f], W.F.J. Müller[d], C. Müntz[e], P. Munkes[f], M. Nabroth[e], E. Nandy[a], S.R. Nayak[aj], F. Nerling[d], S. Neuhaus[q], F. Nickels[d], D. Okropiridze[z], A. Opíchal[ah], P. Otfinowski[ag], Liang-ming Pan[ao], C. Pauly[q], J. Peña Rodríguez[q], Ö. Penek[d], S. Peter[c], V. Petráček[s], M. Petriş[j], M. Petrovici[j], D. Pfeifer[q], K. Piasecki[an], J. Pietraszko[d], R. Płaneta[r], V. Plujko[k], J. Pluta[ap], N. Podgornov[z], T. Povar[q], K. Poźniak[ai], S.K. Prasad[p], M. Pugach[t], V. Pugatch[t], A. Puntke[f], L. Radulescu[j], S. Raha[p], D.A. Ramírez Zaldivar[d], R. Ray[p], A. Redelbach[i], A. Reinefeld[aa], S.P. Reiter[c], O. Ristea[h], J. Ritman[z], D. Rodríguez Garces[d], A. Rodríguez Rodríguez[d], F. Roether[e], R. Romaniuk[ai], A. Rost[y], A. Roy[aq], S. Roy[d], E. Rubio[ac], A. Rustamov[d], R. Sahoo[aq], P.K. Sahu[am], S.K. Sahu[am], J. Saini[a], P. Salabura[r], S. Samal[aq], S.S. Sambyal[l], K. Santos Marrero[d], K. Scharmann[c], C. Schiaua[j], F. Schintke[aa], D. Schledt[e], C.J. Schmidt[d], H.R. Schmidt[ar], K. Schünemann[u], F.-J. Seck[y], T. Sefzick[z], I. Selyuzhenkov[d],

P. Semeniuk[ag], A. Sen[p], A. Senger[u], P. Senger[u], A.K. Sharma[b], Anjali Sharma[p], Anju Sharma[d], P.K. Sharma[a], Shusu Shi[ae], M. Shiroya[d], V. Sidorenko[g], F. Simon[g], C. Simons[d], A.K. Singh[as], B.K. Singh[aj], O. Singh[e], R. Singh[af], V. Singhal[a], D. Smith[u], B. Sobół[r], Y. Söhngen[ac], D. Spicker[e], P. Staszel[r], T. Stockmanns[z], J. Stroth[e], C. Sturm[d], P. Subramani[q], G.S. Subramanya[ar], O. Suddia[d], Kai Sun[ab], Yongjie Sun[al], Zhengyang Sun[al], R. Szczygieł[ag], E.D. Taka[e], J. Taylor[d], M. Teklishyn[d], S.N. Thau[c], J. Thaufelder[d], A. Toia[d], M. Traxler[d], L. Trębacz[r], E. Trifonova[g], A. Twarowska[ai], O. Tyagi[i], F. Uhlig[d], K.L. Unger[g], I. Vassiliev[d], O. Vasylyev[d], R. Visinka[d], E. Volkova[ar], L. Wahmes[f], Kaiyang Wang[al], Yi Wang[ab], P. Weidenkaff[ac], F. Weiglhofer[i], J.P. Wessels[f], D. Wielanek[ap], A. Wieloch[r], A. Wilms[d], P. Wintz[z], M. Wojtkowski[ai], Gy. Wolf[at], Ke-Jun Wu[w], Qiqi Wu[ao], A. Wyżykowski[ai], Huagen Xu[z], Junfeng Yang[al], Ruijia Yang[q], Ming Yao[al], Zhongbao Yin[ae], In-Kwon Yoo[au], W. Zabołotny[ai], H.P. Zbroszczyk[ap], Xiaoming Zhang[ae], Xin Zhang[d], S. Zharko[d], Sheng Zheng[w], Daicui Zhou[ae], Wenxiong Zhou[ao], Yingjie Zhou[d], Xianglei Zhu[ab], G. Zischka[i], W. Zubrzycka[ag] and P. Zumbruch[d]

[a] *Variable Energy Cyclotron Centre (VECC), Kolkata, India,*
[b] *Department of Physics, Aligarh Muslim University, Aligarh, India,*
[c] *Justus-Liebig-Universität Gießen, Gießen, Germany,*
[d] *GSI Helmholtzzentrum für Schwerionenforschung GmbH (GSI), Darmstadt, Germany,*
[e] *Institut für Kernphysik, Goethe-Universität Frankfurt, Frankfurt, Germany,*
[f] *Institut für Kernphysik, Universität Münster, Münster, Germany,*
[g] *Karlsruhe Institute of Technology (KIT), Karlsruhe, Germany,*
[h] *Atomic and Nuclear Physics Department, University of Bucharest, Bucharest, Romania,*
[i] *Frankfurt Institute for Advanced Studies, Goethe-Universität Frankfurt (FIAS), Frankfurt, Germany,*
[j] *Horia Hulubei National Institute of Physics and Nuclear Engineering (IFIN-HH), Bucharest, Romania,*
[k] *Department of Nuclear Physics, Taras Shevchenko National University of Kyiv, Kyiv, Ukraine,*
[l] *Department of Physics, University of Jammu, Jammu, India,*
[m] *Department of Physics, University of Kashmir, Srinagar, India,*
[n] *Nuclear and Radiation Physics Research Laboratory, Department of Physics, Gauhati University, Guwahati, India,*
[o] *Department of Physics and Department of Electronic Science, University of Calcutta, Kolkata, India,*
[p] *Department of Physics, Bose Institute, Kolkata, India,*
[q] *Fakultät für Mathematik und Naturwissenschaften, Bergische Universität Wuppertal, Wuppertal, Germany,*
[r] *Marian Smoluchowski Institute of Physics, Jagiellonian University, Kraków, Poland,*
[s] *Czech Technical University in Prague (CTU), Prague, Czech Republic,*
[t] *High Energy Physics Department, Kiev Institute for Nuclear Research (KINR), Kyiv, Ukraine,*
[u] *Facility for Antiproton and Ion Research in Europe GmbH (FAIR), Darmstadt, Germany,*
[v] *Eötvös Loránd University (ELTE), Budapest, Hungary,*
[w] *College of Science, China Three Gorges University (CTGU), Yichang, China,*
[x] *Institut für Technische Informatik, Universität Heidelberg, Heidelberg, Germany,*
[y] *Institut für Kernphysik, Technische Universität Darmstadt, Darmstadt, Germany,*
[z] *Institut für Experimentalphysik I, Ruhr-Universität Bochum, Bochum, Germany,*
[aa] *Zuse Institute Berlin (ZIB), Berlin, Germany,*
[ab] *Department of Engineering Physics, Tsinghua University, Beijing, China,*
[ac] *Physikalisches Institut, Universität Heidelberg, Heidelberg, Germany,*
[ad] *Institute for Computer Science, Goethe-Universität Frankfurt, Frankfurt, Germany,*
[ae] *College of Physical Science and Technology, Central China Normal University (CCNU), Wuhan, China,*
[af] *National Institute of Science Education and Research (NISER), Bhubaneswar, India,*
[ag] *AGH University of Science and Technology (AGH), Kraków, Poland,*
[ah] *Nuclear Physics Institute of the Czech Academy of Sciences, Řež, Czech Republic,*
[ai] *Institute of Electronic Systems, Warsaw University of Technology, Warsaw, Poland,*
[aj] *Department of Physics, Banaras Hindu University (BHU), Varanasi, India,*
[ak] *Department of Physics, Panjab University, Chandigarh, India,*

[al] Department of Modern Physics, University of Science & Technology of China (USTC), Hefei, China,
[am] Institute of Physics, Bhubaneswar, India,
[an] Faculty of Physics, University of Warsaw, Warsaw, Poland,
[ao] Chongqing University, Chongqing, China,
[ap] Faculty of Physics, Warsaw University of Technology, Warsaw, Poland,
[aq] Indian Institute of Technology Indore, Indore, India,
[ar] Physikalisches Institut, Eberhard Karls Universität Tübingen, Tübingen, Germany,
[as] Indian Institute of Technology Kharagpur, Kharagpur, India,
[at] Institute for Particle and Nuclear Physics, HUN-REN Wigner RCP, Budapest, Hungary,
[au] Pusan National University (PNU), Pusan, Korea,

ARTICLE INFO

Keywords:
silicon
resolution
vertex
reconstruction
tracking
efficiency

ABSTRACT

The Compressed Baryonic Matter (CBM) experiment at the future Facility for Antiproton and Ion Research (FAIR) is a heavy-ion experiment designed to study nuclear matter at the highest baryonic density. For high-statistics measurements of rare probes, event rates of up to 10 MHz are targeted. The experiment, therefore, requires fast and radiation-hard detectors, self-triggered detector front-ends, free-streaming readout architecture, and online event reconstruction.

The Silicon Tracking System (STS) is the main tracking detector of CBM, designed to reconstruct the trajectories of charged particles with efficiency larger than 95%, a momentum resolution better than 2% for particle momenta larger than 1 GeV/c inside a 1 Tm magnetic field, and to identify complex decay topologies. It comprises 876 double-sided silicon strip modules arranged in 8 tracking stations.

A prototype of this detector, consisting of 12 modules arranged in three tracking stations, is installed in the mini-CBM demonstrator. This experimental setup is a small-scale precursor to the full CBM detector, composed of sub-units of all major CBM systems installed on the SIS18 beamline. In various beam campaigns taken between 2021 and 2024, heavy ion collisions at 1–2 AGeV with an average collision rate of 500 kHz have been measured.

This allows for the evaluation of the operational performance of the STS detector, including time and position resolution, hit reconstruction efficiency, charge distribution, signal-to-noise ratio, and its potential for track and vertex reconstruction.

1. Introduction

1.1. The CBM experiment

The Compressed Baryonic Matter (CBM) is a fixed target heavy-ion experiment at the Facility for Antiproton and Ion Research (FAIR) under construction in Darmstadt, Germany. It will investigate the phase diagram of strongly interacting matter in the region of high net-baryon densities and moderate temperatures [1]. For high-statistics measurements of rare probes, event rates of up to 10 MHz are targeted. To meet these demands, the CBM experiment uses fast and radiation-hard detectors, self-triggered detector front-ends, and a free-streaming readout architecture.

1.2. The STS detector

The Silicon Tracking System (STS) is the core detector for tracking and momentum determination. It consists of 876 double-sided silicon micro-strip detectors arranged in eight tracking stations positioned between 30 cm and 100 cm downstream of the target inside a 1 Tm magnetic dipole field [2]. The primary purpose of the STS is the reconstruction of the trajectories of up to $\sim 10^3$ charged particles per beam-target collision event. This should be achieved with an efficiency larger than 95% and momentum resolution better than 2% for primary particles. It also enables the reconstruction of complex event topologies, such as the weak decays of strange or charmed hadrons and hypernuclei. To accomplish these goals at the projected interaction rate, the STS requires a position resolution better than 30 µm in the bending plane, a good time resolution (< 10 ns), low per-channel dead-time and a material budget within 0.3%–1.4% X_0 per tracking station [2].

ORCID(s):

1.3. The STS module

The functional building block of the STS is the module [3]. It comprises a Double-Sided Double-Metal (DSDM) silicon micro-strip sensor and associated readout electronics. The sensor, produced by Hamamatsu Photonics, K.K., Japan [4], are 320 µm thick and 62 mm wide and have four different lengths: 22 mm, 42 mm, 62 mm and 124 mm. Each sensor has 1024 strips per side, spaced at 58 µm pitch. The strips on the p-doped side (p-side) are inclined by 7.5 ° with respect to the n-side, thus providing 2D tracking information with a single sensor. Each sensor side is read out by a front-end board (FEB), equipped with a total of eight custom-designed STS/MUCH-XYTER ASICs (SMX) [5]. Each of these is connected to 128 strips of the sensor via a pair of custom ultra-lightweight aluminium-polyimide microcables.

The SMX ASIC utilizes parallel signal processing to generate signals independently for each channel, featuring a charge-sensitive amplifier (CSA) that feeds into a dual signal path with two shaper amplifiers: a fast shaper for timestamp generation and a slow shaper for amplitude measurement. Each of the 128 analog channels incorporates a 5-bit continuous flash analog-to-digital converter (ADC) to measure signal amplitude, along with a fast leading-edge discriminator to determine the signal's generation time in a 14-bit timestamp message with a resolution of 3.125 ns. The chip is based on a streaming data processing architecture that allows operation without data loss in the digital readout path with an average load of up to 2.8×10^5 signals per channel per second. The readout can be performed with up to five synchronous serial data links per ASIC. A new signal arriving while processing a prior signal is lost, and an Event-Missed flag is activated [5].

1.4. The mCBM setup

Mini-CBM (mCBM) is a demonstrator test setup consisting of prototype or pre-series components of all major CBM systems installed at the SIS18 synchrotron of the GSI Helmholtz Center, constructed to study, commission, and test the complex interplay of the different detector systems, the readout electronic chain with free-streaming data acquisition and fast online event reconstruction and selection [6]. The experiment has been operational at SIS18 since 2018 and measures heavy ion collisions at 1–2 AGeV. The mSTS setup was active in various beam test campaigns between 2021 and 2024.

This paper presents a detailed study of the operational performance of the prototype STS system measured in beam experiments with the mCBM setup.

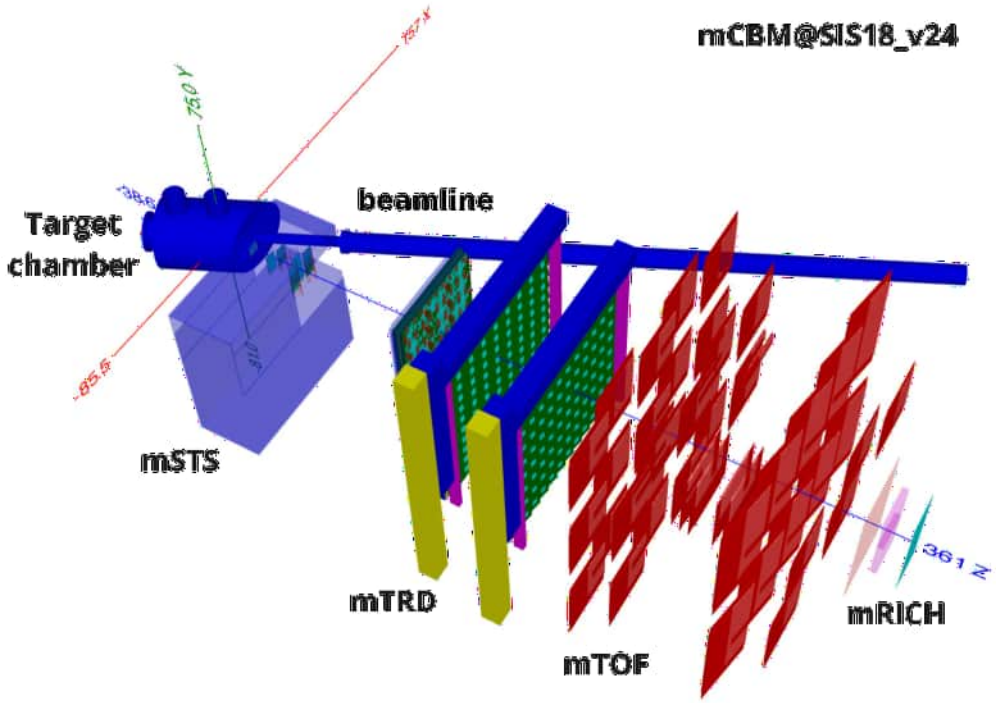

Figure 1: Schematic view of the mCBM setup in the 2024 beam campaign.

2. Experimental conditions

2.1. Experimental setup

Figure 1 presents the schematic of the experimental configuration utilized in this analysis. The primary axis of the mCBM setup (z-axis) is positioned at an angle of 25° relative to the beam axis. With a right-handed coordinate system, the positive y-axis is oriented upwards, and the positive x-axis is directed to the left when looking downstream.

It includes the Beam Monitoring detector prototype (BMon), which serves to measure the start time of the collision. BMon, not shown in Fig. 1, but detailed in a zoom-in view of the target chamber later in Fig. 7a, consists of a $1 \times 1\,\mathrm{cm}^2$ polycrystalline diamond detector placed 20 cm upstream of the target, denoted as T0. In 2024, a second diamond, denoted as B1, was mounted 45 cm upstream of the target. Three layers of the transition radiation detector (TRD) [7] are mounted downstream of the STS, followed by up to four layers of Time-of-Flight (TOF) counters [8]. A Ring-Imaging Cherenkov (RICH) detector is installed downstream [9].

2.2. The STS system

The STS setup installed at the mCBM experiment is shown in detail in Fig. 2. It consists of three tracking stations of an active area of $6 \times 6\,\mathrm{cm}^2$, $12 \times 12\,\mathrm{cm}^2$, and $18 \times 18\,\mathrm{cm}^2$, positioned respectively around 16 cm, 33 cm, 47 cm from the target. The stations are constructed from 12 detector modules of two different sensor sizes, $62 \times 62\,\mathrm{mm}^2$ and $62 \times 124\,\mathrm{mm}^2$. Modules were integrated into the setup in multiple stages. All modules employ series sensors and microcables, along with close-to-final or series-production SMX ASICs. The earliest modules still rely on prototype FEBs, powering, and bias voltage filtering. The ASICs in the two downstream stations use only 1 uplink, while the ASICs in the first upstream station use all 5 available uplinks. Seven Common Read-Out Boards (C-ROB) are used for the readout, and five Power Boards (POB) provide the supply voltages for the FEBs. The modules are mounted on carbon-fiber ladders, which are affixed to aluminum support structures (C-frames) where the front-end electronic boards are placed.

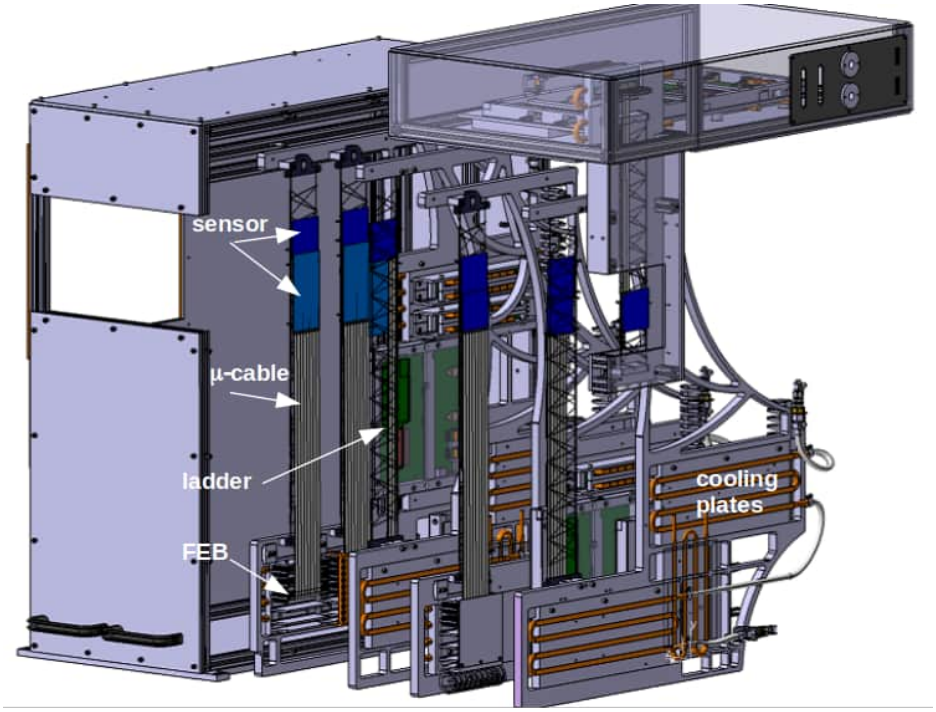

Figure 2: CAD drawing of the mSTS setup shifted outside the enclosure for illustration. The sensors are depicted in blue.

2.3. Commissioning and operation

Before installation in the mCBM cave, an energy calibration was carried out to adjust the dynamic range of the per-channel ADCs. This was done using a calibrated internal pulse generator with gradually increasing amplitudes in the readout chip to record the response of each discriminator. This provides the effective threshold and gain for

each detector channel. The derivative of the discriminator response in the S-curve scan provides a way to estimate the baseline noise level. An Equivalent Noise Charge (ENC) of 1000 e, below the targeted system noise, was measured [3]. The modules were operated with relatively low thresholds, around 3–4 σ RMS amplitude of the noise, i.e., 3000–4000 e. The typical dark rate observed was around 0.5 kHit/s/channel and up to 1.4 kHit/s/channel in the worst case, consistent or better than the expectations [2].

2.4. Data sets

Different beam campaigns have been performed with the mCBM setup since 2021 with heavy-ion collisions in fixed-target configuration, typically using mid-size ion species (O, Ni) at 1–2 AGeV and a moderate beam intensity of about 500 kHz. Additionally, tests with larger colliding systems (Au+Au, U+Au) at higher interaction rates were conducted.

Most of the data presented here were collected in 2024 in Ni+Ni collisions with a beam kinetic energy of 1.93 AGeV. The beam intensity was about 4×10^7 ions per spill, and a spill length of about 8 s, followed by a spill-break of about 2.5 s. The beam profile had a width of 1.5 mm. The Ni-target employed in the experiment measures 15 mm $\times$ 35 mm. It is mounted in a thin Al frame with a cutout of 31 mm in diameter. The target thickness of 4 mm corresponds to 10% interaction probability, resulting in a collision rate of about 500 kHz.

2.5. Data analysis

In line with the free-streaming readout architecture, the data is collected and recorded in Time Slice Archive (TSA) files. A time slice contains the full data recorded by the DAQ [10] in a defined time frame from every detector. In the offline analysis, the TSA files are first decoded into strip-raw signals for the STS, which contain the module and channel information of the activated strip, as well as the signal's time and amplitude. Clusters are reconstructed by correlating signals from neighboring activated strips [11], within a short time window. The amplitudes of signals from individual strips of a cluster are summed up. Time information is the average of the individual signal's time. The center of gravity of a cluster is taken as an estimate for the crossing point of a particle in the sensitive volume of the detector [12]. Hits, i.e., space points, are finally derived by correlating sensor p- and n-side clusters. Events are defined using the signal from a seed detector (BMon in this case) as a time reference and including all signals from the other detectors within a time window that depends on the detector's time resolution. In this prototype beam campaign, a conservative window of $\pm$60 ns was used for the STS. Only a single BMon hit is required to prevent event pile-up. A minimum of eight TOF signals is required to remove empty events triggered by sporadic noise counts and enhance the sample that contains at least one track. Events with more than 100 STS signals are removed to suppress events caused by massive pickup noise.

3. Results

3.1. Throughput of the readout electronics

The throughput of the readout electronics was studied in beam intensity scans with U+Au collisions. In these beam campaigns, only the modules built with one data uplink per ASIC were installed. The maximum data rate reached in measurement was 56 kHit/s/channel. This is consistent with the expected bandwidth saturation limit of 9.41 kHit/s/link (corresponding to 73 kHit/s/channel), measured in the laboratory [5], but limited in beamtime by the microscopic spill structures of the beam. The throughput of the module readout electronics can be increased by a factor of five by using 5 links per ASIC, thereby reaching a bandwidth of 370 kHit/s/channel to cope with the high-intensity heavy-ion beams expected at CBM.

While reaching the maximum throughput, a further increase of beam intensity leads to an observed increase of the Event-Missed flag. Typical values of the data loss rate for the beam intensity used in the performance studies with Ni+Ni data at 500 kHz are well below 1%.

3.2. Time resolution

The detector raw signals are synchronized to ensure proper functionality in a free-streaming operation. Individual subsystem time-offset corrections calculated from a common reference are applied. The T0 detector, part of the BMon system, is used as a reference. The STS time calibration accounts for the time offset and the timing's dependence on the signal amplitude (time walk). It is performed for every ASIC and discriminator.

Figure 3, left part, shows the average time difference between STS and T0 signals as a function of the STS signal amplitude before and after calibration. The points indicate the mean value of the time difference, while the bar stands

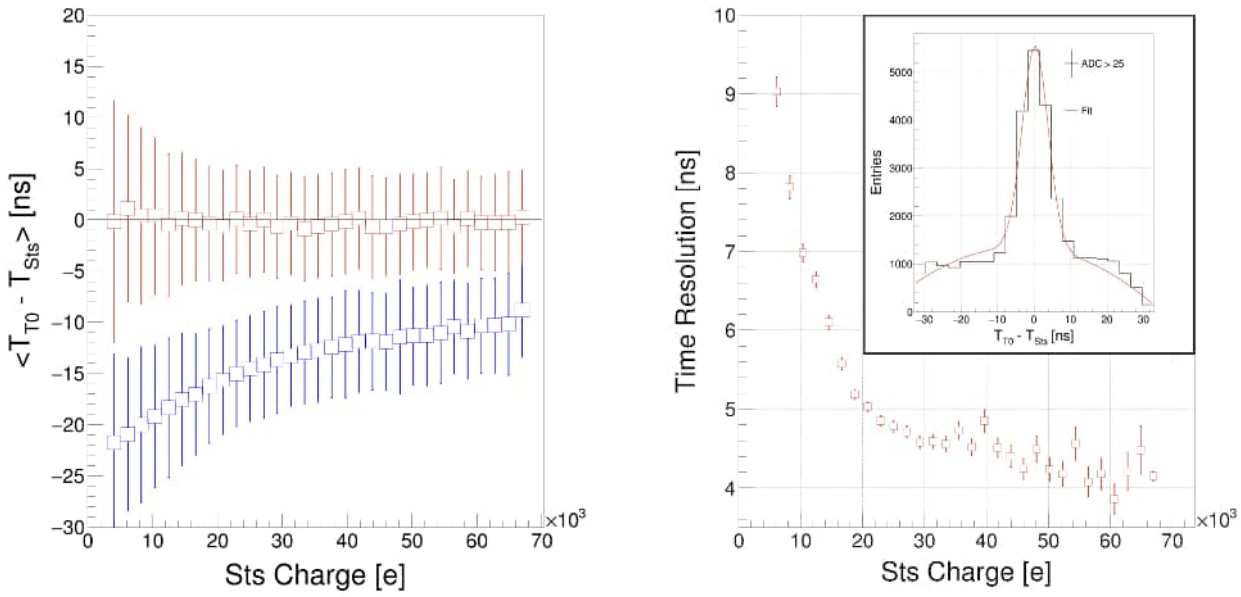

Figure 3: Top: Time difference of raw strip signals of the STS and signal from T0 detector, before (blue) and after (red) time calibration. The points indicate the mean value of the time difference, while the bar stands for the width (σ) of the distribution. Bottom: Time resolution of the STS as a function of the signal amplitude. The error bars reflect the fit uncertainty. The inset shows the time difference between STS and T0 signals for large STS signal amplitude, > 25 ADC.

for the width of the distribution obtained via a Gaussian fit. After the calibration is applied, the signal is correctly synchronized with the T0 detector. The distribution width is influenced by three main components: the STS time resolution, the T0 time resolution, and the spread in time-of-flight of particles from the event vertex to the STS sensors. The T0 has negligible resolution (∼50 ps) compared to the STS. The contribution from the time-of-flight, given by the difference between the fastest and slowest particles in the event, was estimated with simulations and can reach up to 2 ns. Therefore, the distribution width, represented by the error bar in the figure, indicates an upper limit of the STS time resolution.

Figure 3, right part, shows the dependence of the distribution width on the signal amplitude. The distribution is wider for low-amplitude signals due to the walking effect and the lower signal-to-noise ratio. In contrast, once accounting for the time of flight, cleaner samples at larger signal amplitude allow the extraction of a time resolution around or better than 5 ns.

3.3. Dead time

Different effects can be observed when two signals arrive close in time, depending on the time difference between them and the amplitude of the first signal. A pile-up in the first signal might occur for very close signals: the second signal is merged into the first, and its amplitude adds to the first signal. If the second signal arrives during dead time, it is lost. If the second signal arrives when the baseline is not restored, a new signal is created but with reduced amplitude. Figure 4 shows the time difference between two consecutive signals in the same channel versus the amplitude of the first signal. Operating the detector with the shortest shaping time of 90 ns [5], a dead time between 200 ns for low signal amplitude and 350 ns is measured.

3.4. STS alignment

Data-driven, software-based alignment of individual STS components provides sufficient precision to determine tracks and vertices, using only STS hits. This alignment is achieved through beam spot reconstruction as the figure of merit. As the mCBM setup does not include a magnetic field, any particle traverses the detector along a straight line. Every pair of hits in different stations forms a segment (tracklet) that can be extrapolated and projected to the target plane. The distribution of all tracklets extrapolations allows to reconstruct the beam spot. The vertex spread is defined as the RMS of the centers of such a distribution, found by each sensor pair. In the alignment procedure, independent sensor translations are applied through a gradient descent minimization, where the vertex spread is recalculated iteratively.

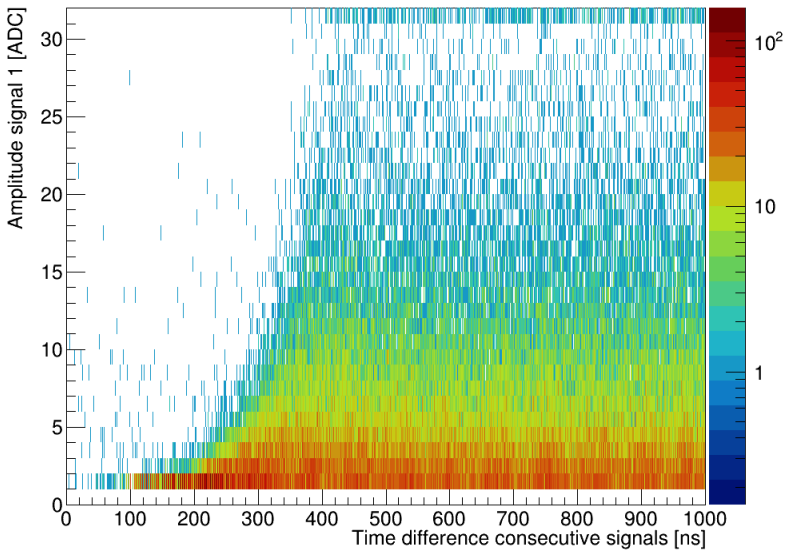

Figure 4: The amplitude of the first signal vs the time difference between consecutive signals in the same channel. The empty region corresponds to the detector dead time, which ranges from 200 ns to 350 ns for low to high charge values. Note that the numbering scheme of the STS XYTER discriminators (ADC) on the y-axis starts from 1.

The final translations, obtained at convergence after eight iterations, are consistent with the assembly precision of ∼100 µm and with the constraints from the mechanical units. After the alignment of all individual sensors, the overall primary vertex position, reconstructed via the beam spot method, is reported in Table 2.

3.5. Spatial Resolution

The evaluation of the single-hit spatial resolution in a sensor requires measuring the differences between the reconstructed impact point by the device under test (DUT) and the predicted points obtained from track extrapolation. To evaluate spatial resolution, we exploit the spatial correlations between STS hits and utilize the outer detector systems (TRD and TOF) via a custom-modified 4D CA-tracking [13] to reduce the number of false hit combinations. STS hits in the first and the last stations are used as reference. The station in the middle is used as the DUT. Using STS hits identified to belong to the same track allows for preserving the fake suppression that the tracking algorithm offers. Therefore, the evaluation of the track at the DUT is a simple straight-line extrapolation given by Eq. 1.

$$\begin{aligned} x_{\mathrm{DUT}} &= x_i + T_x(z_{\mathrm{DUT}} - z_i) \\ y_{\mathrm{DUT}} &= y_i + T_y(z_{\mathrm{DUT}} - y_i) \end{aligned} \tag{1}$$

where T_x, T_y are the components of the track directional vector $\vec{T}$.

$$\vec{T} = (T_x, T_y, 1) = \left(\frac{x_i - x_j}{z_i - z_j}, \frac{x_i - x_j}{z_i - z_j}, 1\right) \tag{2}$$

and (x_i, y_i, z_i), (x_j, y_j, z_j) are the space points given by the STS hits in the first and last station, respectively.

The unbiased hit-track residual is the distance between the measured space point position on the DUT and the point obtained by extrapolating the track at the sensor plane. Figure 5 shows the unbiased hit-track residual distribution along the X (left) and Y (right) directions for a selected sensor.

In a system with ideal geometric alignment, the distribution spread σ_{UR} is influenced by the resolution of the detector being tested σ_{STS}, the precision of track extrapolation σ_{track}, and the track deviation due to multiple Coulomb scattering σ_{MS}.

$$\sigma_{\mathrm{UR}} = \sigma_{\mathrm{STS}} \oplus \sigma_{\mathrm{track}} \oplus \sigma_{\mathrm{MS}} \tag{3}$$

Table 1
Spatial resolution of the STS σ_{STS} in X and Y for different detectors of Station 1. Here, "L" refers to the ladder, and "M" to the module. The values are extracted from the width of the unbiased residuals, σ_{UR} using Eq. 3 as: σ from residual fit, FWHM/2.35, and average RMS. Reported values units are micrometers (µm).

sensor	σ_x^{fit}	σ_x^{FWHM}	$\sigma_x^{<RMS>}$	σ_y^{fit}	σ_y^{FWHM}	$\sigma_y^{<RMS>}$
L0M0	29	25	23	103	101	72
L0M1	28	27	26	102	105	69
L1M0	29	25	24	103	85	75
L1M1	28	29	27	102	110	72

The track extrapolation is done using only the first and last STS stations. Therefore, besides the location of the extrapolation plane, the accuracy σ_{track} is influenced only by the spatial resolution of the STS modules (σ_{STS}) used to determine the track line.

The impact of multiple Coulomb scattering on track residuals can be calculated with:

$$\theta_0 = \frac{13\,\mathrm{MeV}}{\beta\, c\, p}|z|\sqrt{\frac{x}{X_0}}\left[1 + 0.038\ln\left(\frac{x\, z^2}{X_0\,\beta^2}\right)\right] \tag{4}$$

where p, βc, and z are the momentum, velocity, and charge number of the incident particle [14]. The thickness of each module is such that $X/X_0 = 0.38 \pm 0.01\%$.

The STS spatial resolution σ_{STS} can then be extracted from the width of the residual distribution σ_{UR} shown in Fig. 5. A Gaussian fit added to a quadratic polynomial to describe the background provides a reasonably good characterization of the width of the central peak for both x and y distributions. The resolution obtained from the fit is given in Table 1. However, the residual distribution deviates slightly from a Gaussian shape, even after accounting for a quadratic background. This deviation is mainly due to sensor misalignment and ghost hits. Two approaches have been implemented to address local dependencies and non-Gaussian effects. The first assumes that the true Gaussian distribution of the track-hit residuals dominates the peak, allowing extraction of σ_{UR} from the FWHM relationship. The second approach calculates the average RMS of the residuals along the x and y coordinates of the sensor after subtracting the flat background. This method aims to prevent the broadening of the estimated σ_{UR} by avoiding the superposition of multiple Gaussian peaks with different mean values, which results from residual misalignment. The resolution obtained with these other approaches, also given in Table 1, is smaller and closer to the theoretical expectations of $58/\sqrt{12} = 17\,\mu\mathrm{m}$.

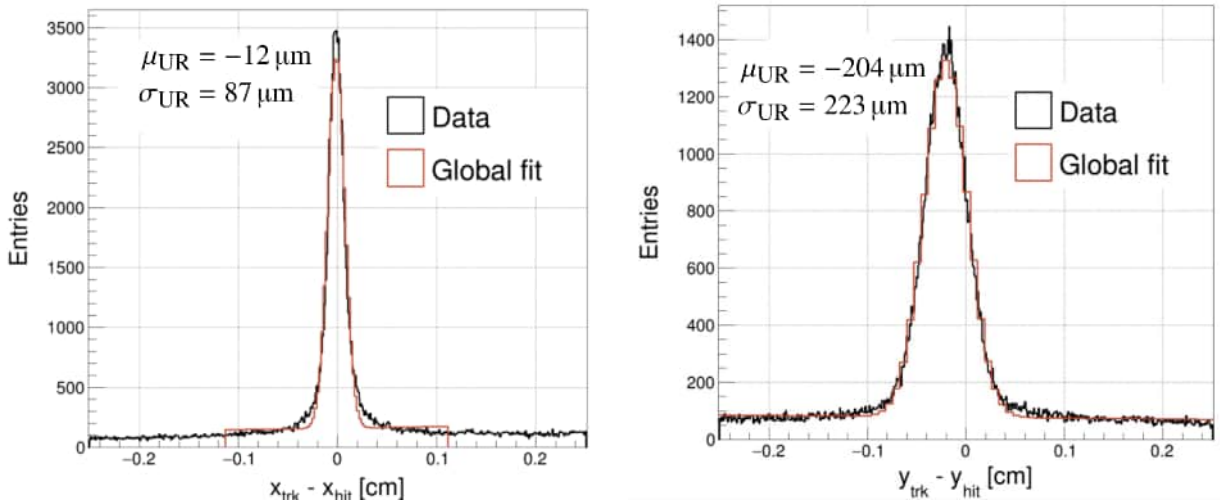

Figure 5: Unbiased hit-track residual distribution for a selected sensor module in X (left) and Y (right), respectively. The distribution is fitted by a Gaussian plus a second-order polynomial.

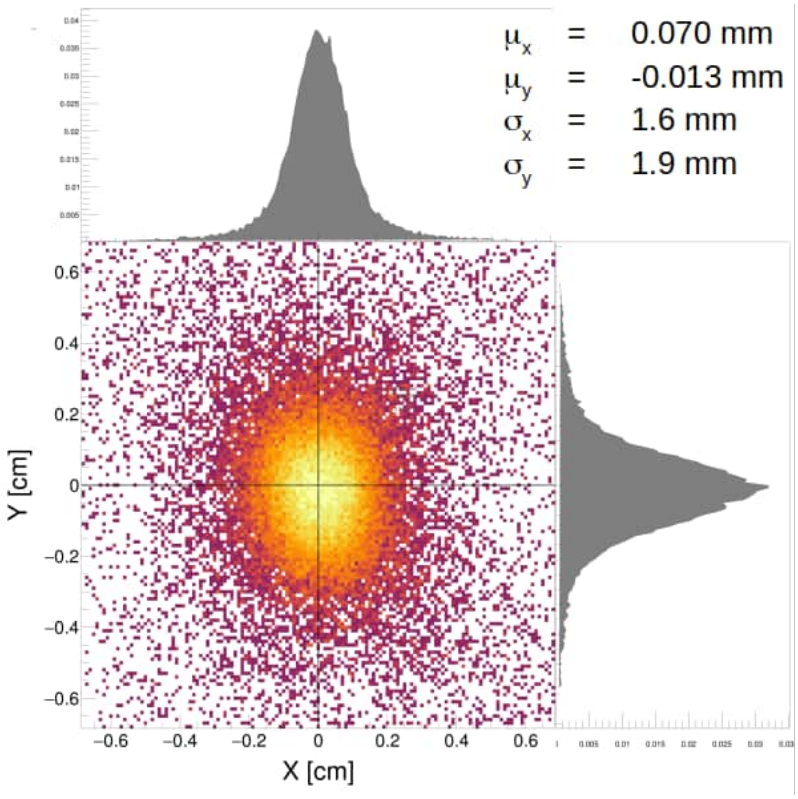

Figure 6: XY projection of the event primary vertex, together with one-dimensional distributions in X and Y, respectively. The mean and the widths of the distributions, obtained from a Gaussian fit, are displayed in the top right panel.

Table 2
Results of the vertex reconstruction with the Point-of-Closest-Approach (PCA) and the beam spot (BS) method. Reported values units are millimeters (mm).

method	μ_x	μ_y	σ_x	σ_y
PCA	0.070	-0.013	1.6	1.9
BS	0.021	0.42	1.6	1.7

3.6. Vertex reconstruction

In contrast to the beam spot, which is determined as an average over many events, the event-by-event primary vertex provides a precise estimate of the primary interaction point of a single collision. The three-dimensional primary vertex is reconstructed with the Point of Closest Approach (PCA) method, i.e., averaging the position of all valid PCAs of any track pairs in the event. A PCA is considered valid if the distance between the point and tracks is not much larger than the vertex resolution ($\sim 100 - -500\,\mu$m).

Figure 6 shows the XY projection of the average position of PCA, together with the one-dimensional distributions in X and Y. The width of the primary vertex distribution, about 1.5 mm, is dominated by the beam size.

The primary vertex resolution is usually estimated by comparing the vertices reconstructed from a track sample that has been randomly split into two parts. Given the very low track multiplicity in the mCBM acceptance, we instead compare the vertex reconstructed using the PCA method to the mean of the beam spot reconstruction. As shown in Table 2, the results of vertex reconstruction using both methods differ only by 50 µm in x and 400 µm in y.

Taking advantage of the tracking algorithm and using tracks with two STS hits, the vertex distribution reveals distinct structures originating from secondary targets, corresponding to different interaction points within the target chamber, highlighted in Fig. 7a.

The different structures can be focused on by changing the z position of the projection planes, depending on where the tracks originated. This can be done for the different secondary target planes (e.g., $z = -20$ cm for the T0 detector). The projection along the x-axis of the vertex reconstruction for each plane is shown with different colors in Fig. 7b.

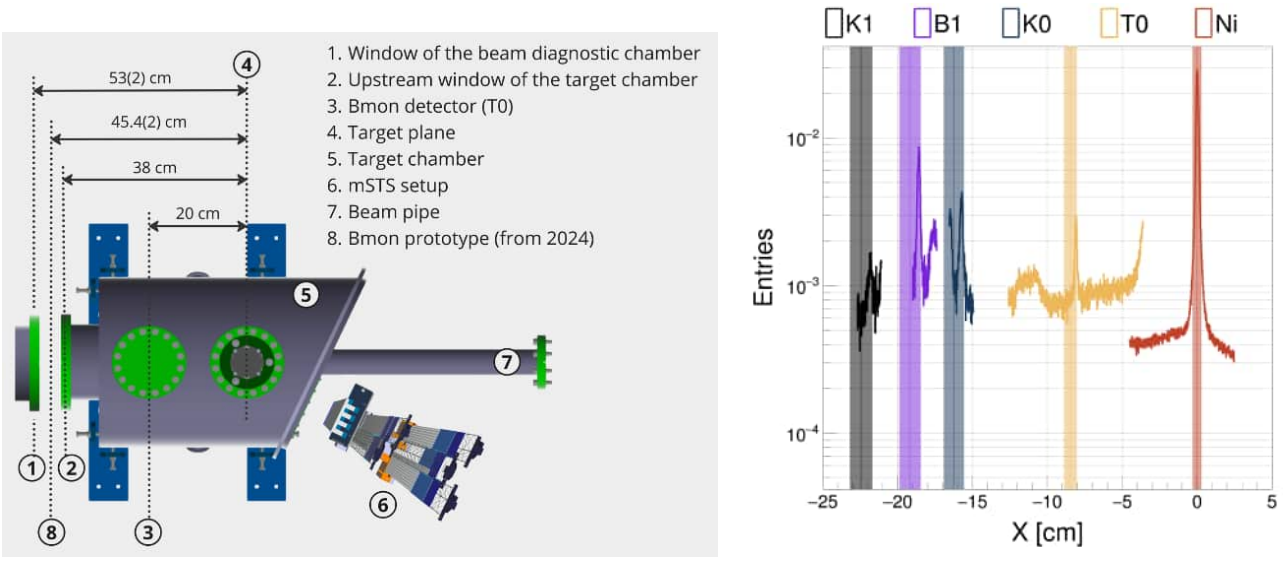

(a) (b)

Figure 7: (left) Zoom-in view of the target chamber region, highlighting the planes of interest for vertex reconstruction. (right) Projection of the reconstructed vertex along the x-axis for different z-planes. The dashed lines indicate the expected position of the vertex, together with the expected width, marked by the corresponding bands for the different secondary targets: Ni (the main Ni target), T0 (the T0 detector), B1 (the 2024 BMon prototype), K0 (the window of target chamber), K1 (the window of the diagnostic chamber).

A dashed line represents the expected position of such peaks, while the shaded box stems from the uncertainty in the projection of the beam spot to different z-planes, which increases with increasing distance in z.

Besides minor deviations due to the detector's non-perfect alignment, the agreement between the measured vertices and the expected position is remarkably good.

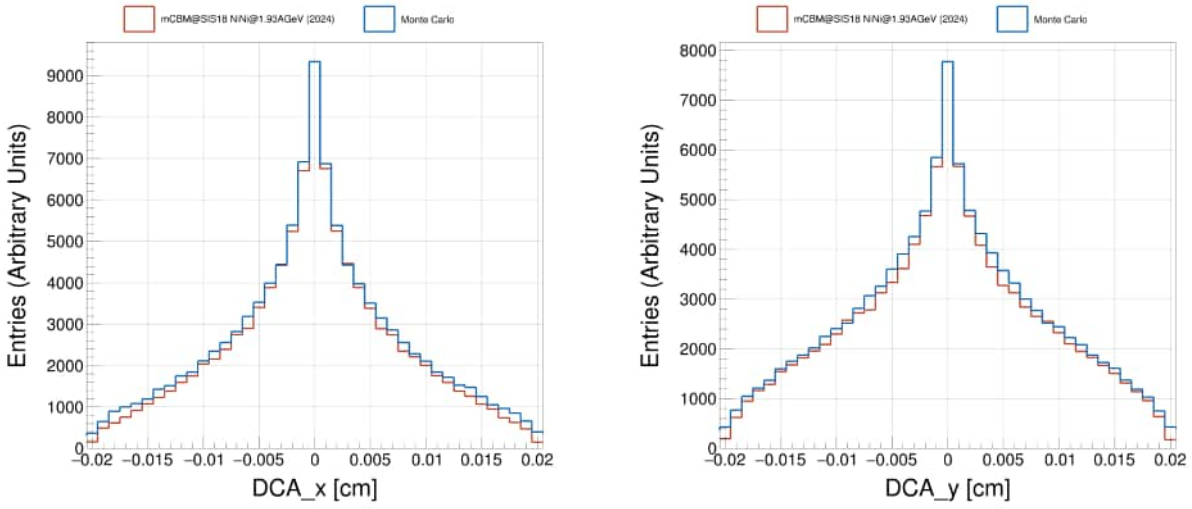

Figure 8: Track impact parameter distribution, in X (left) and Y (right), for real (red) and simulated (blue) data.

3.7. Impact parameter

Track measurements with a precision of a few µm near the interaction point allow the determination of decay vertices, which is crucial for reconstructing complex decay topologies. The impact parameter (IP) of a track is defined as the transverse distance of closest approach (DCA) of a particle trajectory to the primary vertex. Tracks from weak

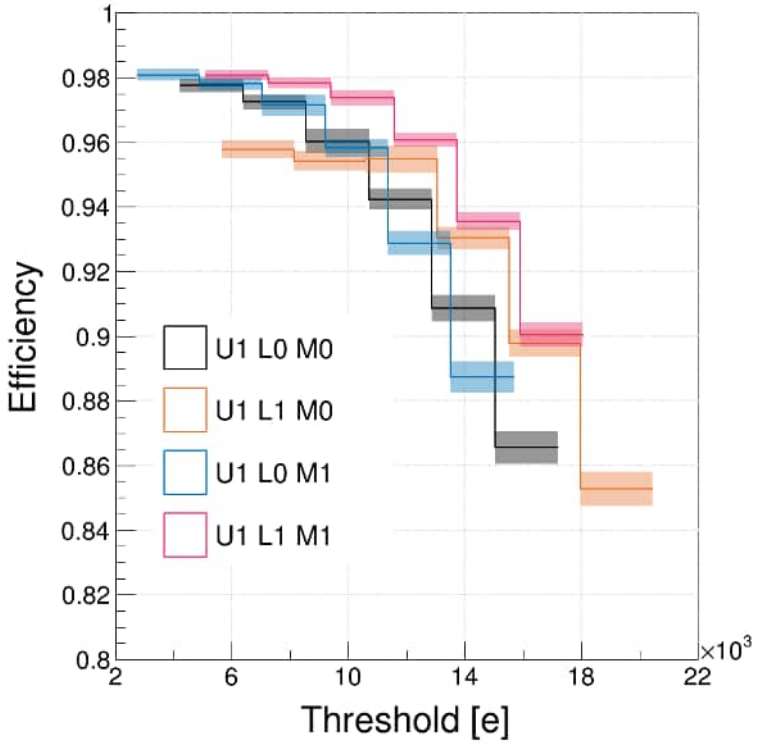

Figure 9: Hit reconstruction efficiency as a function of the threshold for different detectors of Station 1. Here, "U1" refers to the Station, "L" refers to the ladder, and "M" refers to the module. The solid line represents the averaged efficiency for a well-selected active area within the sensor. The error band represents both statistical and systematic uncertainties.

decays typically have larger IPs than those from the PV. Since there is no magnetic field in the mCBM setup, tracks are extrapolated to the primary vertex with a linear extrapolation. The IP resolution is governed by three main factors: multiple scattering of particles in detector material, the single hit resolution, and the distance between the PV and the closest measurement in the detector. The IP resolution can be determined by examining the widths of the distributions of the 1-D projections of the IP in x and y, shown in Fig. 8. The FWHM, proportional to uncertainty in the hit measurement, is about ∼50(60) µm in X (Y), respectively.

The analysis is reproduced with Monte Carlo simulations, in which Ni+Ni collision events were generated using UrQMD [15, 16, 17] and transported using GEANT3 [18]. The primary vertex is smeared according to the distribution obtained from real data. The data were further digitized and processed with the same reconstruction chain as real data, Fig. 6. The IP distributions, shown in Fig. 8 for real data, are in excellent agreement with those extracted from MC simulations.

3.8. Hit reconstruction efficiency

The hit reconstruction efficiency corresponds to the probability of detecting a particle passing through the sensor. It can be determined as the measured fraction of hits on a track per possible hits along the track trajectory. In order to avoid bias from particles that decay (and therefore may have no signal in the first STS station) or are absorbed (and have no signal in the last STS station), this study refers to the middle STS station. Tracks used as references are those reconstructed with hits in all other detector layers, i.e., the first and last STS stations, and at least one hit in a TRD station and one in a TOF station to suppress fake combinations. Furthermore, tracks were requested to originate from the primary vertex, i.e., a cut of 1.5 mm for the DCA of the track to the vertex and 2.5 mm in the z direction. The efficiency is measured as a ratio of the number of tracks where all stations detected a hit over the number of tracks where at least the reference modules detected a hit.

The tracks found using only the reference stations were interpolated to the test module. Only tracks with the projected impact point within the test sensor's sensitive area are used. The region around the projected impact point

was searched for hits using the fit results of the hit-track residual distribution. A hit is considered to belong to a track if its position is within $3\,\sigma$ from the extrapolated impact point, as from Fig. 5.

The efficiency was found to be very uniform across the sensor active area, while the missing hits are concentrated along noisy or dead strips of the module. The particle loss is thus a direct consequence of the module production defects. The efficiency of the module areas with nominal strip noise and absence of bonding defects is about 98%.

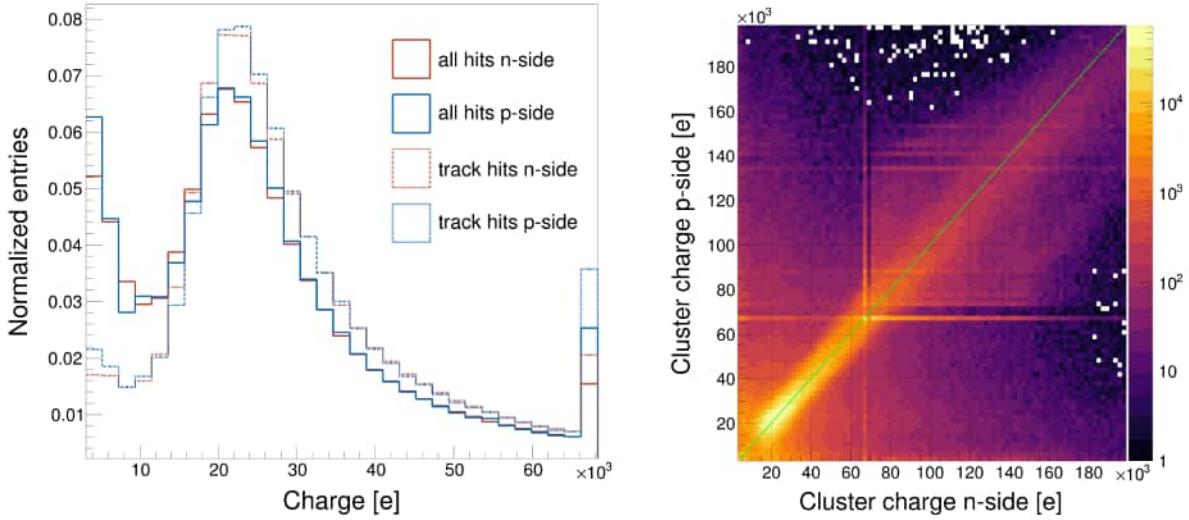

Figure 10: Top: Signal amplitude distribution for n- and p-side. The overflow bin is filled at the upper end of the charge digitization range. Bottom: correlation between the signal amplitude on both sides of a module. Clusters that include one or more signals in the overflow bin result in vertical and horizontal lines at multiples of the digitization range.

Furthermore, the threshold dependence of the hit reconstruction efficiency was studied. If the signal amplitude deposited in a given strip is below the digitization threshold, the signal in that channel is not recorded, resulting in a loss of information. If a major part of the energy deposited by the particle's passage through the detector is recorded by neighboring strips, only the spatial resolution is worsened; however, increasingly high thresholds will result in a reduction of hit detection efficiency. For these studies, the entire data analysis was performed for discrete increments of the digitization thresholds of raw strip signals. Figure 9 shows the hit reconstruction efficiency for the modules in the middle station as a function of the digitization threshold.

3.9. Amplitude measurement and signal-to-noise ratio

The measured signal amplitude is compared to the noise measurements determined beforehand in the module characterization to evaluate the signal-to-noise ratio. The noise (N) is quantified as the average equivalent noise charge of the modules from the smearing of the discriminator response to a given pulse value. It amounts to around 1000 e ENC, in agreement with the estimation based on the total detector capacitance [3]. The signal (S) is determined by the most probable charge amplitude produced by minimum ionizing particles produced in the collision.

Figure 10 shows the signal amplitude distribution for p- and n-side. The left panel shows the correlation between the signal amplitude on both sides of the sensor. The readout ASICs of the STS modules were calibrated in a charge range of approximately 10 fC (65 ke), with ADC gain of 0.335 ± 0.003 fC/LSB (about 2000 e/LSB) both for n- and p-side. The modules were operated at rather low thresholds (down to $3\,\sigma$, i.e., approximately 3000 e). The signal amplitude is shown for all reconstructed hits and, in order to minimize noise and background, only for those hits that were further correlated by tracking to outer detectors. This signal corresponds to the typical admixture produced in heavy-ion collisions of pions, protons, and kaons. The remaining contribution from noise is visible in the lower part of the distribution, i.e., below 10 ke, largely suppressed when requiring that the hits belong to fully reconstructed tracks. The average signal (S) is extracted by fitting the distributions with a Landau function, resulting in a most probable value of 22.7 ± 1.4 ke. For the estimation of the errors, the ADC gain, threshold spread, and the systematic error of the fitting were taken into account. The statistical error of the fitting was considered negligible with respect to the systematic error. Using the corresponding noise measurements of about 1000 e ENC, a signal-to-noise ratio S/N around 23 is determined.

4. Summary

The operational performance of the prototype STS system for the CBM experiment was studied in a heavy-ion collision experiment with a beam energy of around 1–2 AGeV at the mCBM setup at SIS18. Precision track and vertex reconstruction has been demonstrated in the hit-track residual distribution, vertex position, and transverse impact parameter resolutions. Given some residual misalignment in these prototype experiments, a spatial resolution around 25 µm is consistent with the theoretical estimate of the coordinate resolution of the sensor with 58 µm strip pitch. A timing resolution around or better than 5 ns has been demonstrated. The deadtime was estimated between 200 ns and 350 ns. The readout electronics of the modules demonstrated stable operation under conditions of a detector load of 56 MHz/s/channel. Operating the detector with low thresholds, around 3–4 σ RMS amplitude of the noise, the typical dark rate observed was around 0.5 kHit/s/channel, which is less than 1% of the maximum measured or the expected bandwidth saturation limit. In these conditions, the efficiency of hit reconstruction is found to be 98% for the areas where all channels were operational. A signal-to-noise ratio above 20 was measured.

In conclusion, the operational performance of the Silicon Tracking System detector, as evaluated through prototype experiments, aligns with the requirements set for the upcoming CBM experiment. The detector meets the demanding standards for precise tracking, vertex determination, momentum reconstruction, and data throughput, ensuring its readiness to support the CBM experiment's experimental needs.

References

[1] T. Ablyazimov and et al., "Challenges in QCD matter physics - the scientific programme of the compressed baryonic matter experiment at fair," *The European Physical Journal A*, vol. 53, p. 60, 2017.

[2] J. Heuser, W. Müller, V. Pugatch, P. Senger, C. J. Schmidt, C. Sturm, and U. Frankenfeld, eds., *[GSI Report 2013-4] Technical Design Report for the CBM Silicon Tracking System (STS).* Darmstadt: GSI, 2013.

[3] A. R. Rodríguez, O. M. Rodríguez, J. Lehnert, A. Toia, M. Teklishyn, A. Lymanets, D. R. Garcés, J. M. Heuser, and C. J. Schmidt, "Functional characterization of modules for the silicon tracking system of the CBM experiment," *Nuclear Instruments and Methods in Physics Research Section A: Accelerators, Spectrometers, Detectors and Associated Equipment*, vol. 1058, p. 168813, 2024.

[4] "Hamamatsu photonics k.k.," 2023.

[5] K. Kasinski, A. Rodriguez-Rodriguez, J. Lehnert, W. Zubrzycka, R. Szczygiel, P. Otfinowski, R. Kleczek, and C. Schmidt, "Characterization of the STS/MUCH-XYTER2, a 128-channel time and amplitude measurement IC for gas and silicon microstrip sensors," *Nuclear Instruments and Methods in Physics Research Section A: Accelerators, Spectrometers, Detectors and Associated Equipment*, vol. 908, pp. 225–235, 2018.

[6] CBM Collaboration, "mCBM@SIS18," *Darmstadt: CBM Collaboration*, p. GSI 58 S. (2017)., 2017.

[7] CBM Collaboration, "The transition radiation detector of the CBM Experiment at FAIR : Technical Design Report for the CBM Transition Radiation Detector (TRD)," Tech. Rep. FAIR Technical Design Report, Darmstadt, 2018.

[8] N. Herrmann, ed., *Technical Design Report for the CBM Time-of-Flight System (TOF).* Darmstadt: GSI, 2014.

[9] "Technical design report for the CBM ring Imaging Cherenkov Detector," tech. rep., 2013.

[10] "Technical Design Report for the CBM Online Systems – Part I, DAQ and FLES Entry Stage," PUB:(DE-HGF)3 / PUB:(DE-HGF)29 -, Darmstadt, 2023.

[11] V. Friese, "A cluster-finding algorithm for free-streaming data," *EPJ Web of Conferences*, vol. 214, p. 01008, 9 2019.

[12] H. Malygina and V. Friese, "A precision device needs precise simulation: Software description of the CBM silicon tracking system," *Journal of Physics: Conference Series*, vol. 898, p. 042022, 10 2017.

[13] V. Akishina, I. Kisel, I. Vassiliev, and M. Zyzak, "Time-based reconstruction of free-streaming data in cbm," *EPJ Web of Conferences*, vol. 173, p. 04002, 2 2018.

[14] R. L. Workman and et al., "Review of particle physics," *PTEP*, vol. 2022, p. 083C01, 2022.

[15] A. Bass and et al., "Microscopic models for ultrarelativistic heavy ion collisions," *Prog. Part. Nucl. Phys.*, vol. 41, pp. 225–370, 1998.

[16] M. Bleicher and et al., "Relativistic hadron-hadron collisions in the ultra-relativistic quantum molecular dynamics model," *J. Phys. G: Nucl. Part. Phys.*, vol. 25, pp. 1859–1896, 1999.

[17] H. Petersen, J. Steinheimer, G. Burau, M. Bleicher, and H. Stöcker, "Fully integrated transport approach to heavy ion reactions with an intermediate hydrodynamic stage," *Phys. Rev. C*, vol. 78, p. 044901, 2008.

[18] R. Brun, F. Bruyant, F. Carminati, S. Giani, M. Maire, A. McPherson, G. Patrick, and L. Urban, *GEANT: Detector Description and Simulation Tool*. CERN Program Library, Geneva: CERN, 1993. Long Writeup W5013.

Appendix E

Extended acknowledgments

There is a long list of people who contributed in unique ways and managed so this research could meet its completion (at least partially, given that the search for **the truth** is infinite). Therefore, I will take the risk of making such a list and be brief about what I consider the most impactful contribution.

To my friends and colleagues. The names are for those who do not or might not know them, while the brief is meant mainly for their understanding (sorted by last name in alphabetical order):

Kshitij Agarwal: for going through my manuscript with me many times, and the crucial discussion about how to write it. I was truly happy every time I agreed with you that the writing was ugly and lacked structure, always seeking ways to improve.

Rosalia Aguirre Batista: for exercising your profession as a designer and helping me out with ugly figures and color mismatching. Thanks for searching and creating (I forgot how many) different color palettes till I was happy. Thanks for being my "Bruja Tofado".

Diana Alvear Terrero: for the academic support and countless unnecessary corrections of my spoken language. Thanks for your constructive criticisms.

Nora Bluhme: for the discussion on detector alignment and pointing out the good papers.

Raquel Espino Lopez: for being a friend at a distance, that is not easy stuff.

Pablo García Gil: Thanks for the discussion during lunchtime and coffee breaks; it's always helpful to find a new approach to trivial problems.

David Gutierrez Menendez: "A wizard is never late, nor is he early, he arrives precisely when he means to." What better quote than that to thank for the constant support over the last period, preparing the final version of my analysis.

Dr. Johann Heuser, for your active support within the group and the positive reinforcement after almost every talk.

Alexander Helm: for your valuable lessons on German culture, which are quite advantageous for developing smooth research within Germany.

Jose Angel Lesteiro Tejada: for the many discussions on physics, statistical methods, and many hours of existential crisis in the digital world while chopping trees.

Oleksii Lubynets: for the insufferable interruptions and questions, being my office partner.

Adrian Lopéz Vergara: for sharing countless climbing hours, necessary to keep myself sane in the endless writing period.

Osnan Maragoto Rodríguez: for 1000+ hours of Dota2 that brought me almost to Immortal rank (yeah sure), for all those games we bought and played only once, and for all those times, I beat you playing basketball (chopapala). Thanks for your LaTeX templates.

Shaifali Mehta: for the lengthy discussion on CBM STS ladder assembly and vibrational studies. The preparation that you helped me with for that talk was essential in gaining a global picture of my research.

Claire-Anne Reidel: for the detector alignment discussion and taking the time to go into such detail about the methods. For all those "Domino" games you never won against me.

Dairon Rodríguez Garcés: for coming to the rescue of a broken old Russian car during the Cuban tough times. For the lengthy discussions of 'guayabas', purely imaginary metrics, and stupid chess moves. Thanks for being there without complaining every time I called for you.

Adrián Rodríguez Rodríguez: for your couch in the first troubling weeks of my Ph.D journey during the COVID-19 times (and my only fully drunk time). Thanks for facing countless stupid questions and repeating yourself enough till I understood the answers.

Katia Santos Marrero: for being the first person I talk to among my university classmates, for leading by example, facing your fears, going down Bettacorca.

Mehulkumar Shiroya: thanks for the many discussions on analysis, and saving my life every time with ROOT geometry requests.

Maikel Salas Zaldívar: for your expertise in pattern recognition, essential in finding inactive areas. (Gracias primo)

Maksym Teklishin: for the constructive criticism and academic discussions.

Jorge Luis Valdes Albuernes: "mojón", you have always been there, even when we "disappear". All those long study nights are still the reason I remember the important stuff I

need today for my Ph.D.

Norge Viscay Zaldívar: Having a Google expert programmer is handy when you face coding issues. I could not thank you enough for all that I have learned from you, and every pothole you helped me avoid in the coding regard. (por los laguitos tambien, jejeje)

Jennifer Steitz and Annette Zimbelius: for your guidance upon my arrival at GSI, which was fundamental for the rapid establishment and commitment to the research.

Last but not least, a massive thank you to the members of the CBM collaboration, who generously share their knowledge at every meeting. You might never realize it, but I was paying attention and learned a lot from you.

List of Figures

List of Tables

Bibliography

[1] D. Menezes, "Modelling hadronic matter," *Journal of Physics: Conference Series*, vol. 706, p. 032001, 04 2016.

[2] F. Gross *et al.*, "50 years of quantum chromodynamics," *The European Physical Journal C*, vol. 83, p. 1125, 2023.

[3] A. Andronic, P. Braun-Munzinger, K. Redlich, and J. Stachel, "Decoding the phase structure of QCD via particle production at high energy," *Nature*, vol. 561, no. 7723, pp. 321–330, 2018.

[4] T. Galatyuk, "Interaction rate facilities repository," 2025. Accessed: 2025-02-22.

[5] CBM Collaboration, "Cbm GSI website," 2024.

[6] T. Stöhlker, V. Bagnoud, K. Blaum, A. Blazevic, A. Bräuning-Demian, M. Durante, F. Herfurth, M. Lestinsky, Y. Litvinov, S. Neff, R. Pleskac, R. Schuch, S. Schippers, D. Severin, A. Tauschwitz, C. Trautmann, D. Varentsov, and E. Widmann, "Appa at fair: From fundamental to applied research," *Nuclear Instruments and Methods in Physics Research Section B: Beam Interactions with Materials and Atoms*, vol. 365, pp. 680–685, 2015. Swift Heavy Ions in Matter, 18 – 21 May, 2015, Darmstadt, Germany.

[7] A. Herlert, "NUSTAR - The teenage years," *Hyperfine Interact.*, vol. 238, no. 1, p. 35, 2017.

[8] M. Destefanis, "The PANDA experiment at FAIR," *Nuclear Physics B - Proceedings Supplements*, vol. 245, pp. 199–206, 2013.

[9] G. Agakishiev *et al.*, "The high-acceptance dielectron spectrometer hades," *Eur. Phys. J. A*, vol. 41, pp. 243–277, 2009.

[10] B. David, A. Jörg, B. Elena, F. Volker, G. Marek, R. Jørgen, R. Oleg, T. Oleg, and T. Viacheslav, "Topical issue on exploring strongly interacting matter at high densities - NICA white paper," *Eur. Phys. J. A*, vol. 52, p. 267, 2016.

[11] J. Adams *et al.*, "Experimental and theoretical challenges in the search for the quark gluon plasma: The STAR collaboration's critical assessment of the evidence from RHIC collisions," *Nucl. Phys. A*, vol. 757, pp. 102–183, 2005.

[12] L. McLerran, "Quarkyonic matter and the revised phase diagram of qcd," *Nuclear Physics A*, vol. 830, pp. 709c–712c, 2009. Quark Matter 2009.

[13] M. M. Aggarwal *et al.*, "An experimental exploration of the QCD phase diagram: The search for the critical point and the onset of de-confinement," 7 2010.

[14] T. Ablyazimov *et al.*, "Challenges in QCD matter physics - the scientific programme of the compressed baryonic matter experiment at fair," *The European Physical Journal A*, vol. 53, p. 60, 2017.

[15] W. Reisdorf *et al.*, "Systematics of central heavy ion collisions in the 1a gev regime," *Nuclear Physics A*, vol. 848, pp. 366–427, 2010.

[16] J. Steinheimer, J. Auvinen, H. Petersen, M. Bleicher, and H. Stöcker, "Examination of directed flow as a signal for a phase transition in relativistic nuclear collisions," *Phys. Rev. C*, vol. 89, p. 054913, May 2014.

[17] J.-W. Chen, J. Deng, and L. Labun, "Baryon susceptibilities, non-gaussian moments, and the QCD critical point," *Phys. Rev. D*, vol. 92, p. 054019, Sep 2015.

[18] M. A. Stephanov, "Sign of kurtosis near the QCD critical point," *Phys. Rev. Lett.*, vol. 107, p. 052301, Jul 2011.

[19] P. B. Demorest, T. Pennucci, S. M. Ransom, M. S. E. Roberts, and J. W. T. Hessels, "A two-solar-mass neutron star measured using shapiro delay," *Nature*, vol. 467, pp. 1081–1083, 2010.

[20] T. Matsui and H. Satz, "J/ψ suppression by quark-gluon plasma formation," *Physics Letters B*, vol. 178, pp. 416–422, 1986.

[21] P. M. Hohler and R. Rapp, "Is ρ-meson melting compatible with chiral restoration?," *Physics Letters B*, vol. 731, pp. 103–109, 2014.

[22] R. Rapp and H. van Hees, "Thermal dileptons as fireball thermometer and chronometer," *Physics Letters B*, vol. 753, pp. 586–590, 2016.

[23] S. Navas *et al.*, "Review of particle physics," *Phys. Rev. D*, vol. 110, no. 3, p. 030001, 2024.

[24] G. Viehhauser and T. Weidberg, *Detectors in Particle Physics*. CRC Press, 3 2024.

[25] R. L. Workman *et al.*, "Review of particle physics," *PTEP*, vol. 2022, p. 083C01, 2022.

[26] R. Gluckstern, "Uncertainties in track momentum and direction, due to multiple scattering and measurement errors," *Nuclear Instruments and Methods*, vol. 24, pp. 381–389, 1963.

[27] Z. Drasal and W. Riegler, "An extension of the gluckstern formulae for multiple scattering: Analytic expressions for track parameter resolution using optimum weights," *Nuclear Instruments and Methods in Physics Research Section A: Accelerators, Spectrometers, Detectors and Associated Equipment*, vol. 910, pp. 127–132, 2018.

[28] Y. V. Karasev, V. Y. Korpusov, A. V. Malchenkov, I. N. Gubkin, N. I. Salunin, E. V. Nikulenkov, M. V. Polikarpova, P. A. Lukyanov, N. A. Mezentsev, and A. V. Bragin, "The superconducting nbti wire for the CBM dipole magnet," *Journal of Superconductivity and Novel Magnetism*, vol. 35, pp. 705–710, Mar 2022.

[29] M. Koziel *et al.*, "The prototype of the micro vertex detector of the CBM experiment," *Nuclear Instruments and Methods in Physics Research Section A: Accelerators, Spectrometers, Detectors and Associated Equipment*, vol. 732, pp. 515–518, 2013. Vienna Conference on Instrumentation 2013.

[30] J. Stroth and M. Deveaux, "Technical design report for the CBM: Micro Vertex Detector (MVD)," Tech. Rep. 1, GSI Helmholtzzentrum für Schwerionenforschung Gmbh, 2022. BMBF ErUM-FSP-T06: C.B.M.@FAIRBilateral Contract GSI - Goethe University FrankfurtHIC for FAIRHelmholtz Forschungsakademie Hessen fuer FAIRIN2P3-IPHC Strasbourg.

[31] J. Adamczewski-Musch *et al.*, "The CBM RICH detector," *Journal of Instrumentation*, vol. 11, p. C05016, 5 2016.

[32] S. Chattopadhyay, Y. P. Viyogi, P. Senger, W. F. J. Müller, and C. J. Schmidt, eds., *Technical Design Report for the CBM : Muon Chambers (MuCh)*. Darmstadt: GSI, 2015.

[33] R. P. Adak, A. Kumar, A. K. Dubey, S. Chattopadhyay, S. Das, S. Raha, S. Samanta, and J. Saini, "Performance of a large size triple GEM detector at high particle rate for the CBM experiment at fair," *Nuclear Instruments and Methods in Physics Research Section A: Accelerators, Spectrometers, Detectors and Associated Equipment*, vol. 846, pp. 29–35, 2017.

[34] CBM Collaboration, "The transition radiation detector of the CBM Experiment at FAIR : Technical Design Report for the CBM Transition Radiation Detector (TRD)," Tech. Rep. FAIR Technical Design Report, Darmstadt, 2018.

[35] N. Herrmann, ed., *Technical Design Report for the CBM Time-of-Flight System (TOF)*. Darmstadt: GSI, 2014.

[36] M. Petriş *et al.*, "Time and position resolution of high granularity, high counting rate MRPC for the inner zone of the CBM-TOF wall," *Journal of Instrumentation*, vol. 11, p. C09009, sep 2016.

[37] P. Senger and V. Friese, "CBM progress report 2022," Tech. Rep. CBM PR 2022, GSI Helmholtzzentrum für Schwerionenforschung Gmbh, Darmstadt, 2022.

[38] M. Zyzak, *Online selection of short-lived particles on many-core computer architectures in the CBM experiment at FAIR*. Dr., Johann Wolfgang Goethe-Universität Frankfurt, 2016. Johann Wolfgang Goethe-Universität Frankfurt, Diss., 2016.

[39] J. Heuser, W. Müller, V. Pugatch, P. Senger, C. J. Schmidt, C. Sturm, and U. Frankenfeld, eds., *[GSI Report 2013-4] Technical Design Report for the CBM Silicon Tracking System (STS)*. Darmstadt: GSI, 2013.

[40] V. Friese, C. Sturm, and A. Toia, eds., *CBM Progress Report 2015*. Darmstadt: GSI, 2016. Literaturang.

[41] S. Mehta, *Investigation of thermal and structural integrity of modules and ladders of Silicon Tracking System of the CBM experiment*. PhD thesis, Eberhard Karls University of Tuebingen, 2024.

[42] I. Selyuzhenkov and A. Toia, eds., *CBM Progress Report 2016*. Darmstadt: GSI, 2017. Literaturangaben.

[43] P. Senger and V. Friese, "CBM progress report 2021," Tech. Rep. 2022, GSI Helmholtzzentrum für Schwerionenforschung Gmbh, Darmstadt, 2022.

[44] H. Spieler, *Semiconductor Detector Systems*. Oxford University Press, 08 2005.

[45] K. Agarwal, *Thermal Management of the Silicon Tracking System of the CBM Experiment at FAIR*. PhD thesis, Eberhard Karls University of Tuebingen, 2024.

[46] V. Friese, C. Sturm, and A. Toia, eds., *CBM Progress Report 2015*. Darmstadt: GSI, 2016. Literaturang.

[47] https://www.gsi.de/work/forschung/cbmnqm/cbm/activities/mcbm.

[48] J. Stadlmann, L. Bozyk, P. Forck, D. Ondreka, R. Singh, and P. Spiller, "Sis18 operation and recent development," in *14th International Particle Accelerator Conference*, 2023.

[49] U. Blell, J. Florenkowski, U. Kopf, C. Muhle, M. Petryk, I. Petzenhauser, P. Spiller, A. Batrakov, S. Onischenko, and G. Ozur, "Development of the injection- and extraction systems for the upgrade of sis18," in *2007 IEEE Particle Accelerator Conference (PAC)*, pp. 167–169, 2007.

[50] B. Gålnander, E. Kozlova, D. Ondreka, A. Sokolov, P. J. Spiller, and J. Stadlmann, "studying X-ray spectra of the sis18 electrostatic septa to measure their electric field," *Proceedings of IPAC2021*, pp. 4065–4067, 2021.

[51] J. Yang, P. Boutachkov, P. Forck, T. Milosic, R. Singh, and S. Sorge, "Beam characterization of slow extraction measurement at GSI-sis18 for transverse emittance exchange experiments," in *Proceedings of the International Beam Instrumentation Conference, IBIC*, pp. 318–322, JACoW Publishing, 2022.

[52] C. Collaboration, "mcbm@sis18," *Darmstadt : CBM Collaboration*, p. GSI 58 S. (2017)., 2017.

[53] "CBM progress report 2018," Tech. Rep. CBM Progress Report 2018, Darmstadt, 2019.

[54] A. Rost, T. Galatyuk, V. Kedych, M. Kis, W. Krüger, J. Pietraszko, A. Senger, J. Thaufelder, and F. Ulrich-Pur, "beam-diagnostic and t0 system for the mcbm and CBM experiments at GSI and fair," in *Proceedings of the International Beam Instrumentation Conference, IBIC*, pp. 66–69, JACoW Publishing, 2023.

[55] "CBM progress report 2023," Tech. Rep. CBM Progress Report 2023, GSI Helmholtzzentrum für Schwerionenforschung Gmbh, 2024. CCBY4.

[56] I. Panasenko, E. Lavrik, A. Lymanets, and H. R. Schmidt, "A custom probe station for microstrip detector quality assurance of the CBM experiment," *Journal of Physics: Conference Series*, vol. 742, p. 12037, 8 2016.

[57] P. Senger and V. Friese, "Cbm progress report 2020," 2021.

[58] A. R. Rodríguez, O. M. Rodríguez, J. Lehnert, A. Toia, M. Teklishyn, A. Lymanets, D. R. Garcés, J. M. Heuser, and C. J. Schmidt, "Functional characterization of modules for the silicon tracking system of the CBM experiment," *Nuclear Instruments and Methods in Physics Research Section A: Accelerators, Spectrometers, Detectors and Associated Equipment*, vol. 1058, p. 168813, 2024.

[59] R. Brun and F. Rademakers, "Root - an object oriented data analysis framework," *Nuclear Instruments and Methods in Physics Research Section A: Accelerators, Spectrometers, Detectors and Associated Equipment*, vol. 389, no. 1, pp. 81–86, 1997. New Computing Techniques in Physics Research V.

[60] S. A. Bass *et al.*, "Microscopic models for ultrarelativistic heavy ion collisions," *Prog. Part. Nucl. Phys.*, vol. 41, pp. 225–370, 1998.

[61] M. Bleicher *et al.*, "Relativistic hadron-hadron collisions in the ultra-relativistic quantum molecular dynamics model," *J. Phys. G: Nucl. Part. Phys.*, vol. 25, pp. 1859–1896, 1999. Available from LANL e-print.

[62] H. Petersen, D. Oliinychenko, M. Mayer, J. Staudenmaier, and S. Ryu, "Smash - A new hadronic transport approach," *Nuclear Physics A*, vol. 982, pp. 399–402, 02 2019.

[63] J. Aichelin, E. Bratkovskaya, A. L. Fevre, V. Kireyeu, V. Kolesnikov, Y. Leifels, V. Voronyuk, and G. Coci, "Parton-hadron-quantum-molecular dynamics (PHQMD) - A novel microscopic N-body transport approach for heavy-ion collisions, dynamical cluster formation and hypernuclei production," *Phys. Rev. C*, vol. 101, no. 4, p. 044905, 2020.

[64] M. Baznat, A. Botvina, G. Musulmanbekov, V. Toneev, and V. Zhezher, "Monte-carlo generator of heavy ion collisions DCM-smm," *Phys. Part. Nucl. Lett.*, vol. 17, no. 3, pp. 303–324, 2020.

[65] R. Brun, F. Bruyant, M. Maire, A. C. McPherson, and P. Zanarini, "Geant3," 9 1987.

[66] S. Agostinelli *et al.*, "Geant4-a simulation toolkit," *Nuclear Instruments and Methods in Physics Research Section A: Accelerators, Spectrometers, Detectors and Associated Equipment*, vol. 506, no. 3, pp. 250–303, 2003.

[67] J. Allison *et al.*, "Geant4 developments and applications," *IEEE Transactions on Nuclear Science*, vol. 53, no. 1, pp. 270–278, 2006.

[68] J. Allison *et al.*, "Recent developments in geant4," *Nuclear Instruments and Methods in Physics Research Section A: Accelerators, Spectrometers, Detectors and Associated Equipment*, vol. 835, pp. 186–225, 2016.

[69] C. Collaboration, "Technical design report for the CBM online systems - part I, DAQ and FLES entry stage," 2023.

[70] "Technical Design Report for the CBM Online Systems – Part I, DAQ and FLES Entry Stage," PUB:(DE-HGF)3 / PUB:(DE-HGF)29 -, Darmstadt, 2023. FAIR Technical Design Report; ccby4.

[71] K. Kasinski et al., "Characterization of the STS/MUCH-xyter2, a 128-channel time and amplitude measurement IC for gas and silicon microstrip sensors," *Nuclear Instruments and Methods in Physics Research, A*, vol. 908, pp. 225–235, 2018.

[72] K. Kasinski, R. Szczygiel, W. Zabolotny, J. Lehnert, C. Schmidt, and W. Müller, "A protocol for hit & control synchronous transfer for the front-end electronics at the CBM experiment," *Nuclear Instruments and Methods in Physics Research Section A: Accelerators, Spectrometers, Detectors and Associated Equipment*, vol. 835, 08 2016.

[73] V. Akishina, I. Kisel, I. Vassiliev, and M. Zyzak, "Time-based reconstruction of free-streaming data in cbm," *EPJ Web of Conferences*, vol. 173, p. 04002, 2 2018.

[74] V. Friese, "A cluster-finding algorithm for free-streaming data," *EPJ Web of Conferences*, vol. 214, p. 01008, 9 2019.

[75] H. Malygina, *Hit reconstruction for the Silicon Tracking System of the CBM experiment.* doctoralthesis, Universitätsbibliothek Johann Christian Senckenberg, 2018.

[76] I. Momot, *Characterization and radiation hardness studies of the silicon microstrip sensors for the CBM experiment.* PhD thesis, Goethe U., Frankfurt (main), 2019.

[77] O. M. Rodriguez, *Characterization and commissioning of the front-end electronics for the silicon Tracking System of the experiment.* PhD thesis, 2023.

[78] H. Malygina, V. Friese, and M. Zyzak, "Hit reconstruction in the CBM silicon tracking system," in *2016 IEEE Nuclear Science Symposium, Medical Imaging Conference and Room-Temperature Semiconductor Detector Workshop (NSS/MIC/RTSD)*, pp. 1–6, 2016.

[79] V. Akishina, "Four-dimensional event reconstruction in the CBM experiment," 2016.

[80] B. Alpat, "Characterization of a silicon microstrip detector with radioactive source," 2003.

[81] J. J. Hopfield, "Artificial neural networks," *IEEE Circuits and Devices Magazine*, vol. 4, pp. 3–10, 1988.

[82] D. Funke, T. Hauth, V. Innocente, G. Quast, P. Sanders, and D. Schieferdecker, "Parallel track reconstruction in CMS using the cellular automaton approach," *Journal of Physics: Conference Series*, vol. 513, p. 52010, 6 2014.

[83] V. Akishina and I. Kisel, "Online 4-dimensional reconstruction of time-slices in the CBM experiment," *IEEE Transactions on Nuclear Science*, vol. 62, pp. 3172–3176, 2015.

[84] G. Giacomini, "Noise characterization of silicon strip detectors-comparison of sensors with and without integrated jfet source-follower.," 2007.

[85] A. R. Rodríguez, *The CBM Silicon Tracking System front-end electronics : from bare ASIC to detector characterization, commissioning and performance.* doctoralthesis, Universitätsbibliothek Johann Christian Senckenberg, 2020.

[86] A. Rost, T. Galatyuk, V. Kedych, M. Kis, W. Krüger, J. Pietraszko, A. Senger, J. Thaufelder, and F. Ulrich-Pur, "Beam-diagnostic and t0 system for the mcbm and CBM experiments at GSI and fair," *JACoW*, vol. IBIC2023, p. MOP018, 2023.

[87] A. R. Rodriguez, "The silicon tracking system of CBM: towards tests with heavy ion collisions," IEEE, 10 2019.

[88] X. Wang, L. Yan, and Q. Zhang, "Research on the application of gradient descent algorithm in machine learning," pp. 11–15, 2021.

[89] D. Soydaner, "A comparison of optimization algorithms for deep learning," *International Journal of Pattern Recognition and Artificial Intelligence*, vol. 34, p. 2052013, 2020.

[90] N. Bluhme, S. Gorbunov, and V. Lindenstruth, "Application of linear and non-linear constraints in a brute-force based alignment approach for cbm." Poster presentation at the Conference on Computing in High Energy and Nuclear Physics, 2024. Presented in 2024.

Dario Alberto Ramirez Zaldivar

Nuclear Physicist - Data Analyst - Software Developer

Affiliations: Goethe University Frankfurt, Germany
GSI Helmholtzzentrum, Germany
Address: Plankstr 1 64291 Darmstadt
E-mail: d.ramirez@gsi.de, googol23nphy@gmail.com
Born: May 4, 1994, Holguin, Cuba
Homepage: https://googol23.github.io/dramirez/index.html

Skill Summary:

Lenguages: Spanish (native), English (proficient)
Programming: C/C++ (advanced), Python (advanced), LaTeX (advaced), SQL (intermediate), JavaScript (basic)
Additional tools: Git, ROOT, Geant4, Origin
Soft skills: Communication: Making an Impact as an Effective Researcher (HGS-Hire)
Leadership: Leading Teams in a Research Environment (HGS-Hire)

Professional experience:

- **2021 - Present:** Ph.D. researcher, GSI - STS – CBM experiment.
  Performance analysis of Silicon Tracking System based on double-sided silicon microstrip sensor.
- **2018 - 2021:** Junior Researcher, InSTEC - Theoretical nuclear physics department.
  Assistant professor on Quantum Mechanics and Thermodynamics and Statistical Physics lectures

Education:

- **May 2021 - Present:** Ph.D. student, Goethe University Frankfurt.
  Thesis: *Performance evaluation of the prototype CBM Silicon Tracking System: Results from operation in the mCBM at the SIS18 demonstrator experiment*
  Supervisor: Prof. Dr. Alberica Toia
- **Sep 2013 - Jul 2018:** Diploma in Nuclear Physics, Instituto Superior de Tecnologías y Ciencias Aplicadas (InSTEC), Havana, Cuba.
  Thesis: *Quarkonia dynamic in nuclear media*
  Supervisor: Prof. Dr. Fernando Guzmán Martínez

Summer schools and internships:

- **Jul 2019 - Sep 2019:** JINR Summer School, Dubna, Rusia.
  Work Topic: *$\chi c1$ and $\chi c2$ reconstruction from pp collision at $\sqrt{s_{NN}}$ = 26 GeV at SPD.*

Supervisor: Dr. Alexey Guskov

- **Jun 2018 - Aug 2018:** DESY Summer School, Hamburg.
  Work Topic: *Study of Drell-Yan Z-boson production in pPb collision at* $\sqrt{s_{NN}}$ = *5.02 TeV.*
  Supervisor: Doc. Dr. Hannes Jung
- **Mar 2018 - May 2018:** JINR Internship, Dubnam, Rusia.
  Work Topic: *Training on Monte Carlo simulation data analysis.*
  Supervisor: Dr. Alexey Guskov

Publications:

- D. Ramirez et al. (CBM Collaboration), *Performance of the prototype Silicon Tracking System of the CBM experiment tested with heavy-ion beams at SIS18.* Nuclear Inst. and Methods in Physics Research, A
  Submission Being Processed (June 2025)
- D. Ramirez, D. Rodriguez, H. Jung, F. Guzman, *Study of Z-boson production in di-lepton channel on pPb collisions at* $\sqrt{s_{NN}}$ = *5.02 TeV.* Astron. Nachr., 2019
  https://doi.org/10.1002/asna.201913714
- D. Ramirez, *Performance of hit, track, and vertex reconstruction of the Silicon Tracking System of the CBM experiment.*
  Proceedings: FAIR next generation scientists - 8th Edition Workshop (FAIRness2024), Sept 23-27, 2024, Seget, Croatia
  (On Editorial phase)
- D. Ramirez, *Vertex reconstruction and tracking performance of the STS detector with the mCBM setup at SIS18.*
  Proceedings: The 32nd International Workshop on Vertex Detectors (VERTEX2023), Oct 16–20, 2023, Sestri Levante
  https://doi.org/10.22323/1.448.0064
- D. Ramirez, *Performance of the mSTS detector in O+Ni collisions at 2 AGeV with the mCBM setup at SIS18.*
  Proceedings: FAIR next generation scientists - 7th Edition Workshop (FAIRness2022), May 23 - 27, 2022, Paralia (Pieria, Greece)
  https://doi.org/10.22323/1.419.0050
- D. Ramirez and Toia, A., *Beam spot and vertex reconstruction with mSTS in Ni+Ni collisions at 1.93 AGeV.* CBM Progress Report, 2023
  https://doi.org/10.15120/GSI-2024-00765
- D. Ramirez and Toia, A., *Performance of mSTS in Ni+Ni collisions at 1.93 AGeV.* CBM Progress Report, 2022
  https://doi.org/10.15120/GSI-2023-00384
- D. Ramirez and Toia, A., *Performance of the mSTS detector during the mCBM beam campaign 2021.* CBM Progress Report, 2021
  https://doi.org/10.15120/GSI-2022-00599

Conference Participation:

- XXXI International Conference on Ultrarelativistic nucleus-nucleus collisions (Quark-Matter), April 2025, Frankfurt am Main, Germany.
  Contribution: *Performance of hit, track, and vertex reconstruction of the Silicon Tracking System of the CBM experiment at mCBM@SIS18.*
- DPG Annual spring meeting, March 2025, Germany.
  Contribution: *Performance of hit, track, and vertex reconstruction of the Silicon Tracking System of the CBM experiment.*
- 45th CBM Collaboration Meeting, February 2025, Germany.
  Contribution: *Tracking and vertexing performance of the STS (Highlight talk).*
- XIX Workshop on Nuclear Physics (WONP), October 2024, La Habana, Cuba.
  Contribution: *Performance of hit, track, and vertex reconstruction of the Silicon Tracking System of the CBM experiment.*
- 44th CBM Collaboration Meeting, September 2024, Germany.
  Contribution: *Track and event vertex reconstruction in mCBM.*
- DPG Annual spring meeting, March 2024, Germany.
  Contribution: *Current status in the concept design, assembly, and performance evaluation of the Silicon Tracking System for the CBM experiment (Group Report).*
- 43rd CBM Collaboration Meeting, March 2024, Germany.
  Contribution: *Event vertex using CA track reconstruction.*
- 32nd International Workshop on Vertex Detectors, October 2023, Sestri Levante, Italy.
  Contribution: *Vertex reconstruction and tracking performance of the STS detector with the mCBM setup at SIS18.*
- 42nd CBM Collaboration Meeting, September 2023, Germany.
  Contribution: *Performance studies with STS.*
- 41st CBM Collaboration Meeting, March 2023, Germany.
  Contribution: *Performance of the mSTS detector in O+Ni collisions at 2 AGeV with the mCBM setup at SIS18.*
- DPG Annual spring meeting, March 2023, Germany.
  Contribution: *Performance on the STS detector in Ni+Ni collisions at 1.93 AGeV with the mCBM setup at SIS18.*
- 40th CBM Collaboration Meeting, October 2022, Germany.
- 39th CBM Collaboration Meeting, May 2022, Germany.
  Contribution: *mSTS performance analysis (Highlight talk).*
- FAIR next generation scientists - 8th Edition Workshop (FAIRness2022), May 2022, Sestri Levante, Italy.
  Contribution: *Performance of the mSTS detector in O+Ni collisions at 2 AGeV with the mCBM setup at SIS18.*

- XXIX International Conference on Ultra-relativistic Nucleus-Nucleus Collisions (Quark Matter 2022), April 2022, Krakow, Poland.
  Contribution: *Performance of the mSTS detector in O+Ni collisions at 2 AGeV with the mCBM setup at SIS18.*
- DPG Annual spring meeting, March 2022, Germany.
  Contribution: *Performance of the mSTS detector in O+Ni collisions at 2 AGeV with the mCBM setup at SIS18.*
- 38th CBM Collaboration Meeting, September 2021, Germany.
  Contribution: *Performance of the mSTS detector in O+Ni collisions at 2 AGeV with the mCBM setup at SIS18.*
- II Cuban Encounter of Physics for post-graduated students, 2020, .
  Contribution: *Boson Star based on coupled neutrinos.*
- STAR-SMFNS, 2019, La Habana-Varadero, Cuba.
  Contribution: *Study of Z-boson production in di-lepton channel on pPb collisions at* $\sqrt{s_{NN}}$*=5.02 TeV.*
- CERN Latin-American School of High-Energy Physics, 2019, Córdoba, Argentina.
  Contribution: *Study of Z-boson production in di-lepton channel on pPb collisions at* $\sqrt{s_{NN}}$*=5.02 TeV.*
- XIV ICFA School on Instrumentation in Elementary Particle Physics, 2017, Habana, Cuba.

Awards:

- Giersch Excellence Award 2022.